Numerical modelling of the pelvis and acetabular construct following hip arthroplasty

Andrew Thomas Merricks Phillips

Doctor of Philosophy

The University of Edinburgh

August 2005

Declaration

This thesis and the research described and presented within have been completed in total by Andrew Thomas Merricks Phillips, under the supervision of Dr Pankaj, Dr Asif Usmani and Mr Colin Howie, and has not been submitted for any other degree or profession qualification.

Where other sources are quoted full references are given.

Andrew Thomas Merricks Phillips

August 2005

Acknowledgements

Thanks go in the first instance to my supervisor Dr Pankaj, as well as my second supervisors Dr Asif Usmani and Mr Colin Howie, for their continued support and encouragement throughout the PhD. Thanks also go to all my friends in the School of Engineering and Electronics, who were always there to talk over coffee or lunch. In particular I would like to thank Dr. Antonis Giannopoulos for his help in all matters software related. I'd also like to thank the often undervalued computing support team.

Thanks also go to all my friends and family outside the university. Particular thanks go to my parents, Bill and Viv, and my brother and sister, Iain and Jennifer, who are all constant sources of inspiration. Special thanks go to Kathleen, without whose no nonsense support, this thesis would have been a good deal longer in the writing.

Final thanks go to the Scottish Mechanotransduction Consortium, led by Hamish Simpson and Brendon Noble for funding this work, as well as Edinburgh Orthopaedic Engineering Centre in conjunction with Stryker, and the Department of Orthopaedics at the New Edinburgh Royal Infirmary.

"All men dream: but not equally. Those who dream by night in the dusty recesses of their minds wake in the day to find that it was vanity: but the dreamers of the day are dangerous men, for they may act their dreams with open eyes, to make it possible."

- T.E. Lawrence

Abstract

The study presents finite element models of the acetabular construct and the pelvis. Particular attention is given to investigating the behaviour of the acetabular construct following revision hip arthroplasty, carried out using the Slooff-Ling impaction grafting technique. Mechanical tests are carried out on bone graft, and constitutive models are developed to describe its non-linear elasto-plastic behaviour, for inclusion in finite element analyses. Impaction of bone graft was found to have a significant effect in reducing subsequent development of consolidation plastic strains. A novel approach for the inclusion of muscles and ligaments, in finite element analyses, to provide boundary conditions similar to those found *in vivo* is also presented.

2D analyses of the acetabular construct, following revision hip arthroplasty, carried out using impaction grafting, indicate that for idealised load cases, rotation of the acetabular cup increases, as the depth of the bone graft bed increases. This indicates that it is advantageous to use the largest practical diameter of acetabular cup. Results from 3D analyses of the hemi pelvis, following revision arthroplasty, indicate that different patterns of migration and rotation of the acetabular cup, within the bone graft bed are associated with different physiological activities. For example walking is seen to cause migration of the cup in the superior direction, and rotation of the cup in abduction. Results from 3D analyses of the pelvis indicate that the inclusion of muscles and ligaments, in place of fixed boundary conditions cause significant changes to the stress distribution observed in the cortical bone, but comparatively minor changes to the stresses in the trabecular bone, and bone graft in the acetabular region.

Contents

Title

Copyright

Declaration **i**

Acknowledgements **iii**

Abstract **vii**

Contents **ix**

1 Introduction **1**

1.1 Summary of chapters 4

2 Mechanical properties of the materials comprising the acetabular construct **7**

2.1 Synthetic Materials 9

2.2 Cortical and Trabecular Bone 10

2.3 Morsellised Cortico-Cancellous Bone 13

2.3.1 The behaviour of MCB due to compression loading . . 13
2.3.2 The behaviour of MCB due to shear loading 18
2.3.3 MCB subsidence experiments 19
2.4 Conclusions 20

3 Behaviour of morsellised cortico-cancellous bone 21
3.1 Materials and Methods 22
3.2 Testing and Discussion 25
3.2.1 Test 1 25
3.2.2 Tests 2 and 3 30
3.2.3 Test 4A 38
3.2.4 Test 4B 44
3.2.5 Test 5 48
3.3 Conclusions 52

4 Constitutive models for impacted morsellised cortico-cancellous bone 55
4.1 Non-linear elastic behaviour 56
4.2 Visco-elastic behaviour 59
4.3 Non-linear plastic behaviour 64
4.4 Conclusions 70

5 A plane-strain model of the acetabular construct 73
5.1 Geometric definition 74
5.2 Materials definition 78

5.2.1 Drucker Prager constitutive model 79
5.2.2 Drucker Prager Cap constitutive model 81
5.3 Loading definition 82
5.3.1 Load Case A 83
5.3.2 Load Case B 84
5.4 Response using the Drucker Prager constitutive model 85
5.4.1 Load Case A 85
5.4.2 Load Case B 91
5.5 Response using the Drucker Prager Cap constitutive model . . 96
5.5.1 Load Case A 96
5.5.2 Load Case B 101
5.6 Conclusions 102

6 3D models of the hemi pelvis and acetabular construct 109

6.1 Analysis of the natural hemi pelvis 110
6.1.1 Geometric definition 110
6.1.2 Materials definition 112
6.1.3 Loading definition 113
6.1.4 Results and Discussion 115
6.2 Analysis of the hemi pelvis following primary hip arthroplasty 119
6.2.1 Geometric definition 119
6.2.2 Materials definition 120
6.2.3 Loading definition 120

6.2.4 Results and discussion 122

6.3 Analysis of the hemi pelvis following revision hip arthroplasty, subjected to different load histories 126

6.3.1 Geometric definition 126

6.3.2 Materials definition 129

6.3.3 Loading definition 130

6.3.4 Results and discussion 132

6.3.4.1 Single leg stance 132

6.3.4.2 Normal walking 143

6.3.4.3 Sitting down 151

6.3.4.4 Standing up 159

6.4 Conclusions 167

7 Muscular and ligamentous contributions in a 3D finite element model of the pelvis 169

7.1 Function and muscles of the hip joint 170

7.2 Ligaments forming the pelvic ring 173

7.3 Muscle behaviour 175

7.4 Ligament behaviour 183

7.5 Defining muscle and ligament attachments on the pelvis 184

7.5.1 Single reference point origination areas 184

7.5.2 Multiple reference point origination areas 187

7.5.3 Connector element stiffness properties 191

8 3D models of the pelvis and acetabular construct 193

8.1 Analysis of the pelvis, following primary arthroplasty on both sides, excluding muscular and ligamentous contributions (PAEXML model) . . . 195

8.1.1 Geometric definition . . . 195

8.1.2 Materials definition . . . 196

8.1.3 Loading definition . . . 196

8.1.4 Results and discussion . . . 198

8.2 Analysis of the pelvis, following primary, and revision arthroplasty on the right and left sides, excluding muscular and ligamentous contributions (RAEXML model) . . . 204

8.2.1 Model definition . . . 204

8.2.2 Results and discussion . . . 206

8.3 Analysis of the pelvis, following primary arthroplasty on both sides, including muscular and ligamentous contributions (PAINCML model) . . . 212

8.3.1 Model definition . . . 212

8.3.2 Results and discussion . . . 218

8.4 Analysis of the pelvis, following primary, and revision arthroplasty on the right and left sides, including muscular and ligamentous contributions (RAINCML model) . . . 224

8.4.1 Model definition . . . 224

8.4.2 Results and discussion . . . 224

8.5 Conclusions . . . 231

9 Conclusions and recommendations 233

9.1 Conclusions . . . 234

9.1.1 Conclusions relating to MCB . . . 234

9.1.2 Conclusions relating to the plane-strain model of the acetabular construct 235

9.1.3 Conclusions relating to the hemi pelvis, and the pelvis models 236

9.2 Recommendations 237

References **239**

Appendix **251**

Publications **263**

1

Introduction

Hip arthroplasty is one of the most successful operations carried out by orthopaedic surgeons, resulting in significant improvement in the quality of life for the patient. The number of hip arthroplasties performed worldwide is now in excess of 800,000 per year [1]. However prosthetic components used in hip arthroplasty are subject to wear at prosthesis-prosthesis, and

prosthesis-bone interfaces [2]. The biological response to the generation of wear particles is scavenging by macrophages, causing the release of chemical mediators, which lead to the degradation of bone around prosthetic components [3]. Thus skeletal structures that were adequate at the time of primary hip arthroplasty deteriorate to such an extent that revision surgery is required. Around 17% of hip arthroplasties carried out are revision operations [1], often performed at specialist centres. This figure is set to rise, as patients undergoing hip arthroplasties become younger and fitter, increasing the chance of them requiring a revision operation during their lifetime [4]. The Slooff-Ling impaction grafting technique [4–6] for contained femoral and acetabular defects has found favour with many orthopaedic surgeons carrying out revision operations. The technique uses morsellised bone allograft, which is impacted into skeletal defects to form a bed onto which the new prosthetic components are cemented. If short-term stability of the components is achieved, over a period of time the bone graft is incorporated into the host skeleton, ensusuring the long-term stability of the components. A common cause of failure in revision hip arthroplasties is the loss of structural stability in the acetabular construct, and in particular in the bone graft bed [7–11].

Hip arthroplasty involves the insertion of prosthetic components on both the acetabular and femoral sides of the hip joint. This study concentrates on the acetabular construct, which following arthroplasty, experiences a more complex stress environment than the femoral construct. The study presents 2D and 3D finite element models of the acetabular construct, and the pelvis following primary, and revision hip arthroplasty. Impaction grafting is generally used to fill bone defects in the acetabulum, and or the femur at the time of revision arthroplasty. In this study the phrase "revision hip arthroplasty" is used to refer to hip arthroplasty carried out using impaction grafting.

Similarly "primary hip arthroplasty" is used to refer to hip arthroplasty in which bone graft has not been used.

Experimental studies [12–18] on bone graft have shown that its mechanical behaviour (stiffness and strength) can be improved by using an appropriate particle size distribution, washing, and thorough impaction. However the literature does not address the issue of describing its behaviour using constitutive models, that can be incorporated into finite element analyses. This is addressed as part of the study.

Previous studies have examined the behaviour of the natural hip joint, and the hip joint following primary arthroplasty using finite element models [19–35]. However the literature does not include studies on the behaviour of the hip joint following revision arthroplasty, carried out using impaction grafting.

The boundary conditions of the pelvis are complex, and simplifications are required for analysis. Previous studies have assumed fixed boundary conditions on the pelvis. Some investigations have been validated against *in vitro* loading experiments, carried out on the pelvis, taken from cadaveric specimens, and stripped of soft tissue [20,22,33]. However the literature does not include finite element analyses in which boundary conditions closer to those *in vivo* have been applied. In addition to fixed boundary condition analyses, this study presents analyses in which the effect of muscles and ligaments acting on the pelvis has been modelled using non-linear springs.

1.1 Summary of chapters

Chapter 2 presents an overview of the mechanical properties, available in the literature of the materials comprising the acetabular construct. A significant proportional of the chapter is devoted to the published literature on the mechanical properties of bone graft.

Chapter 3 describes a series of confined compression experiments, carried out on morsellised cortico-cancellous bone (MCB). Relationships are developed describing the development of Young's modulus, and consolidation plastic strain with cyclic loading at a range of axial stresses. In addition the visco-elastic behaviour of MCB is investigated.

Chapter 4 presents constitutive models that can be used to describe the non-linear elastic, visco-elastic, and non-linear plastic behaviour of MCB in finite element analyses.

Chapter 5 discusses a 2D plane-strain model of the acetabular construct, following revision hip arthroplasty. The model is subjected to idealised load cases, and used to assess the effect of increasing the depth of the bone graft bed, on the stability of the acetabular construct. The effect of modelling MCB using either the Drucker Prager, or Drucker Prager Cap yield criteria is investigated.

Chapter 6 describes the development of a 3D model of the hemi pelvis. Finite element analyses of the natural hip joint, and the hip joint following primary, and revision arthroplasty are considered. In particular four analyses of the hip joint following revision arthroplasty, subjected to different load

histories, based on typical physiological activities are presented.

Chapter 7 presents a discussion on the inclusion of muscles and ligaments as non-linear spring elements within finite element models. In addition it presents a series of novel algorithms for the automated definition of muscle origination areas, in high definition finite element models.

Chapter 8 presents models of the pelvis, following primary arthroplasty of both hip joints, in which muscular and ligamentous contributions are either excluded, or included. In additional models of the pelvis, following primary arthroplasty of one hip joint, and revision arthroplasty of the other hip joint, in which muscular and ligamentous contributions are either excluded, or included, are also presented.

Chapter 9 summarises the conclusions that can be drawn from this study.

2

Mechanical properties of the materials comprising the acetabular construct

Following revision hip arthroplasty, carried out using impaction grafting, the acetabular construct is composed of a number of synthetic and natural materials as indicated in Figure 2.1. Synthetic materials are bone cement made

from polymethylmethacrylate (PMMA) and the acetabular cup made from ultra high molecular weight polyethylene (UHMWPE). Natural materials can be identified as cortical bone, trabecular bone and impacted morsellised bone graft. In order to develop a finite element model of the acetabular construct following revision surgery each of these materials must be assigned a constitutive driver. In previous studies of the acetabular construct following primary arthroplasty, without the use of bone graft, all of the materials have been assumed to be isotropic linear elastic [19–22, 24–35]. Tests on morsellised bone graft [12–18, 36–54] indicate that it is an isotropic non-linear visco-elasto-plastic material. Thus this and subsequent chapters will discuss the behaviour of bone graft in detail and present constitutive models that can be used to represent bone graft in finite element analysis.

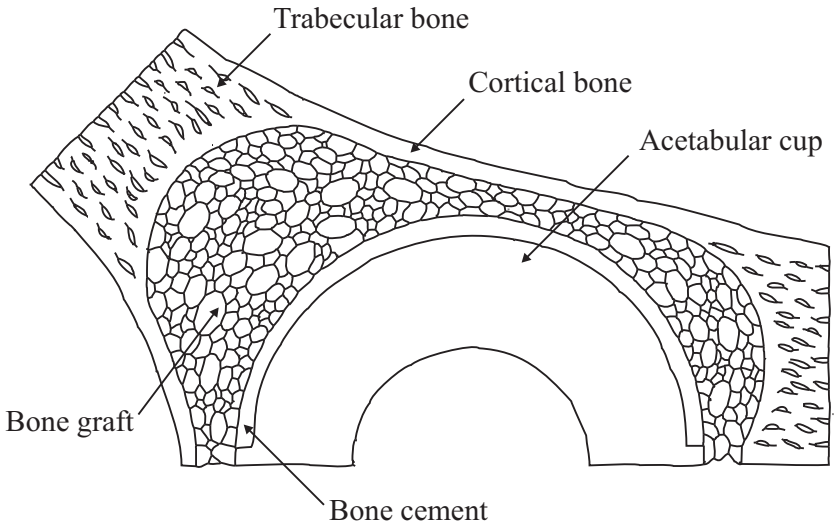

Figure 2.1: A section of the acetabular construct, showing the different materials

2.1 Synthetic Materials

The material properties of PMMA and UHMWPE as used in hip arthroplasty are well documented [55–62]. However due to the range of proprietary products available values of Young's modulus, E and Poisson's ratio, ν to be used in modelling PMMA and UHMWPE are not unique. Table 2.1 gives the range of values found in the literature.

Table 2.1: Reported values of E and ν for PMMA and UHMWPE

Material	Range of E (N/mm^2)	Range of ν
PMMA	1,800–3,200	0.30–0.48
UHMWPE	500–1,200	0.30–0.44

Assuming PMMA and UHMWPE to be isotropic linear elastic materials in the finite element analyses presented here is seen to be acceptable with the literature reporting directionally independent values of E and ν. PMMA is reported to have a compressive yield strength of around 60 N/mm^2, and tensile and shear yield strengths of around 30 N/mm^2 [62]. UHMWPE is reported to have compressive and tensile yield strengths of around 10 and 20 N/mm^2 [61]. These values are above the levels of stress that bone cement and the acetabular cup are expected to be placed under in the acetabular region, due to normal physiological loading [9, 22].

2.2 Cortical and Trabecular Bone

There are a wide range of reported values for the Young's modulus, E and Poisson's ratio, ν of cortical and trabecular bone [23, 63–69]. The variation in values can be attributed to the variation in sample collection sites (which bone the samples are taken from) and the variation in subjects as well as the variation within individual bones. The tissue level properties of cortical and trabecular bone are similar [64, 68], with the macro properties (used in the finite element analyses presented here) varying due to different architectures.

Cuppone et al. [65] performed three-point bending tests to find the value of E in the longitudinal direction for cortical bone in the femur giving a range of 14,000–22,800 N/mm^2. Dong and Guo [66] performed tensile tests to find the values of E in the longitudinal and transverse directions for cortical bone in the femur giving a range of around 13,400–20,700 N/mm^2 in the longitudinal direction and around 6,500–12,800 N/mm^2 in the transverse direction. They also reported values of ν in the longitudinal direction in the range of 0.32–0.44. Wirtz et al. [69] carried out a literature review on the material properties of cortical and trabecular bone in the femur. They reported a relationship between the areal bone mineral density (aBMD) and the values of E in the longitudinal and transverse directions for cortical bone giving a range of E of 7,200–17,600 N/mm^2 in the longitudinal direction and 4,400–6,900 N/mm^2 in the transverse direction for a range of aBMD of 1.5–2.0 g/cm^3. They also reported values of ν for cortical bone in the range of 0.2–0.5 with an average of 0.3. Previous 3D finite element simulations have modelled pelvic cortical bone as isotropic with E values of between 15,000 N/mm^2 and 20,000 N/mm^2 and a ν value of 0.3 [19, 24–26, 31, 34]. Good comparisons

between simulation and experimental results were achieved by Dalstra et al., 1995 [24] and Andersen et al., 2004 [19] using values in this range. Table 2.2 gives the range of values for E and ν for cortical bone found in the literature.

Anglin et al. [63] performed macro (as opposed to tissue level) indentation tests to find the value of E for trabecular bone in the glenoid (part of the scapula) giving an average of 99 N/mm^2 and a standard deviation of 33 N/mm^2. Wirtz et al. [69] reported a relationship between the aBMD and the values of E in the longitudinal and transverse directions for trabecular bone giving a range of E of 40–1000 N/mm^2 in the longitudinal direction and 20–600 N/mm^2 in the transverse direction for a range of aBMD of 0.1–0.7 g/cm^3. They also reported values of ν for trabecular bone in the range of 0.01–0.35 with an average of 0.12. Thompson et al. [67] performed unconfined compression tests on acetabular trabecular bone, finding an average E value of around 150 N/mm^2. Dalstra et al. [23] performed unconfined compression tests and took quantitative computer tomography (Q-CT) measurements to find the relationship between aBMD and E for trabecular bone in the pelvis. They found an average E value of around 50 N/mm^2 with a standard deviation of around 40 N/mm^2. They also reported values of ν in the range of 0.14–0.28. The study indicated that pelvic trabecular bone was not significantly anisotropic and could be modelled as isotropic in finite element simulations [24, 25]. Dalstra et al. [24] used subject specific values of E for for pelvic trabecular bone in the range of around 1–200 N/mm^2. Andersen et al. [19] used subject specific values of E in the range of 20–400 N/mm^2 based on Q-CT measurements of the pelvis. Both studies used a constant ν value of 0.2. In both studies a homogeneous non-subject specific simulation was also carried out assuming trabecular bone to have a single value of E of 70 N/mm^2 [24] and 150 N/mm^2 [19] throughout the pelvis.

The homogeneous models compared well to the subject specific models and were found to be suitable for comparative modelling. Homogeneous models have been used in this study. Table 2.2 gives the range of values for E and ν for trabecular bone found in the literature.

Table 2.2: Reported values of E and ν for cortical and trabecular bone

Material	Range of E (N/mm^2)	Range of ν
Cortical Bone	4,400-22,800	0.20-0.50
Trabecular Bone	1-1,000	0.01-0.35

Assuming cortical and trabecular bone to be isotropic linear elastic materials in the finite element analyses presented here is seen to be acceptable. Although studies [65, 66, 69] indicate that the E values of cortical and trabecular bone are dependent on the direction in which they are measured, for axial bones such as the femur. This was found not to be the case for pelvic trabecular bone [23]. Data could not be found for pelvic cortical bone, although it was observed that the complex geometric shape of the pelvis, would make the implementation of direction dependent properties difficult. Wirtz et al. [69] report compression and tension yield strengths of cortical and trabecular bone of around 100 and 5 N/mm^2 for femoral samples. As for PMMA and UHMWPE these values are above the levels of stress that the materials are expected to be placed under in the acetabular region, due to normal physiological loading [9, 22].

2.3 Morsellised Cortico-Cancellous Bone

Several studies have been carried out attempting to characterise the material behaviour of morsellised cortico-cancellous bone (MCB). These studies can be divided into those examining the behaviour of MCB due to compression loading and impaction, those examining the behaviour of MCB due to shear loading, and those examining the subsidence of MCB in *in vitro* experiments, designed to be similar to *in vivo* settings.

2.3.1 The behaviour of MCB due to compression loading

Brodt et al. [39, 40] performed triaxial compression tests on non-impacted bone graft using a range of confining pressures up to around 0.55 N/mm^2. Based on the stress-strain graphs from their experiments they identified bone graft as having pre-crush and crush phase values of E with both values increasing as the confining pressure increased. However as they did not record unloading data the gradients of the different regions of these graphs cannot be assumed to represent the pure elastic properties of bone graft. Increasing values of ν in the range of 0.14–0.25, were found with increasing confining pressure.

Brodt [38] performed confined compression tests on non-impacted bone graft using normal stresses up to 20 N/mm^2. Compression modulus values of around $6, 12, 18$ and 32 N/mm^2, and void ratio values of around 3, 1.5, 1.0 and 0.75 were recorded for normal stresses of $1, 5, 10$ and 20 N/mm^2. As

unloading data was not recorded these values cannot be assumed to represent the pure elastic properties of bone graft, however they demonstrate that the stiffness of bone graft increases as the applied normal stress increases. The existence of pre-crush and crush regimes was not identified for confined compression testing.

Ohashi et al. [48] compacted MCB samples with a diameter of 10 mm using a dynamic compaction machine, reporting an average maximum load of 4.2 kN giving a stress of above 50 N/mm^2. Reasons for the reported values of apparent moduli close to zero were not discussed and are not consistent with other studies.

Giesen et al. [44] carried out confined compression tests. They pre-conditioned the bone graft by applying an axial load of 2.75 N/mm^2 as a square wave over 24 cycles with a frequency of 0.0167 Hz (one cycle per minute). They then allowed the specimens to relax for a period of 900 *secs* before applying an axial load of either 1.18 or 1.81 N/mm^2 for 900 *secs*. The load was then removed and the specimens were allowed to relax for a further period of 900 *secs*. Based on the strain-time graphs from the post pre-conditioning part of their experiments they concluded that bone graft underwent some irreversible plastic strain due to loading even after pre-conditioning, although the majority of strain was elastic. They also concluded that bone graft was a visco-elastic material with creep occurring during loading and relaxation, although the majority of deformation during loading occurred immediately after load application and the majority of recovery during relaxation occurred immediately after load removal. They calculated a compression modulus for bone graft of around 40 N/mm^2.

Ullmark and Nilsson [50] carried out recoil and loading experiments on

pre-loaded bone graft. In their first series of tests they pre-loaded bone graft for 45 *secs* with an axial load of either 0.55 or 1.95 N/mm^2 before recording its recoil over 60 *secs*. They found that the extent of recoil was significantly higher for the bone graft that had been subjected to a higher level of pre-loading. In their second series of experiments they pre-loaded bone graft with an axial load of either 0.62 or 1.95 N/mm^2 before unloading and loading a smaller area of the bone graft with an axial load up to 12.30 N/mm^2. They found that the extent of subsidence was significantly lower for bone graft that had been subjected to a higher level of pre-loading.

Voor et al. [53, 54] performed confined compression tests. They pre-conditioned the bone graft by compacting it in three layers into a confining ring measuring 63.5 mm in diameter. Compaction was carried out by dropping a 0.885 kg weight from a height of 300 mm ten times onto each layer of bone graft. They then applied an axial load of up to 1.09 N/mm^2. They found that the bone graft showed *"increasing stiffness with increasing load"*. They reported that the confined modulus of bone graft under an axial load of 1.09 N/mm^2 was around 8.0 N/mm^2.

Verdonschot et al. [18] performed cyclic confined compression tests on bone graft, and mixes of bone graft and bone graft extenders. They applied an axial load of 2.78 N/mm^2 as a square wave over 900 cycles with a frequency of 1 Hz. They then allowed the specimens to relax for a period of 900 *secs*. They found that the value of E for bone graft increased as the number of load cycles increased reporting values of around 85 N/mm^2 after 98 cycles and 135 N/mm^2 after 880 cycles. They also examined the visco-elastic behaviour of the bone graft with increasing load cycles. They found that the extent of hysteresis decreased as the number of load cycles increased. They reported

that at the end of the experiment *"human bone grafts did show a lot of cohesion between the particles ... the grafts became one impacted entity"*. They reported that upon unloading at the end of the 900 load cycles MCB recovered 27% of the strain experienced during loading.

Grimm [45] carried out confined compression tests. Bone graft samples 20 mm in diameter were pre-conditioned by applying an axial stress of around 0.03 N/mm^2. An axial stress of 1.59 N/mm^2 was then applied before the bone graft was allowed to stress relax, at a constant strain for a period of 120 *secs*, before being allowed to recoil for a period of 120 *secs*. The bone graft was then reloaded with an axial stress of 3.18 N/mm^2 before being allowed to stress relax and recoil for a second time. Values of the secant modulus, including elastic and plastic deformation were reported for the the first cycle of compression loading between 0.08 and 1.59 N/mm^2, and for the second cycle of compression loading between 0.08 and 1.59 N/mm^2 and between 1.91 and 3.18 N/mm^2. Values of around 4 N/mm^2 were found for the first loading cycle for human, ovine and bovine bone. Values of around 10 to 12 N/mm^2 and 12 to 15 N/mm^2 were found for human bone for the second loading cycle. Similar values were found for ovine and bovine bone, although bovine bone was found to be up to 20% stiffer than human bone.

Bavadekar et al. [12] performed impaction tests dropping a 0.455 kg weight from a height of 1000 mm onto bone graft samples measuring 14.4 mm in diameter. They found that the value of E for bone graft increased as the number of impactions increased reaching a plateau at around 40 N/mm^2 after 30 impactions. They found that the inclusion of cartilage in the bone graft was detrimental to its mechanical behaviour, although the inclusion of cortical bone in the bone graft did not have a significant effect.

Fosse et al., 2004 [16] performed impaction tests dropping a 0.660 kg weight from heights of 100, 200 and 400 mm onto bone graft samples with an equivalent diameter of around 17.8 mm. Following impaction they performed confined compression testing on the samples using axial stresses of up to 2.3 N/mm^2. They reported a confined elastic modulus of around 5 N/mm^2 at an axial stress of 1.4 N/mm^2. However this value was calculated using measurements taken during loading rather than unloading. They reported that the stiffness of MCB increased as the height that the mass was dropped from was increased. They estimated the impulse force due to dropping the mass from a height of 400 mm was around 1250 N.

Heiner and Brown, 2001 [46] developed a technique for adding epoxy resin to MCB samples to simulate the fusion of MCB into host bone. They reported that by adding epoxy in different ratios a range of modulus values close to those found for intact trabecular bone could be achieved. Heiner et al., 2005 [47] performed experiments on "fused" and non-fused MCB in an *in vitro* set-up representative of a human femur. They reported modulus values of around 50 N/mm^2 for non-fused MCB following impaction into the femur representation. In addition they reported that the impulse force due to manual impaction measured using an instrumented hammer with a brass tip was around 25000 N.

It is clear from the range of compression, and impaction experiments described that MCB displays non-linear elastic properties, with the elastic modulus increasing as the applied normal stress increases. MCB also displays visco-elastic properties, with creep occurring upon load application, and recoil occurring upon load removal. It is also evident that the behaviour of MCB can be improved by subjecting it to a number of repeated forceful

impactions. Studies in which MCB was preconditioned, or in which repeated loading or impaction were applied found higher values for the elastic modulus. Studies in which measurements were made during loading of virgin MCB are seen to have included significant plastic consolidation strains, resulting in low compression modulus values.

2.3.2 The behaviour of MCB due to shear loading

Brewster et al. [14] performed shear tests (using a Jenike type direct shear apparatus) with a range of normal stresses up to around 0.14 N/mm^2, using bone graft, and mixes of bone graft and bone graft extender. Based on the shear stress-strain graphs for a range of normal stresses, they calculated the parameters c and θ required for the Mohr Coulomb yield criteria:

$$\tau_f = c - \sigma \ tan \ \theta \tag{2.1}$$

where τ_f is the shear stress at yield, c is the cohesion or interlocking, σ is the normal stress (negative in compression) and θ is the friction angle

They estimated the compactive effort exerted during femoral impaction and pre-conditioned the bone graft prior to testing based on this. For human bone they found the value of c to be close to zero and the value of θ to be around 38°. They found that the shear stress required to reach 9.5% shear strain under a normal stress of 0.095 N/mm^2 increased as the compactive effort increased. Strain hardening was observed during testing. In addition they found that the shear characteristics of bone graft could be enhanced by improving the particle size distribution using bone graft extender. It should

be noted that the range of values of normal stress applied in the study is below that found due to normal physiological loading [9, 22].

Dunlop [42] and Dunlop et al. [15] performed shear tests using a similar testing procedure to Brewster et al. [14] with a range of normal stresses up to around 0.35 N/mm^2. They pre-conditioned the bone graft by compacting it in three layers into a confining ring measuring 60 mm in diameter. Compaction was carried out by dropping a 1.98 kg weight from a height of 65 mm 24 times onto each layer of bone graft. For this compactive effort they found the value of c to be close to zero and values of θ in the range of 30–40°.

Grimm [45] carried out shear testing using a range of normal stresses between around 0.06 and 0.1 N/mm^2. Using the Mohr Coulomb parameters (Equation 2.1) the value of c was found to be close to zero and the value of θ to be around 25° for ovine bone.

2.3.3 MCB subsidence experiments

Ullmark [51] performed eccentric loading experiments on acetabular cups cemented to bone graft beds with different particle size ranges. In addition the effect of washing or not washing the bone graft was examined. It was found that a greater force was required to cause the cup to rotate when the average particle size was larger and when the bone graft had been washed.

Bolder et al. [13] performed concentric loading experiments on acetabular cups cemented to bone graft beds with different particles size ranges that had been prepared using either manual impacting or impaction using the reverse reamer technique. It was found that greater migration of the cup was seen

when the average cup size was smaller and when impaction had been carried out using the reverse reamer technique.

Blom et al. [36] and Grimm [45] recorded the subsidence of a femoral implant in an *in vitro* experimental set-up representative of an ovine femur, using bone graft and mixes of bone graft and bone graft extenders. Significant migration of the implant was found under physiological loading. Migration increased as the magnitude of the loading increased and as the number of load cycles at a given magnitude increased. Grimm [45] also carried out subsidence experiments on a human scale femur representation. The effects of different impaction energies (different weight drop heights) were assessed and it was found that significant subsidence occurred after a certain load was exceeded. The load was found to be dependent on the level of impaction applied to the bone graft.

2.4 Conclusions

It is evident from the range of studies that MCB is a complex material exhibiting non-linear visco-elasto-plastic properties. It is subject to consolidation and shear plastic strains. Its elastic modulus increases as the applied normal stress increases. In addition its shear strength increases as the applied normal stress increases. Subsequent chapters will present a range of experiments carried out as part of this investigation, designed to quantify the non-linear elasto-plastic, and visco-elastic behaviour of MCB.

3

Behaviour of morsellised cortico-cancellous bone

This chapter presents a series of five experiments carried out to investigate the behaviour of morsellised cortico-cancellous bone (MCB) under confined compression [17, 41, 49, 70, 71]. Previous experimental studies have attempted to describe the material properties of MCB due to compressive and shear

loading [12–16, 18, 36–40, 42–48, 50–54]. Reported values for the apparent modulus of MCB ranged from near zero to around 150 N/mm^2. While some variations are expected due to inter-sample variations, bone from different species and different subjects, such a large range has to be seen to be due to other factors. The reported values are seen to be dependent on the preconditioning applied to the the MCB, as well as whether the value was recorded during a single phase of loading [38–40, 44, 53, 54] in which case the reported value will include large irrecoverable plastic strains, or whether values were recorded during the unloading phase of repeated load cycles [18] or following repeated impactions [12]. The experiments presented here examine the effect on the value of the confined elastic modulus, E_c due to increasing maximum axial stress as well as increasing load cycles. Two values of E_c are considered: E_{ic}, the instantenous modulus, and E_{dc}, the delayed modulus allowing for stress relaxation effects. The experiments are also used to examine the development of consolidation plastic strains with increasing maximum axial stress, and the visco-elastic behaviour of MCB.

3.1 Materials and Methods

Confined compression tests were carried out using a Zwick/Roell Z005 testing machine connected to a data logging desk-top PC. Figure 3.1 shows a rendered view (a) and schematic diagram (b) of the test apparatus. The apparatus consisted of a cylindrical test chamber with an internal diameter of 50 mm and a height of 100 mm. The chamber was machined from a single piece of steel with a wall thickness of 9 mm to prevent radial strains from occurring. During sample preparation and testing the chamber was secured

to a baseplate using bolts threaded into the wall of the chamber. Following testing the baseplate was removed to allow sample extraction. A series of sixteen 2 mm diameter holes were drilled through the wall of the chamber to allow exudation of fluids from the MCB during testing. Loading was applied to the MCB using a solid steel load applicator with a diameter of 49 mm. The load applicator was connected to the testing machine using a rigid joint.

Samples of MCB were prepared using bovine femoral condyles obtained from a local abattoir, which were stored at -18°C, and allowed to reach room temperature prior to preparation. Bovine bone was chosen due to the large volume of MCB required for each of the tests. Voor et al. [54] found that the properties of bovine and human MCB were similar, and that the effects of different preparation techniques were the same. Soft tissue and articular cartilage were removed as these have been shown to have a detrimental effect on the properties of MCB [12]. The bone tissue was then cut into cubes of around 25 mm in size, washed and further checked for soft tissue and cartilage before being morsellised using a New splint bone mill with a 9 mm rasping blade. This produced particles, with sizes in the range of around 1–6 mm, consistent with the range of particles used in impaction grafting procedures. Large particles of cortical bone were removed. Small particles of cortical bone were allowed to remain in the sample as these have been shown not to have a detrimental effect on the material properties of MCB [12]. MCB was stored at -18 or 2 °C, depending on the length of time between preparation and testing, and allowed to reach room temperature prior to testing.

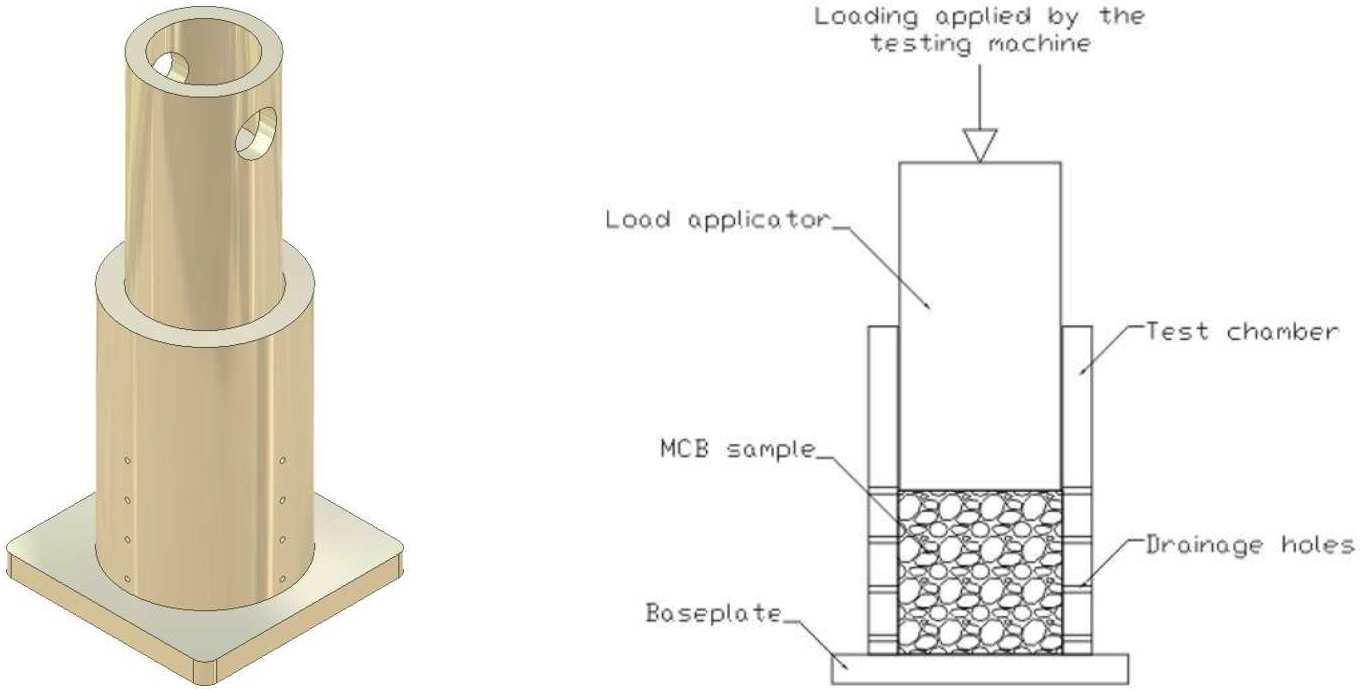

(a) Rendered view

(b) Schematic diagram

Figure 3.1: Testing apparatus

3.2 Testing and Discussion

3.2.1 Test 1

In Test 1 serial testing was carried out on six samples taken from a homogeneous batch of MCB prepared from bovine femoral condyles. Three of the samples were packed into the test chamber in three layers. Each of the layers underwent minimal preconditioning, consisting of placing the 1.70 kg load applicator on top of the MCB for a period of around 5 *secs*. Following packing of the third layer loose MCB was finger packed into the chamber until the sample was level with the top of the chamber. The remaining three samples were packed into the test chamber in five equal layers. Different numbers of impactions were applied to each of these layers using a standard 1.0 kg surgical impaction hammer and the load applicator. 10 impactions were applied to each layer of the first sample, 15 impactions were applied to each layer of the second sample and 20 impactions were applied to each layer of the third sample. Each of the six MCB samples was then subjected to a series of 750 cycles of loading and unloading with a maximum axial stress of 3.0 N/mm^2. The samples were not allowed to stress relax between loading and unloading. The stress value was chosen to be at the upper end of the range of stresses found in the acetabulum due to normal physiological activities [9,22]. For all tests loading and unloading was applied under displacement control at a rate of 0.1667 mm/s. This test was designed to examine whether the properties of MCB were consistent between samples as well as providing information on the development of E_{ic} over an extended number of load cycles. It was also designed to investigate the effect of impacting the bone graft bed at the

time of surgery. In particular to assess whether impacting MCB reduced the development of plastic strains and increased the stiffness. Some stress relaxation was expected to occur during loading and unloading as these were not immediate. The instantaneous confined elastic modulus, E_{ic} was evaluated for each load cycle using:

$$E_{ic} = \frac{(\sigma_a^L - \sigma_a^{UL})}{(\epsilon_a^L - \epsilon_a^{UL})}(1 - \epsilon_a^{UL}) \tag{3.1}$$

where σ_a^L is the axial (positive in the direction of loading) stress at the end of loading, σ_a^{UL} is the axial stress at the end of unloading (close to zero), ϵ_a^L is the axial strain at the end of loading, and ϵ_a^{UL} is the axial strain at the end of unloading.

The values derived for E_{ic} for each of the six samples are shown as discrete data points in Figure 3.2. The values are shown in red for the sample prepared in five layers with 10 impactions applied to each layer; in green for the sample prepared with 15 impactions applied to each layer; in blue for the sample prepared with 20 impactions applied to each layer; and in black for the samples prepared in three layers with no impactions applied.

Figure 3.2 shows that E_{ic} increases as the number of load cycles increases, tending towards a constant value. The development of E_{ic} with increasing load cycles did not seem to be influenced by the way in which the samples had been prepared. It can be seen from Figure 3.2 that the results for the samples prepared with different numbers of impactions are not ordered in any way and are intermixed with the results for the samples prepared without impactions. It was found that a good representation of the development of E_{ic} with increasing load cycles was given by the asymptotic function:

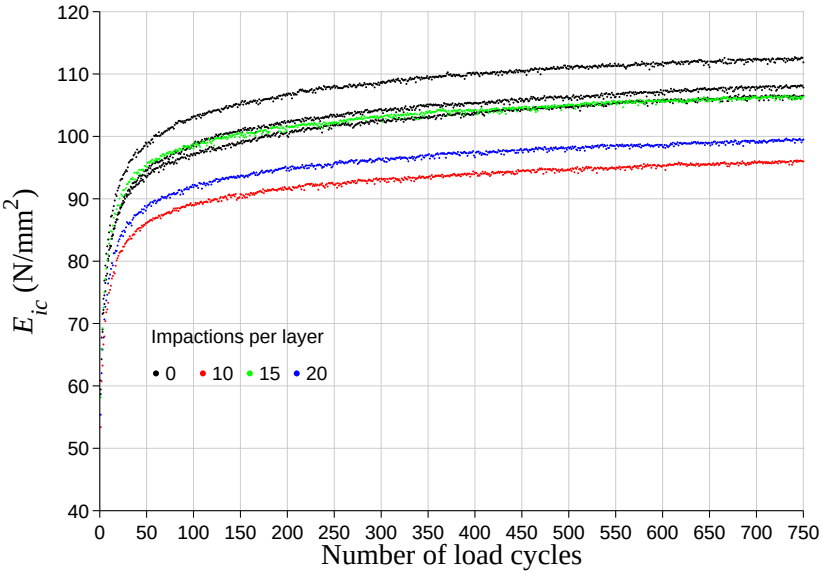

Figure 3.2: E_{ic} values for Test 1

$$E_c = -k_1 C_1^{\,ln(N)} + k_2 \tag{3.2}$$

where E_c is equal to E_{ic} for Test 1, N is the number of load cycles, C_1 is the load cycle convergence rate parameter, and k_1 and k_2 are constants: k_2 represents the value of E_c at $N = \infty$ and $(k_2 - k_1)$ represents the value of E_c at $N = 1$. For the physical basis of Equation 3.2 to be satisfied $0 < C_1 < 1$ and $k_2 > k_1 > 0$.

The mean values derived for k_1, k_2, and C_1 for the six samples, as well as mean values of $(k_1 - k_2)$ and R^2 for the data fit given by Equation 3.2 are given in Table 3.1. Where relevant, standard deviations are also shown.

It can be seen from the values of standard deviation in Table 3.1 that confined compression testing as carried out in this series of experiments gives reasonably consistent results.

Table 3.1: k_1, k_2 and C_1 values for Test 1

	k_1	k_2	C_1	$(k_2 - k_1)$	R^2
μ	64.88	120.20	0.8018	55.33	0.9967
σ	7.64	9.89	0.0239	2.61	

In addition to deriving the values of E_{ic} with increasing load cycles values of the axial strain at the end of unloading, ϵ_a^{UL} for each load cycle were also recorded. ϵ_a^{UL} can be assumed to be close to the value of axial plastic strain, ϵ_a^p at the end of each load cycle (although some elastic strains associated with the visco-elastic properties of MCB will be included in the ϵ_a^{UL} values) and is reported as such. The values derived for ϵ_a^p for each of the six samples are shown as discrete data points in Figure 3.3. It is seen that with increasing load cycles, the value of ϵ_a^p tends towards a constant value.

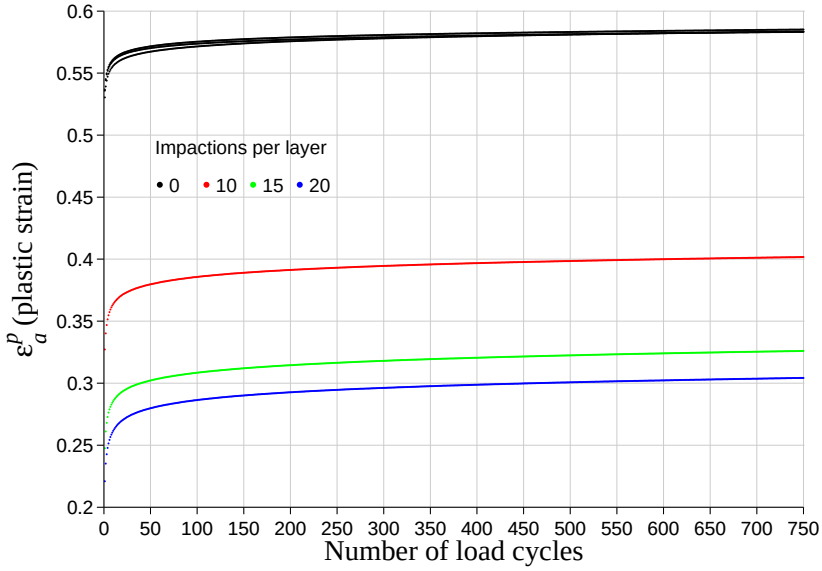

Figure 3.3: ϵ_a^p values for Test 1

It was found that a good fit for the ϵ_a^p values from Test 1 could be achieved using a similar equation to that used to describe the development of E_{ic} with increasing load cycles:

$$\epsilon_a^p = -k_{PE1} \times C_{PE1}^{ln(N)} + k_{PE2} \tag{3.3}$$

where N is the number of load cycles, C_{PE1} is the load cycle convergence rate parameter, and k_{PE1} and k_{PE2} are constants: k_{PE2} represents the value of ϵ_a^p at $N = \infty$ and $(k_{PE2} - k_{PE1})$ represents the value of ϵ_a^p at $N = 1$. For the physical basis of Equation 3.3 to be satisfied $0 < C_{PE1} < 1$ and $k_{PE2} > k_{PE1} > 0$.

The values derived for k_{PE1}, k_{PE2}, and C_{PE1} for the six samples, as well as the values of $(k_{PE2} - k_{PE1})$ and R^2 for the data fit given by Equation 3.3 are given in Table 3.2. The number of impactions used in preparing the samples are also shown.

Table 3.2: k_{PE1}, k_{PE2} and C_{PE1} values for Test 1

Sample	Impactions	k_{PE1}	k_{PE2}	C_{PE1}	$(k_{PE2} - k_{PE1})$	R^2
1	none	0.09866	0.6296	0.8916	0.5309	0.9958
2	none	0.07399	0.6095	0.8460	0.5355	0.9954
3	none	0.06876	0.6023	0.8259	0.5335	0.9948
4	5×20	0.13010	0.3454	0.8476	0.2172	0.9961
5	5×15	0.14200	0.3873	0.8877	0.2484	0.9958
6	5×10	0.12320	0.4477	0.8674	0.3264	0.9960

It can be seen from Figure 3.3 and Table 3.2 that although the way in which the samples were prepared did not have an effect on the development of E_{ic} with increasing load cycles, it does have a significant effect on the development of ϵ_a^p with increasing load cycles. Those samples which were not impacted during packing into the test chamber suffer plastic strains of around 59%. It is interesting to note that all three samples suffer almost indentical plastic strains. The sample which was impacted 10 times per layer

suffered plastic strains of around 40%. The sample which was impacted 15 times per layer suffered plastic strains of around 33%, while the sample which was impacted 20 times per layer suffered plastic strains of around 31%. Hence it can be seen that the role of impaction at the time of surgery is to reduce the development of plastic strains in the graft bed due to further loading. Impaction does not lead to an increase in the stiffness of the bone graft bed. Further tests are needed to provide qualitative and quantitative assessment of the effect of different numbers of impactions and different impaction forces on the long term reduction of plastic strains in MCB.

3.2.2 Tests 2 and 3

Two tests were carried out, using a second homogeneous batch of MCB, evaluating values of the instantaneous confined elastic modulus, E_{ic} and the delayed confined elastic modulus, E_{dc}. Similar to half of the samples for Test 1, samples for Tests 2 and 3 were packed into the test chamber in three layers. Each of the layers underwent minimal preconditioning, consisting of placing the 1.70 kg load applicator on top of the MCB for a period of around 5 *secs*. Following packing of the third layer loose MCB was finger packed into the chamber until the sample was level with the top of the chamber.

In Test 2 one of the MCB samples was subjected to a series of 60 load cycles. Figure 3.4 shows the stress-time and strain-time variations experienced by the sample. The sample was subjected to 10 cycles of loading and unloading, under displacement control with a maximum axial stress of 0.5 N/mm^2 before it was allowed to stress relax for a period of 900 *sec*. The sample was not allowed to stress relax between loading and unloading for each stress

level. This loading pattern was then repeated in increments of 0.5 N/mm^2 up to a maximum axial stress of 3.0 N/mm^2. The range of stresses was chosen to be similar to the range of stresses found in the acetabulum due to normal physiological activities [22, 25]. The test was designed to assess the effects of increasing maximum stress, as well as increasing the number of load cycles when time dependent stress relaxation effects were minimised. The instantaneous confined elastic modulus, E_{ic} was evaluated for each load cycle using Equation 3.1

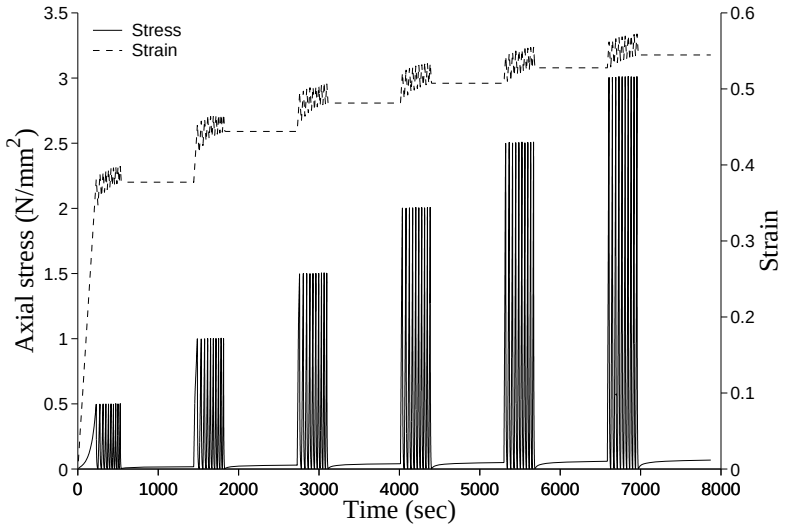

Figure 3.4: Stress-time and strain-time variations for Test 2

In Test 3 one of the MCB samples was subjected to a series of 30 load cycles. Figure 3.5 shows the stress-time and strain-time variations experienced by the sample. The sample was subjected to 5 cycles of loading and unloading with a maximum axial stress of 0.5 N/mm^2. After each period of loading and unloading the sample was allowed to stress relax for a period of 300 *sec*. This loading pattern was repeated in increments of 0.5 N/mm^2 up to a maximum axial stress of 3.0 N/mm^2. The test was designed to assess the effects of increasing maximum stress as well as increasing the number of

load cycles including time dependent stress relaxation effects. In this test the delayed confined elastic modulus, E_{dc} was evaluated for each load cycle using:

$$E_{dc} = \frac{(\sigma_a^{SRL} - \sigma_a^{SRUL})}{(\epsilon_a^{L} - \epsilon_a^{UL})}(1 - \epsilon_a^{UL}) \tag{3.4}$$

where σ_a^{SRL} is the axial stress at the end of stress relaxation following loading, σ_a^{SRUL} is the axial stress at the end of stress relaxation following unloading, ϵ_a^{L} is the axial strain at the end of loading, and ϵ_a^{UL} is the axial strain at the end of unloading.

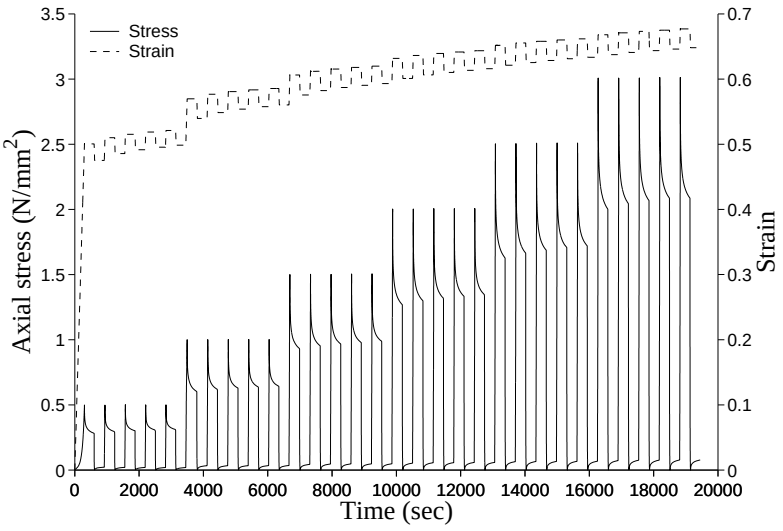

Figure 3.5: Stress-time and strain-time variations for Test 3

Figure 3.6 shows the stress-strain graph for Test 2. The inset in Figure 3.6 shows typical loading and unloading curves for a particular loading cycle. The points used to derive E_{ic} are marked using circles on the inset. Figure 3.6 shows that the MCB sample undergoes significant irrecoverable plastic strains when loaded for the first time at each stress level, with subsequent loading

and unloading curves being packed close together. MCB is shown to be a hysteretic material with large hysteresis areas between the loading and unloading curves for all load cycles, also observed by Verdonschot et al. [18]. It was found that loading curves for Test 2, shown in Figure 3.6, following the first loading curve for each stress level could be represented using a linear function, while unloading curves could be represented using an exponential function. The values derived for E_{ic} for each load cycle for Test 2 are shown as discrete data points in Figure 3.7, the relevance of the solid and dash-dot lines will be discussed later. It was found that E_{ic} increases as the maximum axial stress increases and that for each stress level E_{ic} increases as the number of load cycles increases. Figure 3.7 shows the clear dependence of E_{ic} on the maximum axial stress. It also illustrates that for a given stress level as the number of load cycles increases E_{ic} tends towards an asymptote. It was found that a good representation of the data at each stress level was given by the asymptotic function given in Equation 3.2, where E_c is equal to E_{ic} for Test 2.

Equation 3.2 was found to represent well the values of E_{ic} with increasing load cycles for each stress level using a value of C_1 of 0.8, based on the value found for Test 1. The values derived for k_1 and k_2 as well as values of $(k_2 - k_1)$ and R^2 for the data fit for each stress level are given in Table 3.3. The regression curves are shown as solid lines in Figure 3.7, and are seen to have a good fit for the derived values of E_{ic}.

Figure 3.8 shows the stress-strain graph for Test 3. The inset in Figure 3.8 shows typical loading and unloading, as well as stress relaxation curves for a particular loading cycle. The points used to derive E_{dc} are marked using circles on the inset. Comparing Figures 3.6 and 3.8 it was found that the

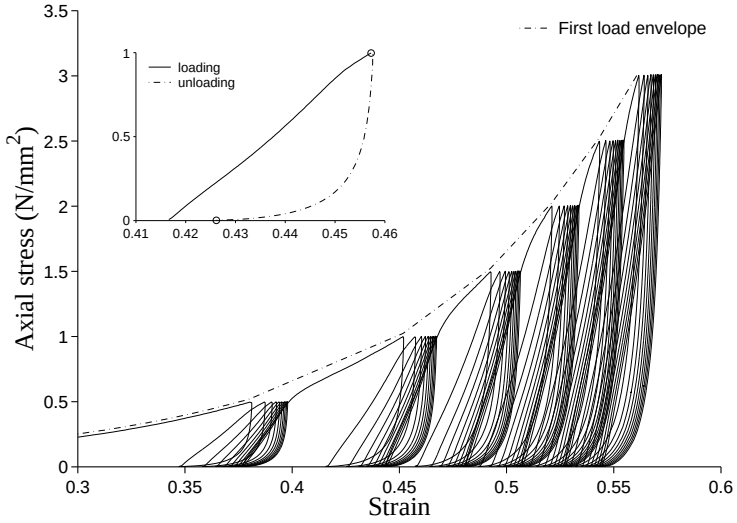

Figure 3.6: Stress-strain graph for Test 2

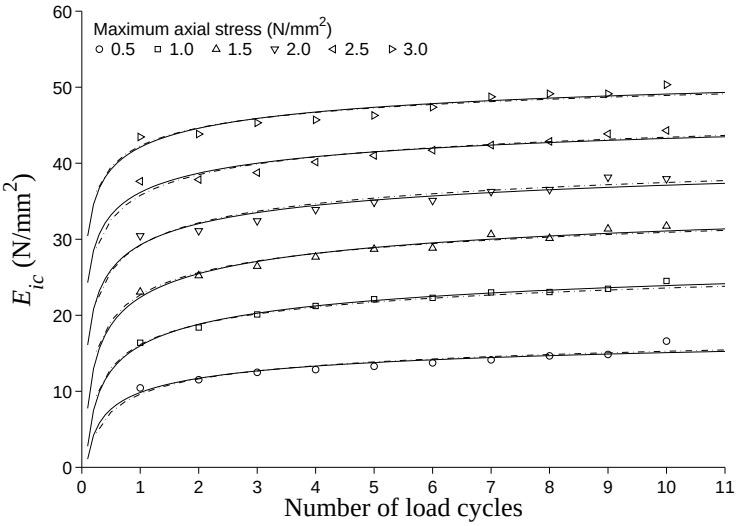

Figure 3.7: E_{ic} values and regression curves for Test 2

strain upon first loading up to a maximum stress of 0.5 N/mm^2 was higher for Test 3 than for Test 2. This variation is to be expected due to the natural variation in packing of the samples before the start of the tests. The subsequent strain range (after first loading) is seen to be similar for both tests

as expected following load application. Figure 3.5 shows that MCB is a time dependent material undergoing significant stress relaxation following loading and unloading. The extent of stress relaxation following loading decreases with increasing load cycles. The extent of stress relaxation following loading was found to be in the range of around 30–40% of the initial stress level over each 300 *sec* stress relaxation period. The values derived for E_{dc} for each load cycle for Test 3 are shown as discrete data points in Figure 3.9, the relevance of the solid and dash-dot lines will be discussed later. It is found that as for E_{ic} in the previous test E_{dc} increases as the maximum axial stress increases and that for each stress level E_{dc} increases as the number of load cycles increases. Figure 3.9 shows the clear dependence of E_{dc} on the maximum axial stress, and illustrates that for a given stress level as the number of load cycles increases E_{dc} tends towards a maximum value. As for the previous test it was found that a good representation of the data at each stress level was given by Equation 3.2 where E_c is equal to E_{dc} for Test 3.

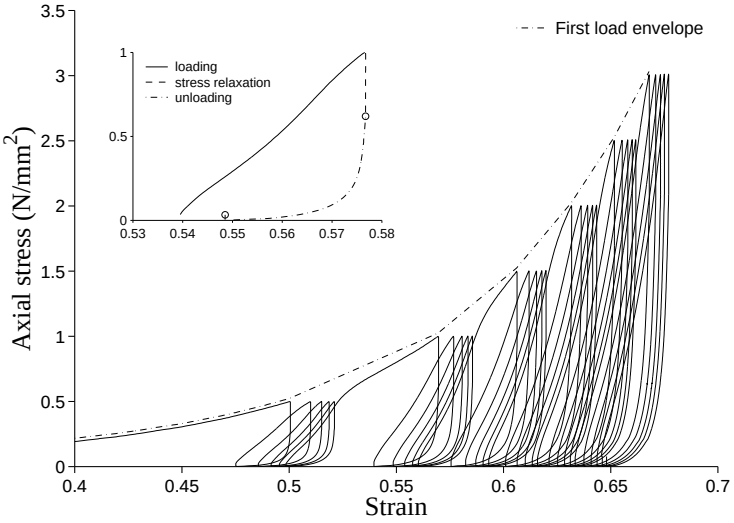

Figure 3.8: Stress-strain graph for Test 3

Equation 3.2 was found to represent well the values of E_{dc} with increasing

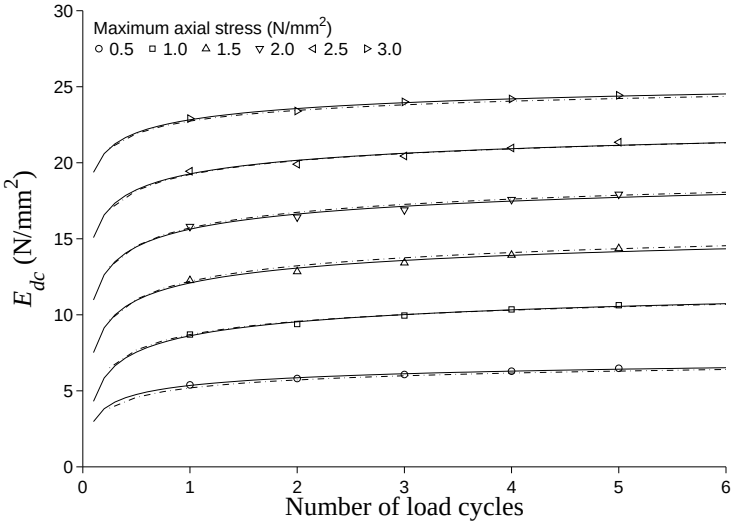

Figure 3.9: E_{dc} values and regression curves for Test 3

load cycles at each stress level for this test using the same value of C_1 of 0.8. The values derived for k_1 and k_2 as well as the values of $(k_2 - k_1)$ and R^2 for the data fit for each stress level for this test are given in Table 3.4. The regression curves for this test are shown as solid lines in Figure 3.9, and are seen to have a good fit for the derived values of E_{dc}.

Table 3.3: k_1 and k_2 values for Test 2

	Maximum Axial Stress (N/mm^2)					
	0.5	1.0	1.5	2.0	2.5	3.0
k_1	13.04	19.69	21.74	19.57	17.68	17.40
k_2	22.88	35.68	44.09	48.81	53.83	59.50
$k_2 - k_1$	9.84	15.99	22.35	29.24	36.15	42.10
R^2	0.8764	0.9842	0.9589	0.8968	0.8648	0.8563

From Tables 3.3 and 3.4, k_1 is seen to rise over the initial stress levels before falling, while k_2 is seen to rise over all six stress levels, although the difference between stress levels decreases as the stress level increases. Tables 3.3 and 3.4 indicate that k_1 and k_2 follow trends based on the maximum

Table 3.4: k_1 and k_2 values for Test 3

	Maximum Axial Stress (N/mm^2)					
	0.5	1.0	1.5	2.0	2.5	3.0
k_1	3.541	6.414	6.818	6.931	6.236	5.154
k_2	8.891	15.03	18.91	22.56	25.50	27.98
$k_2 - k_1$	5.350	8.616	12.09	15.63	19.26	22.83
R^2	0.9861	0.9838	0.9468	0.9386	0.9276	0.9757

axial stress. It was found that over the range of stresses applied to the MCB during Tests 3 and 4 the resulting values of k_2 could be estimated using:

$$k_2 = -k_3 C_2^{\sigma_n^{max}} + k_4 \tag{3.5}$$

where σ_n^{max} is the maximum axial stress, C_2 is the stress convergence rate parameter for k_2, and k_3 and k_4 are constants: k_4 represents the value of k_2 at $\sigma_n^{max} = \infty$ and $(k_4 - k_3)$ represents the value of k_2 at $\sigma_n^{max} = 0$. For the physical basis of Equation 3.5 to be satisfied $0 < C_2 < 1$ and $k_4 > k_3 > 0$.

It was found that over the range of stresses applied the resulting values of $(k_2 - k_1)$ could be estimated using:

$$k_2 - k_1 = k_5 \sigma_n^{max} + k_6 \tag{3.6}$$

where k_5 and k_6 are constants: k_5 represents the rate of rise of $(k_2 - k_1)$ with σ_n^{max} and k_6 represents the value of $(k_2 - k_1)$ at $\sigma_n^{max} = 0$.

It was found that a good fit was given for the values of k_2 with increasing maximum axial stress for Tests 2 and 3 using a value for C_2 of 0.6. The

values derived for k_3, k_4, k_5 and k_6 as well as the values of $(k_4 - k_3)$ and R^2 for the data fit for k_2 and $(k_2 - k1)$ vs. σ_n^{max} for Tests 2 and 3 are given in Table 3.5. The regression curves are shown in Figure 3.10 with curves for k_2 shown as solid lines and curves for $(k_2 - k_1)$ shown as dash-dot lines. As expected it was found that the values of k_1 and k_2 for Test 2, in which stress relaxation effects were minimised were higher than the values of k_1 and k_2 for Test 3, in which stress relaxation effects were included. On average the values of k_1 and k_2 allowing stress relaxation effects were around 40 % lower than the values of k_1 and k_2 minimising these effects. Had the samples been allowed to stress relax for a greater period of time in Test 3 it is expected that this difference would have been greater. Had the rate of exudation of fluids from the samples been reduced it is expected that the rate of stress relaxation would have been reduced resulting in increased values for E_{dc} for a given time.

The five constants (k_3, k_4, C_2, k_5, k_6) from Equations 3.5 and 3.6 can be used with the constant (C_1) from Equation 3.2 to evaluate the confined elastic modulus, E_c for arbitrary stress levels and arbitrary numbers of load cycles over the range of axial stresses applied during the tests. Equations 3.2, 3.5 and 3.6 were used to predict the values of E_c of Tests 2 and 3. The predicted values are shown as dash-dot lines in Figures 3.7 and 3.9, and are seen to have a good fit for the derived values of E_c.

3.2.3 Test 4A

In Test 4A a sample from the same batch of MCB as used for Test 1 was subjected to a series of 650 loading cycles. The sample was packed into the

Table 3.5: k_3, k_4 and k_5 values for Tests 2 and 3

	Test 2	Test 3
k_3	62.86	33.64
k_4	72.36	34.92
$k_4 - k_3$	9.50	1.28
R^2	0.9943	0.9984
k_5	13.07	7.021
k_6	3.078	1.677
R^2	0.9995	0.9997

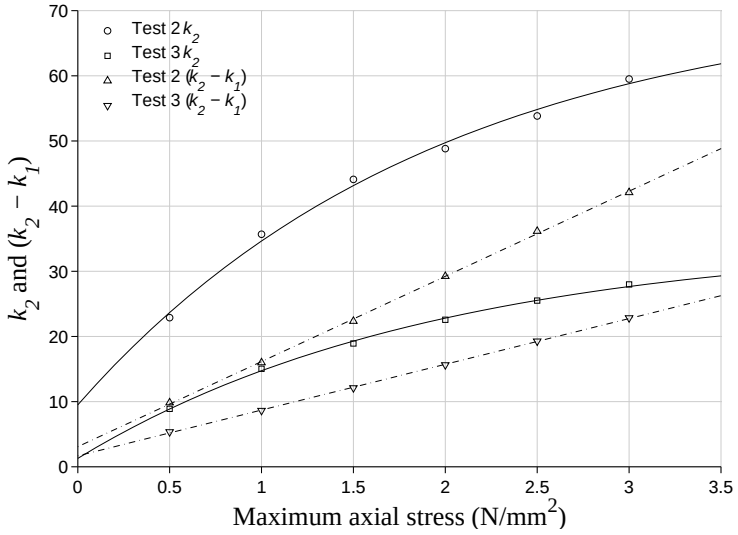

Figure 3.10: k_2 and $(k_2 - k_1)$ vs. σ_n^{max} for Tests 2 and 3

test chamber in a series of 5 layers with 5 impactions applied to each layer. The sample was then subjected to 50 cycles of loading and unloading, under displacement control with a maximum axial stress of 0.25 N/mm^2 before it was allowed to stress relax for a period of 300 *secs*. This loading pattern was then repeated in increments of 0.25 N/mm^2 up to a maximum axial stress of 3.0 N/mm^2.

Following this series of 600 load cycles, the sample was then subjected to

10 cycles of loading and unloading with a maximum axial stress of 2.5 N/mm^2 before it was allowed to stress relax for a period of 300 *secs*. This loading pattern was repeated, decreasing the axial stress in steps of 0.5 N/mm^2 down to a maximum axial stress of 0.5 N/mm^2. The sample was not allowed to stress relax between loading and unloading for each stress level.

This part of the test was designed to further investigate the development of the stiffness of MCB with increasing axial stress, and increasing load cycles. In addition it was designed to examine whether the increase in E_{ic} with increasing axial stress was permanent or whether the value of E_{ic} would reduce when the axial stress was reduced. The values derived for E_{ic} for the first 600 load cycles of Test 4A (when the maximum axial stress was increased over a number of steps) are shown as discrete data points in Figure 3.11.

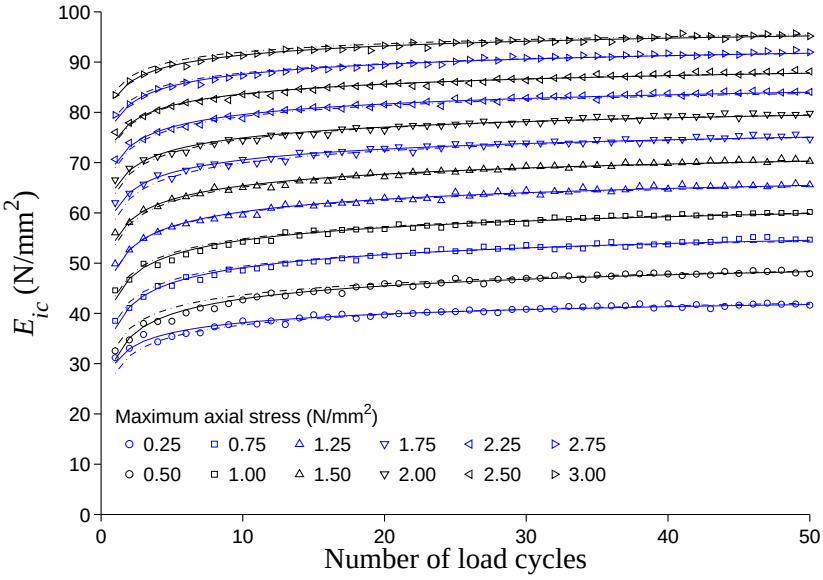

Figure 3.11: E_{ic} values and regression curves for the first 600 load cycles of Test 4A

It is shown in Figure 3.11 that the trends in the development of E_{ic} are the same as those found in Tests 2 and 3 in that E_{ic} increases with

increasing numbers of load cycles, and with increasing maximum axial stress. Equation 3.2 was found to represent well the values of E_{ic} with increasing load cycles for each stress level. Based on the results from Test 1 a C_1 value of 0.8 was chosen when the regression analysis was carried out. The values derived for k_1 and k_2 as well as values of $(k_1 - k_2)$ and R^2 for the data fit for each stress level are given in Table 3.6. The regression curves for this test are shown as solid lines in Figure 3.11, and are seen to have a good fit for the derived values of E_{ic}.

Table 3.6: k_1 and k_2 values for Test 4A found using Equation 3.2

	Maximum Axial Stress (N/mm^2)					
	0.25	0.5	0.75	1.0	1.25	1.5
k_1	20.03	30.04	30.27	29.50	29.10	27.17
k_2	50.13	60.86	67.20	72.19	77.63	81.65
$k_2 - k_1$	30.10	30.82	36.93	42.69	48.53	54.48
R^2	0.9621	0.9808	0.9827	0.9799	0.9847	0.9828
	Maximum Axial Stress (N/mm^2)					
	1.75	2.0	2.25	2.5	2.75	3.0
k_1	25.12	24.95	24.66	22.88	23.28	21.05
k_2	85.56	89.85	94.31	97.35	101.5	104.0
$k_2 - k_1$	60.44	64.90	69.65	74.47	78.22	82.95
R^2	0.9734	0.9753	0.9818	0.9757	0.9820	0.9831

From Table 3.6, k_1 is seen to rise over the initial stress levels before falling, while k_2 is seen to rise over all twelve stress levels. As expected these trends match those found in Tests 2 and 3. It was found that the values of k_2 and $(k_2 - k_1)$ as a function of maximum axial stress for Test 4A could be estimated using Equations 3.5 and 3.6. As for Tests 2 and 3 it was found that a good fit was given for the values of k_2 with increasing maximum axial stress using a value for C_2 of 0.6. The values derived for k_3, k_4, k_5 and k_6 as well as the values of $(k_4 - k_3)$ and R^2 for the data fit for k_2 and $(k_2 - k_1)$ vs.

σ_n^{max} for Test 4A are given in Table 3.7. The regressions curves are shown in Figure 3.12 with the curve for k_2 shown as a solid line and the curve for $(k_2 - k_1)$ shown as a dash-dot line.

Table 3.7: k_3, k_4, C_2, k_5 and k_6 values for Test 4A

k_3	k_4	$k_4 - k_3$	R^2	k_5	k_6	R^2
77.6	119.1	44.02	0.9964	20.43	22.99	0.9945

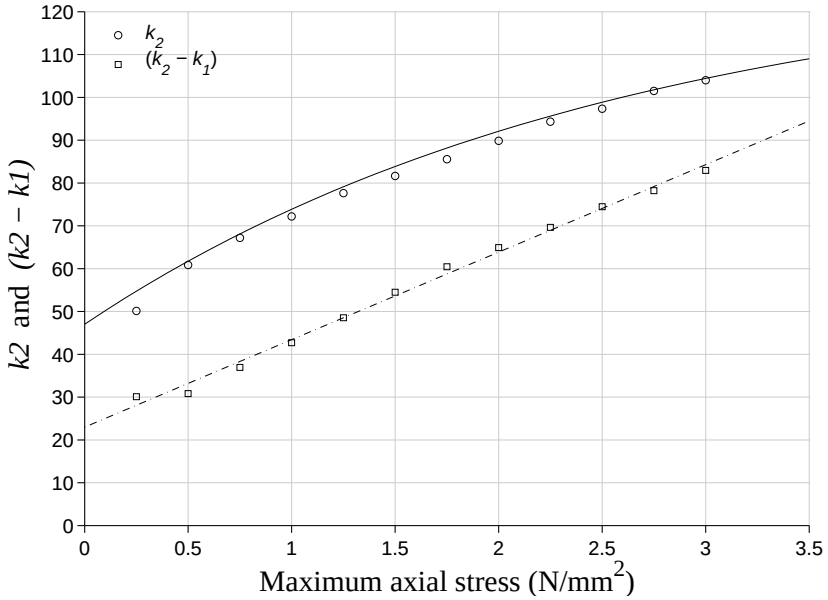

Figure 3.12: k_2 and $(k_2 - k_1)$ vs. σ_n^{max} for Test 4A

Equations 3.2, 3.5 and 3.6 were used to predict the values of E_{ic} for Test 4A. The predicted values are shown as dash-dot lines in Figure 3.11 and are seen to have a good fit for the derived values of E_{ic}.

In addition to deriving the values of E_{ic} with increasing load cycles and increasing maximum axial stress values of the axial plastic strain, ϵ_a^p at the end of each load cycle were also recorded. The values derived for ϵ_a^p for the first 600 load cycles of Test 4A are shown as discrete data points in Figure 3.13. It can be seen that the plastic strains increase (the volume of the

sample decreases) tending towards a constant value with increasing numbers of load cycles at a given stress level. In addition the values of plastic strain depend on the value of maximum axial stress applied. As expected the value of plastic strain did not change during the final 50 load cycles, indicating that the plastic strain is dependent on the absolute maximum axial stress applied to the sample.

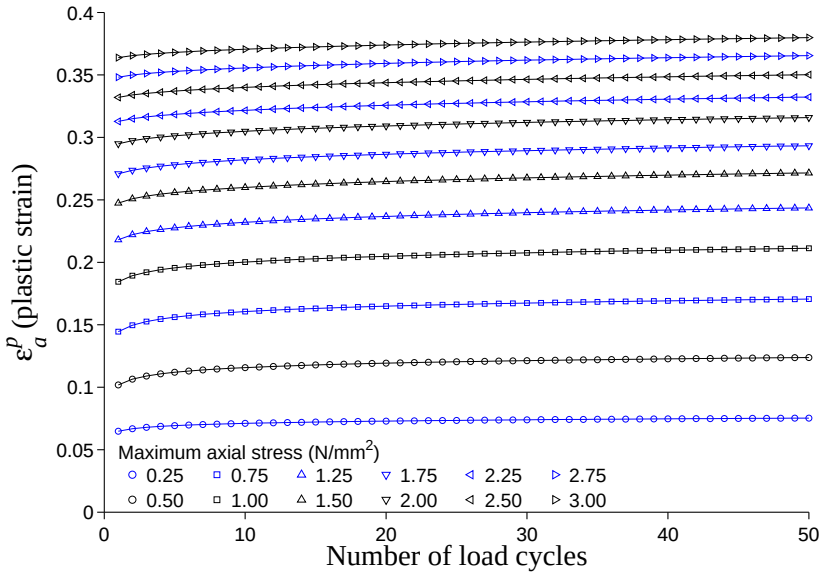

Figure 3.13: ϵ_a^p values for the first 600 load cycles of Test 4A

The values derived for E_{ic} for the final 50 load cycles of Test 4A (when the maximum axial stress was decreased over a number of steps) are shown as discrete data points in Figure 3.14. It can be seen that the range of E_{ic} values for the first 600 loading cycles (Figure 3.11) is around 30–100 N/mm^2 for a range of stresses of 0.25–3.0 N/mm^2. This is similar to the range of E_{ic} values for the final 50 loading cycles (Figure 3.14) of around 40–90 N/mm^2 for a range of stresses of 2.5–0.5 N/mm^2. The same trends are seen for the 600 and 50 load cycle sets with E_{ic} increasing towards a finite value with increasing numbers of load cycles at a given stress level. In addition it can

be seen that for both sets of load cycles the values of E_{ic} depend on the value of axial stress applied. This shows that the increase in E_{ic} with increasing stress is not permanent, with the value of E_{ic} decreasing when the applied axial stress is decreased. This indicates that MCB has non-linear elastic material properties.

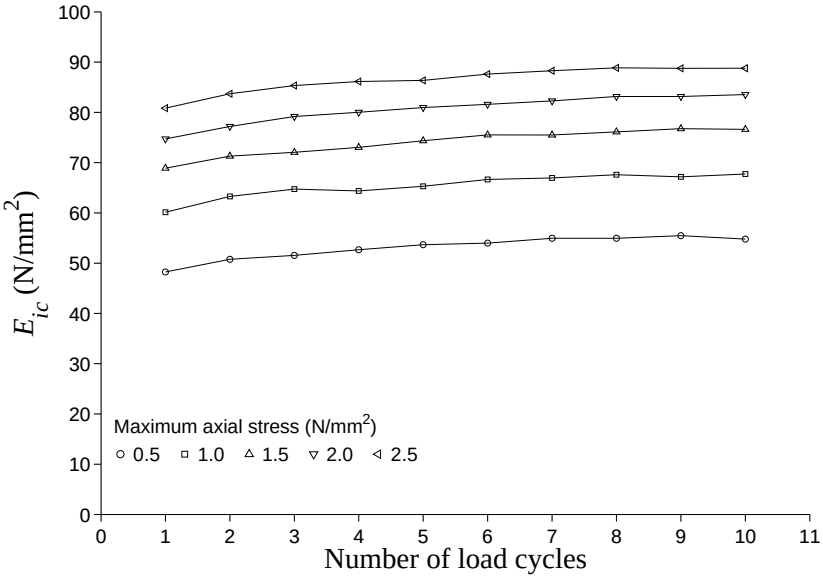

Figure 3.14: E_{ic} values for the final 50 load cycles of Test 4A

3.2.4 Test 4B

Following the first set of 650 load cycles the MCB sample was removed from the test chamber. It was then broken up by hand before being re-packed into the test chamber. The sample was re-packed into the test chamber in a series of 3 layers without impaction as in Tests 2 and 3 before being subjected to a further series of 110 load cycles.

The sample was subjected to 10 cycles of loading and unloading with a

maximum axial stress of 0.5 N/mm^2 before it was allowed to stress relax for a period of 300 *secs*. This loading pattern was then repeated in increments of 0.5 N/mm^2 up to a maximum axial stress of 3.0 N/mm^2.

Following this series of 60 load cycles, the sample was then subjected to 10 cycles of loading and unloading with a maximum axial stress of 2.5 N/mm^2 before it was allowed to stress relax for a period of 300 *secs*. This loading pattern was then repeated, decreasing the axial stress in steps of 0.5 N/mm^2 down to a maximum axial stress of 0.5 N/mm^2. The sample was not allowed to stress relax between loading and unloading for each stress level.

This part of the test was designed to assess whether the impactions and load cycles in the initial part of the test had changed the behaviour of the MCB sample at a particulate level, resulting in changes in the mechanical properties of the sample. The values derived for E_{ic} for the first 60 load cycles of Test 4B (when the maximum axial stress was increased over a number of steps) are shown as discrete data points in Figure 3.15.

It can be seen that the range of values of E_{ic} from the first 60 load cycles of the of Test 4B (Figure 3.15) of 40–90 N/mm^2 is similar to the range of values from the first 600 cycles of Test 4A, Part 1 (Figure 3.11) of 30–100 N/mm^2. The range of axial stresses was similar for the two sets of load cycles. This suggests that the material properties of the individual particles of MCB are not affected by the loading regime placed upon them in Test 4A. This supports the finding of other investigators [18, 40] in that following loading although irrecoverable plastic strains occur in the sample micro-damage was not seen to the MCB particles themselves.

In addition to deriving the values of E_{ic} with increasing load cycles and

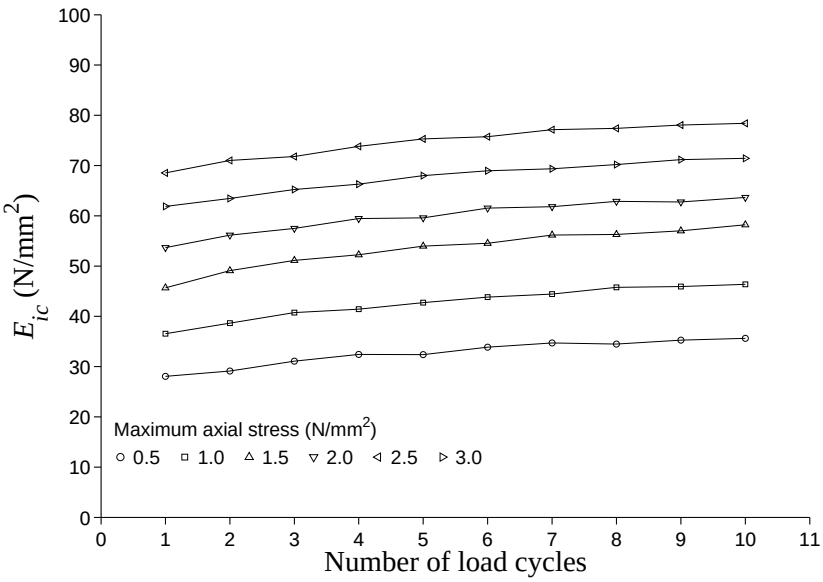

Figure 3.15: E_{ic} values for the first 60 load cycles of Test 4B

increasing maximum axial stress the axial plastic strain, ϵ_a^p at the end of each load cycle was also recorded. The values derived for ϵ_a^p for the first 60 load cycles of Test 4B are shown as discrete data points in Figure 3.16. It can be seen that as for Test 1 and Test 4A the plastic strains increase in an asymptotic manner with increasing numbers of load cycles at a given stress level. In addition the values of plastic strain depend on the maximum axial stress applied. As expected the value of plastic strain did not change during the final 50 load cycles. It can be seen that the values of plastic strain for Test 4B (Figure 3.16) are higher than the values of plastic strain for Test 4A (Figure 3.13). This can be accounted for by the varying methods of sample packing, with impactions being applied during packing of the sample in the first part of the test (Test 4A), but not in the second part of the test (Test 4B).

The values derived for E_{ic} for the final 50 load cycles of Test 4B (when

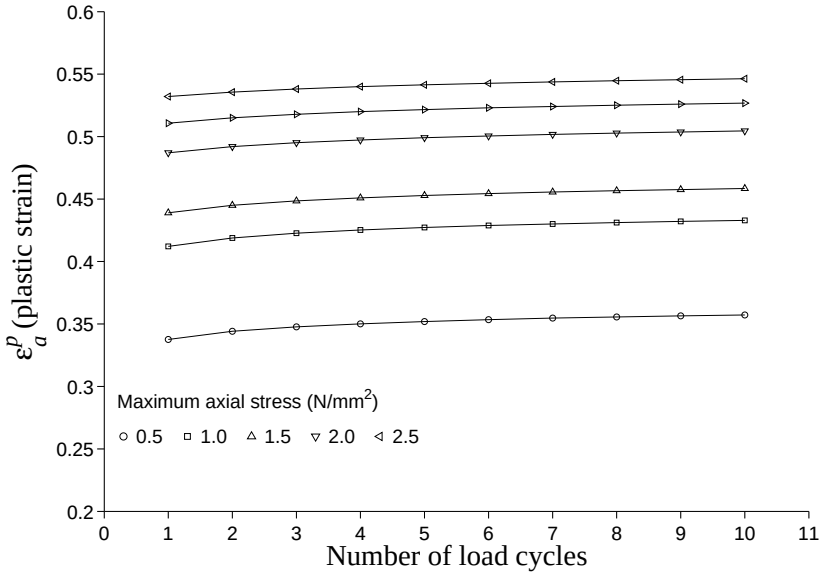

Figure 3.16: ϵ_a^p values for the first 60 load cycles of Test 4B

the maximum axial stress was decreased over a number of steps) are shown as discrete data points in Figure 3.17. It can be seen that the range of values of E_{ic} for the final 50 loading cycles of Test 4B (Figure 3.17) is around 40–80 N/mm^2 for a range of stresses of 2.5–0.5 N/mm^2. This is similar to the range of E_{ic} for the first 60 loading cycles of Test 4B (Figure 3.15) of around 40–90 N/mm^2 for a range of stresses of 0.5–3.0 N/mm^2. As for Test 4A these results indicate that MCB has non-linear elastic material properties with the stiffness increasing with increasing axial stress, but decreasing when the axial stress is decreased.

The results of Test 4 in conjunction with the previous tests show that MCB samples have non-linear elasto-plastic material properties. The value of elastic stiffness is dependent on the value of axial stress applied to the sample. The value of plastic strain is dependent on the absolute maximum axial stress applied to the sample. During cyclic loading MCB experiences

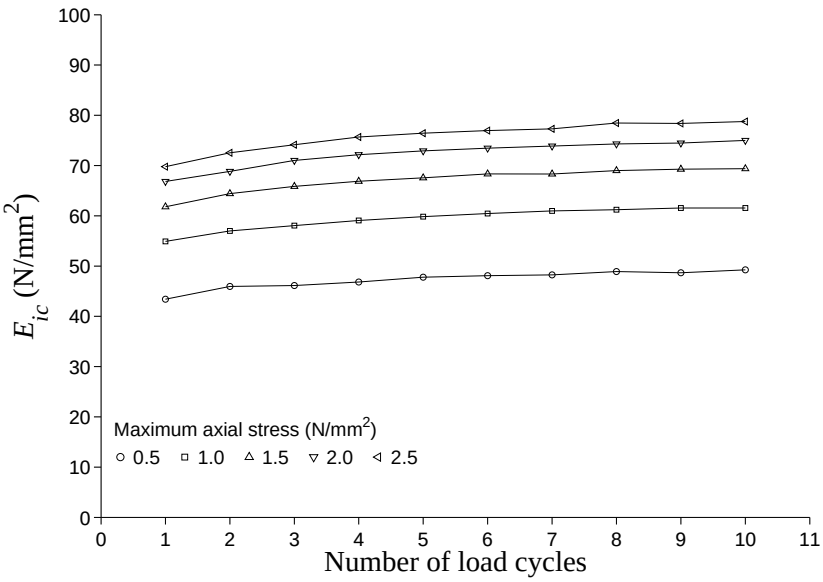

Figure 3.17: E_{ic} values for the final 50 load cycles of Test 4B

a non-permanent increase in stiffness and a permanent increase in plastic strain. The visco-elastic properties of MCB are investigated in Test 5.

3.2.5 Test 5

In Test 5 following the application of 750 load cycles in Test 1 each of the six samples was allowed to rest overnight in the test chamber for a period of around 16 hrs. The samples were then reloaded with axial stresses of 0.5, 1.0, 1.5, 2.0, 2.5 and 3.0 N/mm^2 before being allowed to stress relax for a period of 21600 $secs$ or 6 hrs. During this time the load applicator was held in place and the decrease in stress with time was recorded. The samples were then unloaded to 0.01 N/mm^2 (close to zero) and allowed to stress relax for a further period of 7200 $secs$ or 2 hrs. During this time the load applicator was held in place and the increase in stress with time was recorded. The

constant strain that the samples were subjected to during both stages of stress relaxation was also recorded.

This test was designed to investigate the visco-elastic properties of MCB. The stress-time variations experienced by the samples during the first period of stress relaxation can be seen in Figure 3.18. The stress-time variations experienced by the samples during the second period of stress relaxation can be seen in Figure 3.19. The complete stress-time record for the sample subjected to an initial axial stress of 3.0 N/mm^2 is shown in Figure 3.20.

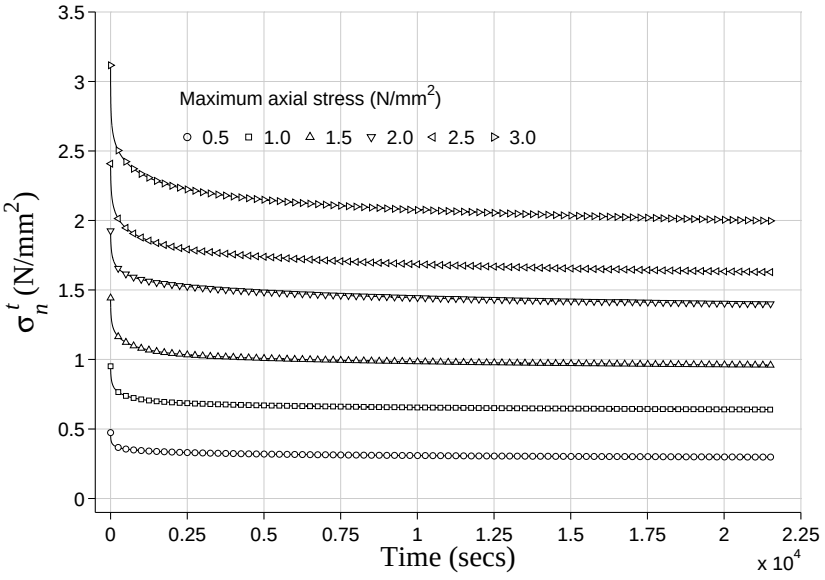

Figure 3.18: First period of stress relaxation for Test 5

Figures 3.18 and 3.19 show that a significant amount of stress relaxation occurs in a short space of time, within the first 300 *secs*. After this period stress relaxation occurs at a decreasing rate tending towards a finite value. It was found that the data from both periods of stress relaxation could be described using a modified Prony series of the form:

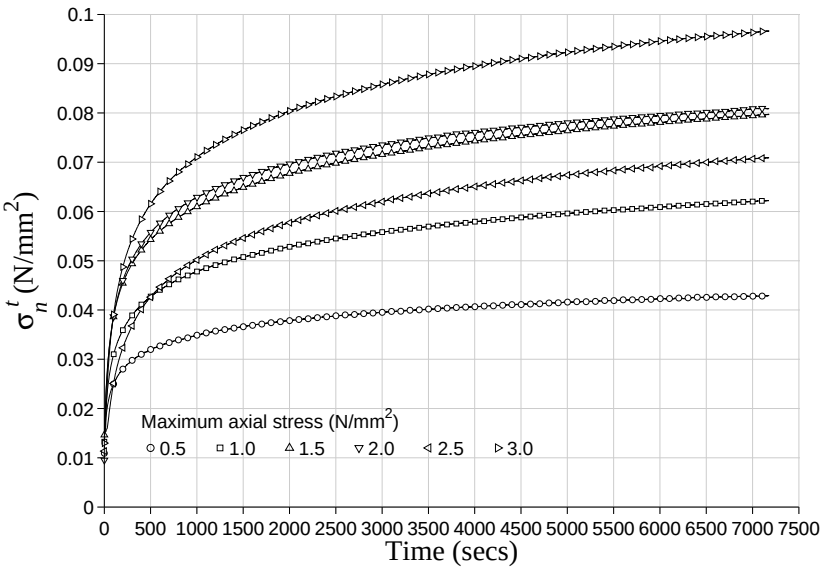

Figure 3.19: Second period of stress relaxation for Test 5

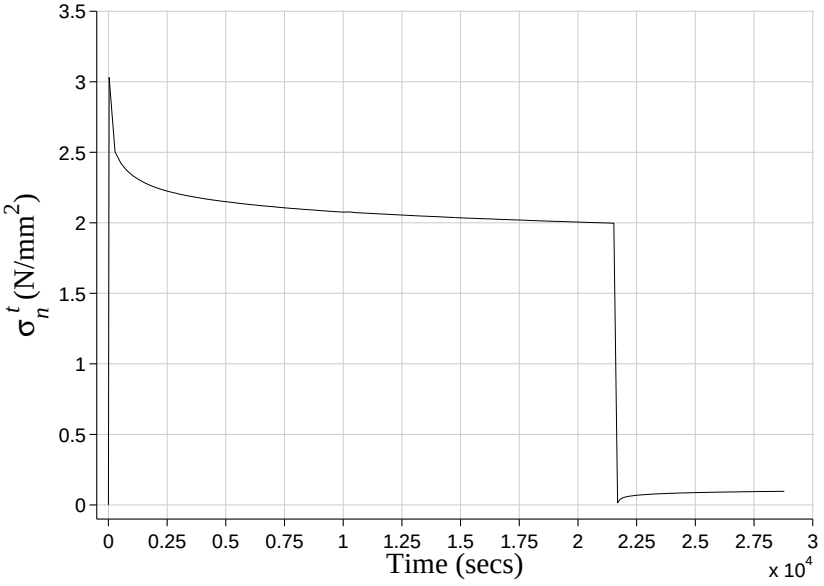

Figure 3.20: Complete stress-time record for the sample subjected to an initial axial stress of 3.0 N/mm^2

$$\sigma_n^t = \sigma_n^\infty + k(e^{-t/k_{t1}} + e^{-t/k_{t2}} \ \ldots \ e^{-t/k_{tn}}) \tag{3.7}$$

where σ_n^t is the axial stress at time t, σ_n^∞ is the axial stress at $t = \infty$, k is a constant, and k_{t1}, k_{t2} $\ldots$ k_{tn} are a series of time constants.

In addition it was found that both periods of stress relaxation could be described using a third order modified Prony series in which the constants k_{t1}, k_{t2} and k_{t3} were set to 100, 1000 and 10000. This suggests that the 750 load cycles applied to the samples during Test 1 provided sufficient pre-conditioning to the MCB that its subsequent behaviour was dominated by elastic as opposed to plastic material properties [17]. The values of σ^∞ and k as well as the values of R^2 found using the above time constants for the first period of stress relaxation are shown in Table 3.8. The values found using the same time constants for the second period of stress relaxation are shown in Table 3.9. Also given in Tables 3.8 and 3.9 are the values of strain experienced by the samples during stress relaxation and E_c^∞, the confined elastic modulus at $t = \infty$.

Table 3.8: Values of σ^∞, k and R^2 for Test 5

First period of stress relaxation						
σ^o	0.5	1.0	1.5	2.0	2.5	3.0
σ^∞	0.2937	0.6296	0.9430	1.388	1.605	1.969
k	0.04109	0.06900	0.1122	0.1515	0.2185	0.2904
R^2	0.9958	0.9802	0.9864	0.9943	0.9990	0.9982
ϵ_a	0.03530	0.05281	0.05440	0.05873	0.05927	0.06010
$E_c^\infty(\sigma^\infty/\epsilon_a)$	8.32	11.92	17.33	23.63	27.08	32.76
σ^∞/σ^o	58.74%	62.96%	62.87%	69.40%	64.20%	65.63%

The modified Prony series given in Equation 3.7 can be related to the classical visco-elastic relationship:

Table 3.9: Values of σ^{∞}, k and R^2 for Test 5

Second period of stress relaxation						
σ^o	0.01	0.01	0.01	0.01	0.01	0.01
σ^{∞}	0.04782	0.07027	0.09072	0.09264	0.08293	0.1122
k	-0.01027	-0.01776	-0.02358	-0.02391	-0.02577	-0.03268
R^2	0.9978	0.9976	0.9977	0.9982	0.9967	0.9989
ϵ_a	0.02158	0.02986	0.03256	0.03106	0.02789	0.02944
$E_c^{\infty}(\sigma^{\infty}/\epsilon_a)$	2.22	2.35	2.79	2.98	2.97	3.81

$$E_c(t) = E_c^{\infty} + \sum_{j=1}^{N} E_{rj} e^{-t/k_{tj}} \tag{3.8}$$

where $E_c(t)$ is the confined elastic modulus at time t, E_c^{∞} is the confined elastic modulus at $t = \infty$, E_{rj} values are a series of relaxation moduli, and k_{tj} values are a series of time constants.

It can be seen from Table 3.8 that the values of E_c^{∞} increase with increasing values of σ^{∞}. It was found that the rise in E_c^{∞} with σ^{∞} could be represented using a linear function over the range of stresses applied. The ratio of σ^{∞} to σ^o is also given in Table 3.8. The amount of stress relaxation is around 30–40% for each of the samples. The extent of stress relaxation is seen to be independent of the initial stress applied to the sample.

3.3 Conclusions

The results of Tests 1 to 5 give a range of E_{ic} values of 10–100 N/mm^2 dependent on the stress level and number of load cycles applied. It is seen

that the range of values of E_{ic} for Test 2 is around 10–50 N/mm^2, which is lower than the range of values for Test 4 which is around 30–100 N/mm^2. This difference might be explained by the use of different batches of bone for Tests 2 and 3 and Tests 1, 4 and 5. It might also be explained by the fact that greater care was taken when washing and preparing the batch of morsellised bone used in Tests 1, 4 and 5, to remove as much of the fat and marrow as possible. The removal of fat and marrow from MCB has been shown to improve its material properties [14]. It is possible to attribute the wider range of values for Test 4 to the increased number of load cycles at each stress level in comparison to Test 2. The results from Tests 3 and 5 show that E_{dc} after 300 *secs* and E_c^{∞} are around 35% lower than E_{ic}. The range of values of E_c found for Tests 1 to 5 are consistent with the range of values found in previous studies of around 0–150 N/mm^2. The development of E_{ic} with increasing numbers of load cycles found during Test 1 compares well with the results of Verdonschot et al. [18] who found values of 85 and 135 N/mm^2 after 98 and 880 cycles using a maximum axial stress of 2.78 N/mm^2 with a load cycle frequency of 1 Hz. Given the drop in E_{ic} when the stress level is lowered after a brief period of stress relaxation found for Test 4 it is thought that the apparent increase in the stiffness of MCB with increasing load cycles at a given stress level could be due to visco-elastic effects. Verdonschot et al. [18] found an increase in E_{ic} over 782 cycles of around 50 N/mm^2. The results of Test 1 indicate an increase of around 10 N/mm^2 over around 650 cycles (100 to 750). It is expected that the reason for this is the higher load cycle frequency used by Verdonschot et al. [18]. Although the experiments reported in this study were displacement controlled a rough calculation indicates that the load cycle frequency was around 0.0625 Hz.

The results of Tests 1 to 4 show that when loaded in confined compression

MCB undergoes significant consolidation plastic strains, causing the sample volume to decrease. Figures 3.3 and 3.13 indicate that most of these irreversible plastic strains occur within the first few load cycles at a given stress level. However the increase in plastic strain with increasing numbers of load cycles indicates that MCB has visco-plastic as well as visco-elastic material properties. Previous studies show that MCB also experiences shear plastic strains [14, 15, 42, 45]. These studies indicate that the shear stress at which MCB exhibits plastic strains is dependent on the normal stress applied to the sample.

In conclusion the experiments carried out as part of this study, as well as previous investigations show that MCB is a complex material exhibiting non-linear visco-elasto-plastic behaviour.

The subsequent chapter will develop constitutive drivers capable of modelling the non-linear elasto-plastic, and visco-elastic aspects of the material behaviour of MCB for use in finite element models.

4

Constitutive models for impacted morsellised cortico-cancellous bone

It is seen from the discussion and experimental results presented in the previous chapters that morsellised cortico-cancellous bone (MCB), is a complex material that cannot be described in sufficient detail, over the range of stress-

es expected due to normal physiological loading, using a simple isotropic linear elastic constitutive model. MCB is seen to have non-linear elasto-plastic, and visco-elastic material properties. In addition MCB displays visco-plastic properties [17, 44], although further tests are required to understand and quantify this aspect of its material behaviour.

This chapter presents constitutive models that can be implemented in finite element analyses to include the non-linear elasto-plastic, and visco-elastic behaviour of MCB, based on the results of the experiments presented in the previous chapter. It is clear that the development of these models is limited by the 1D nature of the confined compression tests performed as part of this, and previous studies. Assumptions made in defining a triaxial constitutive model based on these tests are indicated in the model descriptions.

4.1 Non-linear elastic behaviour

Results from Test 5 described in the previous chapter were used to determine the long term non-linear elastic behaviour of MCB. As mentioned previous, following the application of 750 preconditioning load cycles in Test 1, the behaviour of MCB in Test 5 was seen to be non-linear visco-elastic, with plastic behaviour removed during the preconditioning. Based on the first period of stress relaxation, it was found that for a given applied axial strain, ϵ_a, the confined elastic modulus, E_c^{∞} at $t = \infty$ could be described as a linear function of the axial stress σ^{∞}, at $t = \infty$ (Chapter 3, Table 3.8). Assuming MCB to have a Poisson's ratio, $\nu = 0.2$ [40] the long-term Young's modulus, E^{∞} can be expressed as a function of the pressure, p^{∞}, at $t = \infty$:

$$E^{\infty} = c_1 + c_2 p^{\infty} \tag{4.1}$$

where c_1 and c_2 are constants, and for 1D confined compression:

$$E^{\infty} = \frac{E_c^{\infty}}{c_3} \quad \text{where} \quad c_3 = \frac{(1-\nu)}{(1+\nu)(1-2\nu)} \tag{4.2}$$

$$p^{\infty} = \frac{\sigma^{\infty}}{c_4} \quad \text{where} \quad c_4 = \left(\frac{1}{3} + \frac{2\nu}{3(1-\nu)}\right)^{-1} \tag{4.3}$$

Figure 4.1 shows the discrete values found for E^{∞} and p^{∞} for the first period of stress relaxation for the six MCB samples from Test 5. In addition it shows the regression curve from Equation 4.1 with $c_1 = 3.00$ and $c_2 = 26.64$, giving an R^2 value of 0.9975.

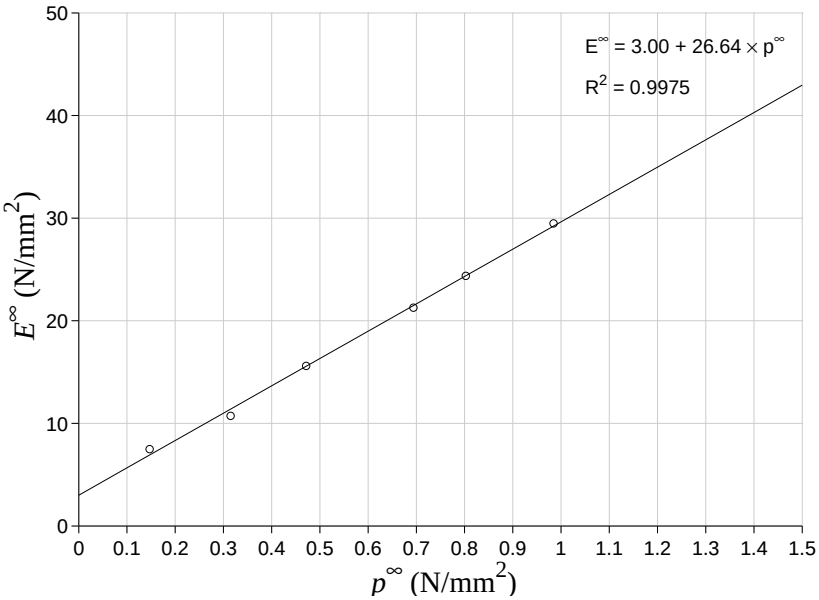

Figure 4.1: E^{∞} vs. p^{∞}

It can be shown that:

$$p^{\infty} = \frac{c_1 \epsilon^e_{vol} c_3}{c_4 - c_2 \epsilon^e_{vol} c_3} \tag{4.4}$$

where ϵ^e_{vol} is the elastic volumetric strain.

Figure 4.2 shows the development of p^{∞} with ϵ^e_{vol} given by Equation 4.4.

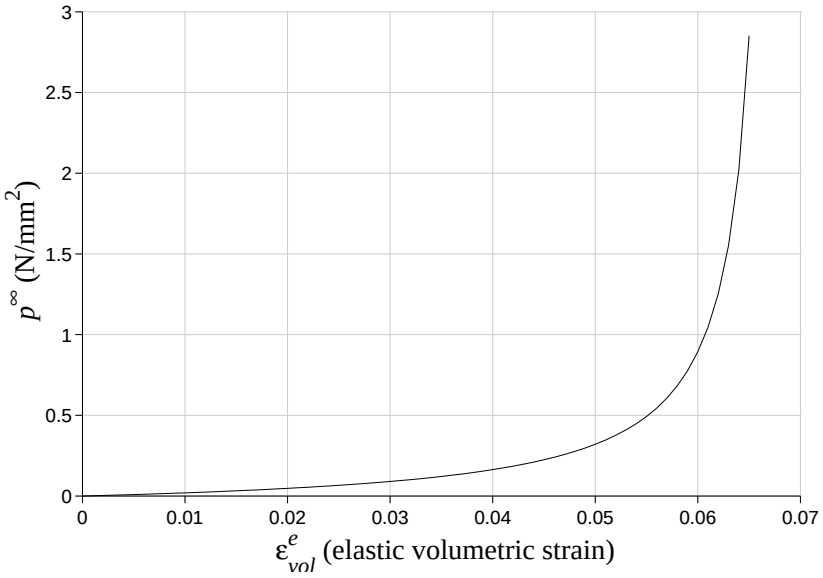

Figure 4.2: p^{∞} vs. ϵ^e_{vol}

The relationships given by Equations 4.1 and 4.4 were used to develop two *Fortran* subroutines, given in the Appendix, for use in force and displacement driven finite element analyses implemented in *Abaqus* [72]. Thus the developed constitutive model includes the effect of the applied stress on the elastic modulus, but ignores the effect of cyclic loading. The latter is seen to be comparatively minor.

4.2 Visco-elastic behaviour

Results from Test 5 described in the previous chapter, were also used to determine the time dependent visco-elastic behaviour of MCB. The classical visco-elastic relationship [72], describing stress relaxation (under constant strain) can be written as a Prony series, in the form:

$$E(t) = E_i(1 - \sum_{j=1}^{N} C_j(1 - e^{-t/k_{tj}})) \tag{4.5}$$

where $E(t)$ is the Young's modulus at time t, E_i is the instantaneous Young's modulus at $t = 0$, values of k_{tj} are a series of time constants, and $C_j = E_{rj}/E_i$ where values of E_{rj} are a series of relaxation moduli.

As discussed in the previous chapter it was found that data from both periods of stress relaxation (following rapid application of a constant strain) for Test 5 could be described using a modified Prony series of the form:

$$\sigma(t) = \sigma^{\infty} + k \sum_{j=1}^{N} e^{-t/k_{tj}} \tag{4.6}$$

where $\sigma(t)$ is the axial stress at time t, σ^{∞} is the axial stress at $t = \infty$, k is a constant, and values of k_{tj} are a series of time constants.

It can be seen from Equation 4.6 that for a third order Prony series, as was found to fit the stress relaxation data from Test 5, the instantaneous stress, σ^i following rapid strain application, at $t = 0$, can be found by substituting $N = 3$, and $t = 0$ into Equation 4.6:

$$\sigma^i = \sigma^\infty + 3k \tag{4.7}$$

Hence Equation 4.6 can be rearranged to give:

$$\sigma(t) = \sigma^i \left(1 - \sum_{j=1}^{3} \left(\frac{k}{\sigma^i}\right)(1 - e^{-t/k_{tj}})\right) \tag{4.8}$$

Comparing Equations 4.5 and 4.8 it is seen that the series of C_j values can be assumed to be equal, and can be represented by a unique constant:

$$C = \frac{k}{\sigma^i} \tag{4.9}$$

Tables 4.1 gives values of σ^∞, k, σ^i, and C, as well as E^∞ and E_i for the first period of stress relaxation for the six samples from Test 5, with values of k_{t1}, k_{t2}, and k_{t3} set to 100, 1000, and 10000.

Table 4.1: Values of σ^∞, k, σ^i and C for Test 5

First period of stress relaxation						
σ^∞	0.2937	0.6296	0.9430	1.388	1.605	1.969
k	0.04109	0.06900	0.1122	0.1515	0.2185	0.2904
σ^i	0.4170	0.8366	1.2796	1.8425	2.2605	2.8402
C	0.0985	0.0825	0.0877	0.0822	0.0967	0.1022
ϵ_a	0.03530	0.05281	0.05440	0.05873	0.05927	0.06010
$E_c^\infty(\sigma^\infty/\epsilon_a)$	8.32	11.92	17.33	23.63	27.08	32.76
E^∞	7.49	10.73	15.60	21.27	24.37	29.49
$E_{ic}(\sigma^i/\epsilon_a)$	11.81	15.84	23.52	31.37	38.14	47.26
E_i	10.63	14.26	21.17	28.24	34.33	42.53

It appears from Table 4.1 that the value of C is independent of the axial

stress applied to the sample. The mean and standard deviation of C were found to be 0.0916 and 0.0086. It was found that E^{∞}/E_i was around 1.38, regardless of the instantaneous stress, σ^i.

Modelling of the visco-elastic behaviour in combination with the non-linear elastic behaviour of MCB was verified using a single element axisymmetric model implemented in *Abaqus*. The boundary conditions of the model, shown in Figure 4.3, were such that it was representative of the confined samples of MCB used in Tests 1 to 5 described previously.

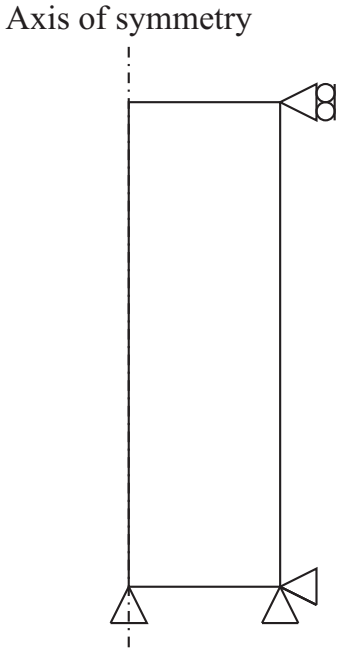

Figure 4.3: Axisymmetric boundary conditions

The model was subjected to three dynamic displacement controlled analyses similar to the procedure used for Test 5. Elastic axial strains of 5.5147, 6.0729 and 6.2849×10^{-2} for the three analyses, corresponding to long term axial stresses of 1.0, 2.0 and 3.0 N/mm^2, were applied over a time period of 30 *secs*. The model was then allowed to stress relax for a period of

21600 *secs* as was the case for Test 5. The elastic axial strain was then lowered to 2.0776×10^{-2} for all three of the analyses, representative of a long term axial stress of 0.1 N/mm^2, over a time period of 30 *secs*. The model was then allowed to stress relax for a period of 7200 *secs* as was the case for Test 5. A sample input file is given in Appendix I.

Figures 4.4 and 4.5 show the stress-time response of the axisymmetric model for each of the three analyses for both periods of stress relaxation. It can be seen that these are very similar to the experimental results shown in the previous chapter (Figures 3.18 and 3.19)

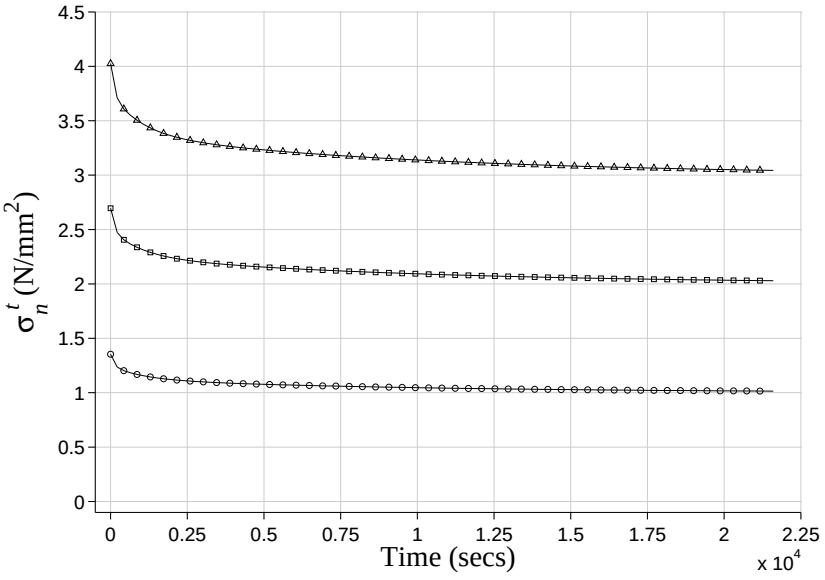

Figure 4.4: First period of stress relaxation from finite element analyses

Figure 4.6 shows the experimental and finite element model results for an MCB sample, subjected to a an axial strain during the first period of stress relaxation, resulting in a σ^{∞} value of around 2.0 N/mm^2, and an axial strain during the second period of stress relaxation, resulting in a σ^{∞} value of around 0.1 N/mm^2. Experimental results are shown as discrete data points, while the finite element model results are shown as a continuous solid line.

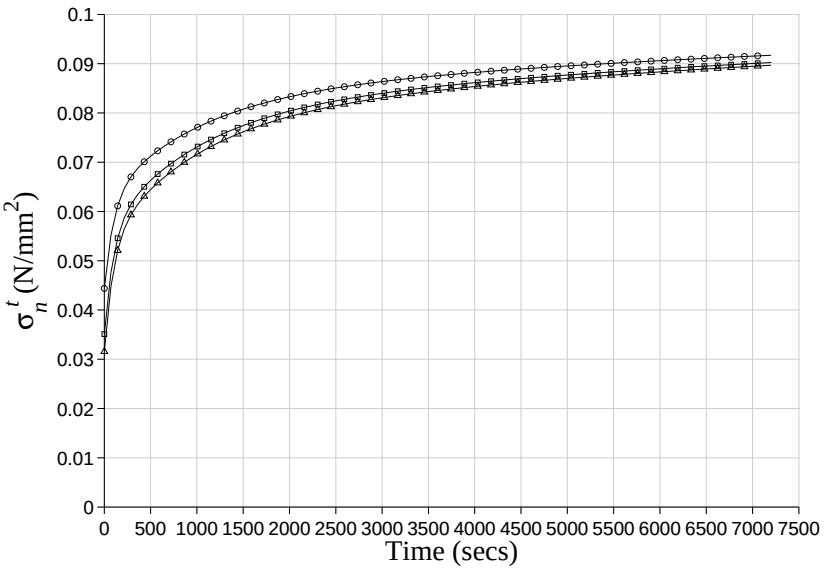

Figure 4.5: Second period of stress relaxation from finite element analyses

There is seen to be good agreement between the experimental data, and the finite element analysis.

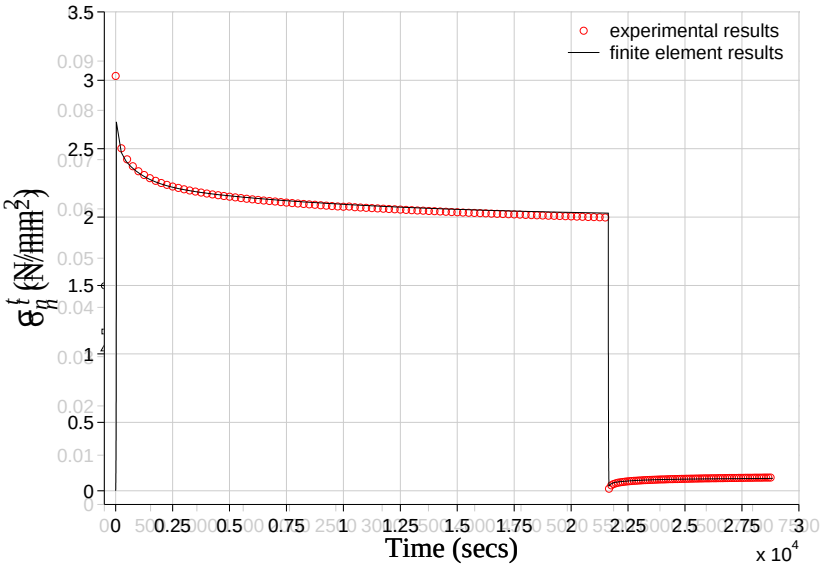

Figure 4.6: Both periods of stress relaxation, experimental and model results

This shows that the developed constitutive model allows the non-linear-visco-elastic properties of MCB as recorded during Test 5, described in the

previous chapter, to be included in finite element analyses. The relationships developed describing E^{∞} as a function of p^{∞} (Equation 4.1), and p^{∞} as a function of ϵ^{e}_{vol} (Equation 4.4) can be used to model the long term non-linear elastic properties of MCB. A third order Prony series (Equation 4.8) with $C = 0.0916$, $k_{t1} = 100$, $k_{t2} = 1000$, and $k_{t3} = 10000$ can be used to model the visco-elastic properties of MCB.

4.3 Non-linear plastic behaviour

The plastic behaviour of bone graft is seen to be similar to that of a soil, with MCB and soil being particulate materials. Soil is composed of soil particles, water, and air. Bone graft is composed of cortico-cancellous bone particles, a mixture of liquids, and air. The most established yield criterion for cohesive and frictional particular materials such as bone graft is the Mohr Coulomb criterion, based on the Mohr Coulomb friction law [73]. In this the yield strength of the material increases in a linear manner with increasing normal stress. The yield criterion is given by two parameters:

$$\tau = c - \sigma_n \tan\theta \tag{4.10}$$

where τ is the shear stress, σ_n is the normal stress (negative in compression), c is the Mohr Coulomb cohesion, and θ is the Mohr Coulomb friction angle.

Previous studies [14,15,42,45] have attempted to characterise MCB using the Mohr Coulomb criterion. However it can be seen that the Mohr Coulomb criterion alone cannot be used to describe the development of consolidation

plastic strains observed in Tests 1 to 5 presented in the previous chapter.

As well as describing the development of consolidation plastic strains with increasing axial compressive stress, observed in the experiments described in the previous chapter, the plastic constitutive model was also required to model the development of irrecoverable plastic strains due to shear stress [14, 15, 42, 45]. The Drucker Prager Cap (DPC) model, as implemented in the commercial package *Abaqus* was chosen as being suitable for modelling the short term non-linear plastic behaviour of MCB [72].

Results from the first 600 load cycles, of Test 4A, described in the previous chapter were used to determine the short term non-linear plastic behaviour of MCB. The development of consolidation plastic strains, as a function of applied axial stress was described by taking the value of plastic strain following the 50th load cycle for each stress level. It was found that the axial plastic strain, ϵ_a^p could be related to the axial stress, σ using:

$$\sigma = c_5 \ (e^{c_6 \epsilon_a^p} - 1) \tag{4.11}$$

where c_5 and c_6 are constants.

Figure 4.7 shows σ against the discrete values found for ϵ_a^p for the MCB sample from Test 4A. In addition it shows the regression curve from Equation 4.11 with $c_5 = 0.5464$ and $c_6 = 4.9120$ giving an R^2 value of 0.9995.

The yield surface of the DPC model is defined by a line representing yielding in shear, and an arc representing yielding in compression, in the meridional (p–q) stress plane. In principal stress space, the yield surface

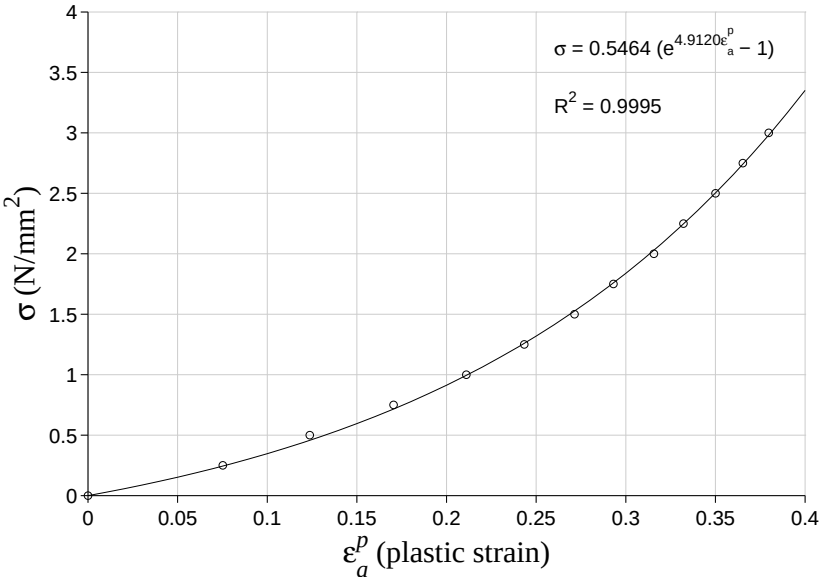

Figure 4.7: σ vs. ϵ_a^p

resembles an ice cream cone, with the shear yield surface representing the cone, and the compression yield surface representing the ice cream.

Figure 4.8 shows the DPC yield surface in the meridional stress plane. The line is defined by:

$$F_s = q - p\tan\beta - d = 0 \tag{4.12}$$

where F_s is the shear yield surface, p is the pressure given by:

$$p = -\left(\frac{\sigma_1 + \sigma_2 + \sigma_3}{3}\right) \tag{4.13}$$

q is the von Mises stress, given by:

$$q = \sqrt{\frac{1}{2}\left[(\sigma_1 - \sigma_2)^2 + (\sigma_2 - \sigma_3)^2 + (\sigma_3 - \sigma_1)^2\right]} \tag{4.14}$$

where stress is taken to be positive in tension.

The parameter d represents the cohesion or particle interlocking, and β is the DPC angle of friction.

The arc is defined:

$$F_c = \sqrt{(p - p_a)^2 + (Rq)^2} - R(d + p_a \tan\beta) = 0 \tag{4.15}$$

where F_c is the cap yield surface, p_a is a cap evolution parameter, and R is a cap configuration parameter.

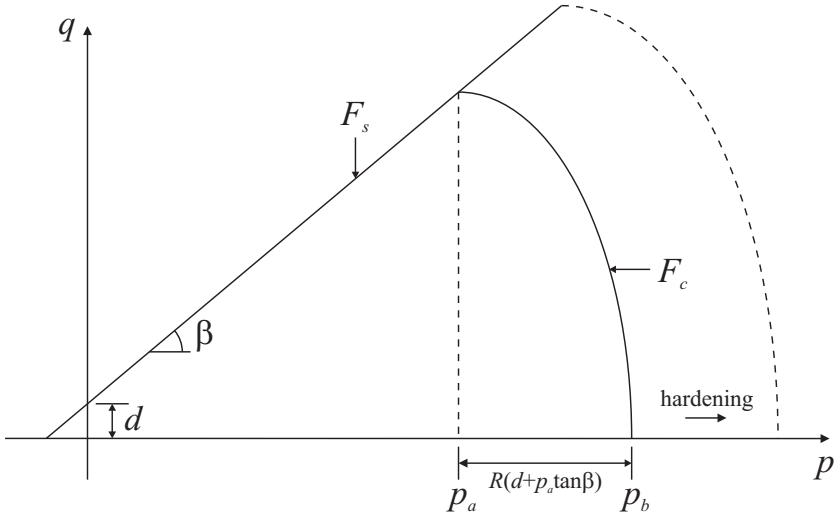

Figure 4.8: Drucker Prager Cap Yield Surface

In addition to the definition of a yield surface, plasticity algorithms require the definition of a flow potential. Figure 4.9 shows the applied DPC flow potential in the meridional stress plane. A non-associated flow rule was

used in the shear region:

$$G_s = \sqrt{[(p_a - p)\tan\beta]^2 + q^2} = d + p_a \tan\beta \tag{4.16}$$

where G_s is the shear flow potential.

The use of a non-associated flow potential in the shear region avoids potential problems associated with numerical singularities occurring at the edges of the yield surface. An associated flow rule was used in the cap region:

$$G_c = F_c \tag{4.17}$$

where G_c is the cap flow potential.

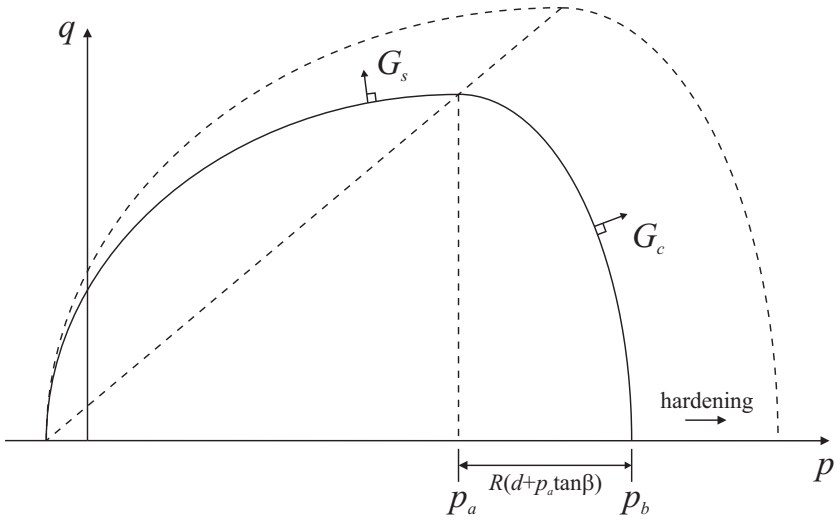

Figure 4.9: Drucker Prager Cap Flow Potential

An estimate for the DPC friction angle, β can be calculated from the Mohr Coulomb friction angle, θ using:

$$\tan\beta \cong \sqrt{3}\sin\theta \tag{4.18}$$

The hardening–softening behaviour (position) of the cap is defined by the evolution of p_b with ϵ^p_{vol}, the plastic volumetric strain. It was assumed that the relationship developed in Equation 4.11, for 1D confined compression, could be adapted to describe the relationship between p_b and ϵ^p_{vol}, giving:

$$p_b = c_7\ (e^{c_8\epsilon^p_{vol}} - 1) \tag{4.19}$$

Modelling of the non-linear plastic behaviour in combination with the non-linear elastic behaviour of MCB was verified using a single element axisymmetric model implemented in *Abaqus*. The short term non-linear elastic behaviour was modelled using the relationship given in Equation 4.1, and calculating E_i based on E^∞. Based on previous studies deriving the Mohr Coulomb friction angle, θ [14,15,42,45] the DPC friction angle, β was set to 40° and the cohesion, d was set close to zero. The cap configuration parameter, R was set to 0.5. An iterative process was used to derive the values of the constants c_7 and c_8 from Equation 4.19, until correlation was observed with the results from Test 4A. It was found that values of $c_7 = 0.5$ and $c_8 = 5.0$ provided a good match with the results from Test 4A. It is observed that the values for c_7 and c_8 are similar to the values found for c_5 and c_6. Figure 4.10 shows the experimental values of σ vs. ϵ^p_a as discrete points, and the values from the finite element analysis as a solid line; a strong correlation is observed.

Figure 4.11 shows the hardening of the Drucker Prager Cap during the

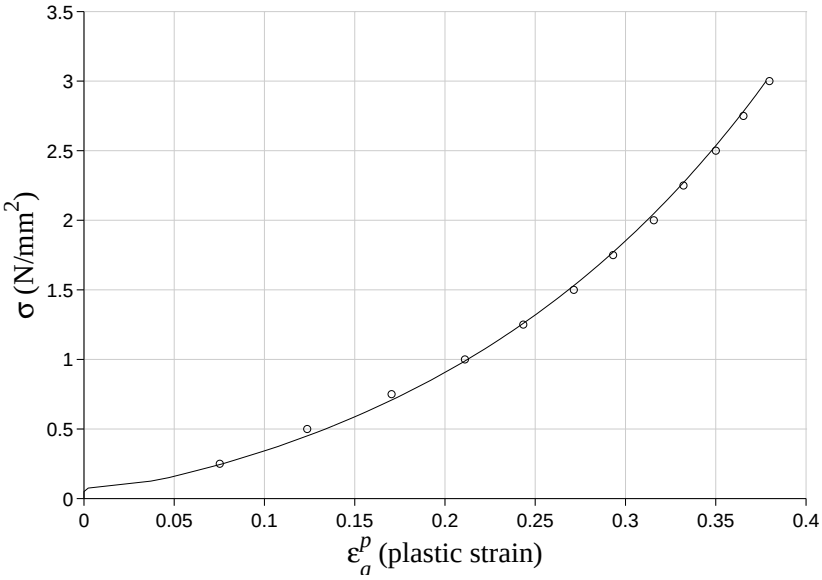

Figure 4.10: σ vs. ϵ_a^p - Experimental and Finite Element Results

finite element analysis. The development of the pressure, p and von Mises stress, q in the sample during the analysis are shown as a red line. The positions of the cap yield surface, and cap flow potential are shown for axial stresses of 0.25–3.0 N/mm^2 in increments of 0.25 N/mm^2. The red circles highlight the values of p and q at these axial stress values. The blue line and blue circle show the development of p and q due to the elastic behaviour of MCB prior to contact with the cap in its initial position. The shear yield surface and series of shear flow potential ellipses are also shown. The *Abaqus* input file used for the analysis is given in the Appendix.

4.4 Conclusions

It is seen that much of the material behaviour of MCB can be modelled using the constitutive models presented. Additional testing of MCB is re-

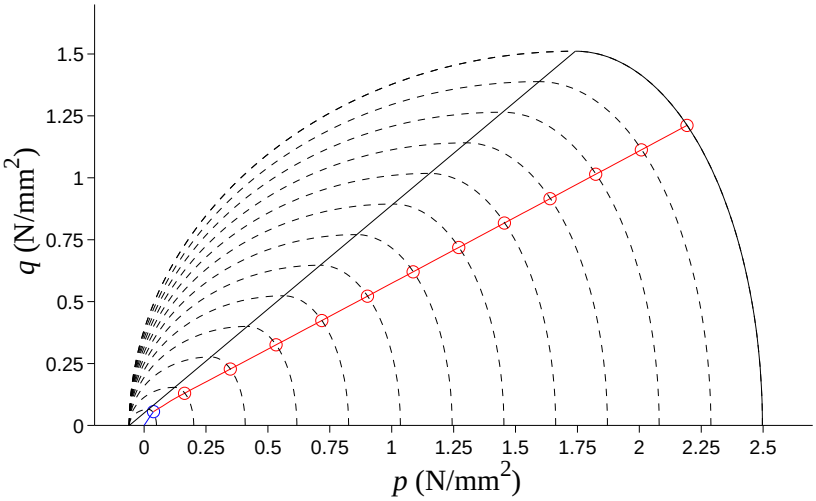

Figure 4.11: Drucker Prager Cap hardening - finite element results

quired to qualify and quantify its complete triaxial visco-elastic-plastic behaviour. However the relationships presented provide for the inclusion of MCB as a non-linear-visco-elastic and non-linear-elasto-plastic material in finite element analyses. The relationships have been verified by correlating the behaviour of finite element models with experimentally observed data. The developed relationships enable the inclusion of MCB in finite element models of revision hip arthroplasty, which was not possible based on the existing published literature.

5

A plane-strain model of the acetabular construct

In order to investigate the behaviour of the acetabular construct, and in particular the bone graft bed following revision hip arthroplasty a two dimensional finite element model was developed in the first instance. Following revision operations the acetabular construct consists of a number of compo-

nents: the host skeleton composed of cortical and trabecular bone, impacted morsellised cortico-cancellous bone (MCB), bone cement and the acetabular cup. The construct is subject to forces of varying magnitude and direction. This chapter details the use of a two dimensional finite element model representative of a transverse section of a reference acetabular cavitory defect in a patient's right hip. The model is subjected to two idealized load cases investigating the effects of changes in loading magnitude and direction. The effect on the short-term stability of the acetabular construct, of increasing the depth of the bone graft bed is investigated. The effect of modelling the plastic behaviour of MCB using the either the Drucker Prager, or Drucker Prager Cap constitutive models was also investigated.

5.1 Geometric definition

Quadrilateral plane-strain elements were used to generate a structured mesh, taken to be representative of a transverse section through the acetabular region, following revision hip arthroplasty carried out using the 'Slooff-Ling' impaction grafting technique. Figure 5.1 shows the line of the section on a diagram of the natural hip joint. The choice of section was based on the work of Bergmann et. al [74, 75] which found that the peak resultant force acting between the femoral head and the acetabular cup during walking occurred in the transverse plane. In addition the variation in the direction of the resultant force during walking, sitting down, and standing up activities was found to be greatest in the transverse plane.

The structured mesh of the acetabular construct consisted of five materials: plastic, cement, bone graft, trabecular bone and cortical bone as shown in

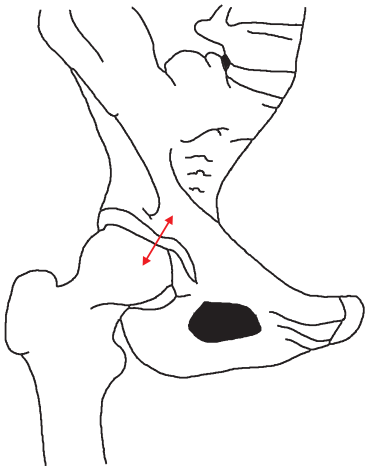

Figure 5.1: Line of the section through the acetabular region shown on a natural hip joint. The plane of the section is perpendicular to the plane of the paper and the double-headed arrow lines within the plane of the section.

Figure 5.2. The mesh of the femoral head was composed of metal as shown in Figure 5.2. The left and right hand side edges of the acetabular construct were restrained and loading was applied at the centre of the femoral head. Smooth sliding surface interactions were used between the femoral head and the acetabular cup allowing the transfer of stresses perpendicular to the surfaces. Previous studies [28, 32] examined primary hip arthroplasty using axisymmetric conditions. However these are not suitable for the non-axisymmetric loading and non-linear material properties considered in this study. Plane-strain conditions were utilised, as these provide confinement in the out-of-plane direction, and are expected to provide representative results in the plane of the model. Dalstra et al [24] noted that a plane-strain model was expected to overestimate the stresses, while an axisymmetric model was expected to underestimate the stresses in the acetabulum, in comparison to the 3D situation.

The mesh shown in Figure 5.2 was arrived at after examining the results

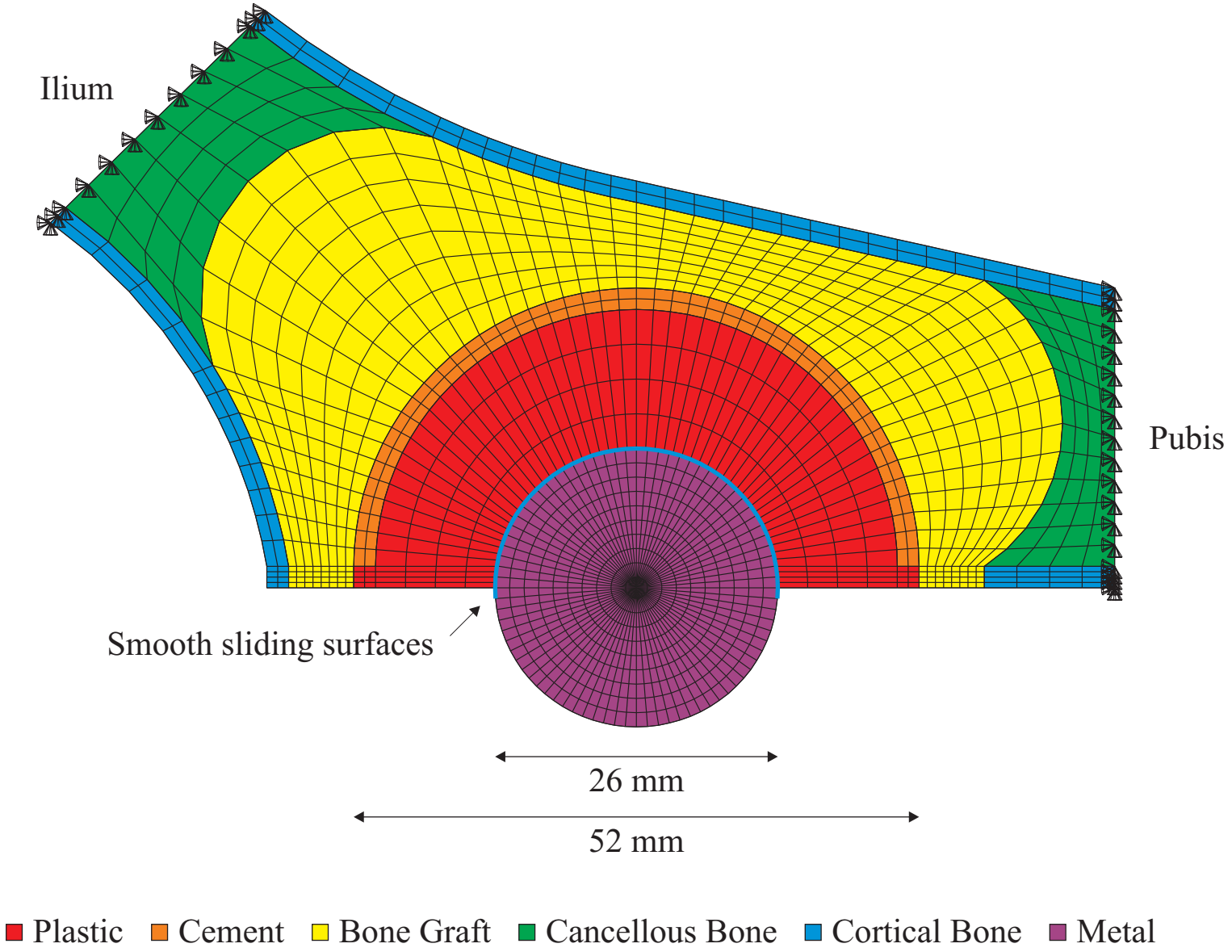

Figure 5.2: 2D structured mesh of the acetabular construct and femoral head

of a number of meshes with different mesh densities subjected to a simple monotonic loading case. Figure 5.2 shows the mesh developed for an acetabular cup with an inside diameter of 26 mm and an outside diameter of 52 mm, including a 2 mm wide flange. This gave a bone graft bed depth of around 8 mm. This mesh was adapted for acetabular cups with inside diameters of 26 mm and outside diameters of 44, 48 and 56 mm (sizes used in practice). The effect of varying the size of the acetabular cup for a reference acetabular defect was to produce four different meshes with minimum bone graft bed depths of around 12, 10, 8 and 6 mm.

5.2 Materials definition

The short term stability of the acetabular construct is for the most part dependent on the behaviour of the bone graft. This is because the bone graft undergoes significant plastic deformation under normal physiological loads. As discussed previous, this is not the case for the other materials comprising the acetabular construct, or the metal femoral head. Plastic, cement, trabecular bone, cortical bone and metal were defined as isotropic linear elastic materials. The values of Young's modulus, E and Poisson's ratio, ν used for these materials are given in Table 5.2.

Table 5.1: Values of E and ν used in the finite element model

Material	E (N/mm^2)	ν
Plastic: UHMWPE†	0.9×10^3	0.4
Cement: PMMA‡	1.8×10^3	0.4
Trabecular bone	1.5×10^2	0.2
Cortical bone	1.8×10^4	0.3
Metal	2.0×10^5	0.3

† Ultra High Molecular Weight Poly-ethylene
‡ Poly-Methyl-Methacrylate

The bone graft was considered in detail and defined as an isotropic elasto-plastic material, using the Drucker Prager, and Drucker Prager Cap constitutive models to describe its plastic behaviour.

Phillips et al. [10] defined the non-linear elastic behaviour of bone graft using a porous elastic model. In the 2D plane-strain analyses presented here the non-linear elastic behaviour of MCB was modelled using the relationship between the Young's modulus, E, and the pressure, p, developed previous

(Chapter 4, Equation 4.1):

$$E = c_1 + c_2 p \tag{5.1}$$

where c_1 and c_2 are constants set to 5 and 35.

5.2.1 Drucker Prager constitutive model

The series of analyses investigating the effect of changing the depth of the bone graft bed were carried out using the Drucker Prager constitutive model. Thus it should be noted that while these include the development of plastic shear strains, they do not include the development of consolidation plastic strains. The Drucker Prager yield criterion is identical to the shear yield criterion of the Drucker Prager Cap constitutive model presented in Chapter 4, described by two parameters:

$$q = d + p \tan \beta \tag{5.2}$$

where q is the von mises stress, p is the pressure, d is the Drucker Prager cohesion, and β is the Drucker Prager friction angle.

Based on previous studies [14,15,42,45] the friction angle, β was set to 40° and the cohesion, d was taken as 0.05 N/mm^2 (close to zero). While the yield criterion determines the onset of yielding, the post yield plastic behaviour is determined by the plastic flow potential function. Often this function is assumed to be the same as the yield criterion. This assumptions, termed

associated plasticity, has been show to predict excessive dilation of materials for the Mohr Coumlomb, and Drucker Prager yield criteria [73, 76]. Some dilation is expected in particular materials because particles ride over each other in the shearing process. However the excessive dilation predicted by the associated flow rule can be corrected by using a non-associated flow rule, in which the plastic potential function is similar to the yield criterion, but uses a dilation angle less than the friction angle. In this study, the dilation angle, ψ was assumed to be half the friction angle, β. An acknowledged drawback of the Drucker Prager yield criterion, addressed later in this chapter, is that it is not capable of describing the consolidation of the bone graft under compressive loading.

In general plasticity algorithms fail to converge when applied loads exceed those that can be sustained by the model. Using the Drucker Prager plasticity model, failure to obtain converged solutions is expected when the material undergoes unconfined stress changes, such as those that occur at the unconfined edges of the bone graft between the flange of the acetabular cup and the cortical bone. In practice bone graft can be removed from these areas of the acetabular construct. In the 2D plane-strain analyses presented here this was addressed by overlaying the bone graft elements with a layer of elastic elements with a very low value of Young's modulus, less than 5% of the lowest value taken for the bone graft. This artifice provides computational stability without altering the overall behaviour of the model.

5.2.2 Drucker Prager Cap constitutive model

Two further analyses were carried out using the Drucker Prager Cap (DPC) constitutive model presented in the previous chapter. The DPC yield criterion is comprised of a shear surface (identical to the Drucker Prager yield criterion) and a cap yield surface, allowing shear and consolidation plastic strains to be described. The hardening–softening behaviour (position of the cap) was defined based on the relationship between the cap evolution parameter, p_b and the volumetric plastic strain, ϵ_{vol}^{p} developed previous (Chapter 4, Equation 4.19):

$$p_b = c_3(e^{c_4\epsilon_{vol}^{p}} - 1) \tag{5.3}$$

where c_3 and c_4 are constants set to 0.5 and 5.0.

Based on advice from orthopaedic surgeons the initial volumetric plastic strain, ϵ_{vol}^{p} experienced by the bone graft was set to 0.2. This gave an initial p_b value (cap position) of around 1.0 N/mm^2. This was seen to be consistent with the bone graft bed following impaction at the time of surgery 'not suffering permanent deformation under thumb pressure'. Thumb pressure was calculated to be around 0.5–1.0 N/mm^2, having found that 50–100 N force could be transferred through a contact area of around 100 mm^2, when load was applied through the thumb in a laboratory setting.

As for the Drucker Prager yield criterion, the friction angle, β was taken to be 40° and the cohesion, d was taken to be 0.05 N/mm^2 (close to zero). The cap configuration parameter R, described in the previous chapter was

taken to be 0.5. As for the Drucker Prager constitutive model, a layer of elastic elements with a very low value of Young's modulus, less than 5% of the lowest value taken for the bone graft, was used to provide computational stability without altering the overall behaviour of the model.

5.3 Loading definition

There has been a considerable amount of research carried out by Bergmann and his team at the University of Berlin [74, 75, 77–81] into the magnitude and direction of the resultant force acting between the femoral head and the acetabulum during activities such as walking and running. However there has been a limited amount of research carried out into the loading distribution caused by the transfer of the resultant force between the femoral head and the acetabular cup. Ipavec et al. [82] and Phillips [9] supported by Hodge et al. [83, 84] proposed the use of cosine and parabolic distributions respectively, acting on the acetabulum. In this study the transfer of the resultant force between the femoral head and the acetabular cup was modelled directly using smooth sliding surfaces, with loading being applied as a point load at the centre of the femoral head, as shown in Figure 5.3. Thus uncertainties associated with pre-defined loading distributions were removed.

Bergmann et al. [74] reported that one-off events such as stumbling gave rise to a resultant force acting on the acetabulum of up to 870 % body weight (BW). Bergmann et al. [75] reported an average median peak resultant force acting on the acetabulum of 238 % BW for four patients walking at 4 km/h. Bergmann et al. [74, 75] also reported that the resultant force in general did not fall to zero even during periods of rest. The findings of Bergmann et

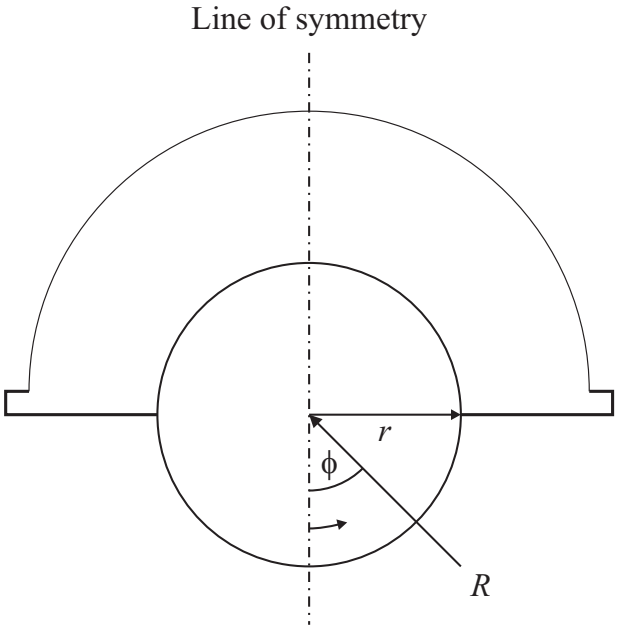

Figure 5.3: The acetabular cup and the femoral head, showing the inner radius, r of the acetabular cup, the resultant force, R acting at the centre of the femoral head and the angle, ϕ to the resultant force.

al. [74,75] are in part supported by a simplified mathematical model presented in Bergmann et al. [80]. Based on the findings of Bergmann et al. two idealised cyclic load cases were developed. For each of these load cases it was assumed that the BW was equal to 1000 N and the maximum resultant force acting at the centre of the femoral head was equal to 300 % BW or 3000 N.

5.3.1 Load Case A

Load case A examined the cyclic change in loading magnitude at a given direction. An initial load of 10 % BW or 100 N was applied to the centre of the femoral head at an angle of $\frac{1}{4}\pi$. The magnitude of the load was then varied bewteen $R = 10\%$ BW and 300% BW over a series of steps as shown in Figure 5.4.

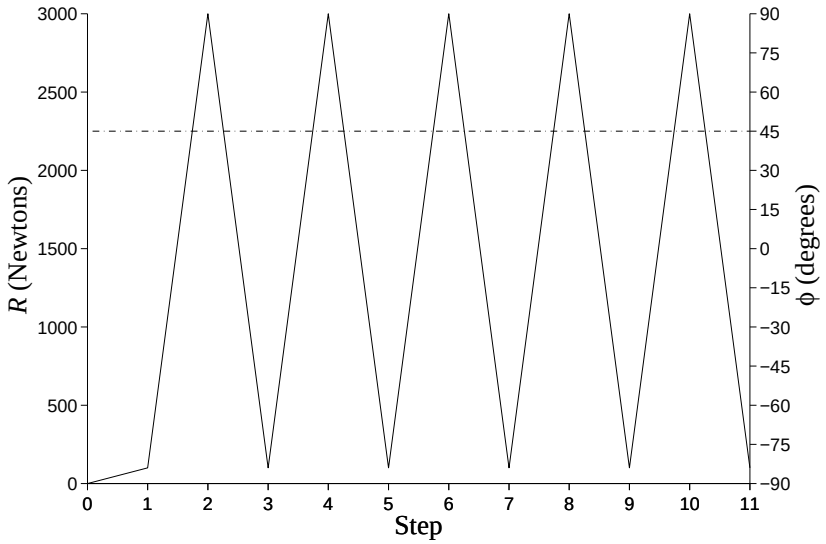

Figure 5.4: Load Case A

5.3.2 Load Case B

Load case B examined the cyclic change in loading direction at a given magnitude. An initial load of 300% BW or 3000 N was applied to the centre of the femoral head at an angle ϕ of $\frac{1}{4}\pi$. The direction of the load was then varied between $\phi = +\frac{1}{4}\pi$ and $\phi = -\frac{1}{4}\pi$ over a series of load steps as shown in Figure 5.5.

It should be noted that these idealised load cases are designed to investigate the effects of changing load magnitude and changing load direction in isolation. The load cases are not an attempt to mimic the exact loading patterns produced by activities such as walking or running.

The out of plane thickness of the finite element model was taken to be $2r$, where r is the inner radius of the acetabular cup, as shown in Figure 5.3. This value was chosen so that the surface contact area between the femoral head and the acetabular construct was the same as the surface contact area

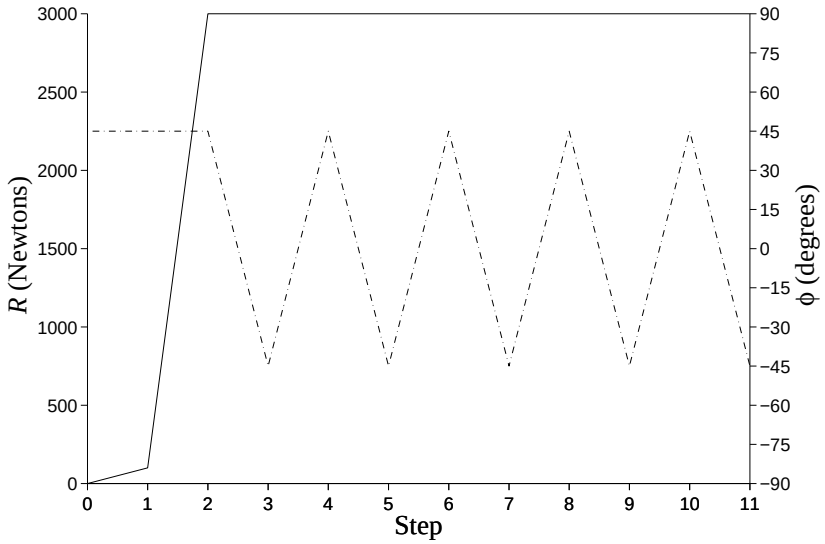

Figure 5.5: Load Case B

between the femoral head and the acetabular cup in the 3D situation, both of which are calculated:

$$S = 2\pi r^2 \tag{5.4}$$

where S is the surface contact area.

5.4 Response using the Drucker Prager constitutive model

5.4.1 Load Case A

Figure 5.6 shows the deformed shapes of the acetabular construct at the end of selected load steps for an acetabular cup of 52 mm outside diameter,

subjected to load case A. When the load is increased to 3000 N over load step 2, there is significant deformation of the bone graft accompanied by clockwise rotation of the acetabular cup. When the loading is decreased to 100 N over load step 3, much of the deformation of the bone graft is recovered. However, the acetabular cup does not return to its virgin position, due to the development of irrecoverable plastic strains in the bone graft. When comparing the displaced shapes at the end of the selected load steps, it is observed that the extent of clockwise rotation of the acetabular cup worsens after each cycle of loading and unloading. It is also observed that, with each loading cycle, bone graft is squeezed out to the left and right hand sides of the acetabular cup.

Figure 5.6 also shows the development of maximum (positive in tension) principal plastic strains in the bone graft, at the end of the selected loading steps. When the load is increased to 3000 N over load step 2, large regions of the bone graft suffer plastic strains to the left and right hand sides of the acetabular cup. There is a progression in the regions of the bone graft affected by plastic strains with each cycle of loading and unloading.

Figure 5.7 shows the displaced shapes following the last applied load step for each of the four meshes. The extent of rotation of the acetabular cup following repeated cycles of loading and unloading decreases as the cup size increases. The extent to which bone graft is squeezed out to the left and right hand side edges of the acetabular cup is reduced as the cup size increases. Figure 5.7 also shows the development of plastic strains following the final load step for each of the four meshes. The extent of the regions in which plastic strains occur reduces as the cup size increases.

In order to investigate the effect of cup size on the short term stability

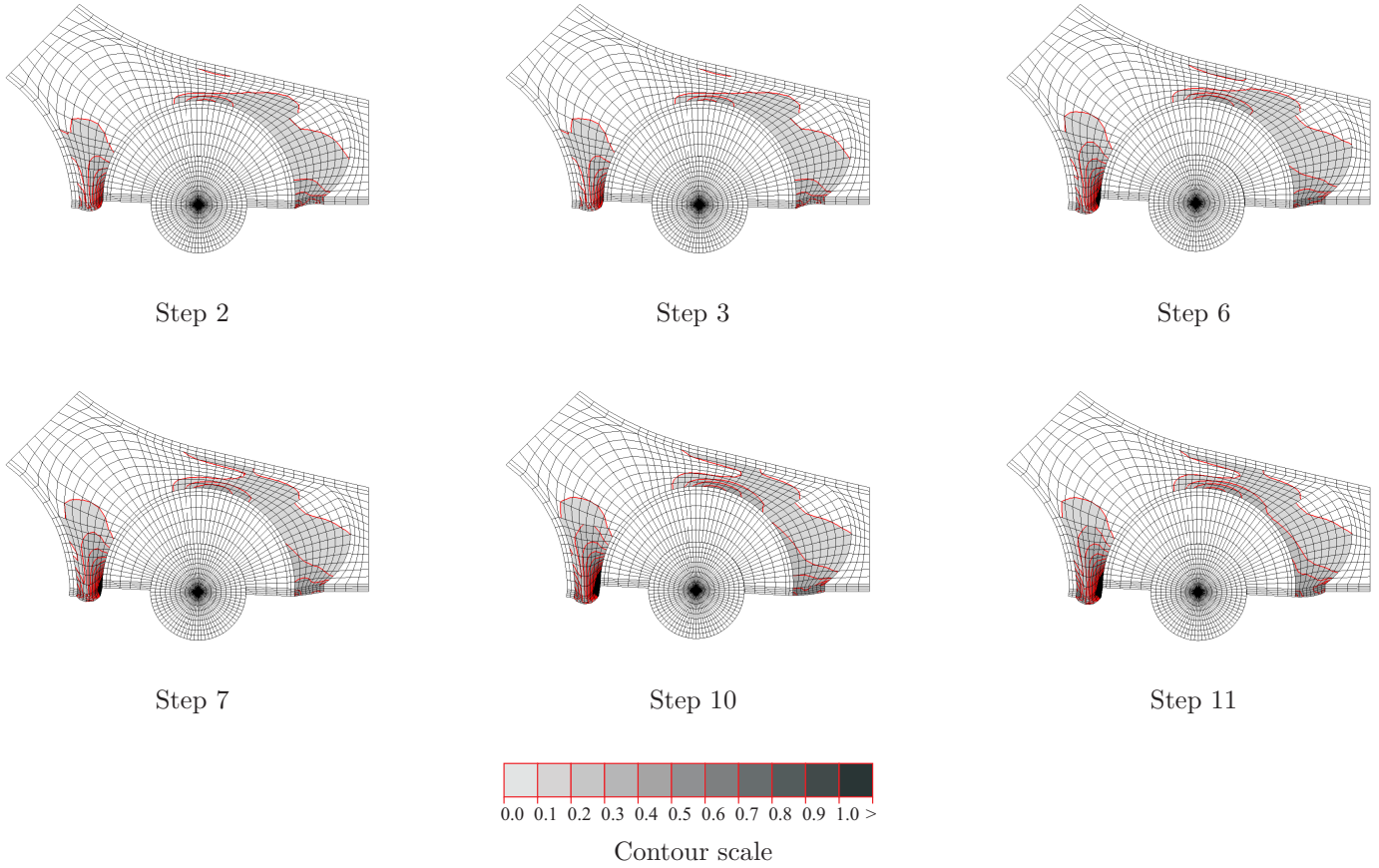

Figure 5.6: Displaced shapes of the acetabular construct and development of maximum principal plastic strains in the bone graft at the end of selected load steps for an acetabular cup of 52 *mm* outside diameter subjected to load case A. The load step number is shown beneath the relevant image.

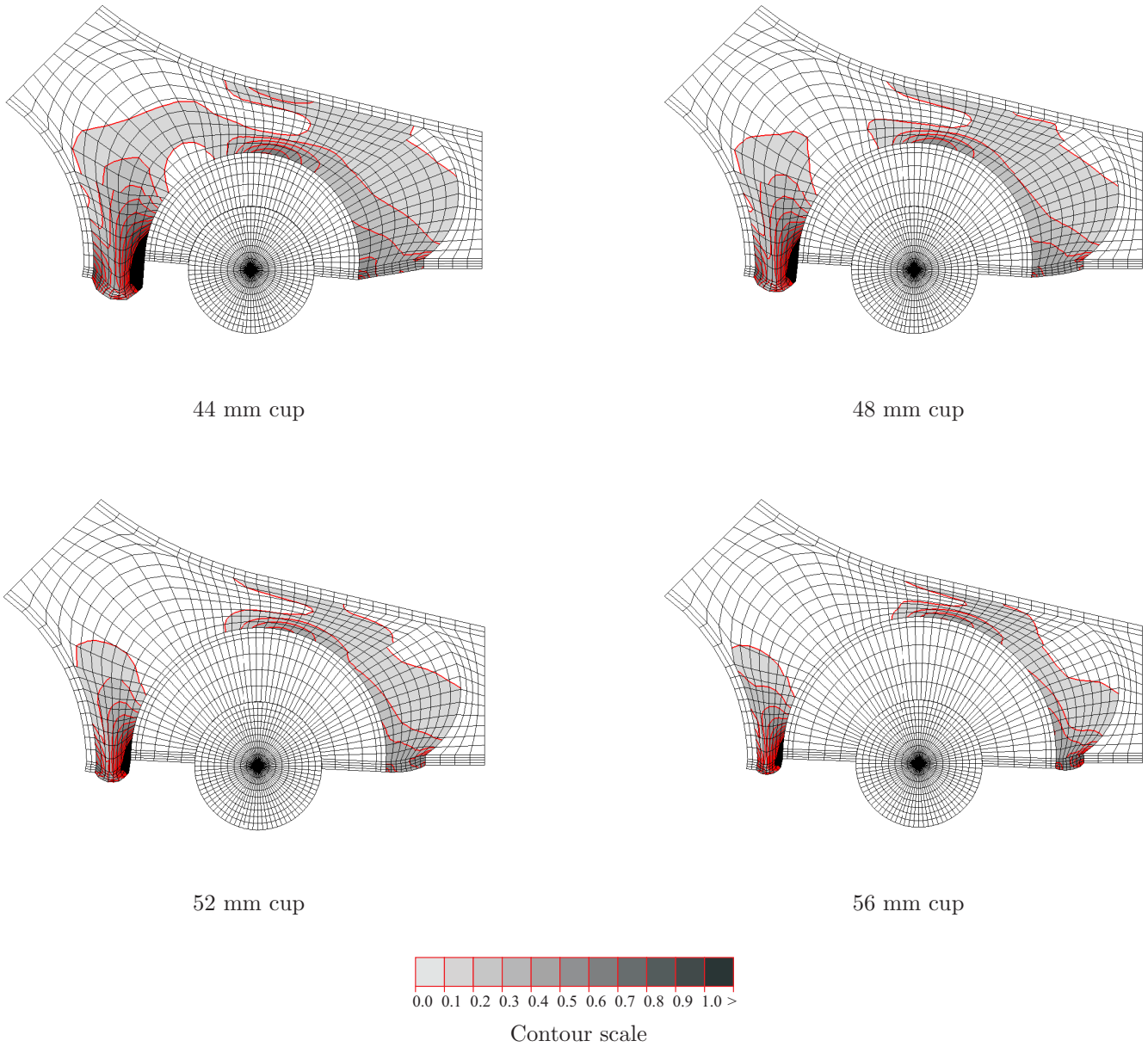

Figure 5.7: Displaced shapes of the acetabular construct and development of maximum principal plastic strains following the final load step for each of the four meshes subjected to load case A. The cup size is shown beneath the relevant image.

of the acetabular construct the extent of rotation of the acetabular cup was measured for each of the four meshes. This measurement was chosen, as it is one of the factors often used in follow up studies [85–87]. It has also been used in experiments to compare bone grafts from different bone mills [51,52]. The extent of rotation was found by taking the displaced position of the left and right inside corners of the acetabular cup. Having confirmed that the deformation of the acetabular cup was minor, the clockwise rotation of the acetabular cup was taken as the angle from the original configuration between these two points.

Figure 5.8 shows the clockwise extent of rotation of the acetabular cups for each of the four meshes. The initial loading of 100 N causes each of the cups to rotate by a small amount. When the loading is increased to 3000 N over load step 2, each of the cups continues to rotate in the clockwise direction. It should be noted that the extent of rotation decreases as the cup size increases. When the load is decreased to 100 N over load step 3, the extent of clockwise rotation for each of the cups decreases.

Figure 5.8 shows two important trends. First, the increase in the extent of rotation for each load cycle decreases as the number of cycles increases for all cup sizes. Second, the increase in the extent of rotation for a given decrease in cup size is not linear, but increases as the cup size decreases. Both of these are of clinical significance. The first suggests that stabilization of the bone graft may occur following initial rotation of the acetabular cup. The second suggests that initial rotation may be minimised by using the largest practical size of acetabular cup.

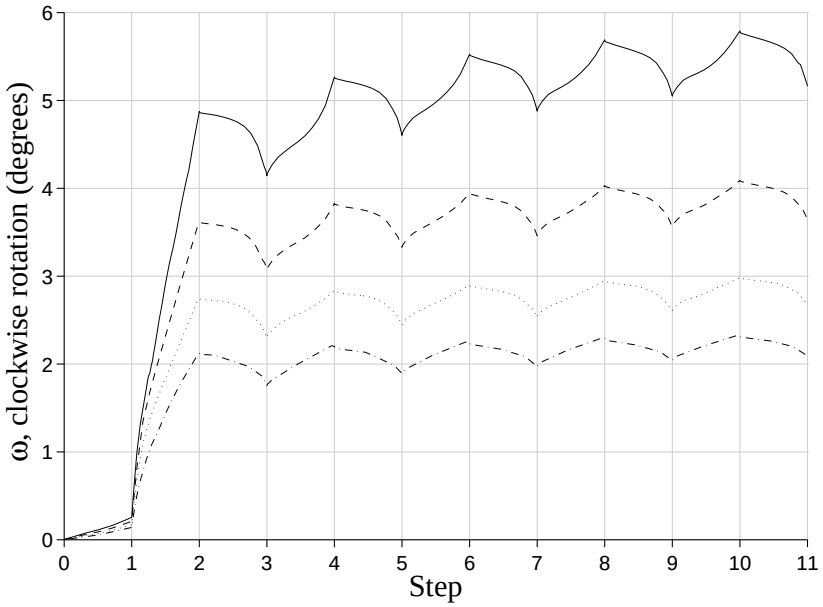

Figure 5.8: Clockwise rotation of the acetabular cup for each of the four meshes subjected to load case A

5.4.2 Load Case B

Figure 5.9 shows the displaced shapes of the acetabular construct at the end of selected load steps for an acetabular cup of 52 mm outside diameter, subjected to load case B. When the loading is increased to 3000 N over load step 2, there is movement of the acetabular cup to the left hand side, accompanied by rotation of the acetabular cup in the clockwise direction. When ϕ is varied from $+\frac{1}{4}\pi$ to $-\frac{1}{4}\pi$ over load step 3, there is movement of the acetabular cup to the right hand side, accompanied by rotation of the acetabular cup in an anticlockwise direction. When comparing the displaced shapes at the end of the selected load steps, it is observed that the extent of rotation either clockwise, or anticlockwise decreases after each cycle of varying ϕ from $+\frac{1}{4}\pi$ to $-\frac{1}{4}\pi$ and back. It is also observed that, with each loading cycle, bone graft is squeezed out to the left and right hand sides of the acetabular cup.

Figure 5.9 also shows the development of maximum principal plastic strains in the bone graft at the end of the selected load steps. When the loading is increased to 3000 N over load step 2, large regions of plastic strains occur to the left and right hand side edges of the acetabular cup. There is a progression in terms of the regions of bone graft affected by plastic strains with each cycle of varying ϕ from $+\frac{1}{4}\pi$ to $-\frac{1}{4}\pi$ and back.

Figure 5.10 shows the displaced shapes following the last applied load step for each of the four meshes. The extent of rotation of the acetabular cup, following repeated cycles of varying ϕ from $+\frac{1}{4}\pi$ to $-\frac{1}{4}\pi$ and back, decreases as the cup size increases. The extent to which bone graft is squeezed out to the left and right had side edges of the acetabular cup is reduced as the

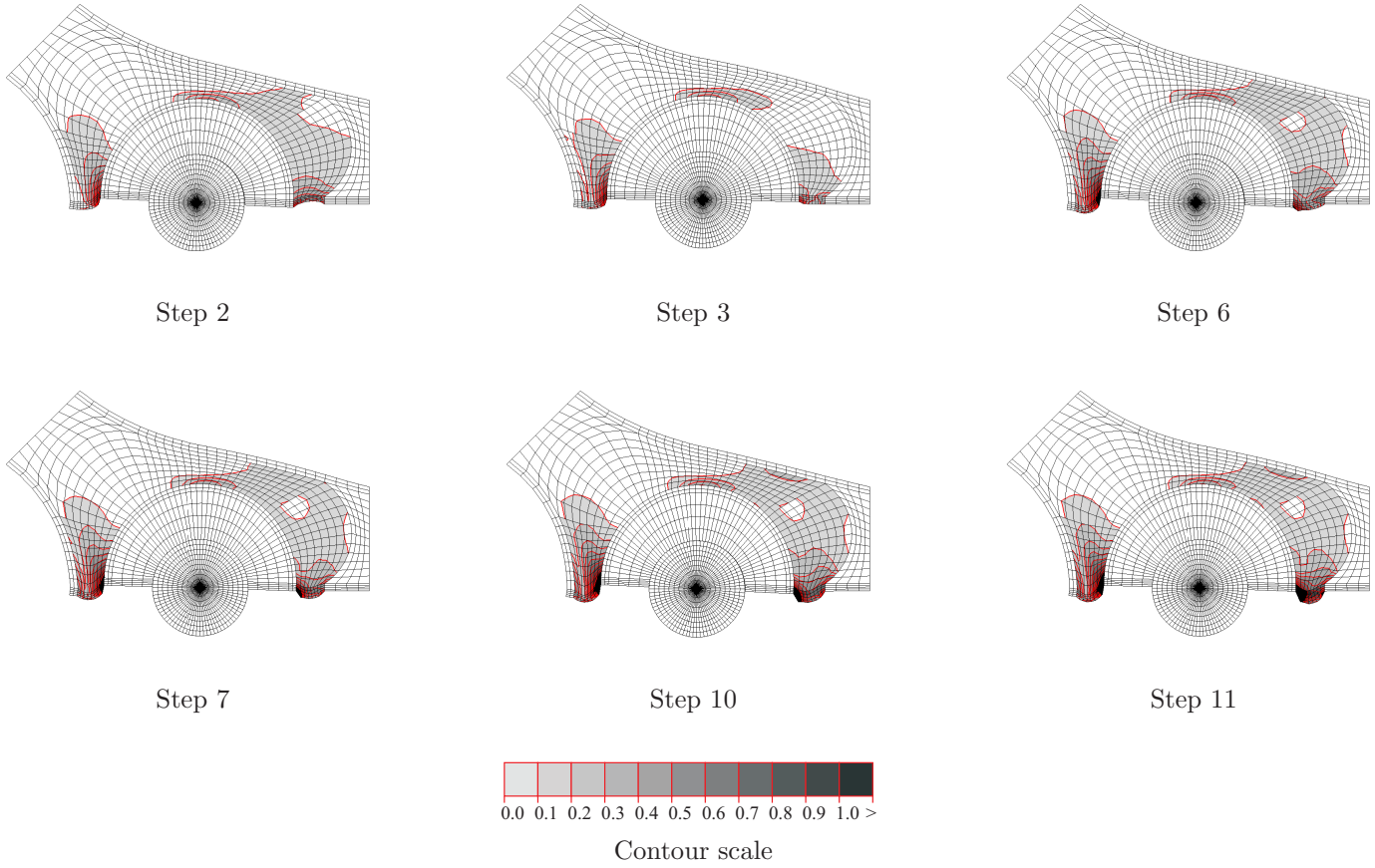

Figure 5.9: Displaced shapes of the acetabular construct and development of maximum principal plastic strains in the bone graft at the end of selected load steps for an acetabular cup of 52 mm outside diameter subjected to load case B. The load step number is shown beneath the relevant image.

cup size increases. Figure 5.10 also shows the development of plastic strains following the final load step for each of the four meshes. The extent of the regions in which plastic strains occur reduces as the cup size increases.

Figure 5.11 shows the clockwise extent of rotation of the acetabular cup for each of the four meshes. Identical to load case A, the initial loading of 100 N causes each of the cups to rotate by a small amount. When the loading is increased to 3000 N over load step 2, each of the cups continues to rotate in a clockwise direction. It should be noted that the extent of rotation decreases as the cup size increases. When ϕ is varied from $+\frac{1}{4}\pi$ to $-\frac{1}{4}\pi$ over load step 3, the extent of clockwise rotation of each of the cups decreases.

It should be noted that the extent of rotation either clockwise or anti-clockwise decreases after each cycle of varying ϕ from $+\frac{1}{4}\pi$ to $-\frac{1}{4}\pi$ and back. This suggests that stabilisation of the acetabular construct may be aided by undertaking a range of activities producing a wide variety of angles to the resultant force.

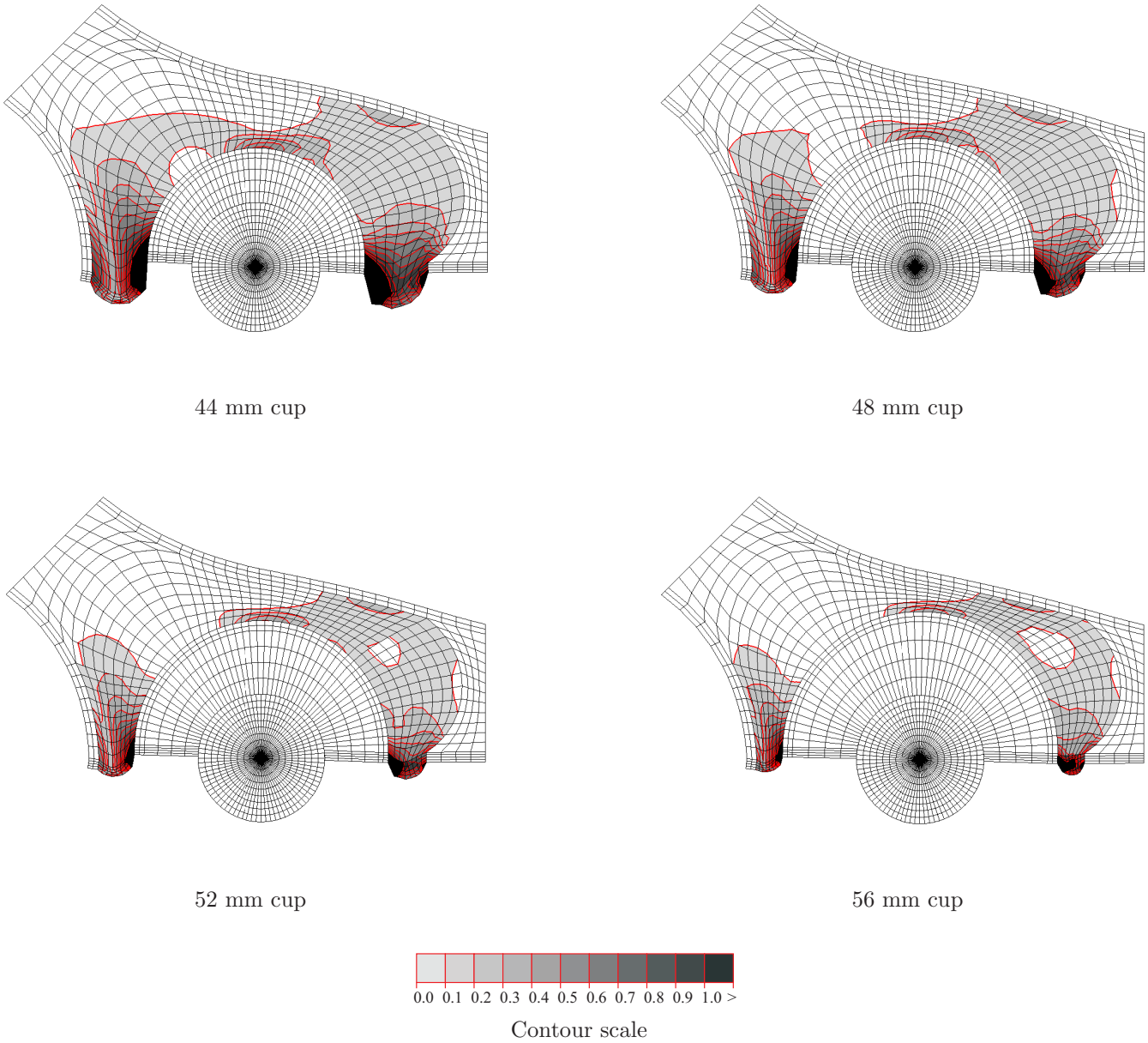

Figure 5.10: Displaced shapes of the acetabular construct and development of maximum principal plastic strains following the final load step for each of the four meshes subjected to load case B. The cup size is shown beneath the relevant image.

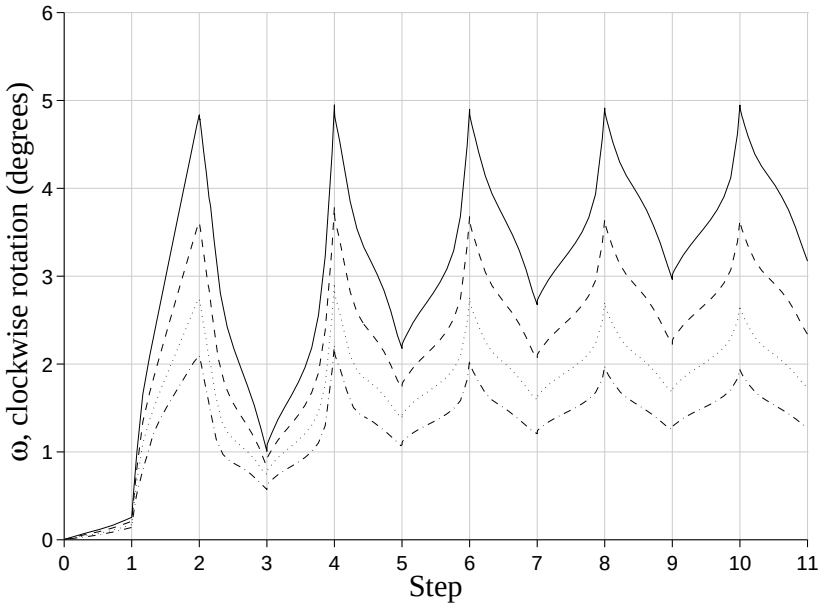

Figure 5.11: Clockwise rotation of the acetabular cup for each of the four meshes subjected to load case B

5.5 Response using the Drucker Prager Cap constitutive model

5.5.1 Load Case A

Figure 5.12 shows the displaced shapes of the acetabular construct at the end of selected load steps, for an acetabular cup of 52 mm outside diameter, subjected to load case A. When the load is increased to 3000 N over load step 2, there is significant deformation of the bone graft accompanied by clockwise rotation of the acetabular cup. When the loading is decreased to 100 N over load step 3, much of the deformation of the bone graft is recovered. However the acetabular cup does not return to its virgin position, due to the development of irrecoverable plastic strains in the bone graft. Comparing the displaced shapes with those found using the Drucker Prager yield criterion, without the cap (Figure 5.6) it is observed the the extent of rotation, and migration of the acetabular cup into the defect is greater using the Drucker Prager Cap yield criterion.

When comparing the displaced shapes in Figure 5.12 at the end of the selected loading steps, it is observed that the extent of clockwise rotation, worsens after each cycle of loading and unloading. This is qualitatively similar to the trend observed using the Drucker Prager yield criterion. It is observed that, with each loading cycle, bone graft is once again squeezed out to the left hand side of the acetabular cup in particular.

Figure 5.12 also shows the development of maximum principal (positive in tension) plastic strains in the bone graft, at the end of the selected loading

steps. When the load is increased to 3000 N over load step 2, large regions of the bone graft suffer plastic strains to the left and right hand sides of the acetabular cup. There is a progression in the regions of the bone graft affected by plastic strains with each cycle of loading. Comparing the regions of bone graft affected by maximum plastic strains using the Drucker Prager yield criterion (Figure 5.6) it is observed that the region affected is increased using the Drucker Prager Cap yield criterion.

Figure 5.13 shows the development of minimum principal (negative in compression) plastic strains in the bone graft, at the end of the selected loading steps. When the load is increased to 3000 N over load step 2, a large area of the bone graft suffers plastic strains behind the acetabular cup in the direction of loading. These plastic strains are due to the consolidation of bone graft under compression loading in this area. They contribute to the increased rotation of the acetabular cup observed under loading using the Drucker Prager Cap yield criterion in comparison to the Drucker Prager yield criterion.

Figure 5.14 shows the clockwise extent of rotation of the acetabular cup using the Drucker Prager and Drucker Prager Cap (DPC) yield criterion. It is observed that the rotation of the acetabular cup due to loading is similar over load step 1 and part of load step 2 for both yield criterion. The development of consolidation plastic strains allowed by the Drucker Prager Cap yield criterion then allows the acetabular cup to rotate to a greater extent using the DPC yield criterion. The increase in the extent of rotation for each load cycle decreases as the number of cycles increases, for each of the yield criterion. It is observed that the rotation of the acetabular cup at the end of unloading steps is around 80% higher using the DPC yield criterion.

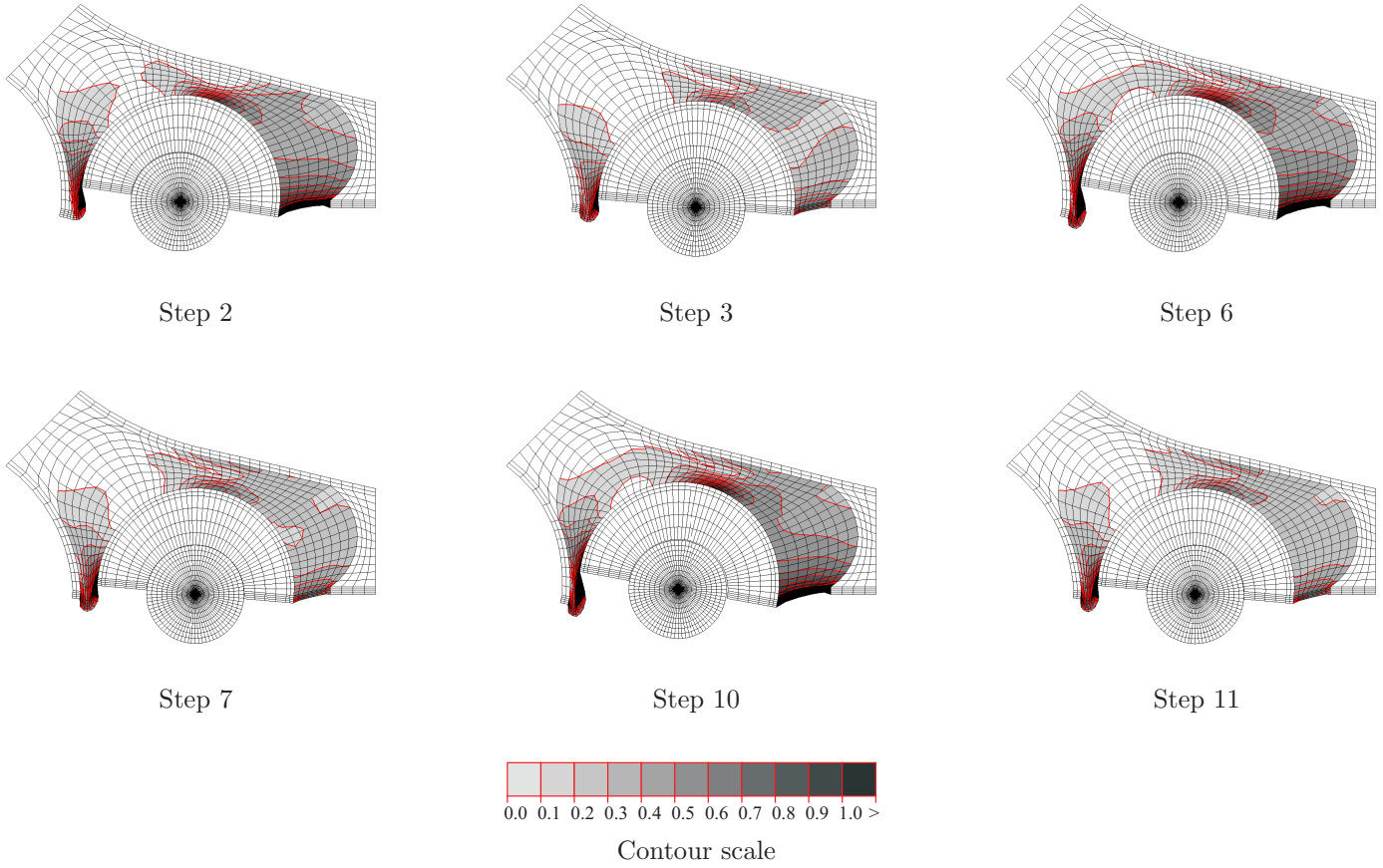

Figure 5.12: Displaced shapes of the acetabular construct and development of maximum principal plastic strains in the bone graft at the end of selected load steps for an acetabular cup of 52 mm outside diameter subjected to load case A. The load step number is shown beneath the relevant image.

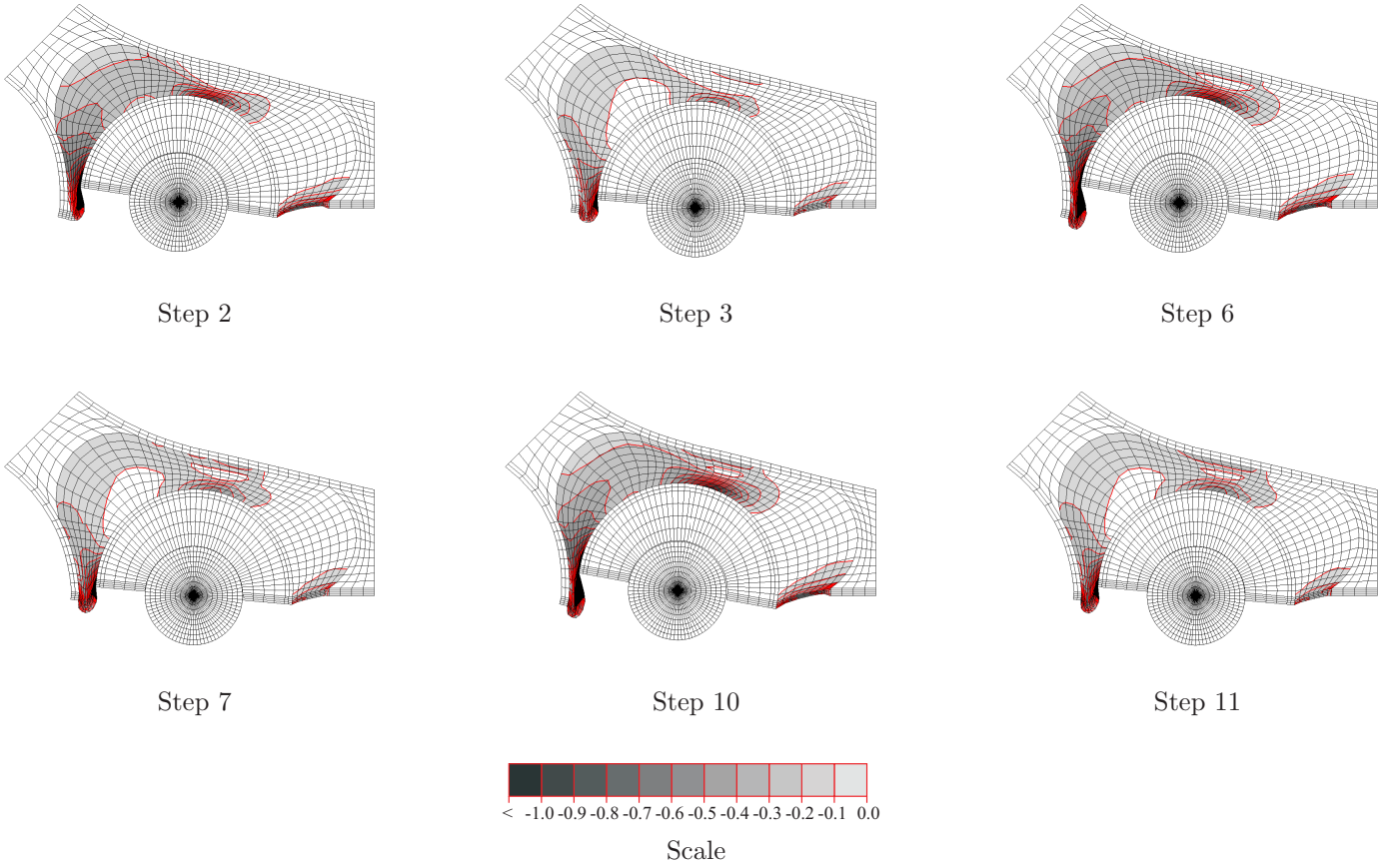

Figure 5.13: Displaced shapes of the acetabular construct and development of minimum principal plastic strains in the bone graft at the end of selected load steps for an acetabular cup of 52 *mm* outside diameter subjected to load case A. The load step number is shown beneath the relevant image.

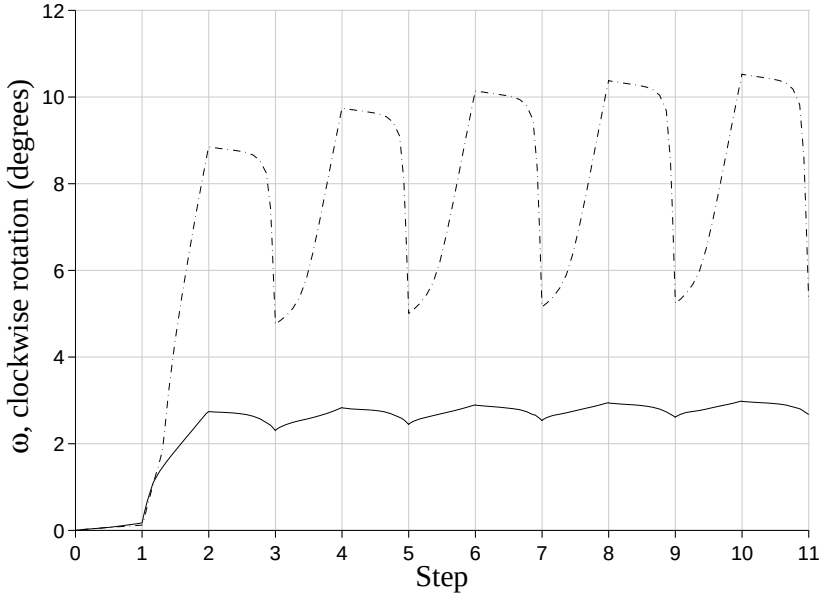

Figure 5.14: Clockwise rotation of a 52 mm acetabular cup subjected to load case A using the Drucker Prager and Drucker Prager Cap failure criteria

5.5.2 Load Case B

Figure 5.15 shows the displaced shapes of the acetabular cup at the end of selected load steps, for an acetabular cup of 52 mm outside diameter, subjected to load case B. When the loading is increased to 3000 N over load step 2, there is movement of the acetabular cup to the left hand side accompanied by rotation of the acetabular cup in the clockwise direction. When ϕ is varied from $+\frac{1}{4}\pi$ to $-\frac{1}{4}\pi$ over load step 3, there is movement of the acetabular cup to the right hand side accompanied by rotation of the cup in the anticlockwise direction. Comparing the displaced shapes with those found using the Drucker Prager yield criterion (Figure 5.9) it is observed the the extent of rotation, clockwise or anticlockwise, and migration of the acetabular cup, to the left or right side is greater using the Drucker Prager Cap yield criterion.

When comparing the displaced shapes at the end of the selected loading steps, it is observed that the extent of rotation either clockwise, or anticlockwise decreases after each cycle of varying ϕ from $+\frac{1}{4}\pi$ to $-\frac{1}{4}\pi$ and back. This is qualitatively similar to the trend observed using the Drucker Prager yield criterion.

Figure 5.15 also shows the development of maximum principal plastic strains in the bone graft at the end of selected loading steps. When the load is increased to 3000 N over load step 2, large regions of plastic strains occur to the left and right hand side edges of the acetabular cup. There is a progression in terms of the regions of bone graft affected by plastic strains with each cycle of varying ϕ from $+\frac{1}{4}\pi$ to $-\frac{1}{4}\pi$ and back. Comparing the regions of bone graft affected by maximum plastic strains using the Drucker

Prager yield criterion (Figure 5.9) it is observed that the area affected is increased using the Drucker Prager Cap yield criterion.

Figure 5.16 shows the development of minimum principal (negative in shortening) plastic strains in the bone graft, at the end of the selected loading steps. When the load is increased to 3000 N over load step 2, a large area of the bone graft suffers plastic strains behind the acetabular cup in the direction of loading. There is a progression in terms of the regions of bone graft affected by plastic strains with each cycle of varying ϕ from $+\frac{1}{4}\pi$ to $-\frac{1}{4}\pi$ and back. These plastic strains are due to the consolidation of bone graft under compression loading.

Figure 5.17 shows the clockwise extent of rotation of the acetabular cup using the Drucker Prager and Drucker Prager Cap yield criterion. It is observed that the rotation of the acetabular cup due to loading is similar over load step 1 and part of load step 2 for both yield criterion. The development of consolidation plastic strains allowed by the Drucker Prager Cap yield criterion then allows the acetabular cup to rotate to a greater extent using the DPC yield criterion.

It should be noted that the extent of rotation either clockwise or anti-clockwise decreases after each cycle of varying ϕ from $+\frac{1}{4}\pi$ to $-\frac{1}{4}\pi$ and back, for both the Drucker Prager and Drucker Prager Cap yield criterion.

5.6 Conclusions

The load cases used in this study are idealised and do not represent specific activities; however, rotations of the kind discussed in this study have been

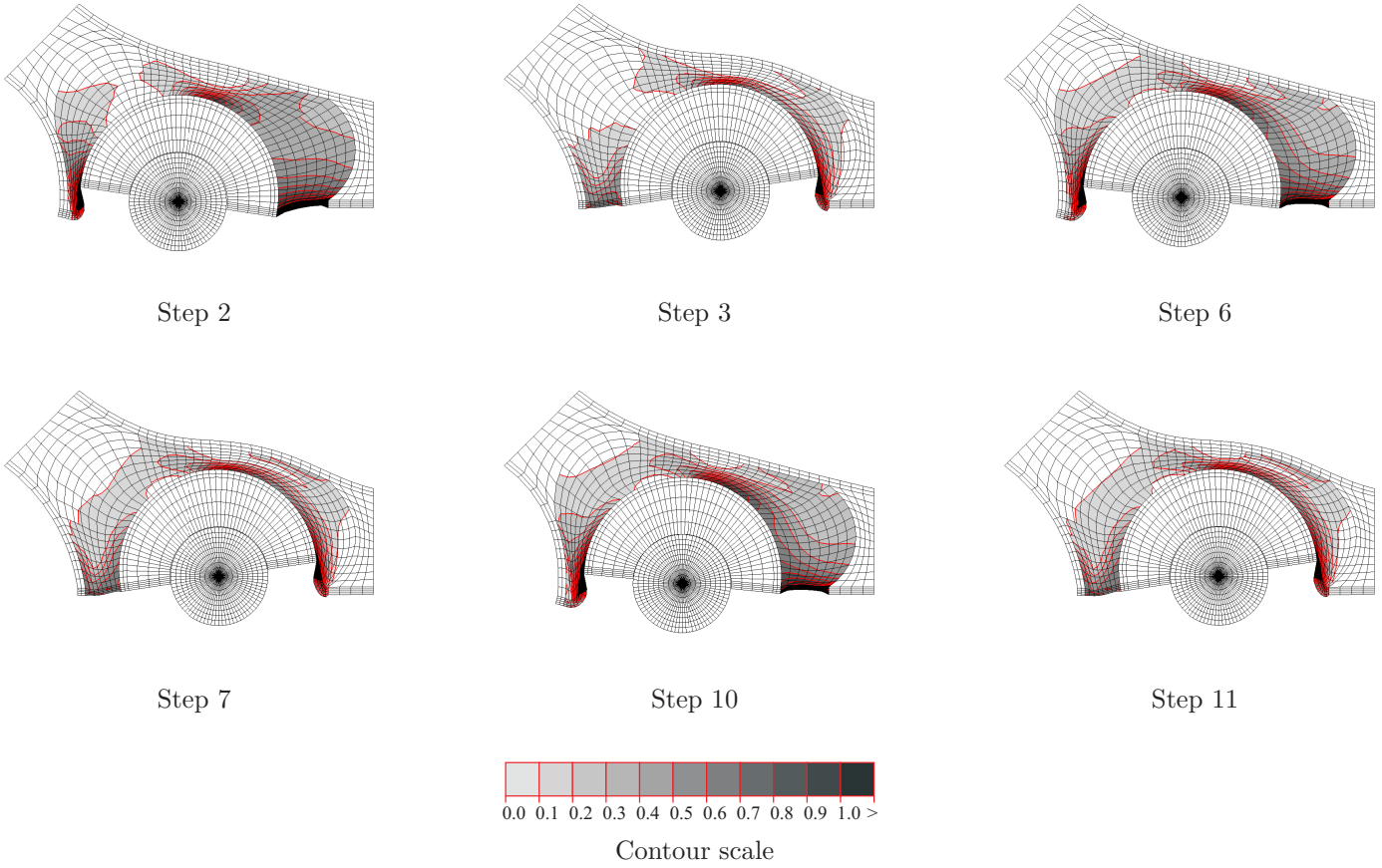

Figure 5.15: Displaced shapes of the acetabular construct and development of maximum principal plastic strains in the bone graft at the end of selected load steps for an acetabular cup of 52 mm outside diameter subjected to load case B. The load step number is shown beneath the relevant image.

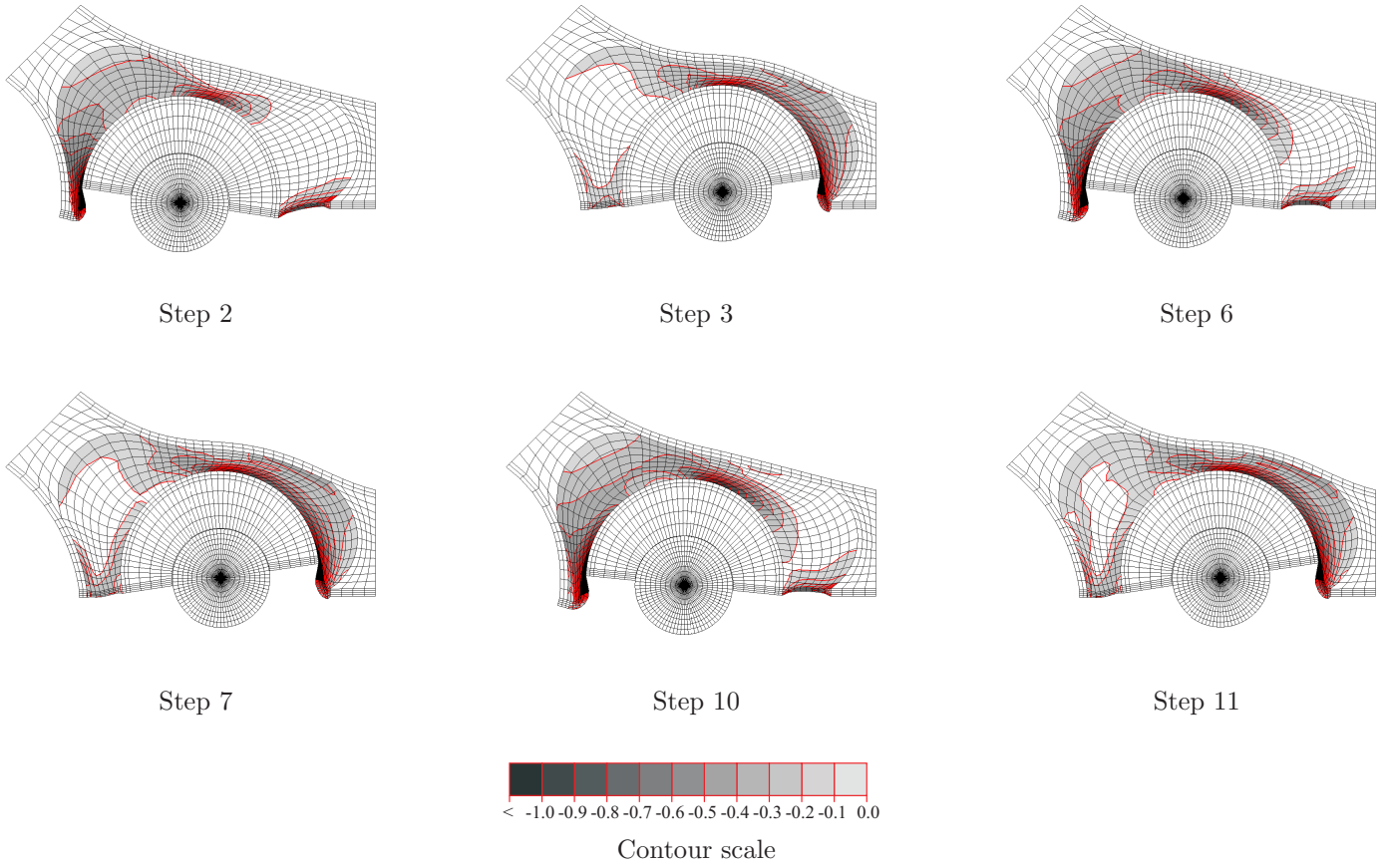

Figure 5.16: Displaced shapes of the acetabular construct and development of minimum principal plastic strains in the bone graft at the end of selected load steps for an acetabular cup of 52 mm outside diameter subjected to load case B. The load step number is shown beneath the relevant image.

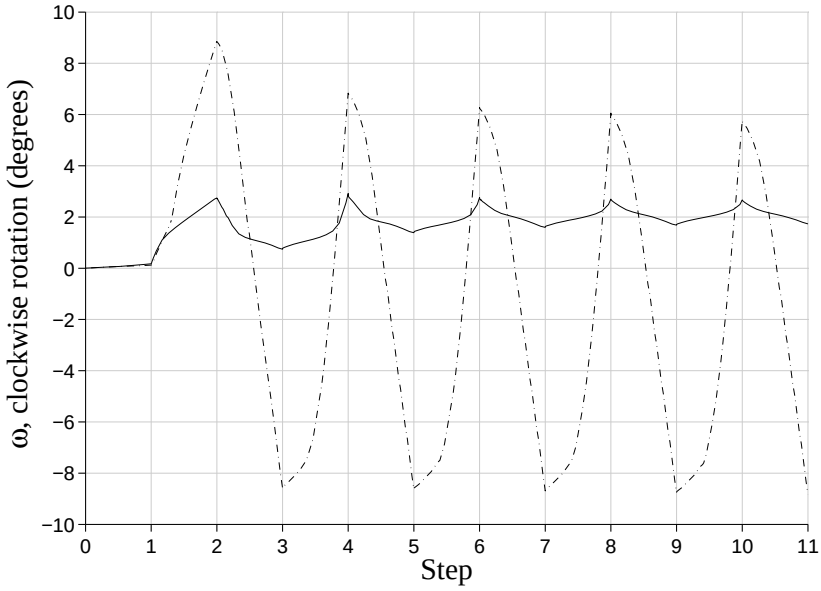

Figure 5.17: Clockwise rotation of a 52 *mm* acetabular cup subjected to load case A using the Drucker Prager and Drucker Prager Cap failure criteria

observed in clinical practice. Ornstein et. al, [85] and Ornstein [86] examined the migration and rotation of the acetabular component at discrete times over a five year period following revision hip arthropalsty using bone graft in a number of patients. These studies showed that rotations were most pronounced soon after surgery. While the acetabular cup "stabilised" in many cases, it continued to rotate in others. In almost all cases the rate of cup rotation reduced with time. Rotations of the kind discussed in this study have also been observed in animal studies carried out by Schimmel [87] and *in-vitro* experiemnts carried out by Bolder [37] and Ullmark [51, 52].

The results from both load cases show that the predicted rotation of the acetabular cup due to loading, is greater using the Drucker Prager Cap yield criterion, than the Drucker Prager yield criterion. It is observed that the consolidation plastic strains modelled by the DPC yield criterion, allow the cup to rotate to a greater extent.

It should be noted that for both yield criteria, for load case A the increase in cup rotation with each load cycle decreases as the number of cycles increases. For both yield criteria, for load case B the extent of rotation either clockwise or anticlockwise decreases as the number of cycles increases.

When compared in a pseudo-quantitative manner with the angles of cup rotation reported by Ornstein et. al [85] and Ornstein [86], the Drucker Prager and Drucker Prager Cap yield criteria give rotation ranges at the lower and upper ends of reported rotation. As discussed previous using the 2D plane-strain assumption, is conservative in comparison to the 3D situation [24], as the out of plane stiffness of the acetabular construct is not accounted for.

The results from both load cases, using the Drucker Prager yield criterion suggest that the chance of achieving short term stability of the acetabular construct is increased by using the largest practical size of acetabular cup, or minimising the depth of the bone graft bed. The area of bone graft affected by plastic strains decreases as the cup size increases, as does the extent to which bone graft is squeezed out at the edges of the acetabular cup. Load case A suggests that the risk that instability occurs in the acetabular construct increases significantly as the cup size decreases, or the depth of the bone graft bed increases. Load case B suggests that the risk that instability occurs in the acetabular construct decreases with each cycle of varying load direction. It should be noted that large cavitory defects might make the use of extensive bone graft masses unavoidable. In these cases, care should be taken to achieve adequate compaction of the bone graft, particularly in areas of increased bed depth as these are subject to the greatest deflections, to maximise the chance of achieving short term stability of the acetabular construct.

This chapter presented indicative studies into the short term stability of the acetabular construct using different yield criteria for the bone graft. Both yield criterion are seen to given qualitative results in keeping with those found in clinical studies. However the Drucker Prager yield criterion will result in material dilation, while the Drucker Prager Cap yield criterion is capable of modelling material consolidation. While the Drucker Prager yield criterion is expected to give indicative results when used to model bone graft, the Drucker Prager Cap yield criterion provides a more complete description of the plastic behaviour of bone graft.

The subsequent chapter will present a 3D model of the hemi-pelvis following revision arthroplasty in which MCB is modelled as an isotropic non-linear elasto-plastic material using the DPC yield criterion.

6

3D models of the hemi pelvis and acetabular construct

The previous chapter presented 2D plane-strain models of the acetabular construct following revision arthroplasty. It was demonstrated that these models can be used in indicative studies, examining the rotation and migration of the acetabular cup due to the development of plastic strains in the bone

graft bed, following revision hip arthroplasty. However, the 3D nature of the geometry of the acetabular construct, and the loading that it is subjected to make it desirable to conduct a 3D analysis.

This chapter presents 3D hemi pelvis models to which realistic 3D loading patterns are applied. Prior to developing a 3D model of the hemi pelvis following revision arthroplasty, with impaction grafting, models of the natural hemi pelvis, and hemi pelvis following primary arthroplasty, without impaction grafting, were developed as points of reference.

6.1 Analysis of the natural hemi pelvis

6.1.1 Geometric definition

The geometry of a patient's left hand side hemi pelvis was described based on a *Sawbones* anatomic model. Laser topography was carried out using a 3D laser scanner, with an accuracy of around 0.1 mm, consisting of a laser strip sensor, position sensing arm, and desktop PC. The *ModelMaker* package was used to produce a point cloud of the outer surface of the anatomic model. The *Polyworks* package was used to convert the point cloud to a triangular surface mesh. Interpolative repairs were made to the surface mesh in a few areas where laser topography had failed to fully describe the surface of the anatomic model. This surface mesh was used to produce cross sections along an axis running from the connection between the ischium and the pubis, through the acetabulum, to the iliac crest. In total 50 cross sections were produced at a spacing of around 4.5 mm.

Each of the cross sections was then edited using the *Autodesk Inventor* package to define the boundaries of the various materials to be included in the different hemi pelvis models. This package was then used to create the solid geometry of the various materials for each of the models. Previous 3D finite element studies of the natural hip joint [19, 20, 24–27, 29, 31, 33] and the hip joint following primary arthroplasty [22, 34] used either membrane or shell elements to represent the cortical bone of the pelvis. In general this was to avoid problems associated with excessive length to depth ratios that could occur using solid elements. In the models presented here solid elements were used to represent cortical bone. The mesh density adopted ensured that the element aspect ratios were appropriate. Previous studies have used uniform cortical bone thicknesses in the range 1–2 mm [11, 19, 20, 24, 26, 27, 29, 31, 33, 34]. Subject specific studies in which the cortical bone thickness was varied based on computed tomography (CT) scans found a range of around 0.5–5.0 mm [19, 20, 22, 24, 25, 33]. The thickness of cortical bone close to the acetabulum was found to be around 2 mm [24]. In the models presented here the thickness of the cortical bone was assumed to be around 2 mm throughout.

Following generation of the solid geometry of cortical bone, and trabecular bone using *Autodesk Inventor*, 3D four noded tetrahedral elements were used in *Abaqus/CAE* to generate an unstructured mesh of the natural hemi pelvis. The average element edge length used was 2 mm. Tied constraint conditions were assumed between the coincident surfaces of trabecular and cortical bone. The model was constrained at the sacro-iliac joint and the pubic-symphysis, as indicated in Figure 6.1. Figure 6.2 shows the trabecular bone mesh (205858 elements). The trabecular bone mesh was encased within the cortical bone mesh (139079 elements), shown with the mesh of the

femoral head in Figure 6.2. As stated previous a cortical bone thickness of 2 mm was used throughout. Some adjustment was made to the geometry of the acetabulum to allow loading to be applied using a spherical femoral head, with a radius of 24 mm. The model was orientated in 3D space based on the pelvis co-ordinate system, in the anatomic position described in Bergmann et al. [75], with the x axis running between the centres of the femoral heads, the y axis pointing forwards, and the z axis in the lateral view running from the centre of the femoral head, though the L5S1 disc. Loading was applied at the centre of a near rigid femoral head. Smooth sliding surface interactions were used between the femoral head and hemi-spherical surface of the acetabulum.

6.1.2 Materials definition

Cortical and trabecular bone were defined as isotropic linear elastic materials. Previous studies have indicated the use of isotropic linear elastic material properties to be acceptable in modelling the hip joint in its natural state, and following primary arthroplasty [11, 19, 20, 22, 24–27, 29, 31, 33, 34]. In addition Dalstra et al. [23] found trabecular bone from the pelvis to be isotropic in its structure. The values of Young's modulus, E and Poisson's ratio, ν used for trabecualr bone, and cortical bone were the same as those used in the 2D plane-strain models of the acetabular construct described in Chapter 5.

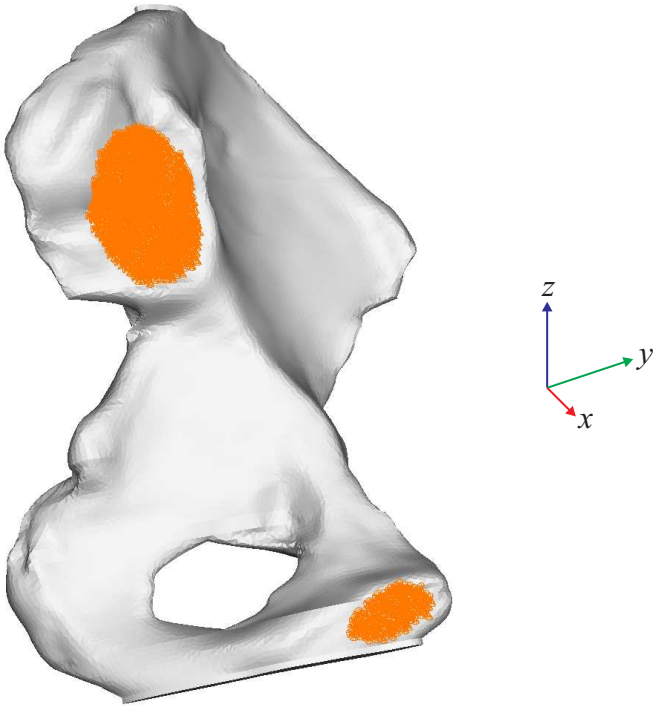

Figure 6.1: Constrained boundary conditions at the sacro-iliac joint, and the pubic-symphysis

6.1.3 Loading definition

The natural hemi pelvis model was subjected to a 3D load case taken to be representative of single leg stance, based on the average of recordings made by Bergmann et al. [75]. It was assumed that body weight (BW) was equal to 1000 N, with the resultant force, R acting at the centre of the femoral head. Table 6.1 gives the values of R_x, R_y, and R_z applied during the analysis.

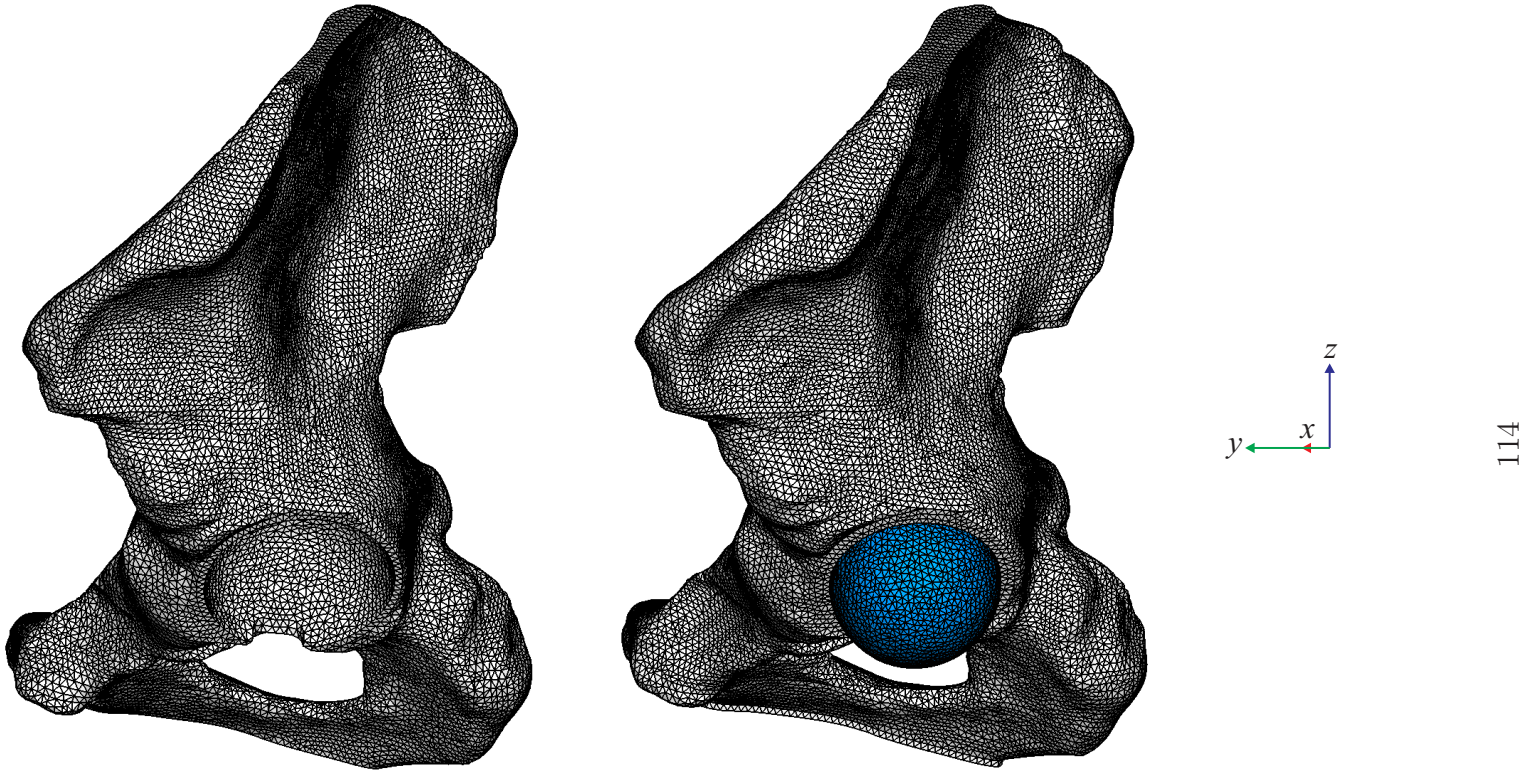

trabecular bone cortical bone and femoral head (shown in blue)

Figure 6.2: 3D mesh of the natural hemi pelvis

Table 6.1: Values of R_x, R_y, R_z and R for single leg stance

Force	R_x	R_y	R_z	R
(N)	300	142	2292	2316

6.1.4 Results and Discussion

Figure 6.3 shows the von Mises stresses (based on the deviatoric stress invariant) found in the cortical bone for the natural hemi pelvis model subjected to a single leg stance load case. The von Mises stresses were chosen for comparison to Dalstra et al. [24]. It was found that von Mises stresses of up to around 25 N/mm^2 occurred within the cortical bone. Stresses were concentrated around the superior edge of the acetabulum, and along the central column of the iliac bone. It can be seen that there are stress concentrations towards the constrained boundary conditions at the sacro-iliac joint, and the pubic-symphysis. The distribution of stresses is similar to that found by Dalstra et al. [24]. Small variations in the stress distributions are expected due to the difference in boundary conditions between the two studies. Dalstra et al. [24] found stresses up to around 6 N/mm^2 in the cortical bone, for a resultant force of 600 N; around that found for two leg stance [75]. Thus the increased values of von Mises stress found for the analysis presented here can be explained by the increased value of R applied to the model.

Goel et al. [27] found von Mises stress values in the cortical bone, for single leg stance, of around 0.06 BW, or 60 N/mm^2 when compared to the results presented here. The model used by Goel et al. [27] was thought to be too flexible [24], due to the use of a cortical bone thickness of 1 mm. Oonishi et al. [31] reported values of stress in the cortical bone, of less than

1 N/mm^2. However it appears an error was made in converting between kilograms and Newtons. Using a corrected conversion their reported stress values are comparable to those of Goel et al. [27]. Oonishi et al. [31] also used a cortical bone thickness of 1 mm, resulting in an over flexible model [24].

Figure 6.4 shows the von Mises stresses found in the trabecular bone for the natural hemi pelvis subjected to a single leg stance load case. It was found that von Mises stresses of up to around 1 N/mm^2 occurred within the trabecular bone. Stresses were concentrated in the acetabulum, and the central column of the iliac bone. The distribution, and magnitudes of the von Mises stress found in the trabecular bone is consistent with those reported by Dalstra et al. [25]. The E and μ values adopted for trabecular bone in the analyses presented here are consistent with the experimental values found by Dalstra et al. [23], and the values adopted for subject specific models in previous studies [19,20,24,25,33]. Goel et al. [27] and Oonishi et al. [31] used higher values of E, more in keeping with the values found for trabecular bone in directional bones such as the femur and tibia.

Examining the natural hemi pelvis model presented here, it can be seen that the qualitative and quantitative results are similar to those found by Dalstra et al. [24, 25], used as a comparison by other studies [19, 20, 26, 29, 33, 34]. It supports the description of the pelvic bone as a "sandwich structure" [24], used in engineering to achieve a combination of high strength and low weight, with cortical bone experiencing large stresses, and trabecular bone acting as a spacer to the cortical bone. Thus the natural hemi pelvis model presented here provides a suitable reference point for the development of models of the hemi pelvis following primary and revision hip arthroplasty.

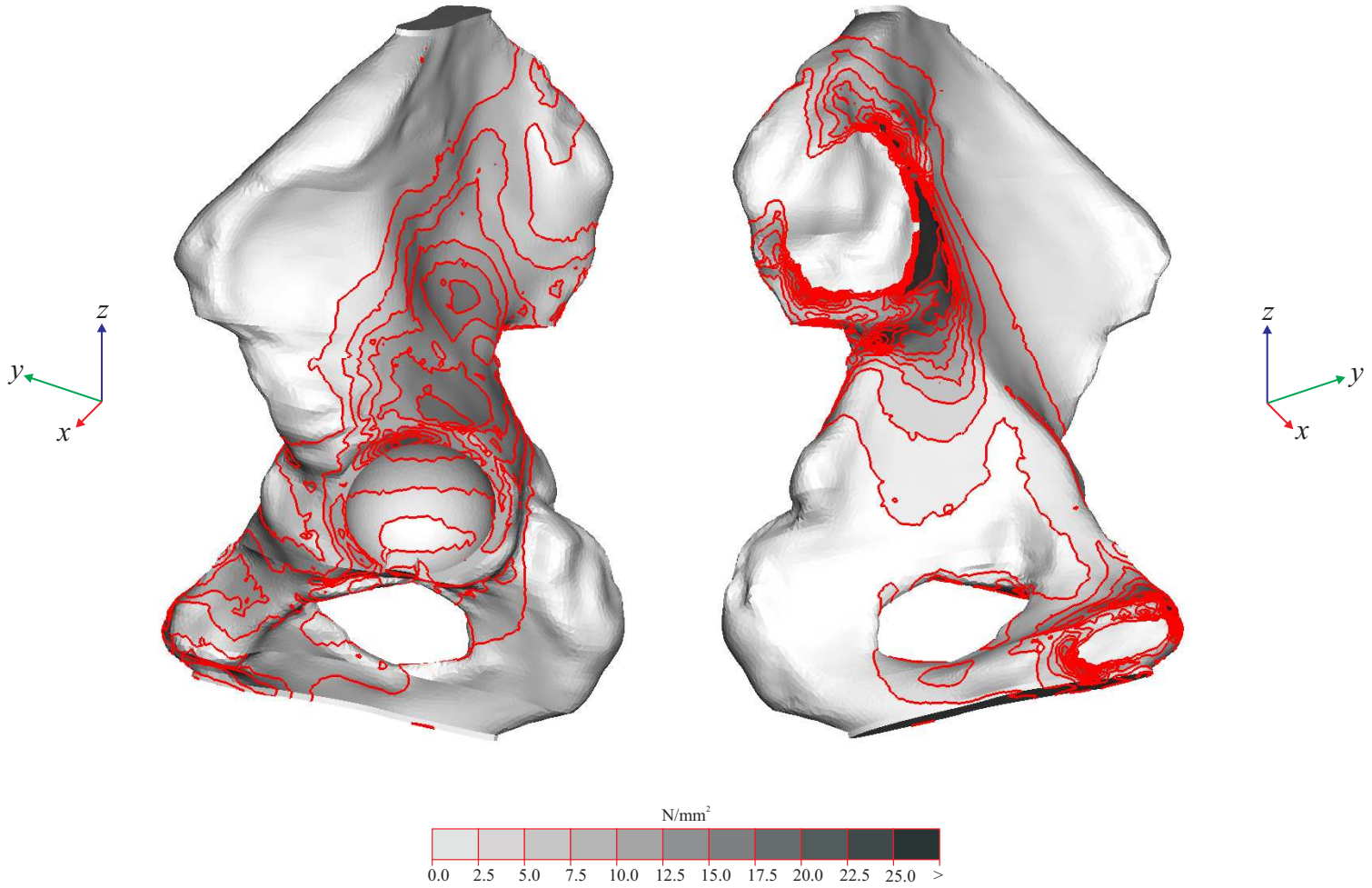

Figure 6.3: von Mises stresses in the cortical bone of the natural hemi pelvis, due to a single leg stance load case

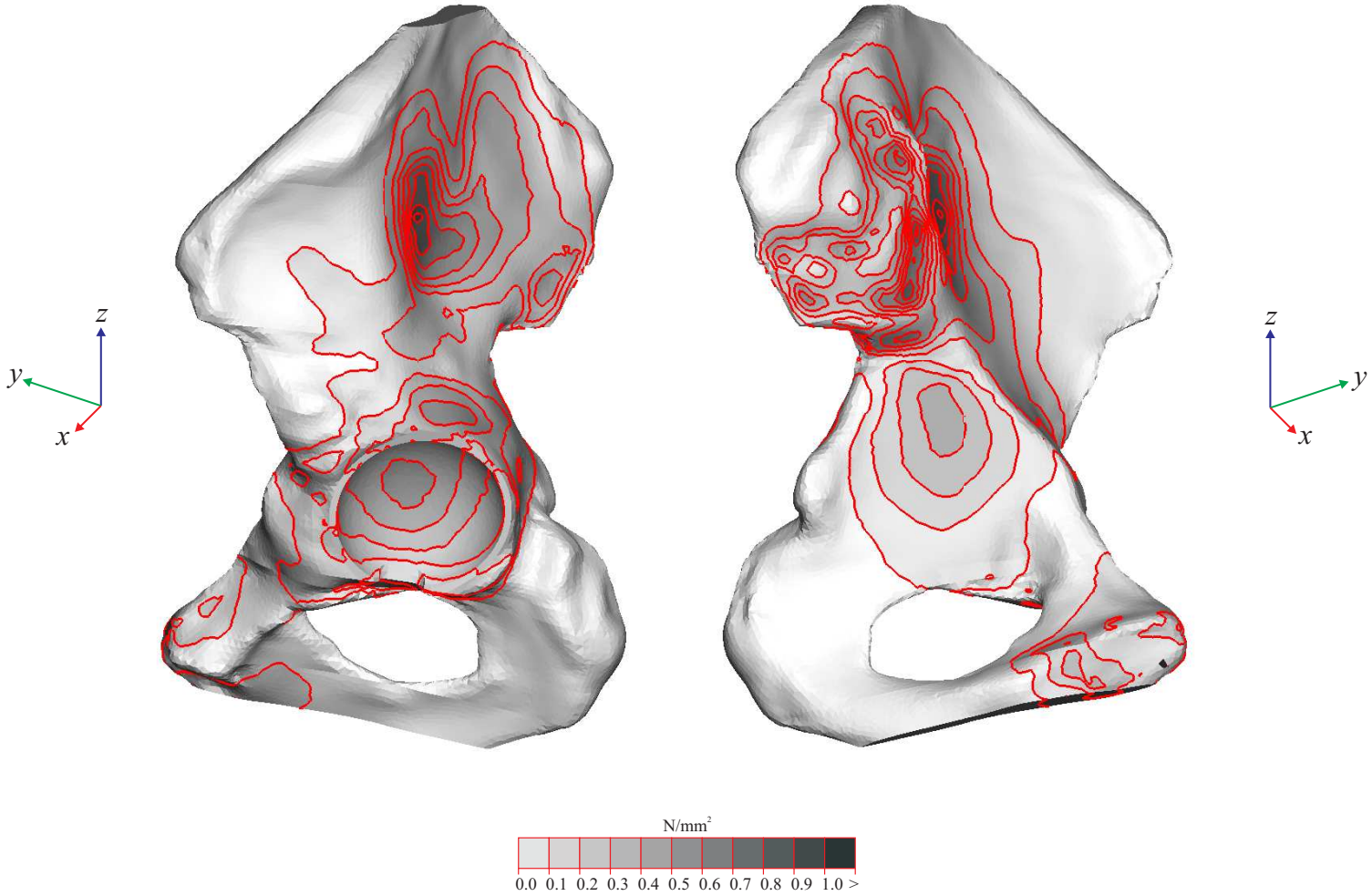

Figure 6.4: von Mises stresses in the trabecular bone of the natural hemi pelvis, due to a single leg stance load case

6.2 Analysis of the hemi pelvis following primary hip arthroplasty

6.2.1 Geometric definition

The model of the hemi pelvis following primary hip arthroplasty was composed of cortical bone, trabecular bone, bone cement, the acetabular cup, and the femoral head. It was assumed that subchondral cortical bone had been removed from the acetabulum, and that bone cement, and the acetabular cup were resting on trabecular bone alone. The solid geometry of the various materials was generated using the *Autodesk Inventor* package, as discussed earlier. 3D four noded tetrahedral elements were then used in *Abaqus/CAE* to generate an unstructured mesh of the hemi pelvis following primary hip arthroplasty. The average element edge length used was 2 mm. Tied constraint conditions were assumed between the coincident surfaces of the trabecular and cortical bone, the trabecular bone and bone cement, and the bone cement and acetabular cup. Figure 6.5 shows the trabecular bone mesh (182163 elements), with the meshes of the acetabular cup, and femoral head. The trabecular bone mesh was surrounded by the cortical bone mesh (132632 elements), shown in Figure 6.5. As before, a cortical bone thickness of 2 mm was used throughout. Loading was applied using a spherical metal femoral head, with a radius of 9 mm. The acetabular cup had an outside radius of 18 mm including a 2 mm wide flange. The depth of the bone cement was taken to be 2 mm. The model was orientated in 3D space based on the pelvis co-ordinate system described previous. Also as before, the model was constrained at the sacro-iliac joint and the pubic-symphysis,

and loading was applied at the centre of the femoral head. Smooth sliding surface interactions were used between the femoral head and the acetabular cup. In order to provide better resolution of the stresses the average element edge length was reduced to 0.5 mm at the interface between the surfaces. The average element edge length in the femoral head was reduced to 1.0 mm to provide better distribution of the stresses due to the application of point loading acting at its centre.

6.2.2 Materials definition

Trabecular bone, cortical bone, bone cement, the plastic acetabular cup, and the metal femoral head were defined as isotropic linear elastic materials. The values of Young's modulus, E and Poisson's ratio, ν used for the various materials, were the same as those used in the 2D plane-strain models of the acetabular construct described in Chapter 5.

6.2.3 Loading definition

As for the natural hemi pelvis model, the model of the hemi pelvis following primary hip arthroplasty was subjected to a 3D load case taken to be representative of single leg stance, with the resultant force, R acting at the centre of the femoral head. The applied loads were those given earlier, in Table 6.1.

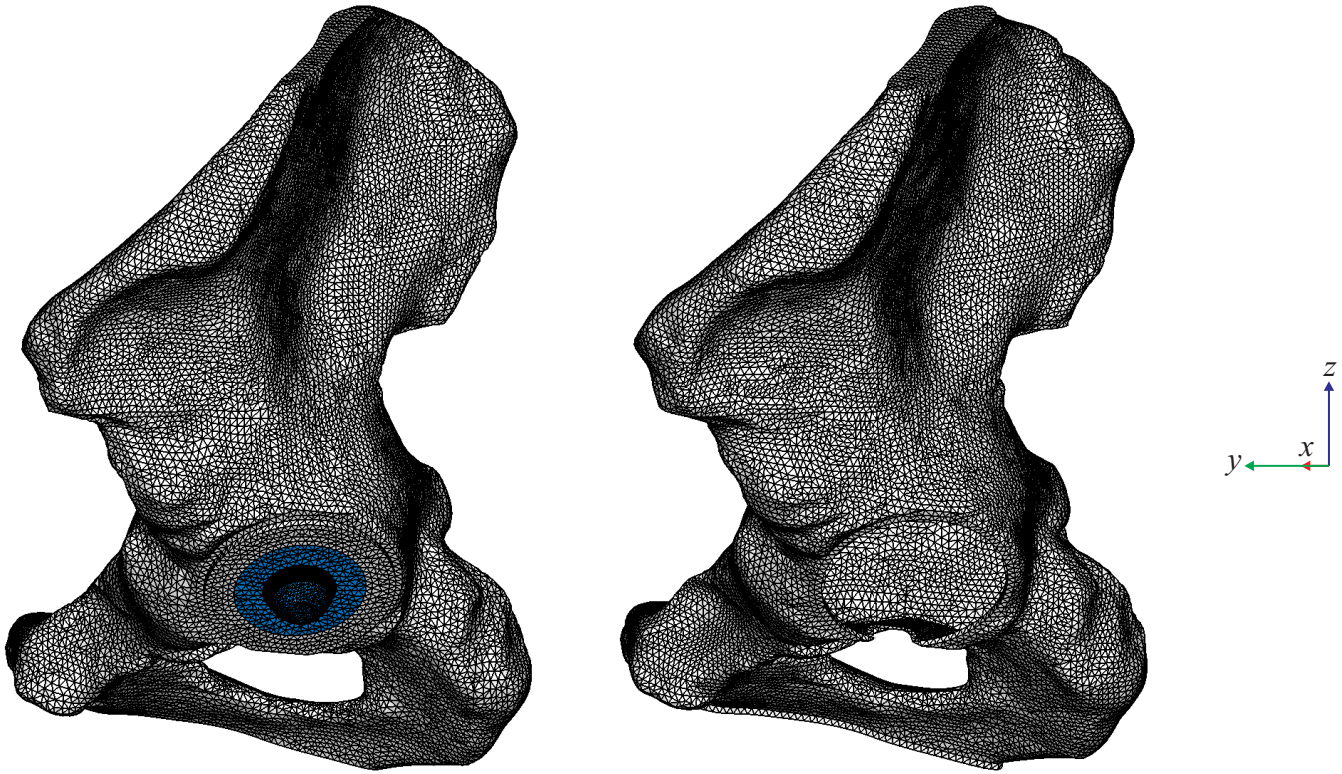

trabecular bone, acetabular cup (shown in blue), and femoral head (shown in blue)

cortical bone

Figure 6.5: 3D mesh of the hemi pelvis following primary hip arthroplasty

6.2.4 Results and discussion

Figure 6.6 shows the von Mises stresses found in the cortical bone for the model of the hemi pelvis following primary hip arthroplasty, subjected to a single leg stance load case. In comparison to the stresses found for the natural hemi pelvis (Figure 6.3) stress concentrations were not observed to the superior edge of the acetabulum. This is expected as the direct stress transfer path to the cortical bone has been removed, as bone cement, and the acetabular cup were supported by the trabecular bone alone. The stress concentrations towards the constrained boundary conditions are similar to those found in the natural hemi pelvis. However regions of increased stress are observed around the sacro-iliac joint, suggesting a stress transfer path through the trabecular bone, towards this region of cortical bone. These findings are in general agreement with those of Dalstra [22]. Differences in the stress distribution can be attributed to the fact that Dalstra [22] assumed that subchondral cortical bone remained intact.

Figure 6.7 shows the von Mises stresses found in the trabecular bone for the hemi pelvis following primary hip arthroplasty, subjected to a single leg stance load case. In comparison to the stresses found for the natural hemi pelvis (Figure 6.4) increased stresses were found towards the superior edge of the acetabulum, as the acetabular construct, following primary hip arthroplasty it is not "stress shielded" by cortical bone. The maximum von Mises stress experienced by the trabecular bone in the acetabulum was found to be around 3.3 N/mm^2. The stress distributions away from the acetabulum are similar to those found in the natural hemi pelvis, also observed by Dalstra [22].

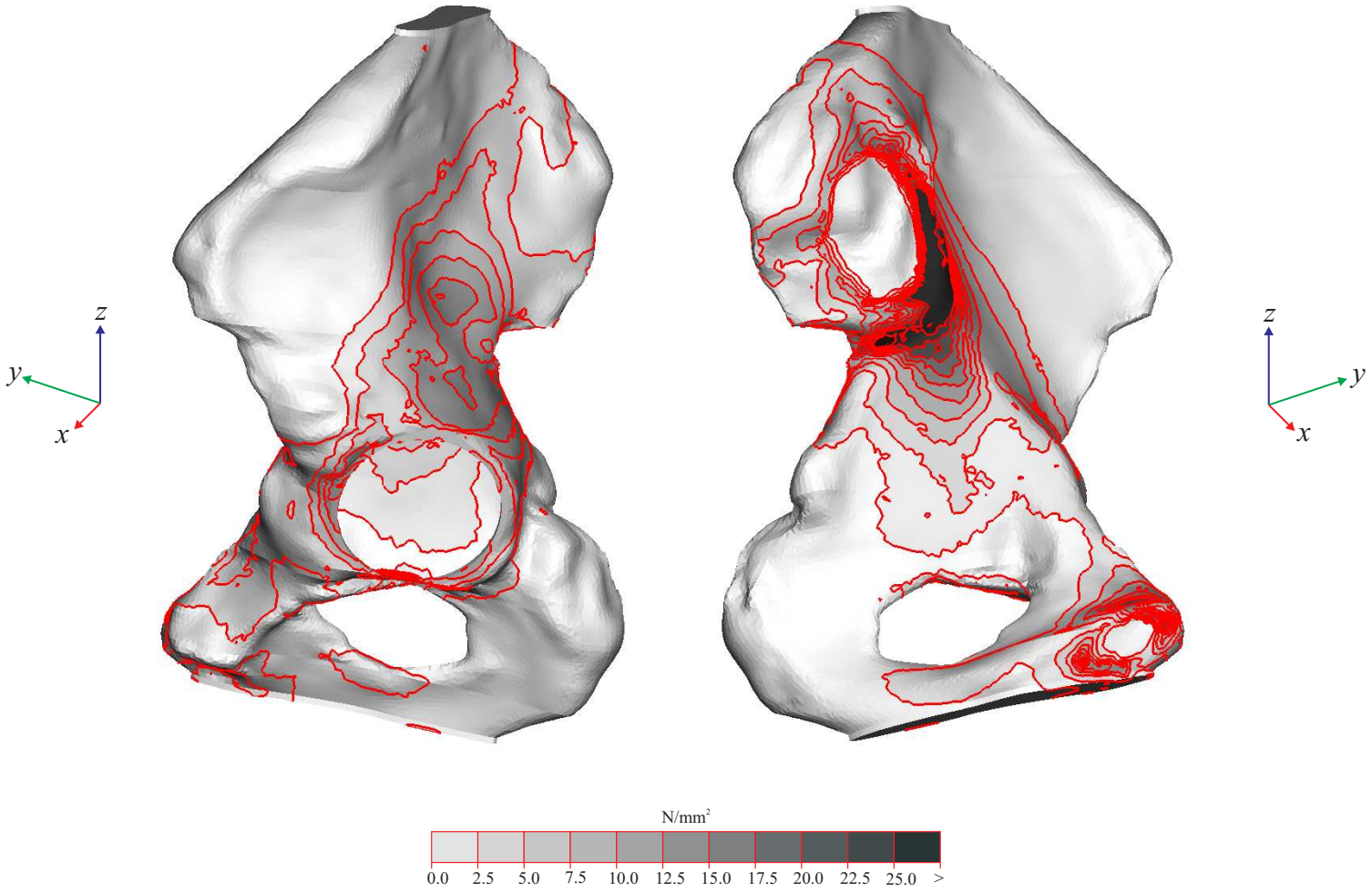

Figure 6.6: von Mises stresses in the cortical bone of the hemi pelvis following primary hip arthroplasty, due to a single leg stance load case

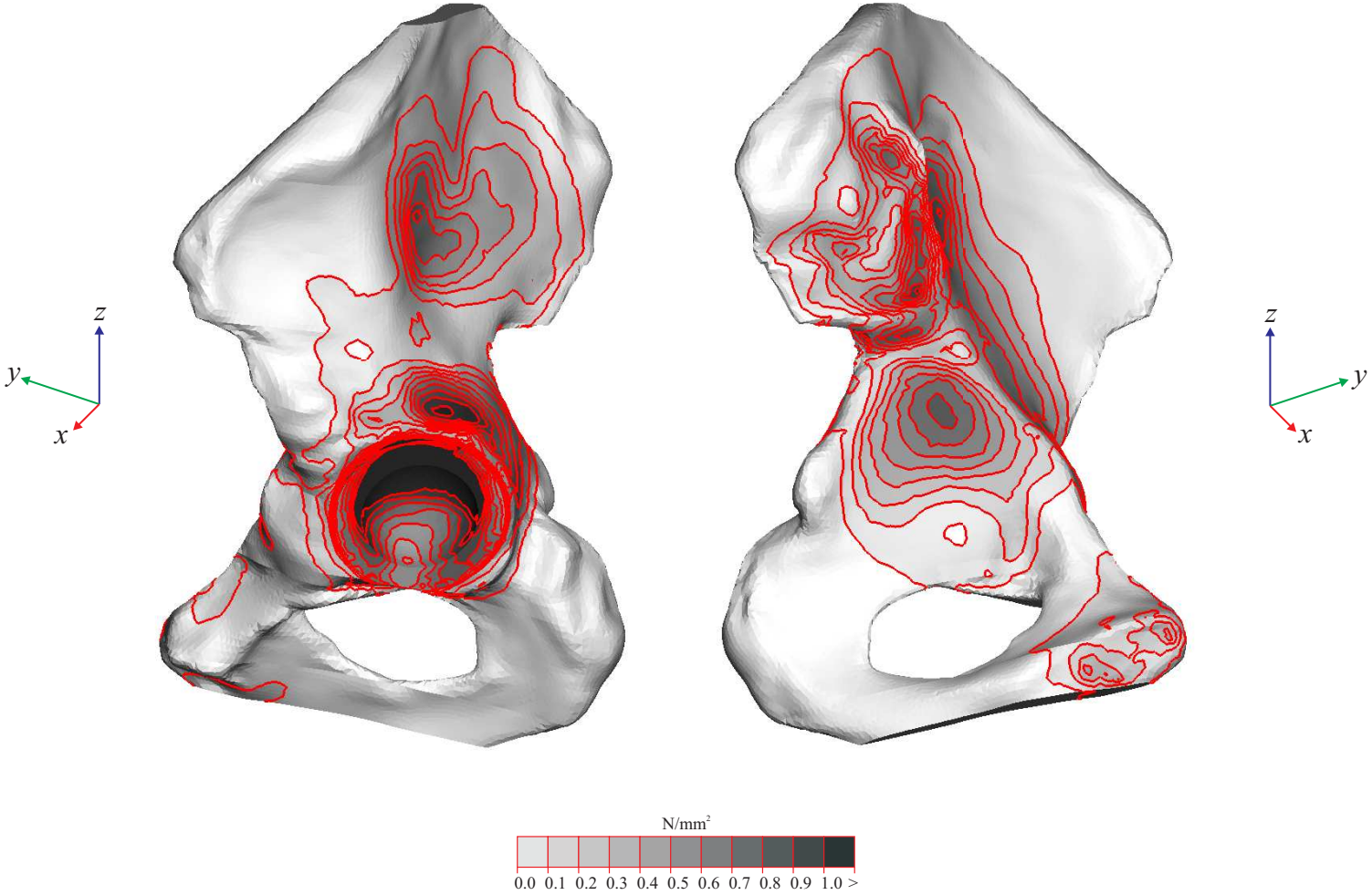

Figure 6.7: von Mises stresses in the trabecular bone of the hemi pelvis following primary hip arthroplasty, due to a single leg stance load case

The model of the hemi pelvis following primary hip arthroplasty presented here, was developed with a view to giving an indication of the magnitude of stresses that impacted morsellised bone graft might be subjected to following revision hip arthroplasty. Thus subchondral cortical bone was assumed to be absent. Comparing the results presented here, to Dalstra [22], in which subchondral bone was included, both studies found that the stress distributions in the cortical and trabecular bone, away from the acetabulum, remained similar to those found for the natural hemi pelvis [24, 25, 27, 31]. Thus it is concluded that the model of the hemi pelvis following primary hip arthroplasty presented here, provides a suitable reference point for the development of a model of the hemi pelvis following revision hip arthroplasty.

6.3 Analysis of the hemi pelvis following revision hip arthroplasty, subjected to different load histories

6.3.1 Geometric definition

The model of the hemi pelvis following revision hip arthroplasty was taken to be representative of a reference cavitory defect in a patient's left hip, revised using impaction grafting. Thus in addition to the materials included in the model of the hemi pelvis, following primary arthroplasty, morsellised cortico-cancellous bone (MCB) was also included. As discussed earlier, 3D four noded tetrahedral elements were used to generate an unstructured mesh, with an average element edge length of 2 mm. Figure 6.8 shows the trabecular bone mesh (189763 elements). The trabecular bone mesh was surrounded by the cortical bone mesh (132632 elements), shown in Figure 6.8. As before, a cortical bone thickness of 2 mm was used throughout. Figure 6.9 shows the MCB mesh (42847 elements) with the outlines of the trabecular bone, and cortical bone also shown. Figure 6.10 shows frontal and lateral views of the meshes of the bone cement, acetabular cup, and femoral head, with the outline of the MCB also shown. Boundary conditions, and loading were applied as described for the model of the hemi pelvis, following primary arthroplasty. Changes to mesh densities at the interface between the femoral head, and the acetabular cup, as well as within the femoral head, were also made as described for the model of the hemi pelvis, following primary arthroplasty.

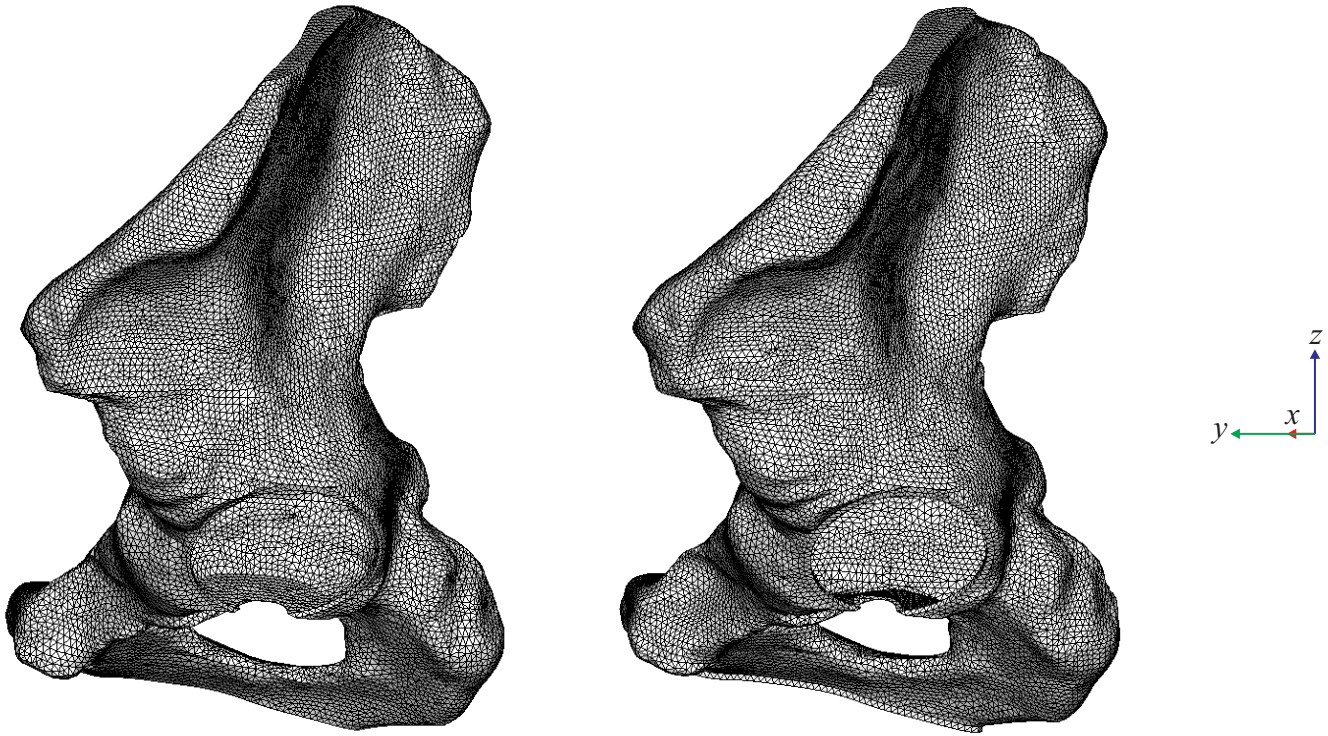

trabecular bone cortical bone

Figure 6.8: 3D meshes of the trabecular and cortical bone, following revision hip arthroplasty

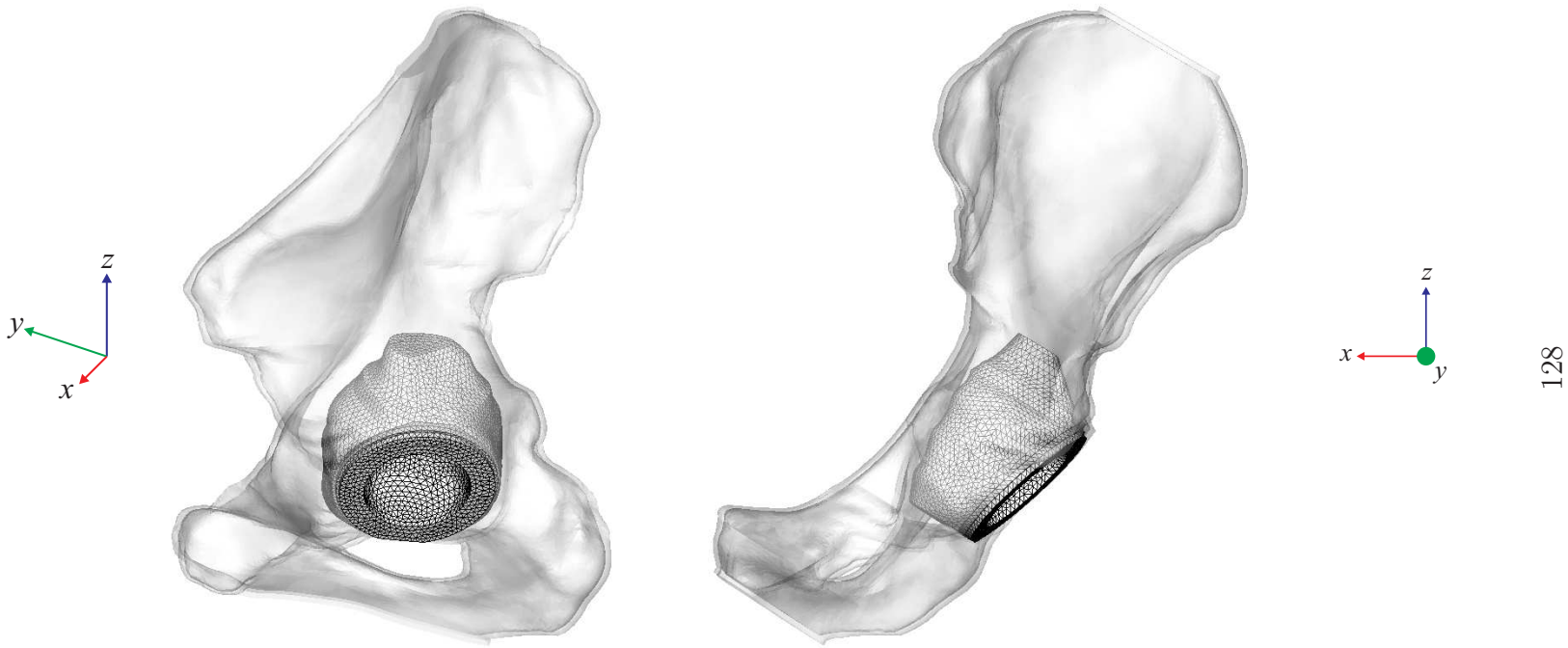

Figure 6.9: 3D mesh of the MCB bed, following revision hip arthroplasty

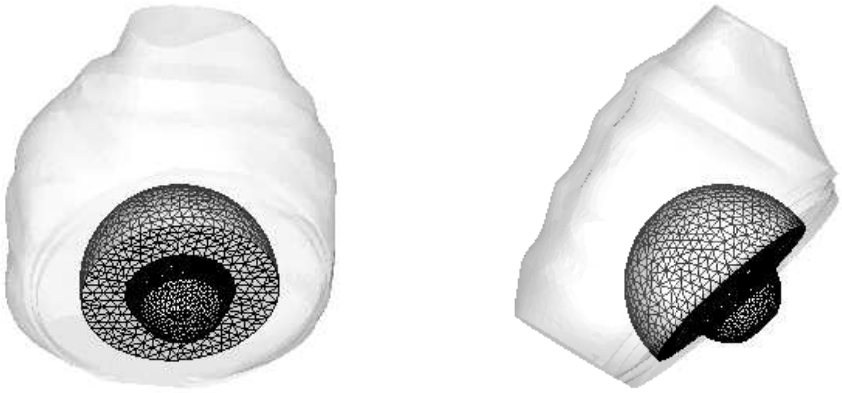

Lateral view Frontal view

Figure 6.10: 3D mesh of the bone cement, acetabular cup, and femoral head, following revision hip arthroplasty

6.3.2 Materials definition

Cortical and trabecular bone, bone cement, the plastic acetabular cup, and the metal femoral head were defined as isotropic linear elastic materials. The values of Young's modulus, E and Poisson's ratio, ν used for the various materials, were the same as those used earlier in the this chapter.

MCB was modelled as an isotropic elasto-plastic material. The non-linear elastic behaviour of MCB was defined by varying the value of Young's modulus, E as a function of pressure, p, as described for the 2D plane-strain model of the acetabular construct presented in Chapter 5. The non-linear plastic behaviour of the MCB was defined using a Drucker Prager Cap (DPC) yield criterion, also as described for the 2D plane-strain model of the acetabular construct presented in Chapter 5. As before a layer of additional elastic element with a very low value of Young's modulus, less than 5% of the lowest value taken for bone graft, was used to provide computational

stability.

6.3.3 Loading definition

The model of the hemi pelvis following revision hip arthroplasty was subjected to four 3D load histories, representative of single leg stance, a normal walking cycle, sitting down, and standing up, with the resultant force, R acting at the centre of the femoral head. The co-ordinate system used was the one described earlier in this chapter. The aim of each load history was to investigate the development of plastic strains in the bone graft, leading to migration and rotation of the acetabular cup, from its virgin position, due to the load pattern caused by that activity.

It is noted that due to the elastic nature of the natural hemi pelvis, and hemi pelvis following primary arthroplasty models, that the results from these models are not dependent on the applied loading history. Due to the elasto-plastic nature of the MCB, included in the hemi pelvis following revision hip arthroplasty model, it is clear that the results from this model are dependent on the applied loading history. Thus complete R_x, R_y, R_z amplitude curves were applied, based on Bergmann et al. [75]. Figure 6.11 shows the resultant force amplitude curves for the various activities.

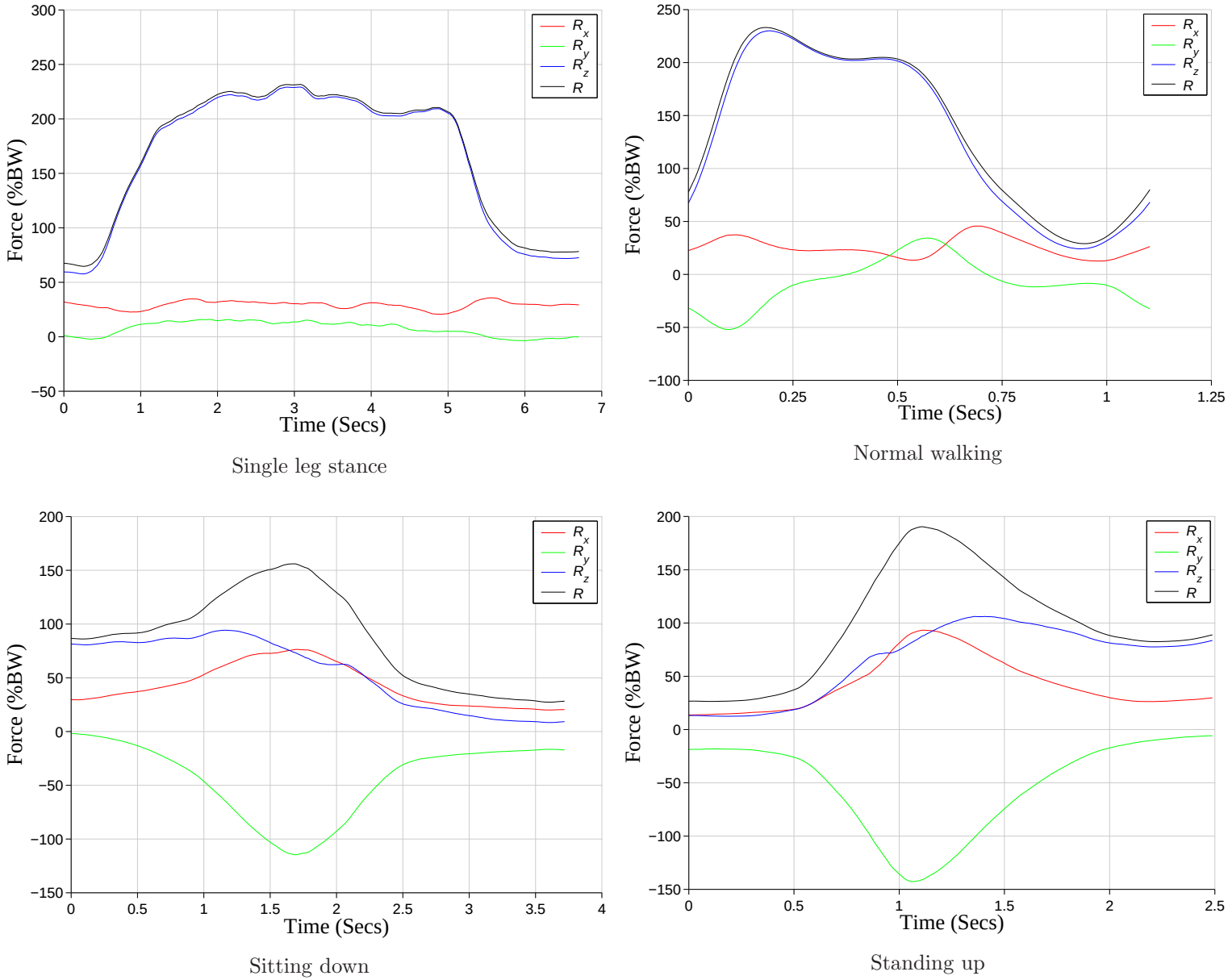

Single leg stance

Normal walking

Sitting down

Standing up

Figure 6.11: R_x, R_y, R_z amplitude curves for various activities [75]

6.3.4 Results and discussion

6.3.4.1 Single leg stance

Figures 6.12 and 6.13 show frontal and lateral views, of the displacement of the acetabular cup, within the MCB bed, at the end of a single leg stance load history. It is observed that the cup migrates in the superior direction, and rotates in abduction. This corresponds with the strong vertical nature of the resultant force, R for single leg stance.

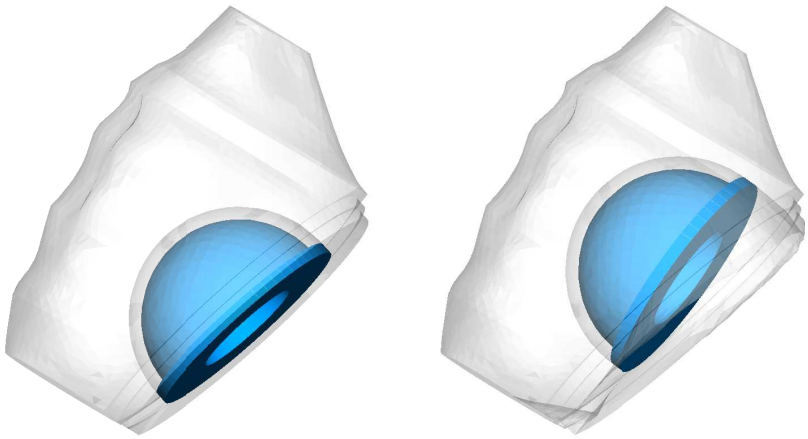

non-displaced displaced

Figure 6.12: Frontal view of the movement of the acetabular cup, within the MCB bed, at the end of a single leg stance load history

Figure 6.14 shows the von Mises stresses found in the cortical bone, for the model of the hemi pelvis following revision hip arthroplasty, at the instance when maximum resultant force, R_{max} acts during single leg stance. In comparison to the stresses found in the hemi pelvis following primary hip arthroplasty (Figure 6.6) additional stresses were observed superior to the edge of the acetabulum, and in the cortical wall at the rear of the ac-

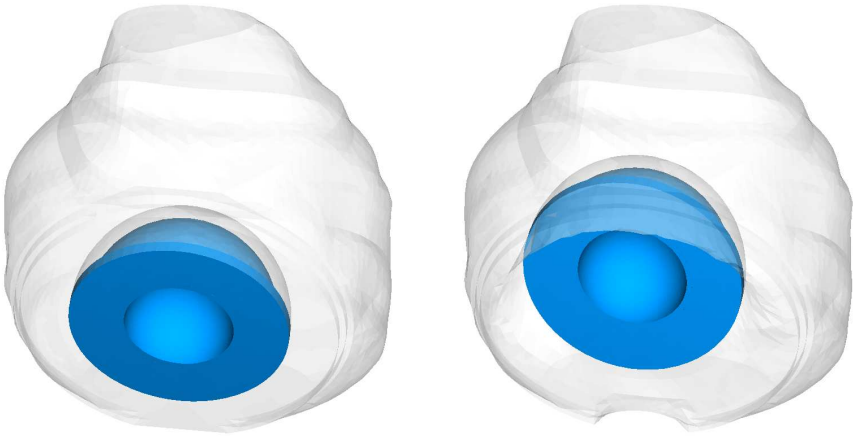

Figure 6.13: Lateral view of the movement of the acetabular cup, within the MCB bed, at the end of a single leg stance load history

etabulum. These are indicative of an altered load transfer path due to the displacement of the acetabular cup within the MCB bed.

Figure 6.15 shows the von Mises stresses found in the trabecular bone, for the model of the hemi pelvis following revision hip arthroplasty, for R_{max} during single leg stance. Similar to the cortical bone, in comparison to the stresses found for the hemi pelvis following primary hip arthroplasty (Figure 6.7) additional stresses were observed at the superior edge of the acetabulum, and at the rear of the acetabulum. The stress distribution away from the acetabulum was similar to that found for the hemi pelvis following primary hip arthroplasty, and the natural hemi pelvis (Figure 6.4).

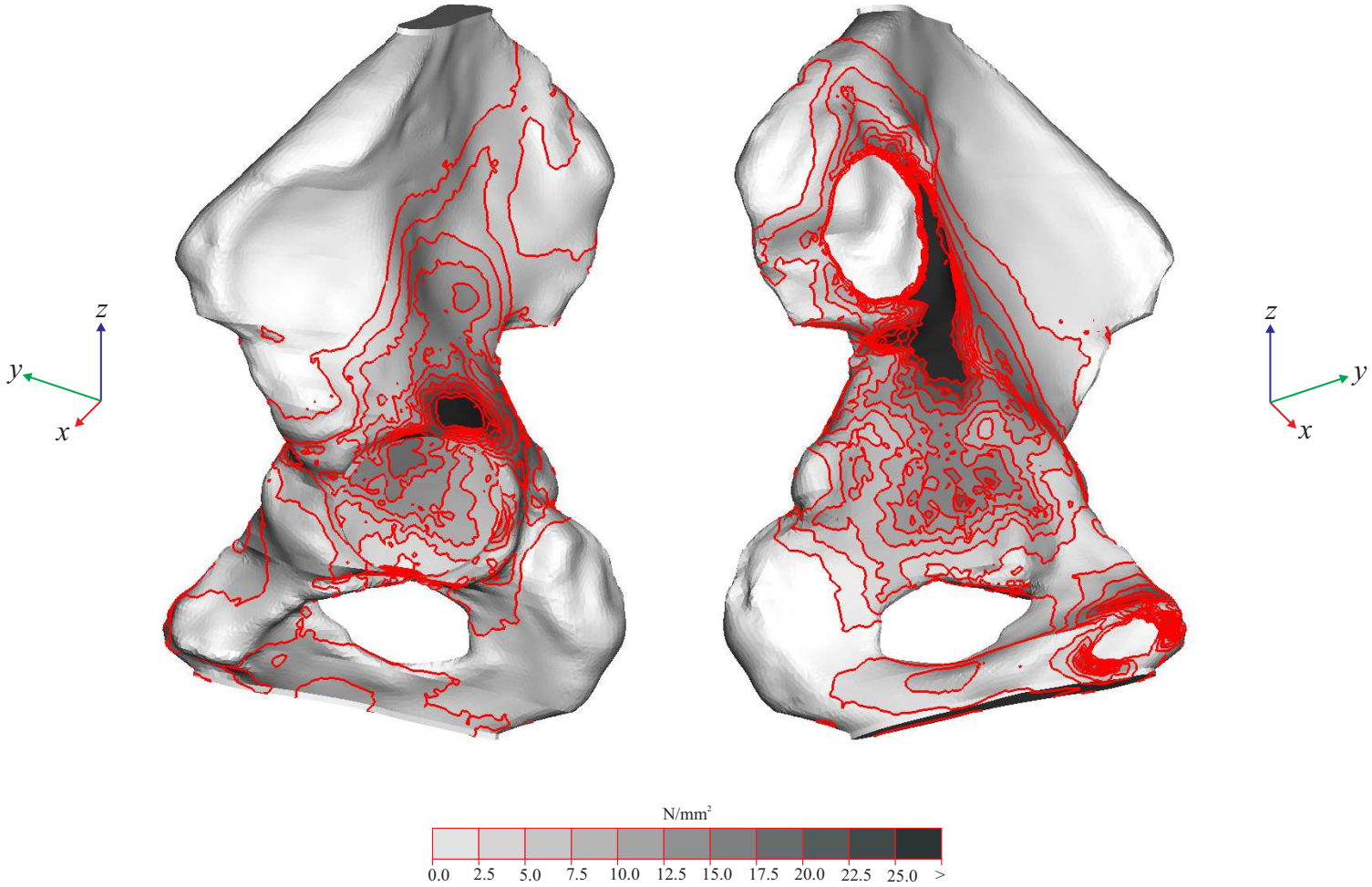

Figure 6.14: von Mises stresses in the cortical bone of the hemi pelvis following revision hip arthroplasty, for R_{max} during single leg stance

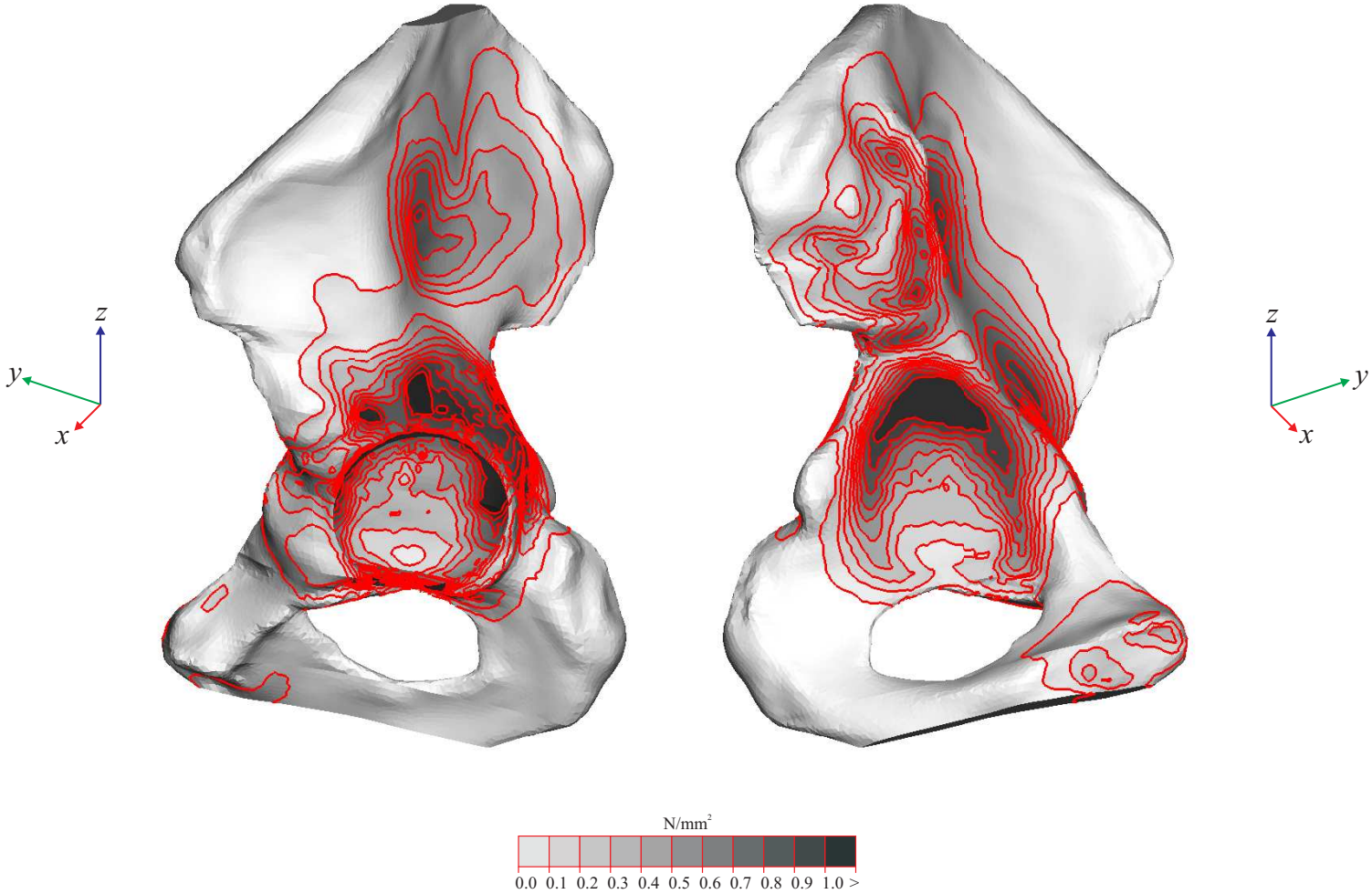

Figure 6.15: von Mises stresses in the trabecular bone of the hemi pelvis following revision hip arthroplasty, for R_{max} during single leg stance

Figure 6.16 shows lateral views, at 45° from the horizontal axis, of the distribution of pressure, and von Mises stress, found in MCB, for R_{max} during single leg stance. It was observed that regions of high pressure, and von Mises stress, were concentrated towards the superior edge of the acetabulum, corresponding with the vertical nature of the resultant force, R. It was found that the maximum von Mises stress experienced by MCB in the acetabulum was around 2.2 N/mm^2, around 30% less than that experienced by the trabecular bone in the model of the hemi pelvis following primary hip arthroplasty. The maximum pressure experienced by MCB in the acetabulum was around 2.6 N/mm^2. Regions of high pressure are indicative of locations in which consolidation plastic strains are expected to occur.

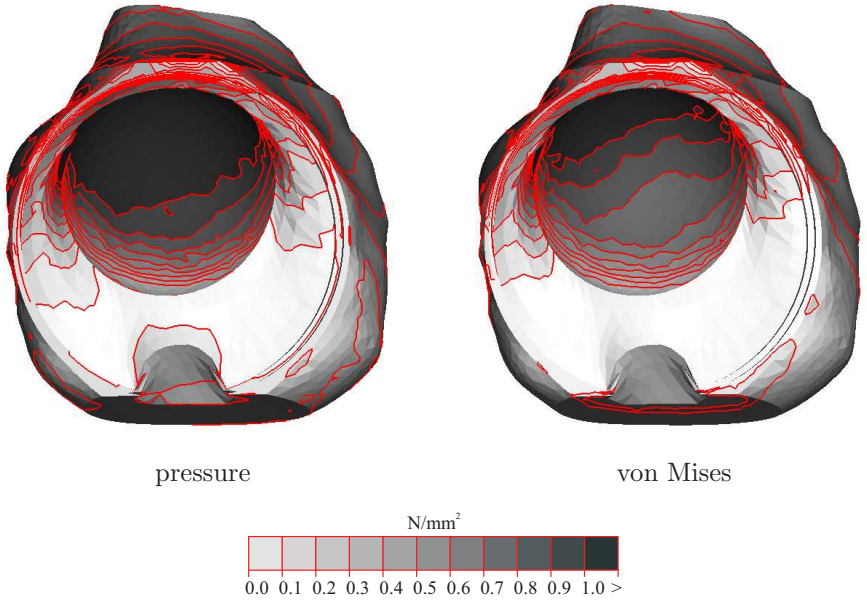

Figure 6.16: Lateral view, at 45° from the horizontal axis, of the distribution of pressure, and von Mises stress in MCB, for R_{max} during single leg stance

Figure 6.17 shows lateral views, at 45° from the horizontal axis, of maximum (tensile), and minimum (compressive) principal plastic strains, found in MCB at the end of a single leg stance load history. It is observed that

maximum plastic strains are concentrated around the superior edge of the acetabular cup, extending towards the notch in the acetabulum, consistent with MCB being "squeezed", or "pulled" in those regions. Minimum plastic strains are concentrated towards the superior edge of the acetabular cup, consistent with MCB being placed under high compressive stress in those regions. It is interesting to note that significant plastic strains are not seen beneath the dome of the cup, at the centre of the acetabulum.

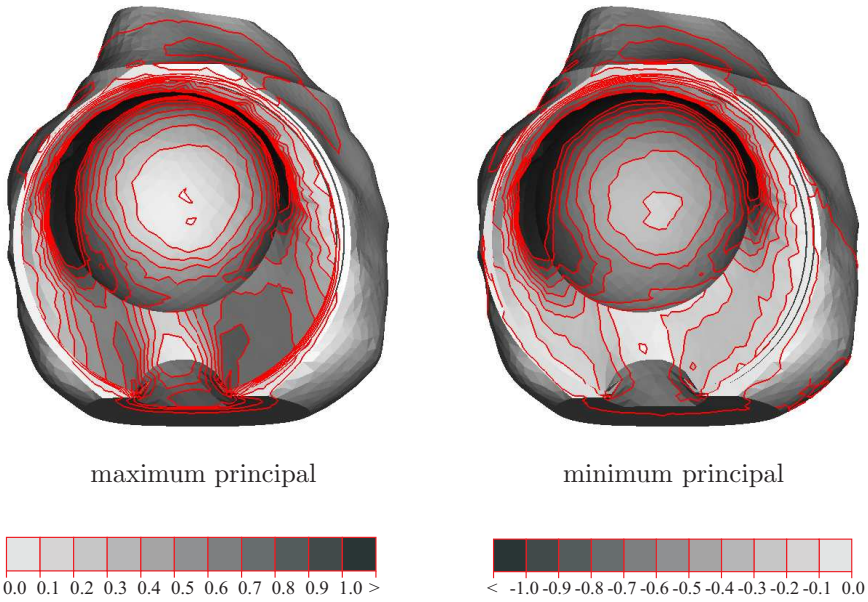

Figure 6.17: Lateral view, at 45° from the horizontal axis, of the distribution of maximum, and minimum principal plastic strains, at the end of a single leg stance load history

In order to compare the effect of various activities, and provide a comparison with clinical studies [85, 86] the displacement, and rotation of the acetabular cup, within the acetabular construct was recorded for each of the four load histories.

The displacment of the acetabular cup was taken as the average displacement in the x, y and z directions, of a series of points on the outer edge of

the flat surface of the acetabular cup. This was found to be the same as the displacement of the centre of the femoral head. The rotation of the cup about the x, y and z axes was found by taking vectors from the centre of the femoral head to a series of points on the outer edge of the flat surface of the acetabular cup. The cross product of any two of these vectors gives the surface normal vector. The vector describing the intersection between a plane coincident to the surface, and the $y-z$ plane is given by the cross product of the surface normal vector, and the x axis vector. The rotation of the cup about the x axis, ω_x is calculated from the change in this vector, with the applied load history, where ω_x is positive in an anticlockwise direction, *w.r.t.* to the positive x direction. This process can be repeated to find ω_y and ω_z, the rotations about the y and z axes.

Figures 6.18 and 6.19 show the displacment, and rotation of the acetabular cup, within the acetabular construct for single leg stance. Figures 6.18 and 6.19 use normalised time scales, with the load history being applied over a unit step time. Comparing the displacment of the cup, with the applied resultant force (Figure 6.11) it is observed that the displacement in the y (anterior) and z (superior) directions follows R_y and R_z. Towards the end of the load history it is observed that these migrations are not recovered, due to the development of plastic strains in the MCB bed. It is interesting to note that the displacement of the cup in the x (medial) direction does not follow R_x. This is due to rotation of the cup about the z axis, dependent on the direction of R_y.

Examining the rotation of the acetabular cup, it is observed that large rotations occur about the y axis, associated with high values of R_z. Rotations also occur about the x and z axes, associated with the direction of R_y. As

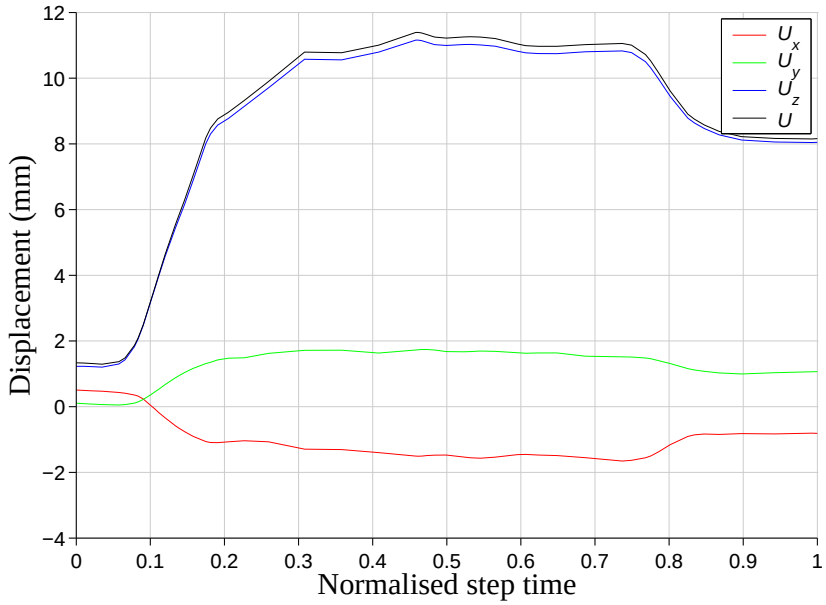

Figure 6.18: Displacement of the acetabular cup for single leg stance

for the migration of the cup, rotations are not recovered towards the end of the load history due to the development of plastic strains in the MCB bed.

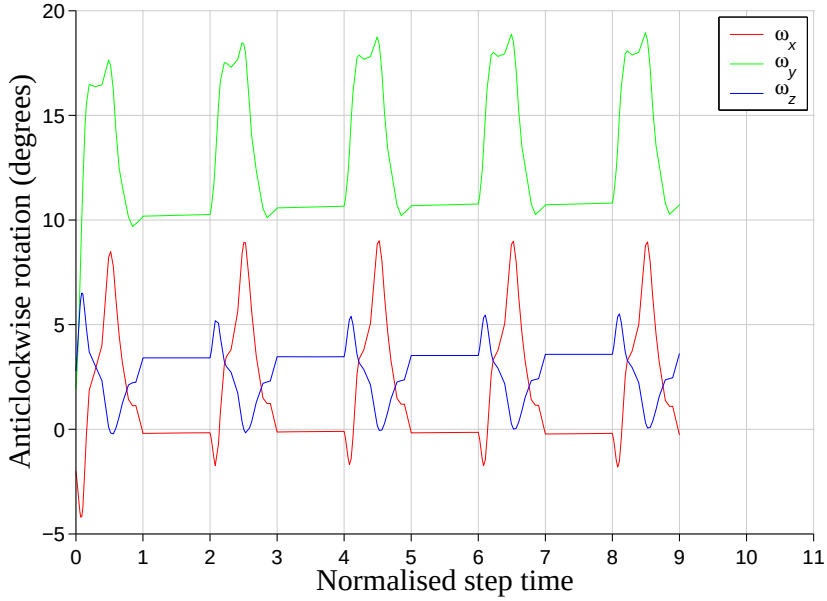

Figure 6.19: Rotation of the acetabular cup for single leg stance

Excessive rotation about the y axis has been identified as a failure mechanism in both primary and revision hip arthroplasty, illustrated by the x-rays, from the Department of Orthopaedics at the New Edinburgh Royal Infirmary, shown in Figure 6.20. In sequence these show the failure of a primary arthroplasty, Figure 6.20(a); followed by the acetabular construct immediately after revision arthroplasty, using impacting grafting, Figure 6.20(b); followed by the failure of the revised acetabular construct, Figure 6.20(c).

Ornstein et al. [85] investigated the *in vivo* migration and rotation of acetabular cups following revision arthroplasty, carried out with MCB, using radiostereometric analyis (RSA) over a five year period. They reported that at two years post surgery, cup migrations of 0.5–6.4 mm were observed in the superior direction (20 of 21 cups), 0.4–1.2 mm in the medial (6 cups) and lateral (6 cups) directions, and 0.3–2.3 mm in the posterior (14 cups) and anterior (1 cup) directions. The results from the model, for a single leg stance load history, show clear migration in the superior direction, also observed by Ornstein et al. [85]. Ornstein et al. [85] found most cups to migrate in the posterior direction, not confirmed for the results for single leg stance found in this study.

Ornstein [86] reported that at five years post revision hip arthroplasty, carried out using MCB, cup rotations of 2.2–8.3° had occured in anteversion-retroversion (about the z axis) in 7 of 17 cups, 2.5–9.3° in anterior-posterior rotation (about the x axis), in 7 cups, and 1.4–13.1° in abduction-adduction (about the y axis), in 11 cups. The direction of rotation was not reported by Ornstein [86], although the range of rotation angles is consistent with the results reported here.

It is clear that the clinical observations of cup migration, and rotation

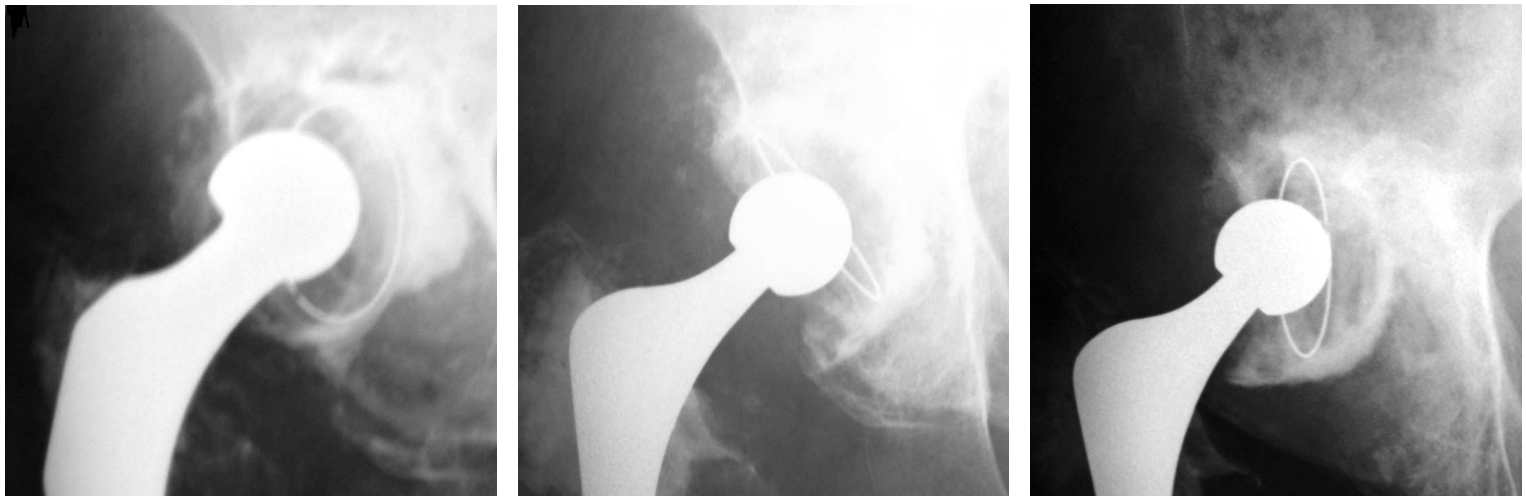

(a) Failed primary (b) Revision with MCB (c) Failed revision

Figure 6.20: Failure of the acetabular construct, due to cup rotation about the y axis, in primary and revision arthroplasty

made by Ornstein et al. are due to many cycles, of many different activities. However Orstein [86] observed that the majority of migration, and rotation of the acetabular cup, occurred immediately after surgery. In addition the material properties of the MCB are subject to significant improvement as the bone graft bed is re-vascularised, and incorporated into the host skeleton. Thus the values of cup migration, and rotation for the 3D analyses presented here are expected to be at the upper end of the range recorded by Ornstein et al. It should also be noted that the 3D analyses presented here were carried out using a large reference defect, without the use of cup fixation devices, and that the assumed body weight (BW) of 1000 N, applied when calculating the resultant forces based on Bergmann et al. [75] is conservative.

6.3.4.2 Normal walking

Figures 6.21 and 6.22 show frontal and lateral views, of the displacement of the acetabular cup, within the MCB bed, at the end of a single cycle normal walking load history. In comparison to the non-displaced cup it is observed that the cup migrates in the superior direction, and rotates in abduction, in a similar manner to that found for single leg stance (Figures 6.12 and 6.13). This is expected, as examining the resultant force curves in Figure 6.11 it can be seen that those for single leg stance, and normal walking are similar. Normal walking gives rise to negative (backwards), as well as positive values of R_y. Comparing the displacement of the acetabular cup for single leg stance (Figures 6.12 and 6.13), and normal walking (Figures 6.21 and 6.22), this is seen to result in a reduction in medial rotation of the cup for normal walking.

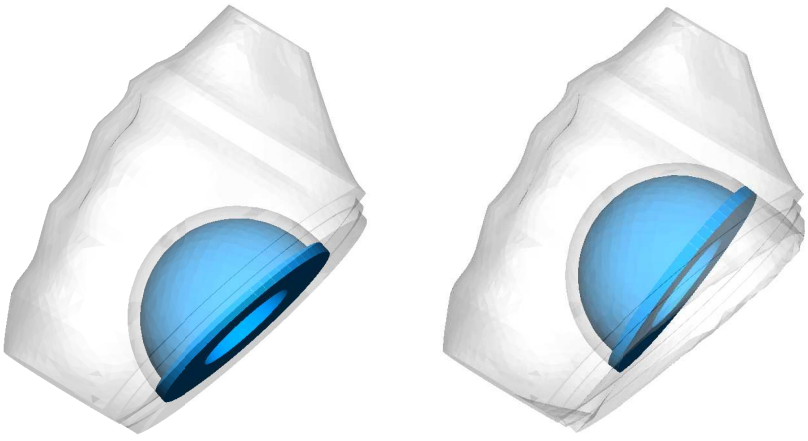

non-displaced displaced

Figure 6.21: Frontal view of the movement of the acetabular cup, within the MCB bed, at the end of a single cycle normal walking load history

Figure 6.23 shows the von Mises stresses found in the cortical bone, for R_{max} during normal walking. It is observed that the stress distribution is similar to that found for R_{max} during single leg stance (Figure 6.14). This

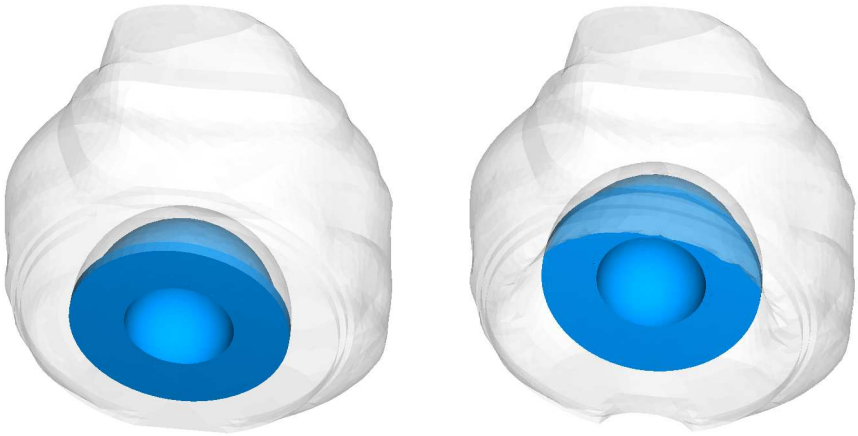

non-displaced displaced

Figure 6.22: Lateral view of the movement of the acetabular cup, within the MCB bed, at the end of a single cycle normal walking load history

indicates that the load transfer path is similar for the two load histories.

Figure 6.24 shows the von Mises stresses found in the trabecular bone, for R_{max} during normal walking. The stress distribution is observed to be similar to that found for R_{max} during single leg stance (Figure 6.15). However the stress concentrations at the edge of the acetabulum are observed to extend in a more posterior direction. This can be attributed to the negative (backwards) value of R_y, for normal walking at R_{max}, compared to a positive value of R_y for single leg stance at R_{max}.

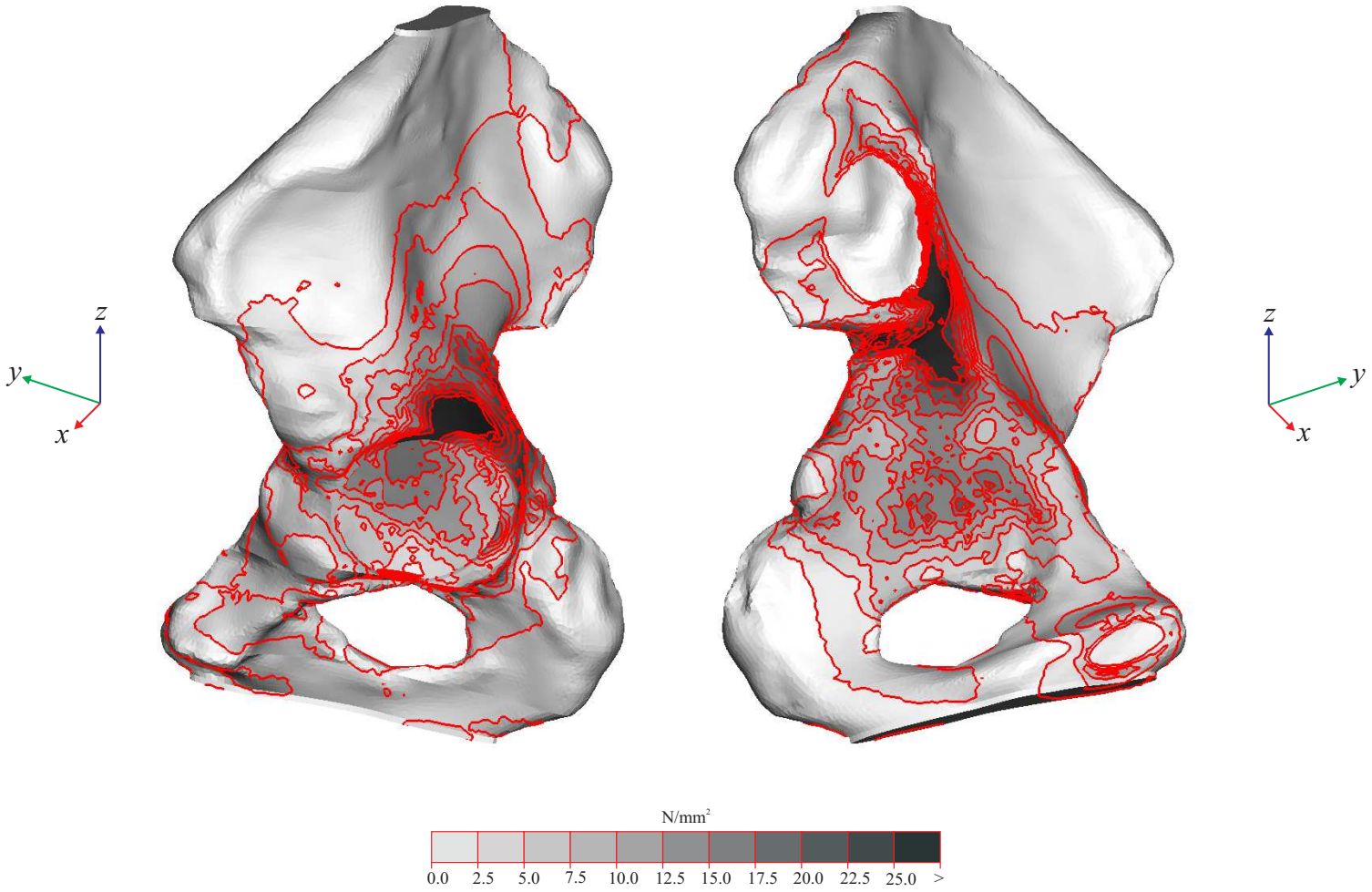

Figure 6.23: von Mises stresses in the cortical bone of the hemi pelvis following revision hip arthroplasty, for R_{max} during normal walking

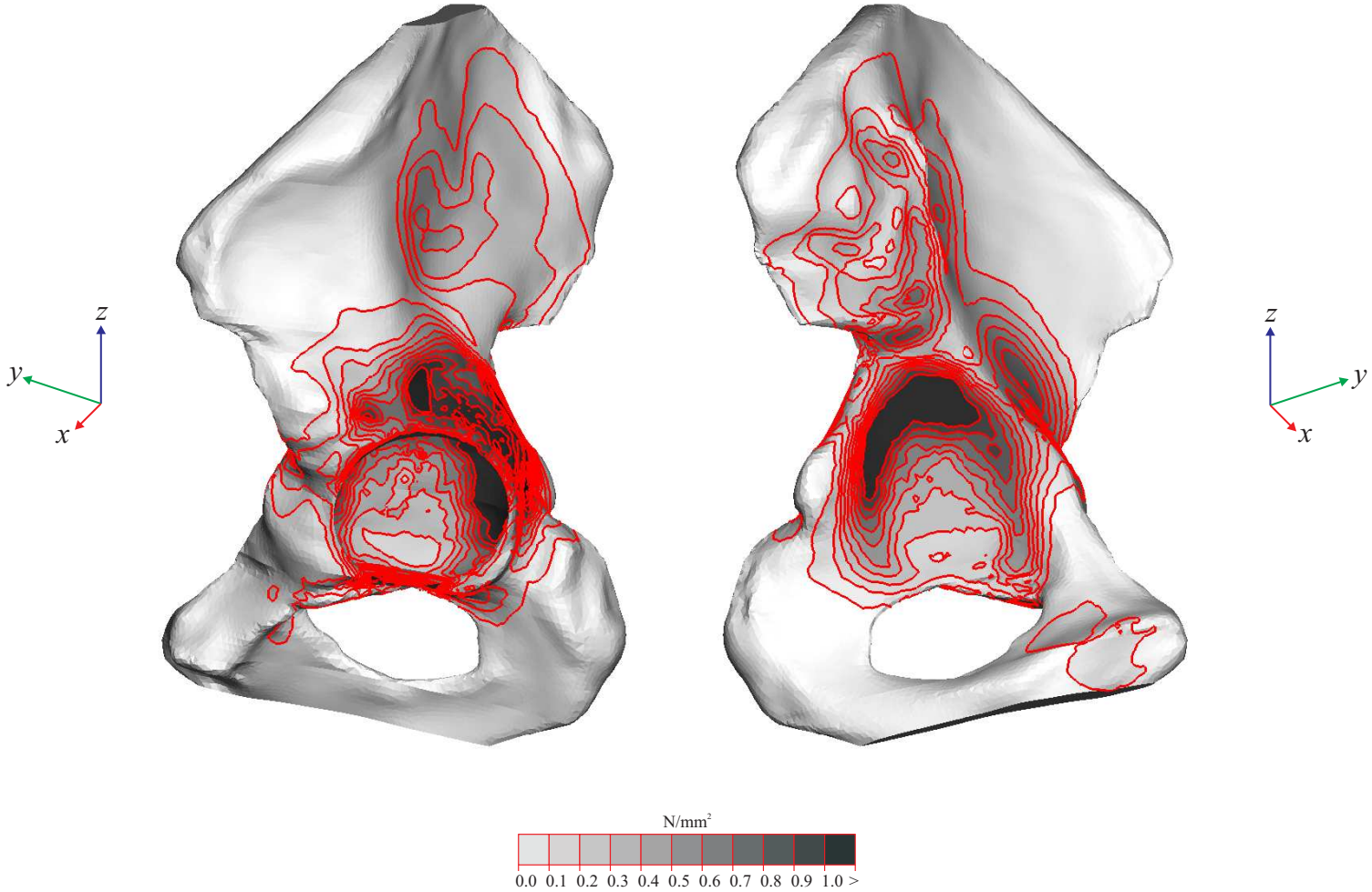

Figure 6.24: von Mises stresses in the trabecular bone of the hemi pelvis following revision hip arthroplasty, for R_{max} during normal walking

Figure 6.25 shows lateral views, at 45° from the horizontal axis, of the distribution of pressure, and von Mises stress, found in MCB, for R_{max} during normal walking. It is observed that the distributions of both pressure, and von Mises stress are orientated in a more posterior direction compared to those found for single leg stance (Figure 6.16) As for the variation in the von Mises stress in the trabecular bone between the two load histories, this can be attributed to the variation in the direction of R_{max} between the two load histories. The maximum von Mises stress experienced by MCB in the acetabulum was around 2.1 N/mm^2, similar to the value found for single leg stance. The maximum pressure experienced by MCB in the acetabulum was around 2.5 N/mm^2, also similar to the value found for single leg stance.

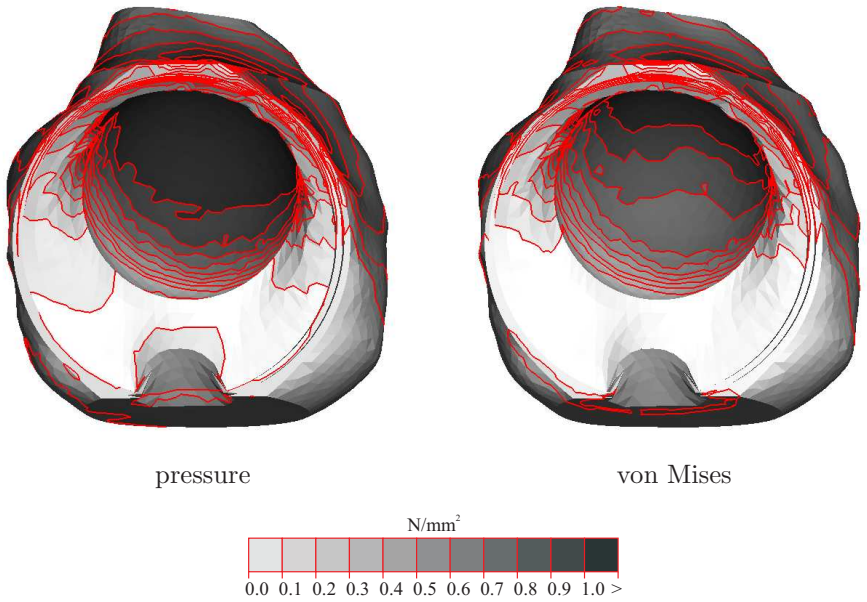

Figure 6.25: Lateral view, at 45° from the horizontal axis, of the distribution of pressure, and von Mises stress in MCB, for R_{max} during normal walking

Figure 6.26 shows lateral views, at 45° from the horizontal axis, of the distribution of maximum, and minimum principal plastic strains, found in MCB at the end of a single cycle normal walking load history. Similar to sin-

gle leg stance, maximum plastic strains are concentrated around the superior edge of the acetabular cup, extending towards the notch in the acetabulum. Minimum plastic strains are concentrated towards the superior edge of the acetabular cup, consistent with MCB being placed under high compressive stress in those regions. As for single leg stance, significant plastic strains are not observed beneath the dome of the cup at the centre of the acetabulum.

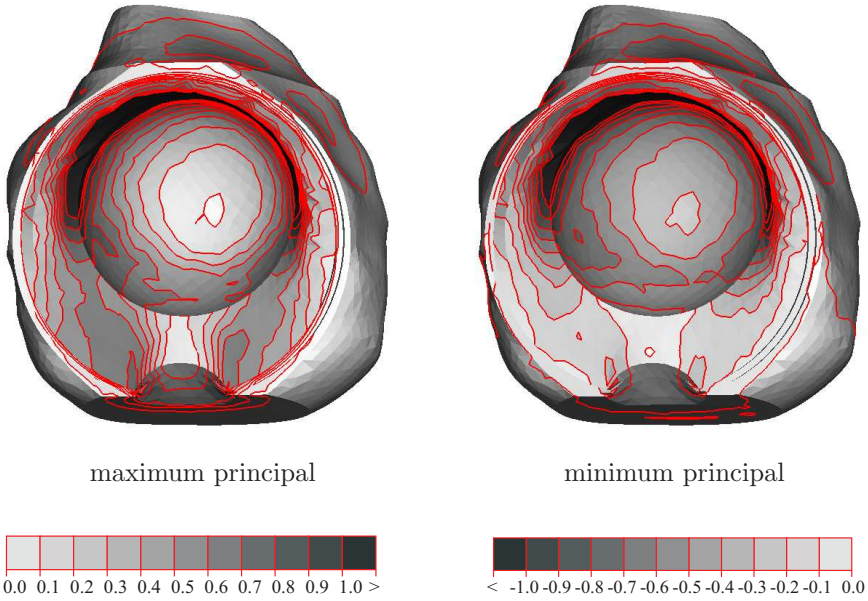

Figure 6.26: Lateral view, at 45° from the horizontal axis, of the distribution of maximum, and minimum principal plastic strains, at the end of a single cycle normal walking load history

Figures 6.27 and 6.28 show the migration, and rotation of the acetabular cup, within the acetabular construct for a single cycle of normal walking. Comparing the displacement of the acetabular cup with the applied resultant force (Figure 6.11) it is observed that, as for single leg stance, the displacement in the y and z directions follows R_y and R_z. Towards the end of the load history these migrations are not recovered due to the development of plastic strains in the bone graft. As for single leg stance displacement in the

x direction does not follow R_x, due to rotation of the cup about the z axis, dependent on the direction of R_y.

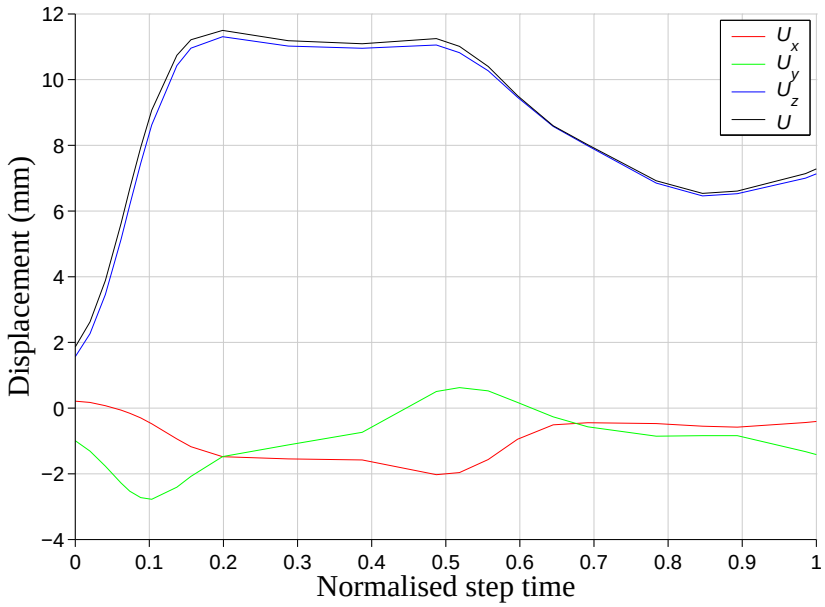

Figure 6.27: Migration of the acetabular cup for a single cycle of normal walking

Examining the rotation of the acetabular cup, it is observed that large rotations occur about the y axes, associated with high values of R_z. Rotations also occur about the x and z axes, associated with the direction of R_y. When R_y is positive rotations about the x axis tend to be positive, while rotations about the z axis tend to be negative. As for the migration of the cup, rotations are not recovered towards the end of the load history due to the development of plastic strains in the MCB bed.

Comparing the results presented here in a pseudo-quantitative manner with Ornstein et al. [85] and Ornstein [86] it is observed that as for single leg stance, the extent of migration and rotation, found using the finite element model is in broad agreement with clinical observations. In addition for a single cycle normal walking load history it was found that the cup migrated

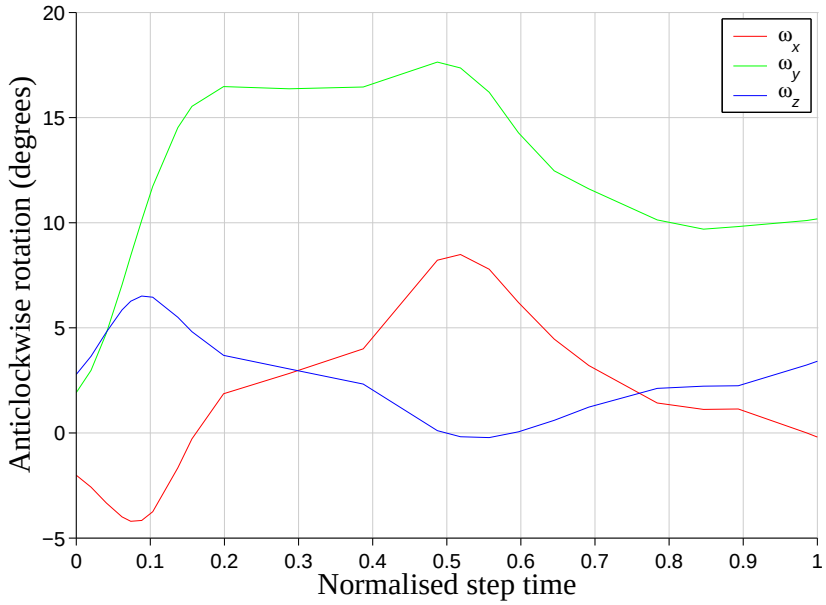

Figure 6.28: Rotation of the acetabular cup for a single cycle of normal walking

in a posterior direction, similar to the findings of Ornstein et al. [85]. The cup was found to migrate in an anterior direction for single leg stance. For both load histories the cup was found to migrate a large amount in the superior direction, and a small amount in the lateral direction.

6.3.4.3 Sitting down

Figures 6.29 and 6.30 show frontal and lateral views, of the displacement of the acetabular cup, within the MCB bed, at the end of a sitting down load history. In comparison to the non-displaced cup it is observed that the cup migrates in a posterior direction, and undergoes lateral rotation. The migration, and rotation of the cup due to sitting down, is found to be quite different to that found for single leg stance (Figures 6.12 and 6.13) and normal walking (Figures 6.21 and 6.22). Examining the resultant force curves in Figure 6.11 it is seen that for single leg stance, and normal walking R is dependent for the most part on R_z. For sitting down R is for the most part dependent on R_y.

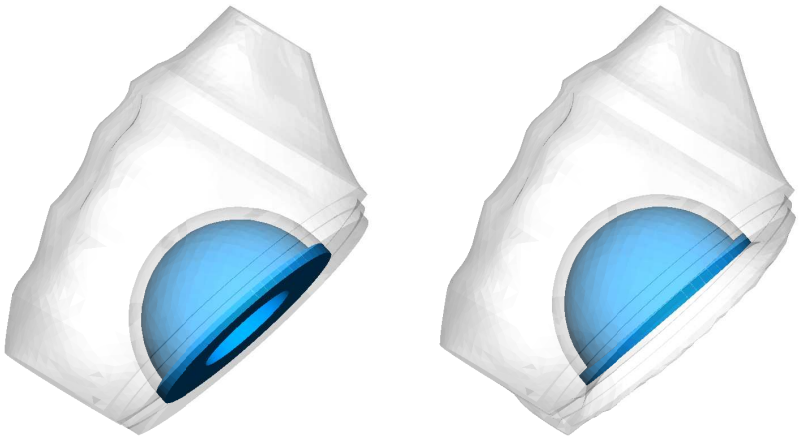

non-displaced displaced

Figure 6.29: Frontal view of the movement of the acetabular cup, within the MCB bed, at the end of a sitting down load history

Figure 6.31 shows the von Mises stresses found in the cortical bone, for R_{max} during sitting down. It is observed that the stress distribution is different to that found for single leg stance (Figure 6.14) and normal walking (Figure 6.23). Stresses are concentrated towards the superior-posterior edge

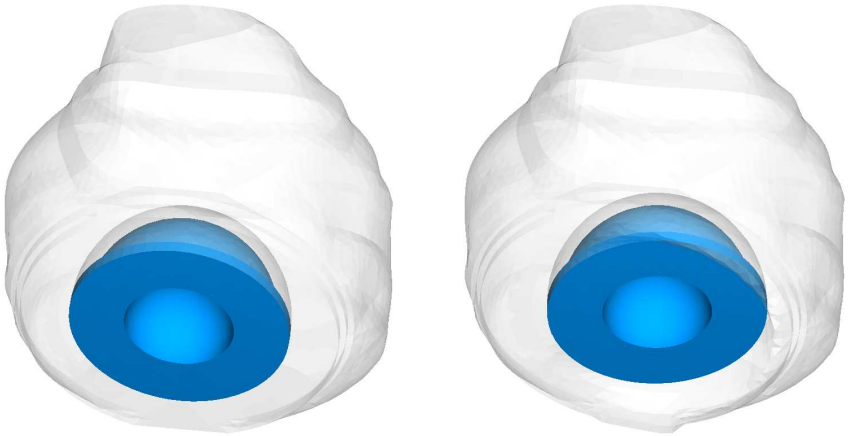

non-displaced displaced

Figure 6.30: Lateral view of the movement of the acetabular cup, within the MCB bed, at the end of a sitting down load history

of the acetabulum, extending towards, and round the greater sciatic notch. In addition stress concentrations are observed at the pubic-symphysis constrained boundary condition, to a greater extent than found for single leg stance, and normal walking.

Figure 6.32 shows the von Mises stresses found in the trabecular bone, for R_{max} during sitting down. As for the stress distribution in the cortical bone, the stress distribution in the trabecular bone is different to that found for single leg stance (Figure 6.15) and normal walking (Figure 6.24). Stresses are concentrated towards the posterior edge of the acetabulum, progressing towards the ischium, and to the posterior side at the rear of the acetabulum.

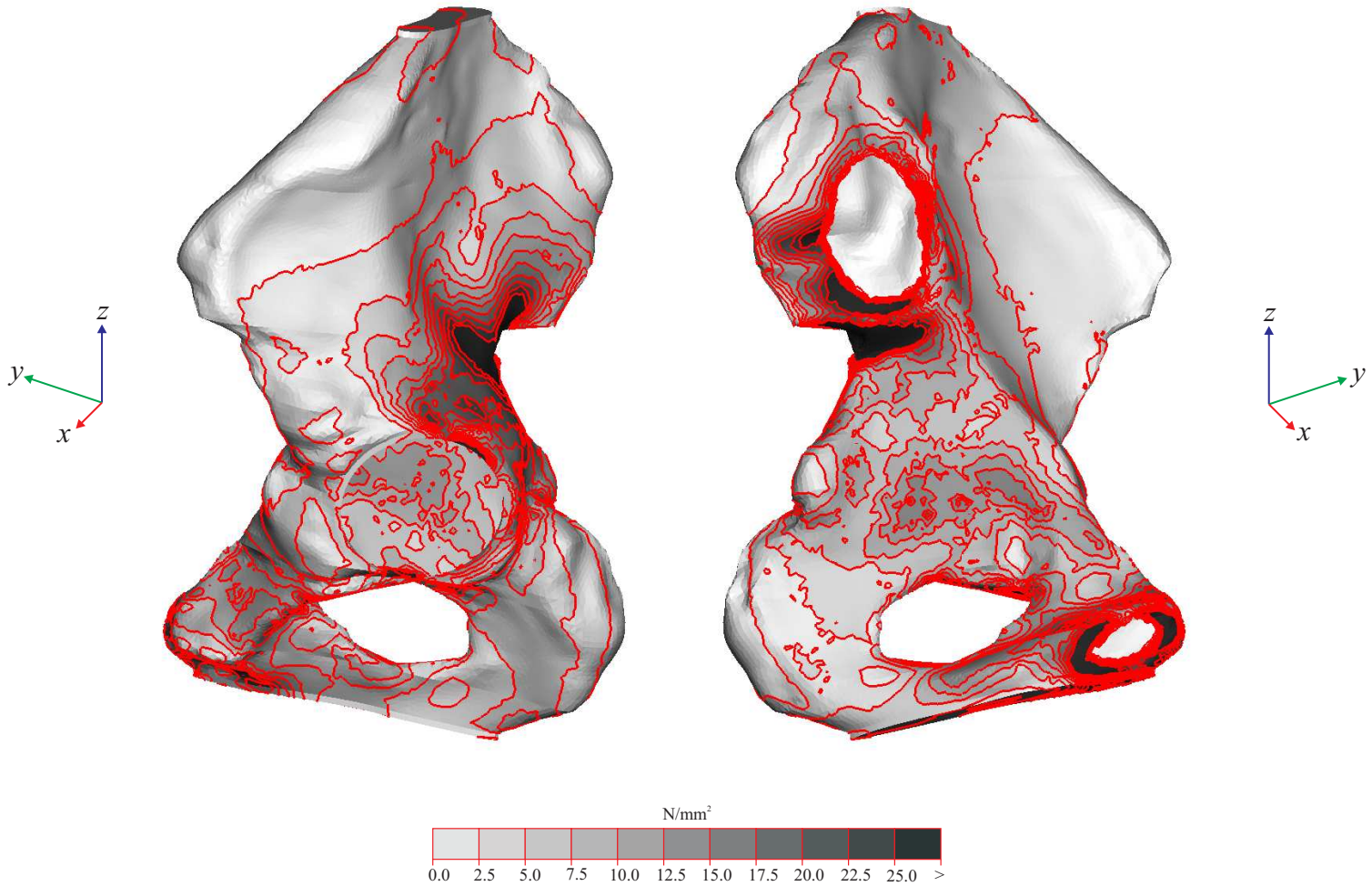

Figure 6.31: von Mises stresses in the cortical bone of the hemi pelvis following revision hip arthroplasty, for R_{max} during sitting down

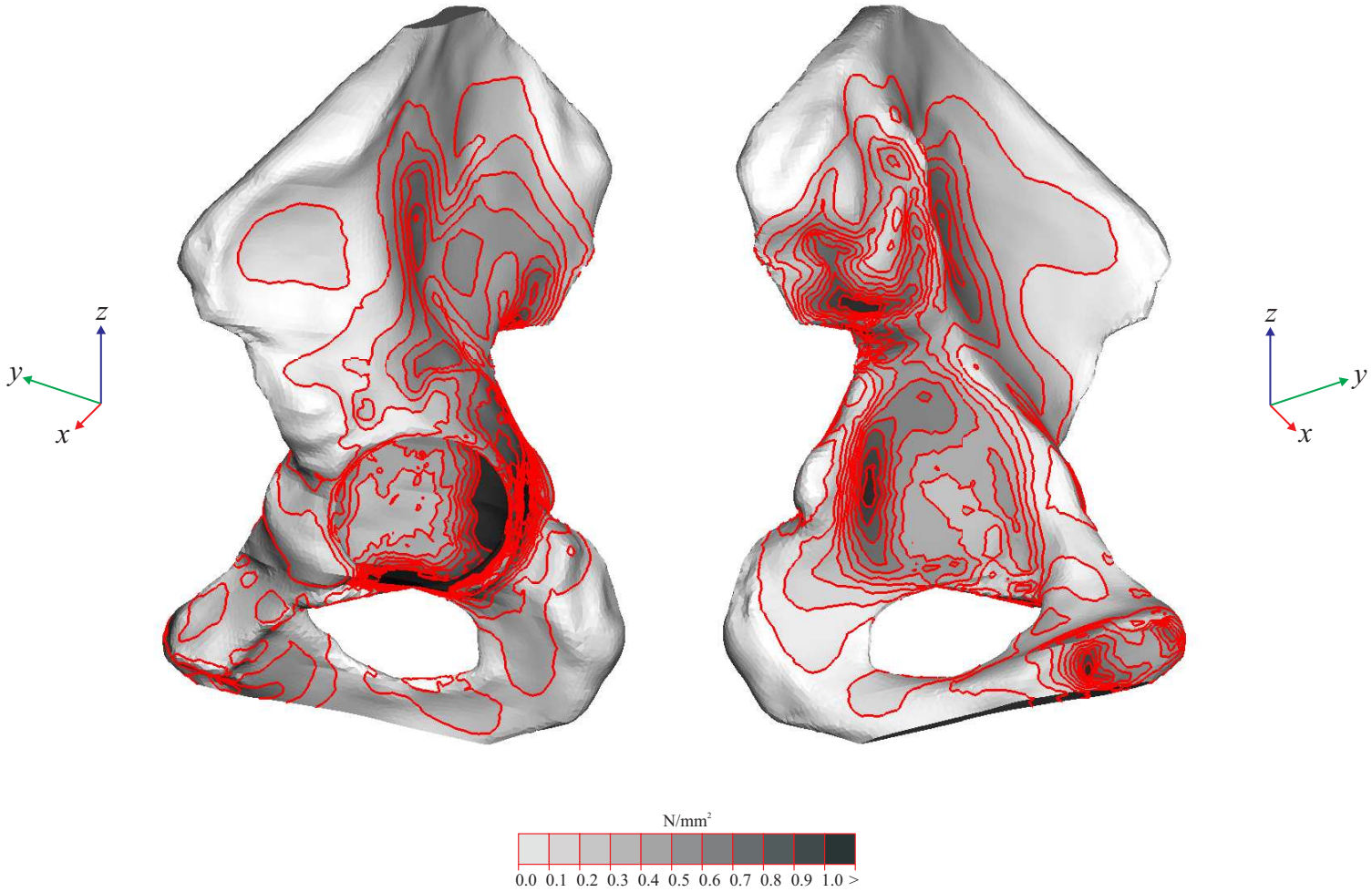

Figure 6.32: von Mises stresses in the trabecular bone of the hemi pelvis following revision hip arthroplasty, for R_{max} during sitting down

Figure 6.33 shows lateral views, at 45° from the horizontal axis, of the distribution of pressure, and von Mises stress, found in MCB, for R_{max} during sitting down. It is observed that the distributions of both pressure, and von Mises stress are orientated towards the posterior edge of the acetabular cup. This can be attributed to a large negative (backwards) value of R_y. The maximum von Mises stress experienced by the MCB in the acetabulum was around 1.7 N/mm^2 The maximum pressure experienced by MCB in the acetabulum was around 2.1 N/mm^2.

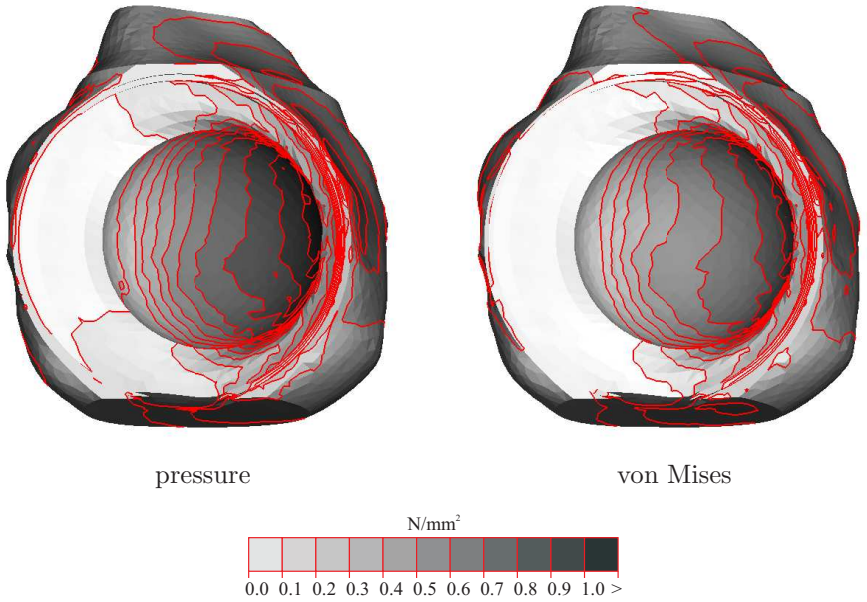

Figure 6.33: Lateral view, at 45° from the horizontal axis, of the distribution of pressure, and von Mises stress in MCB, for R_{max} during sitting down

Figure 6.34 shows lateral views, at 45° from the horizontal axis, of the distribution of maximum, and minimum principal plastic strains, found in MCB at the end of a sitting down load history. Both maximum, and minimum plastic strains are concentrated towards the posterior edge of the acetabular cup, consistent with MCB being placed under high compressive stress in these regions, and with unconfined MCB being "squeezed out" between the

acetabular cup, and the cortical bone at the edge of the acetabulum. It is observed that although the distribution of plastic strains is quite different to that found for single leg stance (Figure 6.17) and normal walking (Figure 6.26) significant plastic strains are not seen beneath the dome of the acetabular cup for any of the three load histories.

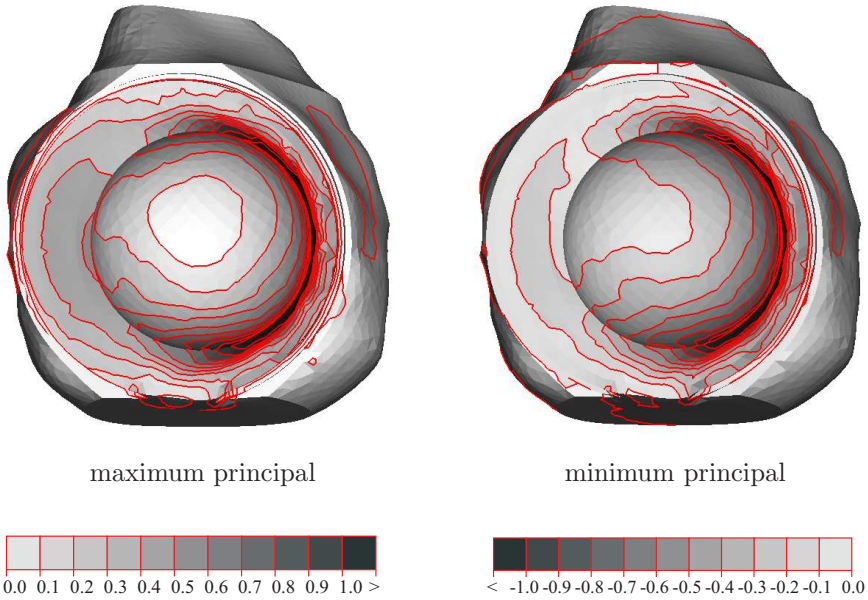

Figure 6.34: Lateral view, at 45° from the horizontal axis, of the distribution of maximum, and minimum principal plastic strains, at the end of a sitting down load history

Figures 6.35 and 6.36 show the displacement, and rotation of the acetabular cup, within the acetabular construct for sitting down. Comparing the displacement of the acetabular cup with the applied resultant force (Figure 6.11) it is observed that the migration in the x, y and z directions follows R_x, R_y and R_z. Towards the end of the load history these migrations are not recovered due to the development of plastic strains in the bone graft. In addition to significant migration in the posterior direction, migrations are also seen in the superior and medial directions.

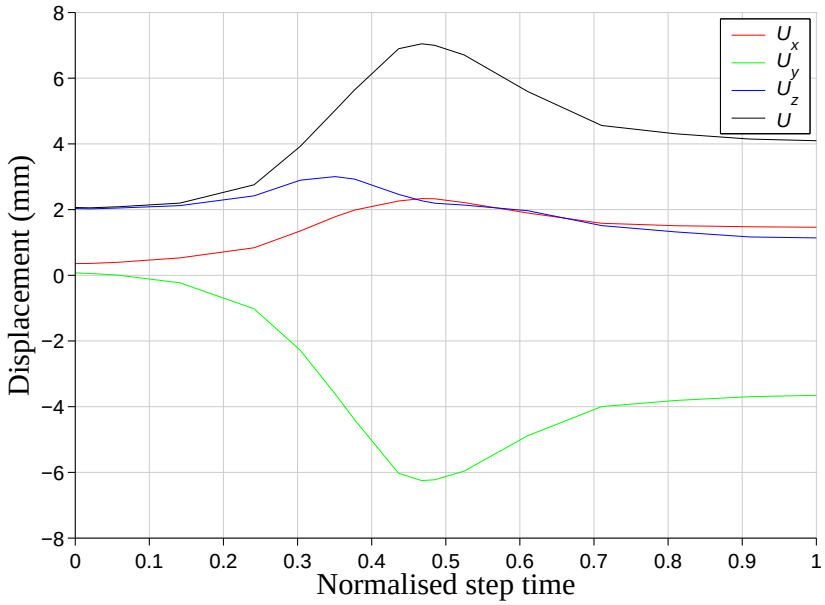

Figure 6.35: Migration of the acetabular cup for sitting down

Examining the rotation of the acetabular cup it is observed that large rotations occur about the x and z axes, associated with high values of R_y. In contrast to the rotations found for single leg stance (Figure 6.19) and normal walking (Figure 6.28) rotations about the y axis are limited. As for the migration of the cup, rotations are not recovered towards the end of the load history due to the development of plastic strains in the MCB bed.

Comparing the results presented here with Ornstein et al. [85] it was found that sitting down caused the cup to migrate in a posterior direction, in support of the findings of Ornstein et al. [85]. In contrast to the results for single leg stance, and normal walking, sitting down was found to cause migration of the cup in the medial direction. Ornstein et al. [85] found an equal split between cups migrating in the medial and lateral directions.

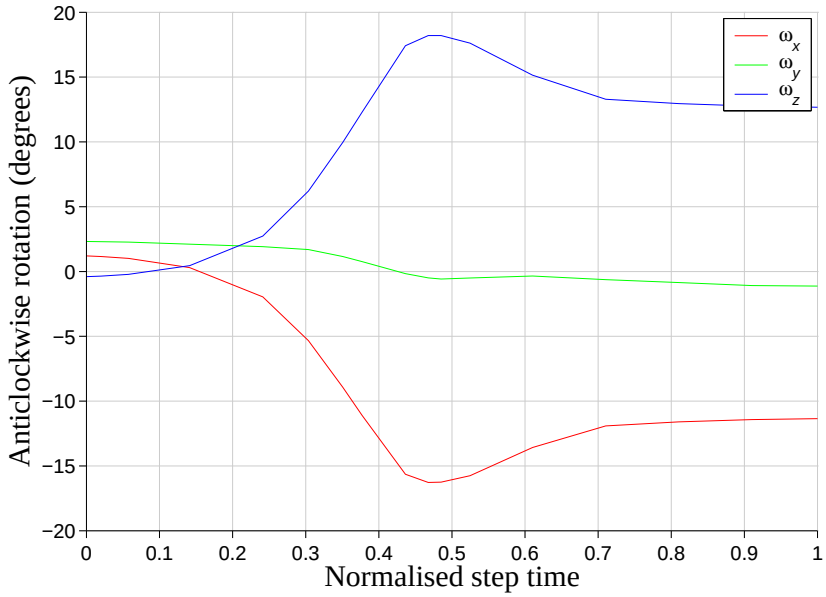

Figure 6.36: Rotation of the acetabular cup for sitting down

6.3.4.4 Standing up

Figures 6.37 and 6.38 show frontal and lateral views, of the displacement of the acetabular cup, within the MCB bed, at the end of a standing up load history. It is observed that as for sitting down (Figures 6.29 and 6.30) the cup migrates in the posterior direction, and undergoes lateral rotation. This can be attributed to R_{max} acting in a similar direction for standing up as for sitting down. Examining the resultant force curves (Figure 6.11) it is seen that the load history for standing up is similar to a reversed load history for sitting down.

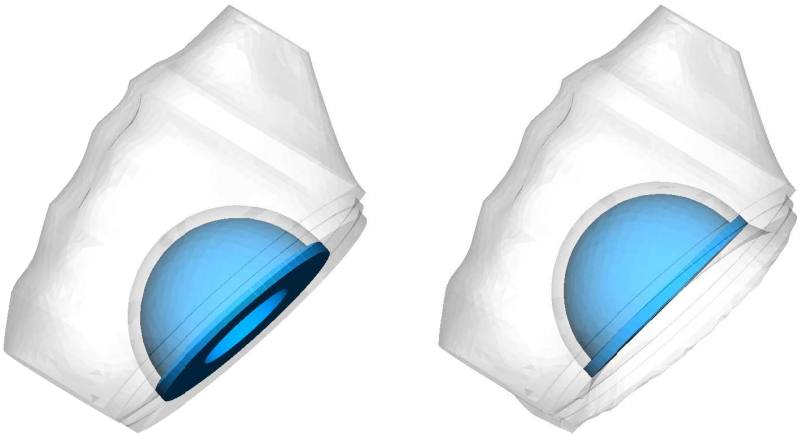

non-displaced displaced

Figure 6.37: Frontal view of the movement of the acetabular cup, within the MCB bed, at the end of a standing up load history

Figure 6.39 shows the von Mises stresses found in the cortical bone, for R_{max} during standing up. It is observed that the stress distribution is similar to that found for R_{max} during sitting down (Figure 6.31). However, there is an increase in the extent of the region around the greater sciatic notch affected by high stresses, which can be attributed to a higher R_{max} value for standing up, compared to sitting down.

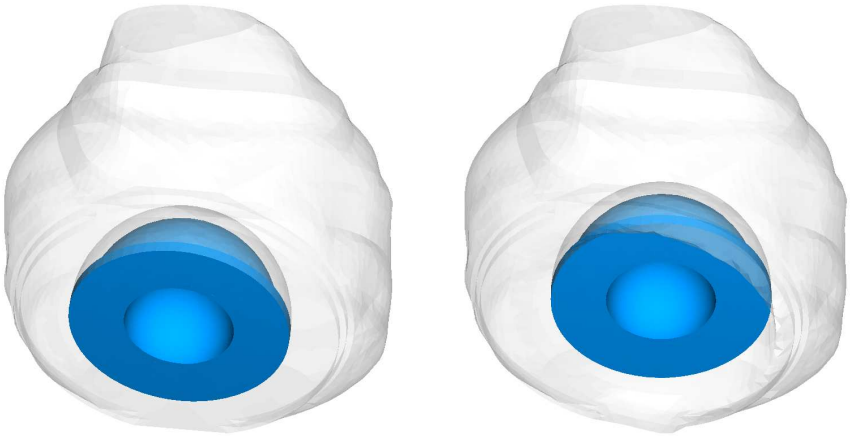

non-displaced displaced

Figure 6.38: Lateral view of the movement of the acetabular cup, within the MCB bed, at the end of a standing up load history

Figure 6.40 shows the von Mises stresses found in the trabecular bone, for R_{max} during standing up. The stress distribution is observed to be similar to that found for R_{max} during sitting down (Figure 6.32). However, as for the cortical bone there is a increase in the extent of the regions affected by high stresses, due to the higher R_{max} value.

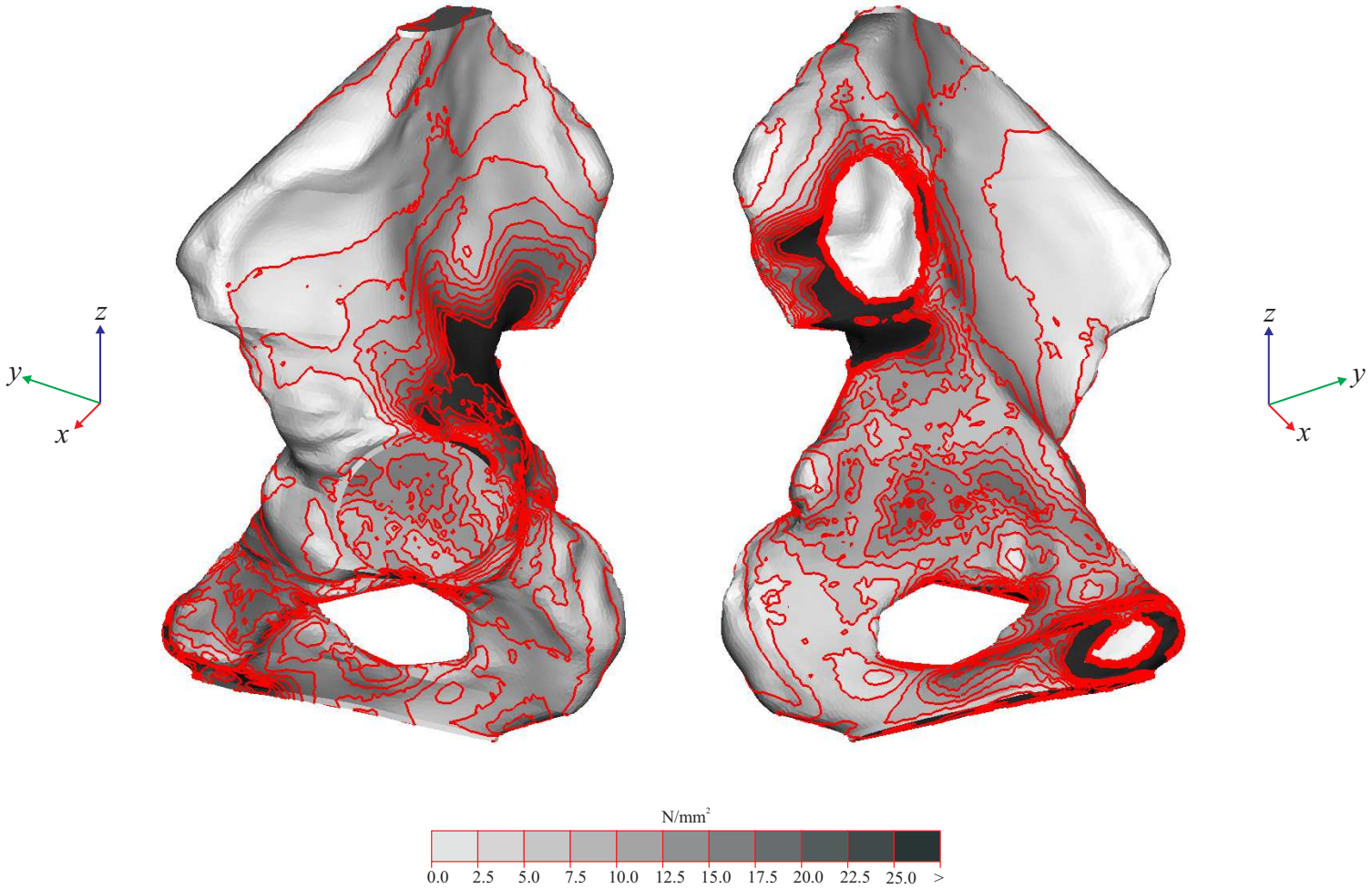

Figure 6.39: von Mises stresses in the cortical bone of the hemi pelvis following revision hip arthroplasty, for R_{max} during standing up

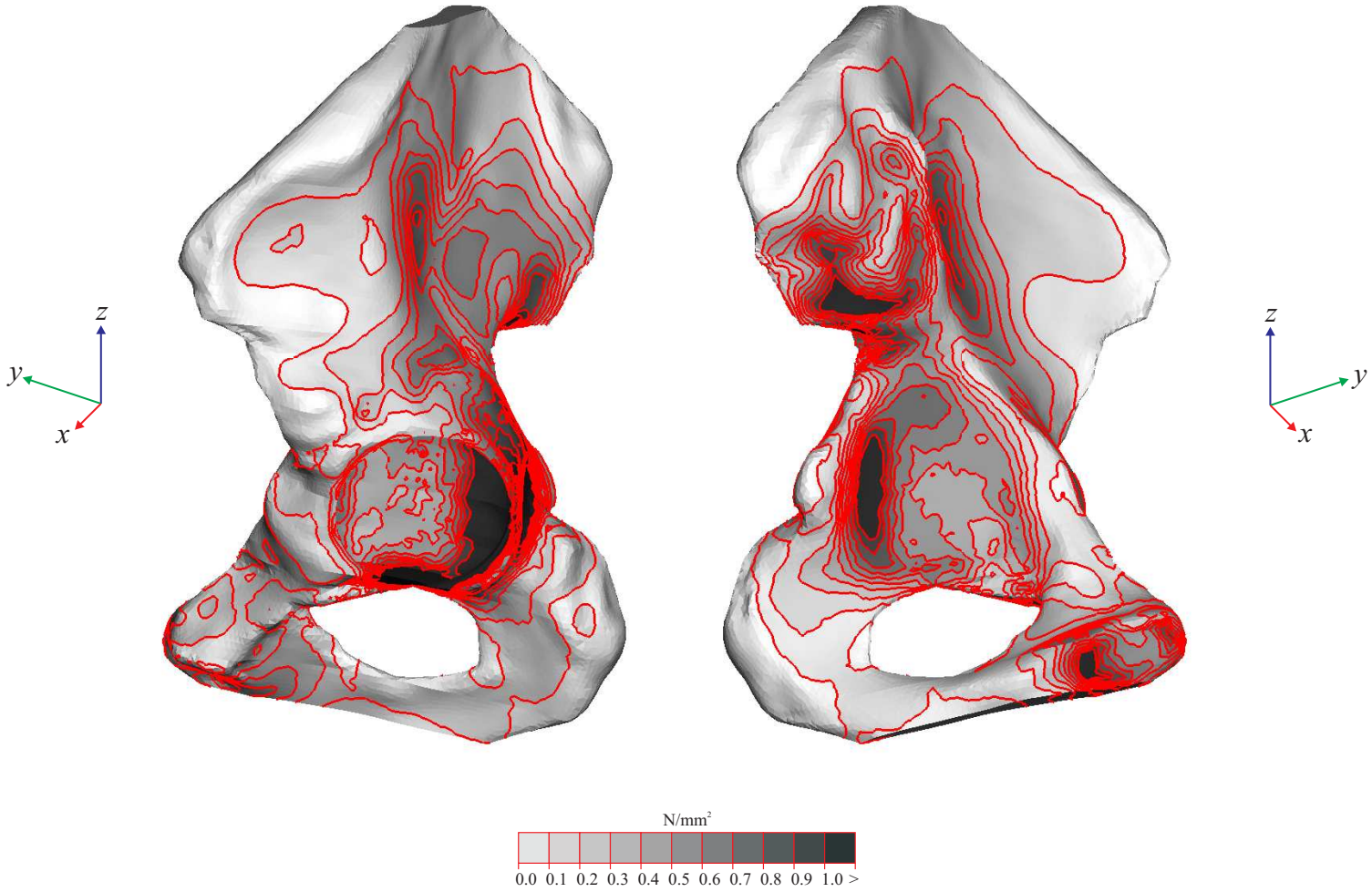

Figure 6.40: von Mises stresses in the trabecular bone of the hemi pelvis following revision hip arthroplasty, for R_{max} during standing up

Figure 6.41 shows lateral views, at 45° from the horizontal axis, of the distribution of pressure, and von Mises stress, found in MCB, for R_{max} during standing up. It is observed that the distributions of both pressure, and von Mises stress are similar to those found for sitting down (Figure 6.33), due to R_{max} acting in a similar direction for both load histories. The maximum von Mises stress experienced by MCB in the acetabulum was around 2.5 N/mm^2, around 45% higher than for sitting down. The maximum pressure experienced by MCB in the acetabulum was around 3.0 N/mm^2, also around 45% higher than for sitting down.

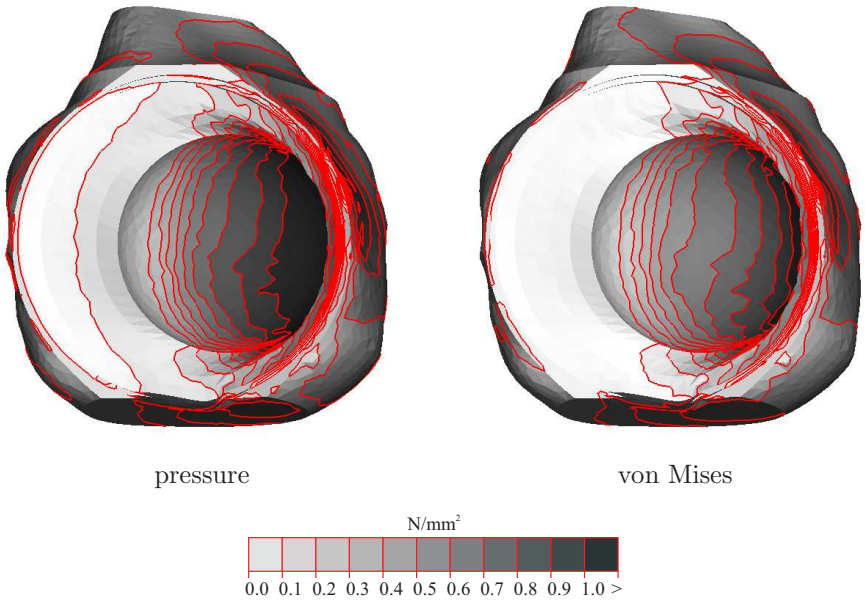

Figure 6.41: Lateral view, at 45° from the horizontal axis, of the distribution of pressure, and von Mises stress in MCB, for R_{max} during standing up

Figure 6.42 shows lateral views, at 45° from the horizontal axis, of the distribution of maximum, and minimum principal plastic strains found in MCB, at the end of a standing up load history. Similar to sitting down, both maximum, and minimum plastic strains are concentrated towards the posterior edge of the acetabular cup. As for the other three load cases,

significant plastic strains are not observed beneath the dome of the acetabular cup.

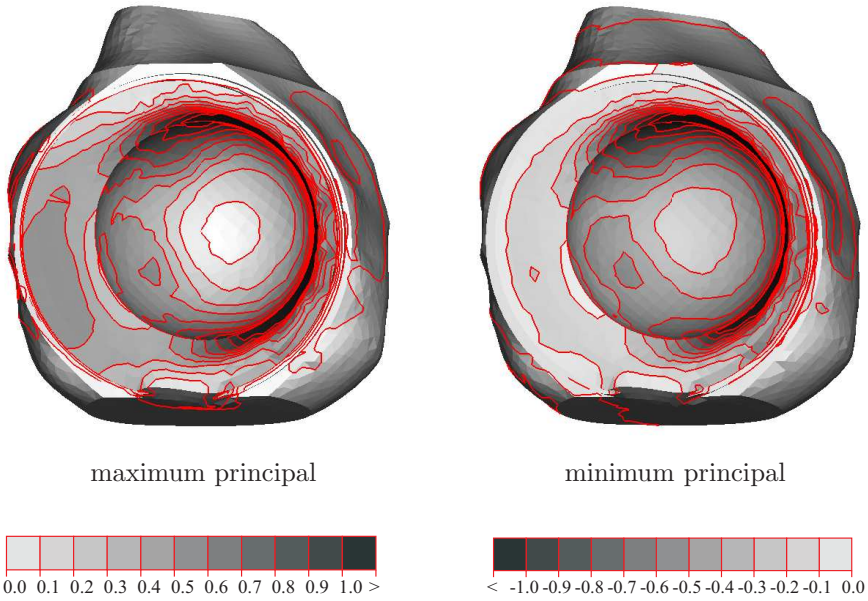

Figure 6.42: Lateral view, at 45° from the horizontal axis, of the distribution of maximum, and minimum principal plastic strains, at the end of a standing up load history

Figure 6.43 and 6.44 show the displacement, and rotation of the acetabular cup, within the acetabular construct for standing up. Comparing the displacement with the applied resultant force (Figure 6.11) it is observed that, as for sitting down, the migration in the x, y and z directions follows R_x, R_y and R_z. As for sitting down, in addition to significant migration in the posterior direction, migrations are also seen in the superior and medial directions.

Examining the rotation of the acetabular cup, similar to sitting down, it is observed that large rotations occur about the x and z axes, associated with high values of R_y. Rotations about the y axis are limited. As for the migration of the cup, rotations are not recovered towards the end of the load

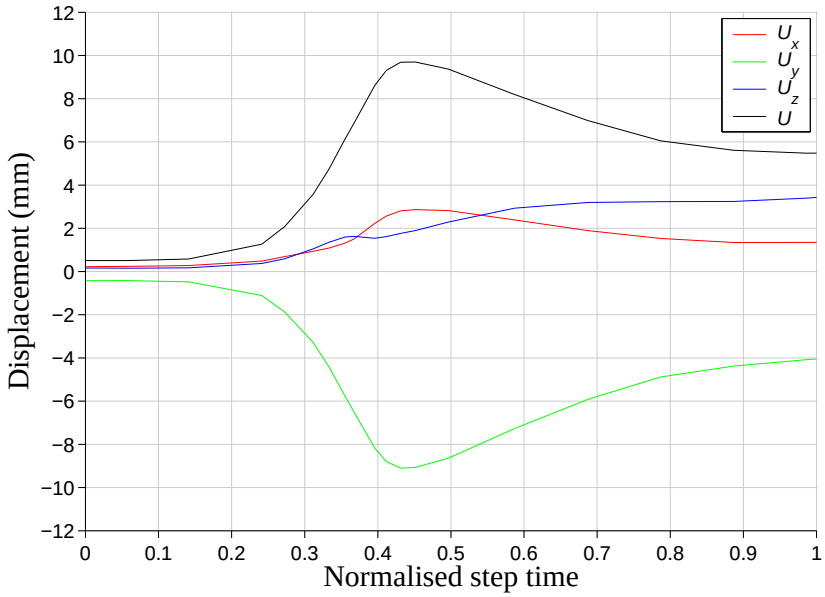

Figure 6.43: Migration of the acetabular cup for standing up

history due to the development of plastic strains in the MCB bed.

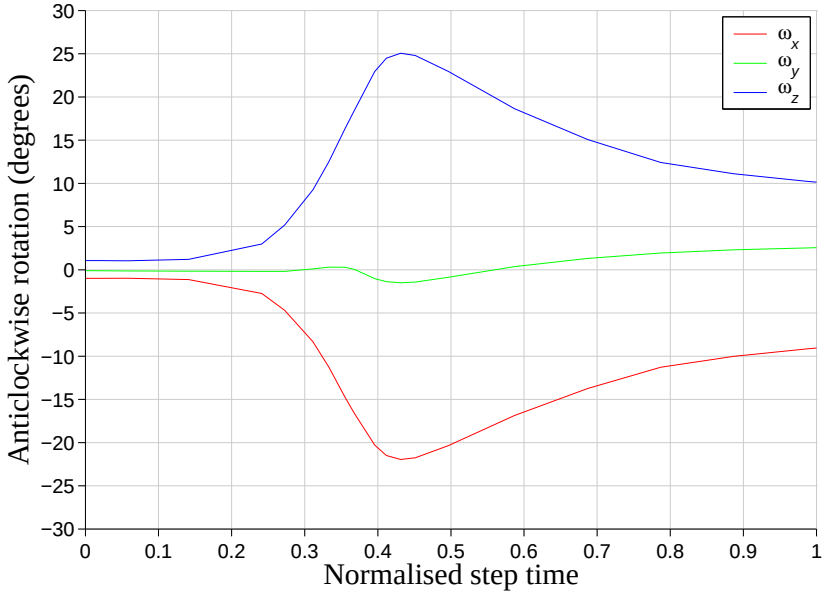

Figure 6.44: Rotation of the acetabular cup for standing up

Comparing the results presented for the four load cases with Ornstein et al. [85] and Ornstein [86] it is observed that different load histories give

rise to distinctive patterns of cup migration and irrecoverable rotation. As discussed earlier, it is evident that the clinical observations of cup migration, and rotation made by Ornstein et al. are due to many cycles, of many different activities. It is clear that the results presented here are qualitatively, indicative of the patterns of cup migration and rotation, expected due to certain activities. In all cases superior migration of the cup was seen. Sitting down, and standing up gave rise to posterior migration, seen for the majority of cups by Ornstein et al. [85] suggesting these activities present a particular risk to the stability of the acetabular cup. The absolute values of cup migration, and rotation presented here are seen to be at the high end of the range found by Ornstein [86]. However this is expected, given the material properties assigned to MCB, the size of the chosen reference defect, and the use of an acetabular cup supported on the bone graft bed alone, without the use of cup fixation devices.

6.4 Conclusions

3D analyses of the natural hemi pelvis, and the hemi pelvis following primary and revision hip arthroplasty, subjected to loading histories corresponding to physiological activities, were presented in this chapter. The analyses of the natural hemi pelvis, and the hemi pelvis following primary hip arthroplasty, subjected to a single leg stance load case, showed that the observed stress distributions and magnitudes, were similar to those found by other investigators [22–25, 27, 31].

These models were used as reference points in the development of a model of the hemi pelvis following revision hip arthroplasty, carried out using impaction grafting. The bone graft bed was modelled as an isotropic non-linear elasto-plastic material, based on the constitutive models, and 2D plane-strain analyses presented in previous chapters. 3D analysis of the hemi pelvis and acetabular construct, including realistic non-linear modelling of MCB are not available in the literature.

This model was then subjected to a series of realistic 3D loading histories [75] to evaluate the effect of different activities on the potential migration and rotation of the acetabular cup, due to the development of plastic strains in the MCB bed. Results were found to be qualitatively similar to those from clinical observations [85, 86]. The results were also found to be similar when compared in a pseudo-quantitative manner, although caution should be exercised in making direct comparisons due to the factors discussed earlier.

It is seen that the results, and analyses presented here are of use in informing those in the fields of revision hip arthroplasty, and impaction grafting of

possible failure mechanisms in the acetabular construct, leading to instability of the acetabular cup following surgery. Difference activities are seen to cause the acetabular cup to migrate, and rotate in different ways. It is suggested that activities such as sitting down and standing up, present unique risks, alongside activities such as single leg stance and walking. Clinical and numerical studies should bear this in mind, as results for a single activity, such as walking, are shown not to be applicable for all activities.

The 3D model of the hemi pelvis, following revision arthroplasty presented here, could be adapted to assess the performance of cup fixation devices, and alternative prosthesis designs.

7

Muscular and ligamentous contributions in a 3D finite element model of the pelvis

Previous 3D finite element studies of the pelvis have been successful in correlating numerical models of the pelvis with the results of *in vitro* loading experiments carried out on pelvic bones (stripped of soft tissue) taken from

cadaveric specimens [19,20,22,24,33]. While these studies provide verification of the modelling of the hard tissues of the pelvis, the boundary conditions used in both the numerical models and laboratory testing do allow conclusions regarding the behaviour of the pelvis *in vivo* to be drawn. Thus it is desirable to develop a complete model of the pelvis in which muscles and ligaments are included in an explicit manner, in order to assess the influence these structures have on the pelvis in its natural state. The inclusion of muscles and ligaments allows the behaviour of the pelvis to be examined under boundary conditions more representative of those found *in vivo*.

7.1 Function and muscles of the hip joint

The hip joint can be viewed as a ball and socket joint, about which the muscles act to resist external forces placed upon it. The joint allows movement of the leg with respect to the trunk of the body, and *visa-versa*. Movement of the thigh or trunk around the hip joint can be classified as Figure 7.1:

- **Flexion:** movement of the thigh towards the trunk of the body in the sagittal (median) plane
- **Extension:** movement of the thigh away from the trunk of the body in the sagittal (median) plane
- **Adduction:** movement of the thigh towards the mid-line of the body in the coronal (frontal) plane
- **Abduction:** movement of the thigh away from the mid-line of the body in the coronal (frontal) plane

- **Medial rotation:** rotation of the thigh about the axis of the femur towards the mid-line of the body in the transverse (horizontal) plane

- **Lateral rotation:** rotation of the thigh about the axis of the femur away from the mid-line of the body in the transverse (horizontal) plane

- **Transverse adduction:** movement of the thigh towards the mid-line of the body (when the hip joint is in flexion) in the transverse plane.

- **Transverse abduction:** movement of the thigh away from the mid-line of the body (when the hip joint is in flexion) in the transverse plane.

Muscles of the hip joint are associated with specific movements [88], though it should be noted that individual muscles are involved at different stages of multiple movements. The association of muscles with particular movements can be described:

- **Flexion:** psoas major, and iliacus, assisted by rectus femoris, sartorius, pectineus, and adductor muscles (initial stages)

- **Extension:** gluteus maximus, semitendinosus, and semimembranosus, biceps femoris (long head)

- **Adduction:** adductor magnus, adductor longus, and adductor brevis, assisted by gracilis, and pectineus

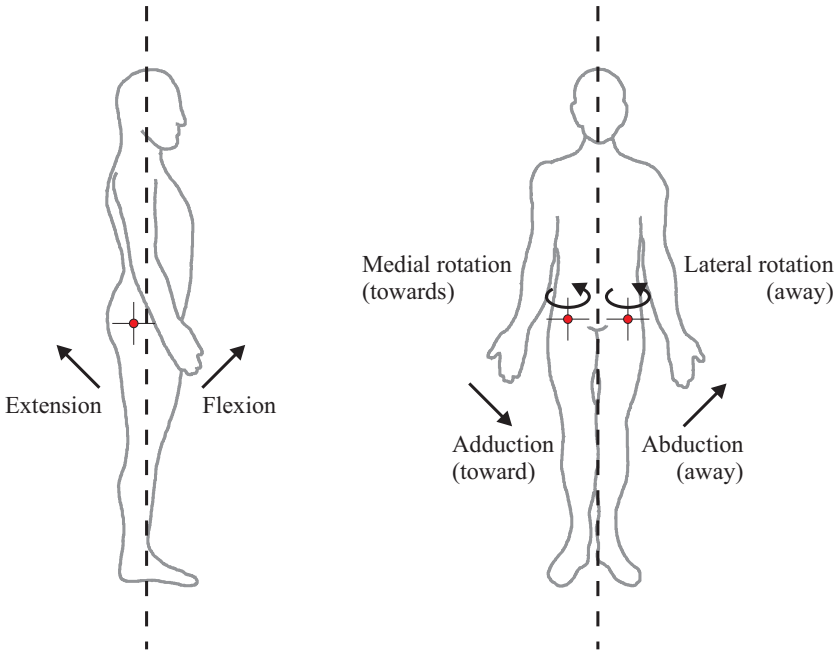

Figure 7.1: Classification of movements around the hip joint, in the saggital (left) and coronal (right) planes

- **Abduction:** gluteus medius, and gluteus minimus, assisted by gluteus maximus, tensor fasciae latae, and sartorius
- **Medial rotation:** tensor fasciae latae, gluteus medius (anterior fibres), and gluteus minimus (anterior fibres), assisted by gracilis, and adductor muscles (position dependent)
- **Lateral rotation:** obturator internus, obturator externus, gemellus superior, gemellus inferior, and quadratus femoris, assisted by piriformis, gluteus maximus, and sartorius
- **Transverse adduction:** adductor magnus, adductor longus, and adductor brevis assisted by: pectineus, gracilis, and tensor fasciae latae
- **Transverse abduction:** gluteus maximus, gluteus medius, and

gluteus minimus assisted by piriformis, and obturator externus

Attachment areas of the hip joint muscles on the pelvic bone, and their approximate directions of action in the anatomic position are shown in Figure 7.2.

In order to assess the role of the hip joint muscles with regard to the behaviour and stability of the pelvis, methods discussed later in this chapter, were developed allowing the muscles to be modelled as non-linear springs, operating with realistic geometries around the hip joint.

As well as acting in a agonist manner to prompt movement, muscles also act in an antagonistic manner in order to control movement. Thus gluteus maximus for example, acts as a agonistic muscle to prompt extension, and acts as an antagonistic muscle to control flexion. Through including muscles as non-linear springs it is expected that antagonistic, as well as agonistic behaviour will be identified, as discussed later in the chapter.

7.2 Ligaments forming the pelvic ring

In addition to hip joints muscles, the behaviour and stability of the pelvis is influenced by the ligaments, which in combination with the two halves of the pelvis, and the sacrum form the pelvic ring [89–93]. These ligaments have a clear role in restricting movement at the sacro-iliac joints and the pubic-symphysis. Ligaments forming the pelvic ring were identified as:

- Anterior sacroiliac, interosseous sacroiliac, and posterior sacroiliac, forming a ligament ring around the sacro-iliac joints

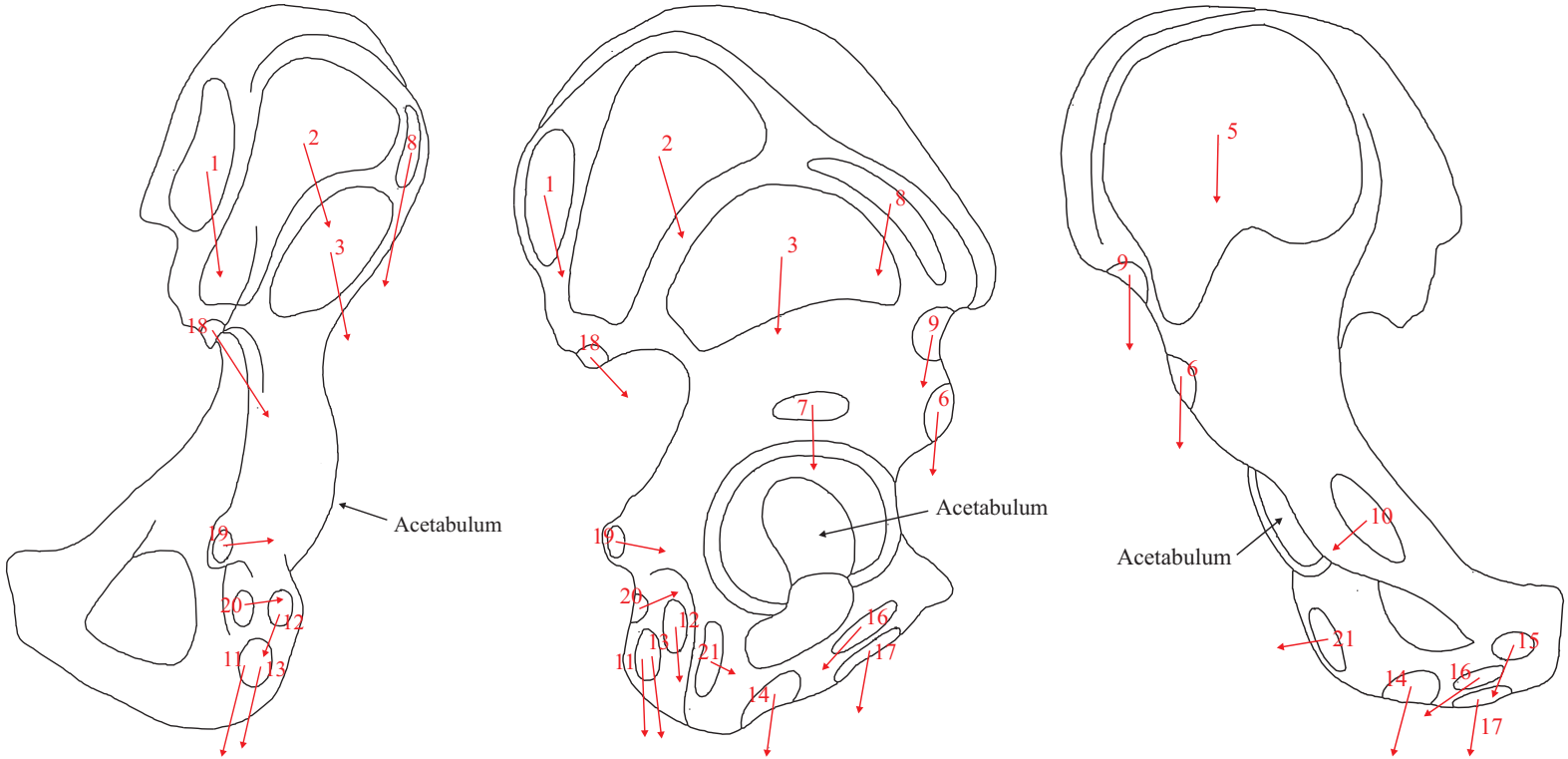

Figure 7.2: Muscles attachment areas on the pelvic bone (direction of action indicated)

1. Gluteus maximus; 2. Gluteus medius; 3. Gluteus minimus; 4. Psoas (not shown); 5. Iliacus; 6. Rectus femoris (straight head); 7. Rectus femorus (reflected head); 8. Tensor fasciae latae; 9. Sartorius; 10. Pectineus; 11. Semitendinosus; 12. Semimembranosus; 13. Biceps femoris (long head); 14. Adductor magnus; 15. Adductor longus; 16. Adductor brevis; 17. Gracilis; 18. Piriformis; 19. Gemellus superior; 20. Gemellus inferior; 21. Quadratus femoris

- Sacrospinous
- Sacrotuberous
- Iliolumbar
- Inguinal
- Superior pubic, arcuate pubic

The positions of ligaments forming the pelvic ring are shown on anterior and posterior views of the pelvis in Figure 7.3

Similar methods to those developed to include the hip joint muscles, were used to include the pelvic ring ligaments in the 3D pelvis model. Ligaments crossing the hip joint itself were not included in the model as these are considered to have a role in restraining the hip joint at extremes of movement, but not to have a significant role during the normal ranges of movement [94, 95], considered for the analyses presented in this study. In addition, in the context of the hip joint following hip arthroplasty, ligaments around the hip joint capsule would not be present.

7.3 Muscle behaviour

The muscles around the hip joint are striated skeletal muscles structured as illustrated in Figure 7.4. The muscles consist of bundles of muscle fibres surrounded by perimysium. Individual muscle fibres are surrounded by endomysium, and are composed of myofibrils, which can be broken down into sacromeres containing actin and myosin filaments, providing the mechanism

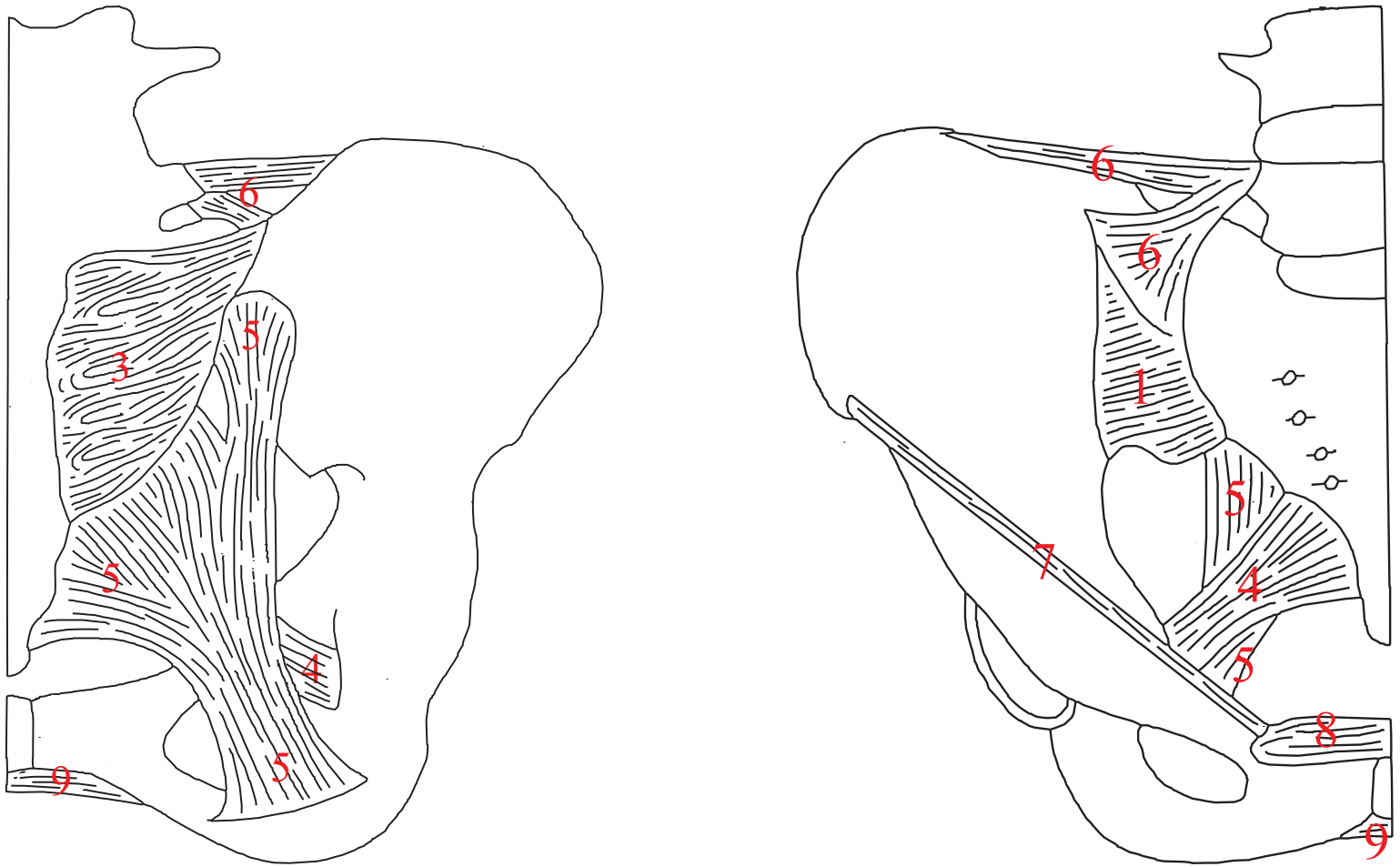

Posterior view

Anterior view

Figure 7.3: Ligaments forming the pelvic ring

1. Anterior sacroliliac; 2. Interosseus sacroiliac (hidden); 3. Posterior sacroliliac; 4. Sacrospinous; 5. Sacrotuberous; 6. Iliolumbar; 7. Inguinal; 8. Superior pubic; 9. Arcuate pubic

for muscle contraction. Collections of muscle fibre bundles are surrounded by epimysium to form individual muscles. Epimysium, perimysium, and endomysium extend beyond the the muscle fibres to form rope like tendons, or sheet like aponeurosis, which connect the muscles to the pelvis and femur.

The behaviour of the musculotendon unit is often represented using a Hill type contraction model as shown in Figure 7.5 [96],

The development of passive tendon stiffness, PT and passive muscle stiffness, PM in tension can be treated as non-linear or linear as shown in Figures 7.6 and 7.7. The behaviour of the active muscle contraction element, AM can be treated as a function of muscle length, L^M and muscle activation, α as shown in Figure 7.7. α varies between zero and one, with complete muscle activation occurring at $\alpha = 1$.

Previous studies have attempted to predict muscle forces required to produce zero moment, and force equilibrium at the hip joint through force and endurance optimization criteria [94, 97–104]. Correlation with EMG (electromyography) data, and measured hip joint forces was found when muscle physiological cross-sectional area, $PCSA^M$ was used as a guide to peak muscle contractile force, F^M_{peak}, where $PSCA^M$ is given by:

$$PCSA^M = \frac{V^M}{L^M_{peak}} \tag{7.1}$$

where V^M is the volume of the muscle, and L^M_{peak} is the muscle fibre length corresponding to peak muscle contractile force.

Muscle contraction can be considered to be either isometric, where the

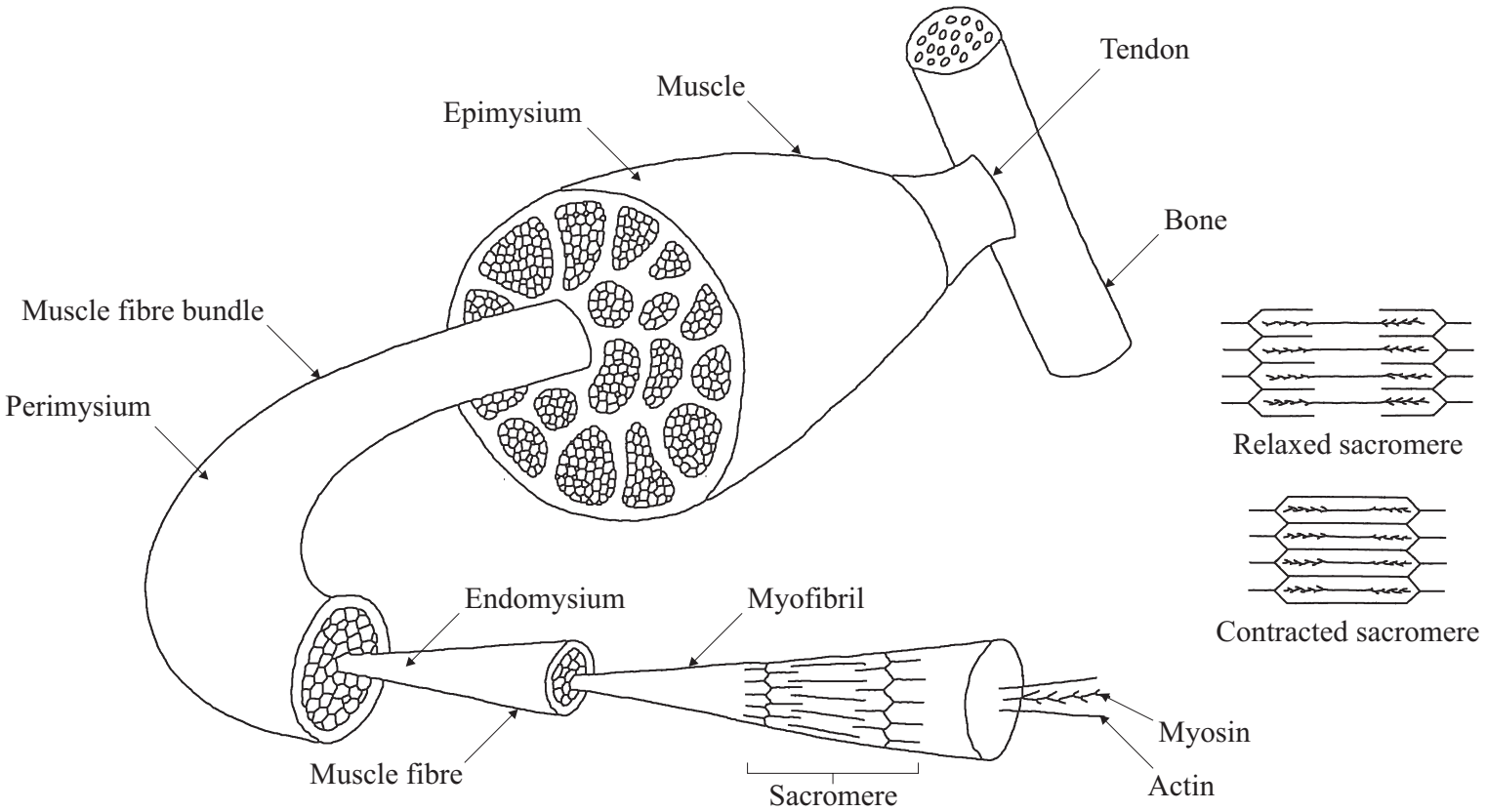

Figure 7.4: Muscle structure

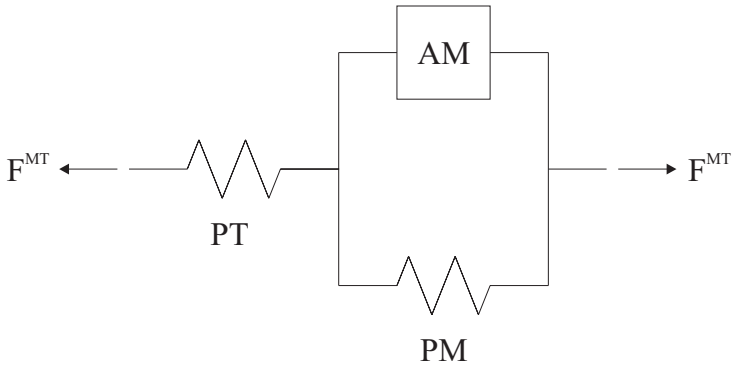

Figure 7.5: Hill type musculotendon contraction model, where F^{MT} is the force in the musculotendon unit, PT is the passive tendon stiffness, PM is the passive muscle stiffness, and AM is the active muscle contraction element.

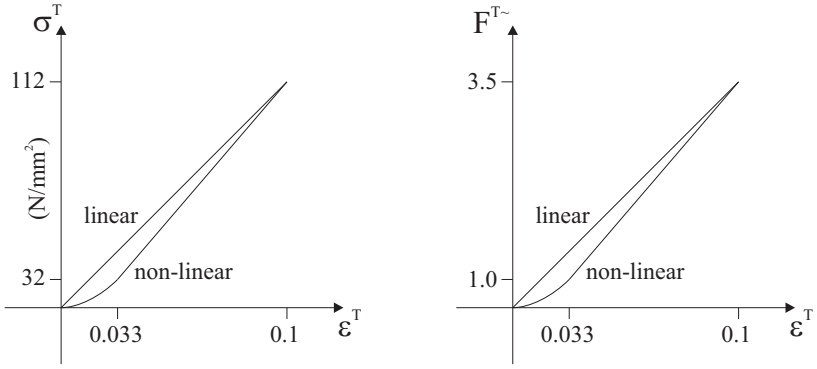

Figure 7.6: Passive tendon stiffness relationship, where ϵ^T is the tendon strain, σ^T is the tendon stress, and $F^{T\sim}$ is the normalised tendon force (F^T/F^M_{peak}) where F^T is the force in the tendon and F^M_{peak} is the peak muscle contraction force.

force in the muscle changes, but the length of the muscle remains the same; or isokinetic, where the force in the muscle remains the same, but the muscle shortens (concentric contraction) or lengthens (eccentric contraction).

In the finite element analyses presented here non-linear spring (connector) elements were to model muscular and ligamentous contributions based on the following assumptions:

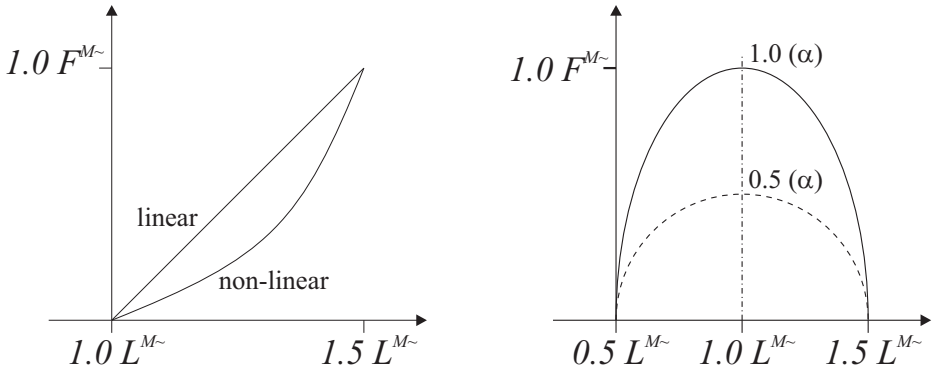

Figure 7.7: Passive and active muscle relationships, where $L^{M\sim}$ is the normalised muscle length (L^M/L^M_{peak}) where L^M is the muscle length and L^M_{peak} is the muscle fibre length corresponding to peak muscle contractile force; and $F^{M\sim}$ is the normalised muscle contractile force (F^M/F^M_{peak}) where F^M is the force in the muscle and F^M_{peak} is the peak muscle contractile force.

1. In the Hill type musculotendon contraction model it was assumed that muscle-lengthening as allowed by passive muscle stiffness, PM was equal to muscle-shortening as controlled by the the active contraction element, AM. This assumption seems reasonable for isometric muscle contraction.

2. The passive tendon stiffness, PT was assumed to be linear in tension and near zero in compression.

The finite element analyses presented here are static, with the muscles being modelled in a re-active, as opposed to active manner. The force developed in individual muscles is seen for some part, to be dependent on the direction of the force applied at the centre of the femoral head. Thus, forces are expected to develop in antagonistic as well as agonistic muscles.

The assumptions described above allow the behaviour of the musculotendon unit to be defined using:

1. L^T_{slack}, the tendon slack length.

2. F^M_{peak}, the peak muscle contractile force.

Based on Zajac [96] L^M_{peak} is taken to be equal to the average length of muscle fibres in a relaxed state following dissection [96, 97, 105–107]. Zajac [96] defines L^T_{slack} as:

$$L^{MT}_a = L^T_{slack} + L^M_{peak} \cos\beta \tag{7.2}$$

where L^{MT}_a is the length of the musculotendon unit between origin and insertion, close to the anatomic position and β is the muscle angle of pennation (the angle at which muscle fibres are orientated with respect to the tendon).

Hence the isometric (static) stiffness, k^{MT} of the musculotendon unit can be estimated as:

$$k^{MT} = \frac{F^T_{peak}}{\left(\frac{0.1}{3.5}\right) L^T_{slack}} \tag{7.3}$$

where (0.1/3.5) is seen to give the tendon strain at $F^{T\sim} = 1$, or $F^T = F^M_{peak}$ based on the linear passive tendon stiffness relationship shown in Fig. 7.6.

It can be seen from Equation 7.3 that k^{MT} increases as F^M_{peak} (based on $PSCA^M$) increases, and decreases as L^T_{slack} increases.

Delp [105] derived values for F^M_{peak}, L^M_{peak}, and β based on Wickiewicz et al. [106] Brand et al. [97], and Friederich and Brand [107]. In addition Delp derived values of L^T_{slack}. These values, and the values derived as part

of this study for L_a^{MT} and k^{MT} are given in Table 7.3. Delp split some muscles to give multiple lines of action (up to three) and properties for an individual muscle. In this study an automated process is described to derive multiple lines of action (above 100 for large muscles) and properties for each muscle. This process relies on single values of muscle properties for each area of muscle origination on the pelvis. Appropriate manipulation of the values reported by Delp has been carried out to allow this.

Table 7.1: Properties of the hip muscles

Muscle	F_{peak}^M (N)	L_{peak}^M (mm)	L_{slack}^T (mm)	β	L_a^{MT} (mm)	k^{MT} (N/mm)
Gluteus Maximus	1300	144	132	3°	276	344
Gluteus Medius	1365	68	61	9°	128	779
Gluteus Minimus	585	54	31	4°	85	660
Psoas	370	104	130	8°	233	100
Iliacus	430	100	90	7°	190	167
Rectus Femoris (SH)	390	84	346	5°	430	39
Rectus Femoris (RH)	390	84	346	5°	430	39
Tensor Fasciae Latae	155	95	425	3°	520	13
Sartorius	105	579	40	0	619	92
Pectineus	175	133	20	0	153	306
Semitendinosus	330	201	262	5°	462	44
Semimembranosus	1030	80	359	15°	436	100
Biceps Femoris (LH)	720	109	341	0	450	74
Adductor Magnus	1100	113	150	4°	263	257
Adductor Longus	420	138	110	6°	247	134
Adductor Brevis	285	133	20	0	153	499
Gracilis	110	352	140	3°	492	28
Piriformis	295	26	115	10°	141	90
Gemellus Superior	55	24	39	0	63	49
Gemellus Inferior	55	24	39	0	63	49
Quadratus Femoris	225	54	24	0	78	372

Note: The value of L_{slack}^T for the pectineus muscle was adjusted as the value proposed by Delp [105] was found to be inconsistent with the data recorded by Wickiewicz et al. [106] and Friederich and Brand [107].

7.4 Ligament behaviour

Experimental studies show the behaviour of ligaments to be similar to the behaviour of the tendinous part of the musculotendon unit [90,93,108]. Thus ligament stiffness was assumed to be linear in tension and near zero in compression. Ligament stiffness values, k^L were chosen based on Zheng et al. [93] and Dakin et al. [90], and are given in Table 7.4.

Table 7.2: Properties of the pelvic ring ligaments

Ligament	k^L (N/mm)
Sacroiliac ligament ring	5000
Sacrospinous	1500
Sacrotuberous	1500
Iliolumbar	1000
Inguinal	250
Superior pubic	1000
Arcuate pubic	1000

Note: the stiffness values for the anterior, interosseous, and posterior sacroiliac ligaments from Zheng et al. [93] were combined to give a single value for the sacroiliac ligament ring. Stiffness values of the iliolumbar and inguinal ligaments were based on comparison with other pelvic ring ligaments.

7.5 Defining muscle and ligament attachments on the pelvis

Having defined isometric stiffness values for the hip joint muscles a series of novel algorithms were used to define connector elements running from nodes within muscle origination areas on the pelvis to discrete points representing muscle insertions. Due to the fineness of the mesh it was possible to define the muscle origination areas with a good degree of accuracy. It was desirable to develop an automated process, as manual definition of individual connector elements would have been time consuming, and specific to the current model.

Data defining the external surface of the cortical bone, of the hemi pelvis was extracted using a *Python* script in *Abaqus/CAE* [72]. This data was then used as input for a *Matlab* script, which was in turn used to write a *Python* script capable of adding connector elements to a 3D pelvis model in *Abaqus/CAE* [72].

Muscle origination areas were defined using series of points in 3D space. Initial values for these points were taken from Dostal and Andrews [109] and refined visually, on the basis of attachment areas shown on the Interactive Hip CD [110].

7.5.1 Single reference point origination areas

Origination areas of some muscles were defined using a single point, and a radius of influence in 3D space. In order to do this the closest node on the surface mesh was found to the defined point, and the distance of all other

nodes from that node was calculated:

$$d_i^n = |[x_i \ y_i \ z_i] - [x_{ref} \ y_{ref} \ z_{ref}]| \tag{7.4}$$

where d_i^n is the distance from the reference node, n_{ref} with co-ordinates x_{ref}, y_{ref}, z_{ref} to node n_i with co-ordinates x_i, y_i, z_i.

Nodes with $d_i^n \leqslant r_{in}^n$, where r_{in}^n is the defined radius of influence were deemed to be within the origination area of the muscle. However it can be seen that for a complex 3D geometry such as the pelvis the use of Equation 7.4 alone could result in nodes on opposite sides of the surface mesh falling within the origination area (for example on the inner and outer surfaces of the ilium). In order to address this issue an algorithm was developed which excluded nodes, the average surface normal of which was greater than a given angle from the average surface normal of the reference node. The average surface normal for each node was calculated by first constructing a connectivity array for each node; listing element faces of which the node was a member.

The surface normal of each element face was calculated using the cross product of two of the vectors defining the sides of the element face:

$$\vec{N}_j^e = \vec{V}_{12}^e \times \vec{V}_{13}^e \tag{7.5}$$

where $\vec{N}_j^e$ is the surface normal of element face e_j, comprised on nodes n_1, n_2, and n_3. $\vec{V}_{12}^e$ is the vector going from n_1 to n_2 of the element face, and $\vec{V}_{13}^e$ is the vector going from n_1 to n_3 of the element face given by:

$$\vec{V}_{12}^{e} = [[x_2\ y_2\ z_2] - [x_1\ y_1\ z_1]] \quad \text{and} \quad \vec{V}_{12}^{e} = [[x_2\ y_2\ z_2] - [x_1\ y_1\ z_1]] \tag{7.6}$$

where (x_1, y_1, z_1) are the co-ordinates of n_1 of the element face, (x_2, y_2, z_2) are the co-ordinates of n_2 of the element face, and (x_3, y_3, z_3) are the co-ordinates of n_3 of the element face as shown in Figure 7.8:

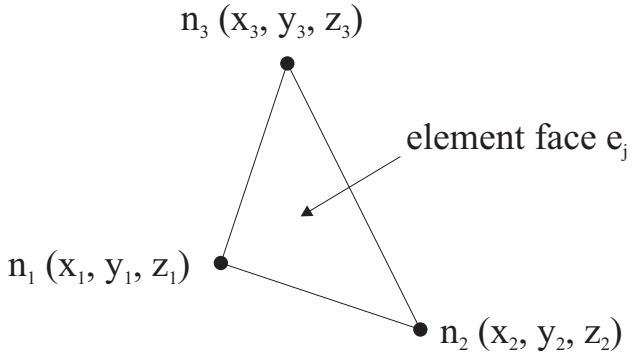

Figure 7.8: Node co-ordinates for a triangular element face

$\vec{N}_j^e$ can be given unit magnitude:

$$\vec{N}_j^{e\sim} = \frac{\vec{N}_j^e}{|\vec{N}_j^e|} \tag{7.7}$$

where $\vec{N}_j^{e\sim}$ is the unit surface normal of element face e_j. The average surface normal for a node can then be calculated:

$$\vec{N}_i^{n\sim} = \frac{1}{Q^i} \sum_{k=1}^{Q^i} (\vec{N}_{j=nc_k^i}^{e\sim}) \tag{7.8}$$

where $\vec{N}_i^{n\sim}$ is the unit average surface normal (unit node normal) for node

n_i, nc^i_k is the kth member of the node connectivity array, nc^i for node n_i, and Q^i is the number of entries in the connectivity array for node n_i.

The angle of a node normal from the reference node normal can then be calculated using the dot product:

$$\theta_i = |\arccos(\vec{N}^{n\sim}_{ref} \cdot \vec{N}^{n\sim}_i)| \tag{7.9}$$

where θ_i is the angle between the node normals, $\vec{N}^{n\sim}_{ref}$ is the unit node normal for the reference node n_{ref} and $\vec{N}^{n\sim}_i$ is the unit node normal for node n_i. Hence it can be seen that if $d^n_i \leqslant r^n_{in}$ and $\theta_i \leqslant \theta_{max}$, where θ_{max} is the maximum allowable angle between node normals (taken as $\pi/2$) then node n_i is taken to have a connection element attached to it.

7.5.2 Multiple reference point origination areas

Origination areas of several of the muscles were defined using a series of points, and three radii of influence in 3D space. Similar to an origination area defined using a single point, the closest node to each defined point in the series was established. r^{in}_l, r^{in}_s, and r^{in}_f are the radii of influence around the line running between the reference nodes, the starting node, and the finishing node as shown in Figure 7.9.

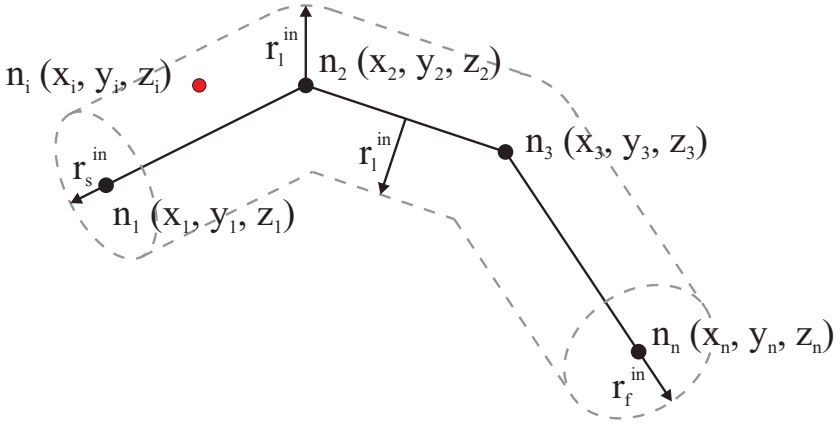

Figure 7.9: Nodes and radii of influence used to define the origination area

Based on Fig. 7.9 vectors $\vec{V}_{12}$, $\vec{V}_{1i}$, $\vec{V}_{21}$, $\vec{V}_{2i}$ are derived:

$$\vec{V}_{12} = [x_2\ y_2\ z_2] - [x_1\ y_1\ z_1]; \quad \vec{V}_{1i} = [x_i\ y_i\ z_i] - [x_1\ y_1\ z_1]$$
$$\vec{V}_{21} = [x_1\ y_1\ z_1] - [x_2\ y_2\ z_2]; \quad \vec{V}_{2i} = [x_i\ y_i\ z_i] - [x_2\ y_2\ z_2] \qquad (7.10)$$

where (x_1, y_1, z_1) and (x_2, y_2, z_2) are the co-ordinates of the 1st (n_1) and 2nd (n_2) nodes on the line, and (x_i, y_i, z_i) are the co-ordinates of node n_i.

It can be seen that if $d_i \leqslant r_l^{in}$ and $\theta_i \leqslant \theta_{max}$ with respect to any of the reference nodes forming the line (with the exception of the start and finish nodes) then node n_i is taken to have a connection element attached to it.

In addition it can be shown that node n_i can form a perpendicular with the section of line running between the 1st and 2nd reference nodes if:

$$\theta_{1i} = \left| \frac{\arccos(\vec{V}_{12} \cdot \vec{V}_{1i})}{|\vec{V}_{12}||\vec{V}_{1i}|} \right| \leqslant \frac{\pi}{2} \quad \text{and} \quad \theta_{2i} = \left| \frac{\arccos(\vec{V}_{21} \cdot \vec{V}_{2i})}{|\vec{V}_{21}||\vec{V}_{2i}|} \right| \leqslant \frac{\pi}{2} \tag{7.11}$$

where θ_{1i} is the angle between vectors $\vec{V}_{12}$ and $\vec{V}_{1i}$, and θ_{2i} is the angle between vectors $\vec{V}_{21}$ and $\vec{V}_{2i}$.

Figure 7.10 shows a condition when node n_i can form a perpendicular with the section of line. Figure 7.10 shows a condition when node n_i cannot form a perpendicular with the section of line.

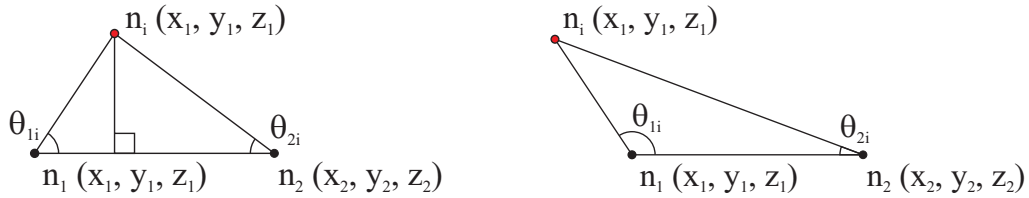

Figure 7.10: Conditions allowing and preventing a perpendicular from being formed between node n_i and the section of line

If the conditions given in Equation 7.11 are satisfied then the perpendicular distance of node n_i from the section of the line is be calculated as:

$$d_i^l = |\vec{V}_{1i}| \sin\theta_{1i} \quad \text{or} \quad |\vec{V}_{2i}| \sin\theta_{2i} \tag{7.12}$$

where d_i^l is the perpendicular distance from the section of line between the 1st and 2nd reference nodes to node n_i.

It can be seen that for the section of line between the 1st and 2nd reference nodes, if θ_{1i} and $\theta_{2i} \leqslant \pi/2$, and $d_i^l \leqslant r_l^{in}$, and $\theta_i \leqslant \theta_{max}$ then node n_i is taken

to have a connection element attached to it. This process can be repeated for each section of the line.

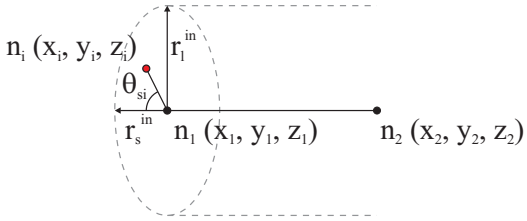

Figure 7.11: r_s^{in}, r_l^{in}, and θ_{si} used to define the origination area around the starting node of the line

In order to allow greater manipulation of the shape of the origination area separate radii of influence (r_s^{in} and r_f^{in}) were assigned to the start and finish nodes forming the line. This allowed the ends of the tube of influence around the line to be started and finished using a smartie shaped disc. Looking at Figure 7.11 it is seen that the angle θ_{si} is given by the dot product:

$$\theta_{si} = \left| \frac{\arccos(\vec{V}_{21} \cdot \vec{V}_{1i})}{|\vec{V}_{21}||\vec{V}_{1i}|} \right| = \pi - \theta_{1i} \tag{7.13}$$

If $\theta_{si} \leqslant \pi/2$, and $\theta_i \leqslant \theta_{max}$ then node n_i is taken to have a connection element attached to it provided all of the following conditions are true:

$$|\vec{V}_{1i}| \cos\theta_{si} \leqslant r_s^{in} \cos\theta_{si} \tag{7.14}$$

$$|\vec{V}_{1i}| \sin\theta_{si} \leqslant r_l^{in} \sin\theta_{si} \tag{7.15}$$

$$|\vec{V}_{1i}| \leqslant |[(r_s^{in} \cos\theta_{si})\ (r_l^{in} \sin\theta_{si})]| \tag{7.16}$$

This process can be repeated for the finishing node of the line.

Thus it can be seen that a series of algorithms have been developed that allow nodes with connector elements attached to them to be defined in an automated manner for each muscle, based on a series of points and radii of influence in 3D space.

7.5.3 Connector element stiffness properties

The properties of each connection element must also be defined. Stiffness properties in tension were apportioned to each connector element using:

$$k^{CE} = k_{MT} \left(\frac{A^{CE}}{A^{MT}} \right) \tag{7.17}$$

where k^{CE} and A^{CE} are the stiffness, and associated surface area of the connector element, and k^{MT} and A^{MT} are the stiffness (defined previously) and associated surface area of the musculotendon unit.

The surface area associated with each node of the mesh was defined as:

$$A_i^n = \frac{1}{Q^i} \sum_{k=1}^{Q^i} (A^e_{j=nc_k^i}) \tag{7.18}$$

where A_i^n is the surface area associated with node n_i, nc_k^i is kth member of the node connectivity array, nc^i for node n_i, Q^i is the number of entries in the connectivity array for node n_i, and A_j^e is the surface area of element face e_j calculated:

$$A_j^e = \frac{1}{2}|\vec{V}_{12}^e||\vec{V}_{13}^e| \sin \left| \frac{\arccos\left(\vec{V}_{12}^e \cdot \vec{V}_{13}^e\right)}{|\vec{V}_{12}^e||\vec{V}_{13}^e|} \right| \tag{7.19}$$

Origination areas, and properties of the connector elements representing the pelvic ring ligaments were defined using the same techniques used to define the the hip joint muscles.

Thus a series of protocols have been developed allowing the inclusion of muscles and ligaments as non-linear connector elements in an isometric 3D finite element model of the complete pelvis. The implementation and verification of the presented method of including muscular and ligamentous contributions is discussed in the subsequent chapter.

8

3D models of the pelvis and acetabular construct

Previous chapters presented 2D plane-strain models of the acetabular construct following revision hip arthroplasty, and 3D models of the hemi pelvis following primary, and revision arthroplasty. The 2D models were shown to be of use in indicative studies, examining the rotation and migration of the

acetabular cup, within the bone graft bed following revision hip arthroplasty. The 3D hemi pelvis models were shown to provide qualitatively similar results to those observed in clinical studies. Different activities were demonstrated to result in different patterns of rotation and migration of the acetabular cup, within the bone graft bed. In both sets of analyses described above, only part of the pelvis was modelled, and fixed boundary conditions were assumed. It is desirable to develop a model of the pelvis, with boundary conditions more representative of those found *in vivo* to assess what effect this has on the observed stress transfer paths, compared to fixed boundary condition models.

This chapter presents the development of a model of the complete pelvis, in which muscular and ligamentous contributions are included, as non-linear spring (connector) elements as discussed in Chapter 7, providing pseudo-realistic boundary conditions. This represents a significant improvement on models developed in previous studies of the pelvis [11, 19, 20, 22, 24–27, 29–31, 33, 34].

For comparison, complete models of the pelvis, using boundary conditions similar to those used in previous studies [19, 20, 22, 24, 25], and in the 3D models of the hemi pelvis presented as part of this study are developed in the first instance. Results are presented for one load case, representative of single leg stance.

8.1 Analysis of the pelvis, following primary arthroplasty on both sides, excluding muscular and ligamentous contributions (PAEXML model)

8.1.1 Geometric definition

The geometry of the complete pelvis model, following primary arthroplasty on both sides was based on the model of the hemi pelvis, following primary hip arthroplasty. A copy of the model was made, and mirrored in the $y-z$ plane. The two hemi pelvis models were then positioned with a gap of around 2.5 mm at the pubic-symphysis. Due to restrictions on the available computing resources, it was necessary to modify the meshing of the complete pelvis model, in comparison to that used for the hemi pelvis models. Thus four noded tetrahedral elements, with an average edge length of 5 mm were used to mesh the trabecular bone on both sides of the pelvis. Three noded shell elements, with a thickness of 2 mm, and an average edge length of 5 mm were used to mesh the cortical bone on both sides of the pelvis.

The inter-pubic disc was represented using connector elements with a high value of stiffness in compression, and a near zero value in tension. The superior and arcuate pubic ligaments were represented using connector elements with values of stiffness in tension taken from Chapter 7, and a near zero value in compression. Figure 8.1 shows a frontal view of the cortical bone mesh (2×9352 elements) including the connector elements used to represent

the inter-pubic disc and pubic ligaments. The model was constrained at the sacro-iliac joints, as shown in Figure 8.1. Loading was applied at the centre of near rigid femoral heads. Smooth sliding surface interactions were used between the femoral heads, and the acetabular cups.

8.1.2 Materials definition

Trabecular bone, cortical bone, bone cement, the plastic acetabular cups, and the metal femoral heads were defined as isotropic linear elastic materials. The values of Young's modulus, E and Poisson's ratio, μ used for the different materials, were those given in Chapter 5, Table 5.2.

8.1.3 Loading definition

The model of the complete pelvis, excluding muscular and ligamentous contributions, was subjected to a 3D load history, representative of a single leg stance (with the patient standing on their left leg), with the resultant forces R_L and R_R acting at the centres of the patient's left and right hand side femoral heads. The x, y, z directions were those for the 3D hemi pelvis models presented in Chapter 6. Table 8.1 gives the resultant force values applied during single leg stance. Monotonic loading was applied up to the values given in Table 8.1, with all results presented at that stage.

Table 8.1: Values of the resultant force on both legs for single leg stance

Force	R_{Lx}	R_{Ly}	R_{Lz}	R_L	R_{Rx}	R_{Ry}	R_{Rz}	R_R
(N)	300	142	2292	2316	-133	-85	244	291

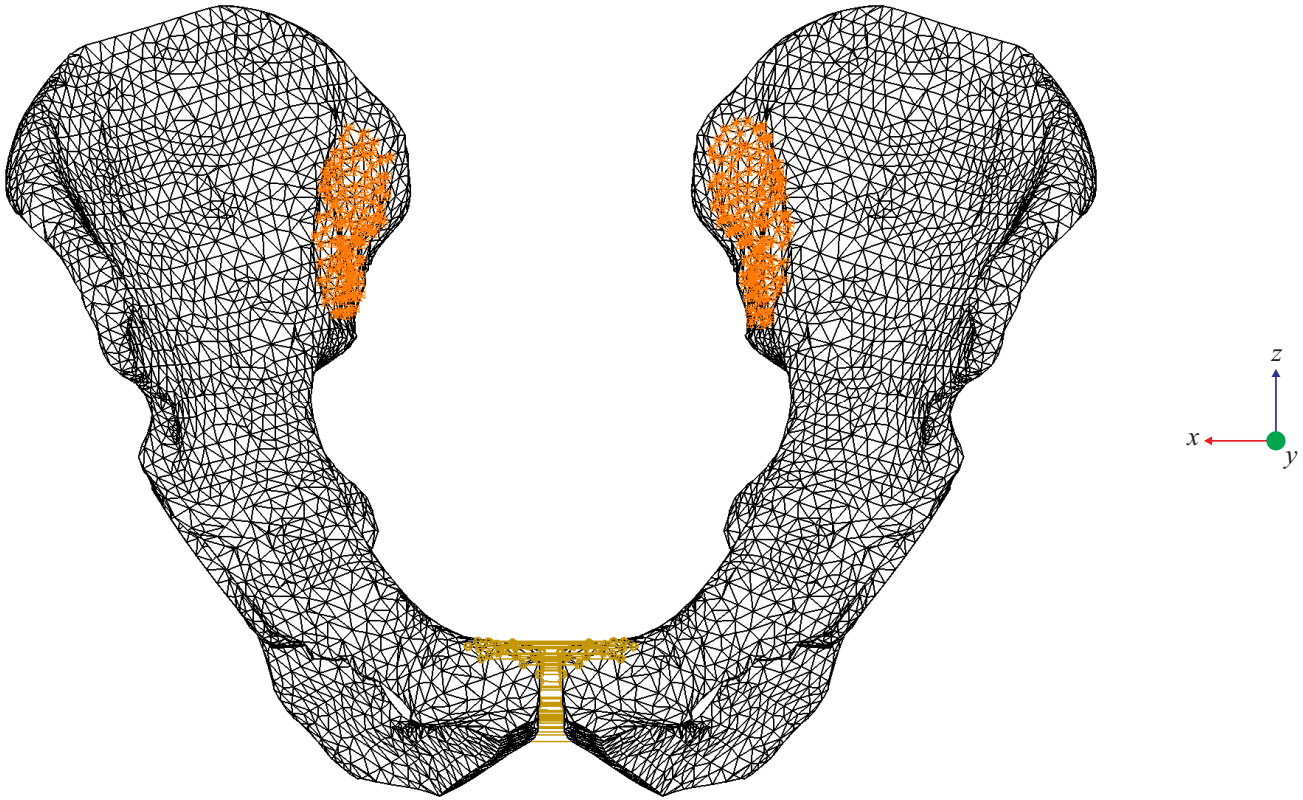

Figure 8.1: 3D mesh of the cortical bone, including connector elements representing the inter-pubic disc and ligaments; constrained boundary conditions at the sacro-iliac joints are also shown.

8.1.4 Results and discussion

Figure 8.2 shows a frontal view, of the von Mises stresses found in the cortical bone, for the PAEXML model of the pelvis, subjected to a single leg stance load case. It is observed that on both sides of the pelvis there are stress concentrations close to the constrained boundary conditions at the sacro-iliac joints. As expected the von Mises stresses in the left hemi pelvis are greater than those in the right hemi pelvis, with higher loading being applied to the left femoral head, than the right femoral head. Figure 8.3 shows the von Mises stress in the cortical bone of the patient's left hemi pelvis, at two views similar to those used for the hemi pelvis model described in Chapter 6. Comparing the stresses shown in Figure 8.3 with those found for the model of the hemi pelvis, following primary arthroplasty (Chapter 6, Figure 6.6) in which constrained boundary conditions were applied at the sacro-iliac joint, and the pubic symphysis, it is observed that there are increased stress concentrations towards the sacro-iliac joint, and a reduction in stress concentrations towards the pubic symphysis. In addition there is an increase in the regions of the ilium, either side of central column of the iliac bone, affected by von Mises stresses. It is evident that the change in boundary conditions, even for the complete pelvis model, excluding muscular and ligamentous contributions, results in somewhat altered stress distributions, in particular at the pubic-symphysis, in comparison to the hemi pelvis model. The magnitude of the stresses given by the two models is similar.

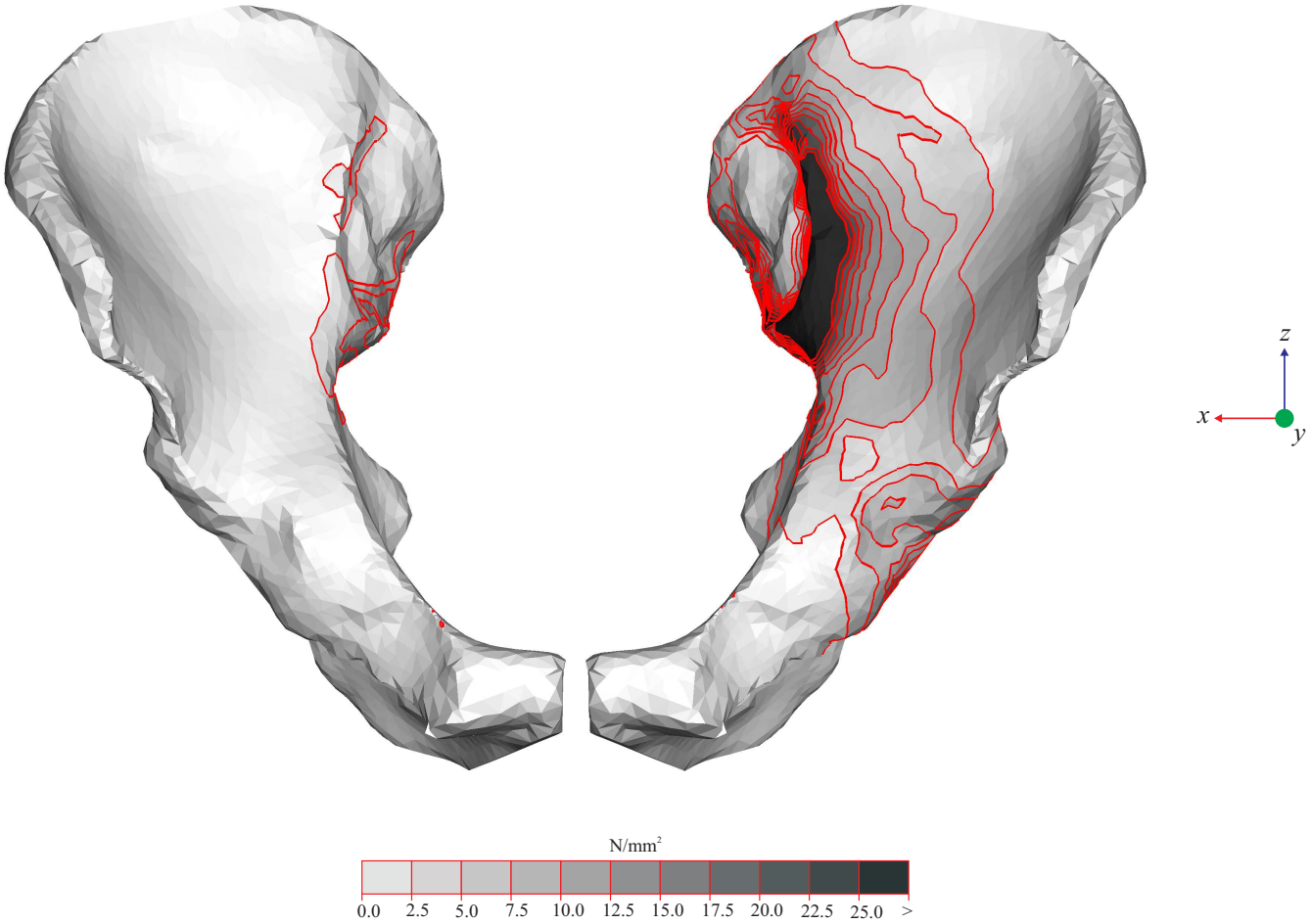

Figure 8.2: von Mises stresses in the cortical bone of the pelvis, following primary arthroplasty on both sides, due to a single leg stance load case, excluding muscular and ligamentous contributions

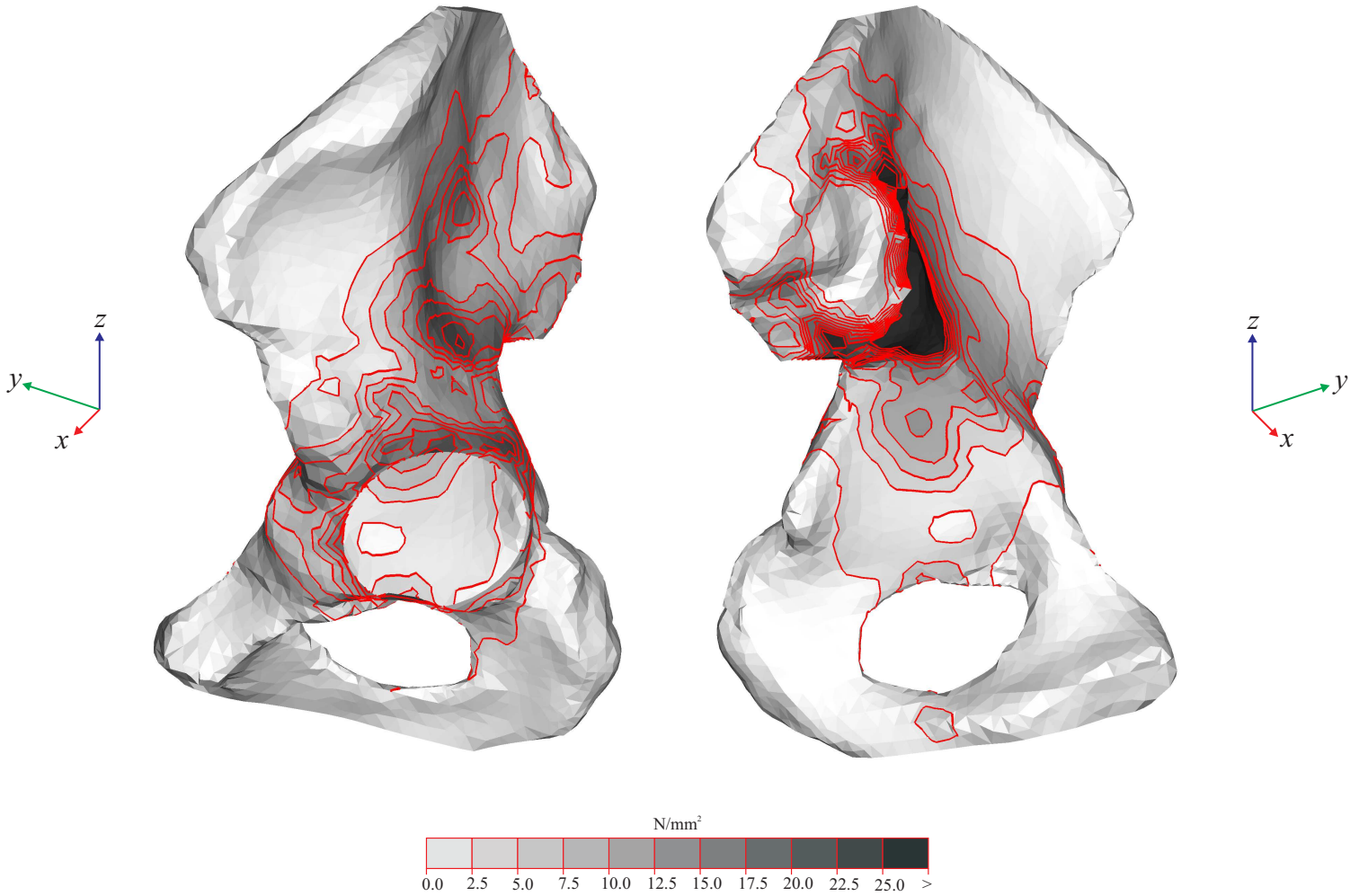

Figure 8.3: von Mises stresses in the cortical bone of left hemi pelvis, following primary arthroplasty on both sides, due to a single leg stance load case, excluding muscular and ligamentous contributions

Figure 8.4 shows a frontal view, of the von Mises stress found in the trabecular bone, for the PAEXML model of the pelvis. It is observed that on both sides of the pelvis stress concentrations are seen at the sacro-iliac joint, and acetabulum. Similar to the stresses found in the cortical bone, the stresses in the trabecular bone, in the left hemi pelvis are greater than those in the right hemi pelvis. Figure 8.5 shows the von Mises stress in the trabecular bone of the patient's left hemi pelvis. Comparing the stresses shown in Figure 8.5 with those found for the model of the hemi pelvis, following primary arthroplasty (Chapter 6, Figure 6.7) trends similar to those observed in the cortical bone are found. Increases in stress concentrations towards the sacro-iliac joint are observed, while reductions in stress concentrations towards the pubic symphysis are also observed. In addition there is an increase in stress concentrations at the superior edge of the acetabulum. These trends can be attributed to the removal of constrained boundary conditions at the pubic symphysis in the complete pelvis model.

It is observed that altering the boundary conditions at the pubic symphysis, between the hemi pelvis and complete pelvis models, affects the stress distributions within the trabecular and cortical bone, although the range of stresses are similar. The boundary conditions applied to the hemi pelvis model cause it to behave in a similar fashion to a fixed beam, supported at each end (the pubic-symphysis and sacro-iliac joint), while the boundary conditions applied to the complete pelvis model, cause each half of the pelvis to behave in a similar fashion to a cantilever beam, supported at one end (the sacro-iliac joint).

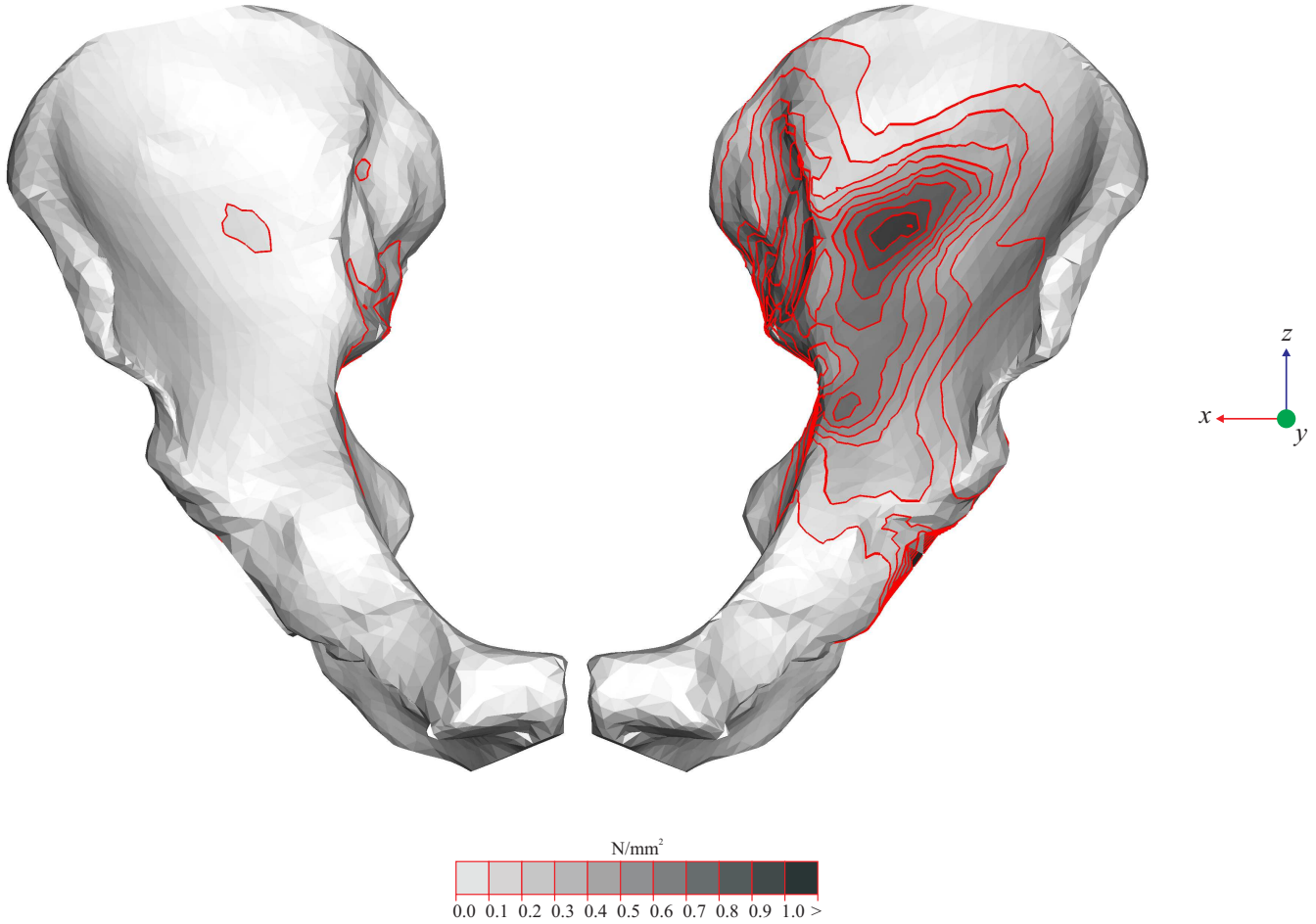

Figure 8.4: von Mises stresses in the trabecular bone of the pelvis, following primary arthroplasty on both sides, due to a single leg stance load case, excluding muscular and ligamentous contributions

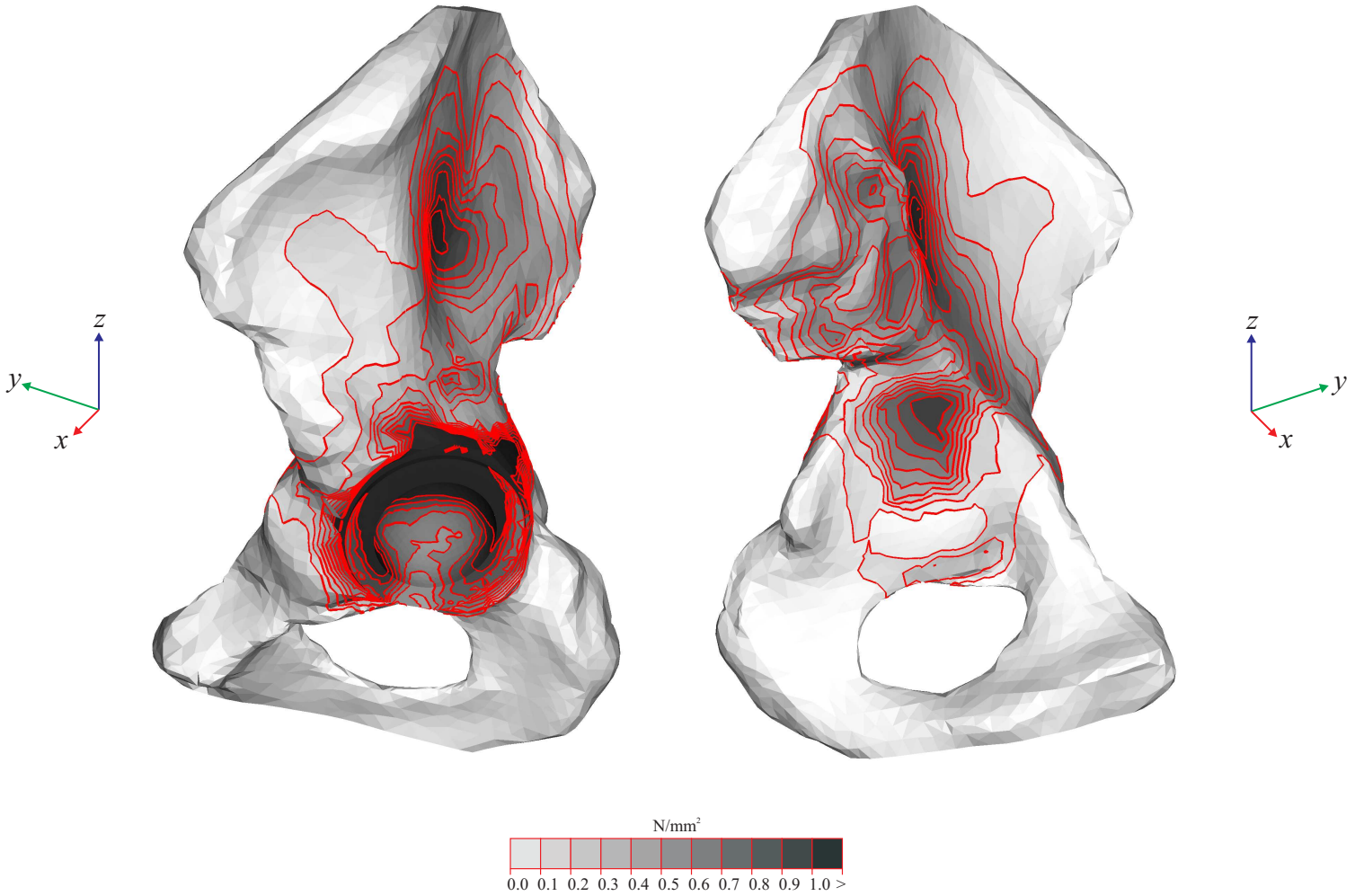

Figure 8.5: von Mises stresses in the trabecular bone of left hemi pelvis, following primary arthroplasty on both sides, due to a single leg stance load case, excluding muscular and ligamentous contributions

8.2 Analysis of the pelvis, following primary, and revision arthroplasty on the right and left sides, excluding muscular and ligamentous contributions (RAEXML model)

8.2.1 Model definition

The geometry of the complete pelvis model, following primary and revision arthroplasty, on the right and left sides, was defined in a similar way to the geometry of the pelvis, following primary arthroplasty on both sides. A copy of the hemi pelvis model, following primary arthroplasty was made, and mirrored in the $y - z$ plane. This was then used, with a copy of the hemi pelvis model, following revision hip arthroplasty to produce the complete pelvis model. The two hemi pelvis models were positioned with a gap of around 2.5 mm at the pubic symphysis. As for the complete pelvis model, following primary arthroplasty on both sides, restrictions on the available computing resources, meant it was necessary to modify the meshing of the complete pelvis model, in comparison to the hemi pelvis models. As before four noded tetrahedral elements, with an average edge length of 5 mm were used to mesh the trabecular bone on both sides of the pelvis. Three noded shell elements, with a thickness of 2 mm, and an average edge length of 5 mm were used to mesh the cortical bone on both sides of the pelvis. Other geometric details and boundary conditions were as per the PAEXML model

of the pelvis.

Cortical bone, trabecular bone, bone cement, the plastic acetabular cups, and the metal femoral heads were defined as isotropic linear elastic materials using the values given in Chapter 5, Table 5.2. The bone graft was defined as an isotropic non-linear elasto-plastic material, as was the case for the hemi pelvis model, following revision hip arthroplasty.

The use of additional elastic elements, with a low value of Young's modulus, layered over the bone graft elements, in order to provide numerical stability was described in Chapter 5, and utilised in the 2D plane-strain model of the acetabular construct, and the 3D model of the hemi pelvis, following revision hip arthroplasty. It was found that due to issues relating to loss of the interface between bone graft, and cortical bone, at the unconfined edges of the bone graft bed, due to the use of shell elements, as opposed to solid elements to model cortical bone, it was necessary to increase the Young's modulus of the additional elastic elements to around 50% of the lowest value taken for bone graft. In tests conducted on the hemi pelvis model, this was found to affect the extent of migration, and rotation of the acetabular cup. However it was not found to affect the direction of migration or rotation, and also was not found to affect the stress distribution within the bone graft, and other materials.

The pelvis model, following primary and revision arthroplasty, on the right and left hand sides was subjected to a single leg stance load case, using the values of resultant force given in Table 8.1.

8.2.2 Results and discussion

Figure 8.6 shows a frontal view, of the von Mises stresses found the cortical bone, for the RAEXML model of the pelvis, subjected to a single leg stance load case. Comparing the stresses to those found in the cortical bone, for the model of the pelvis, following primary arthroplasty on both sides (Figure 8.2), it is observed that the stress distribution is almost identical. Figure 8.7 shows the von Mises stresses in the cortical bone of the patient's left hemi pelvis (revision arthroplasty). It is observed that compared to the model of the pelvis, following primary arthroplasty on both sides (Figure 8.3), there is an increase in stress concentrations at the superior edge of the acetabulum. This was also observed in Chapter 6 when comparing the models of the hemi pelvis following primary, and revision arthroplasty.

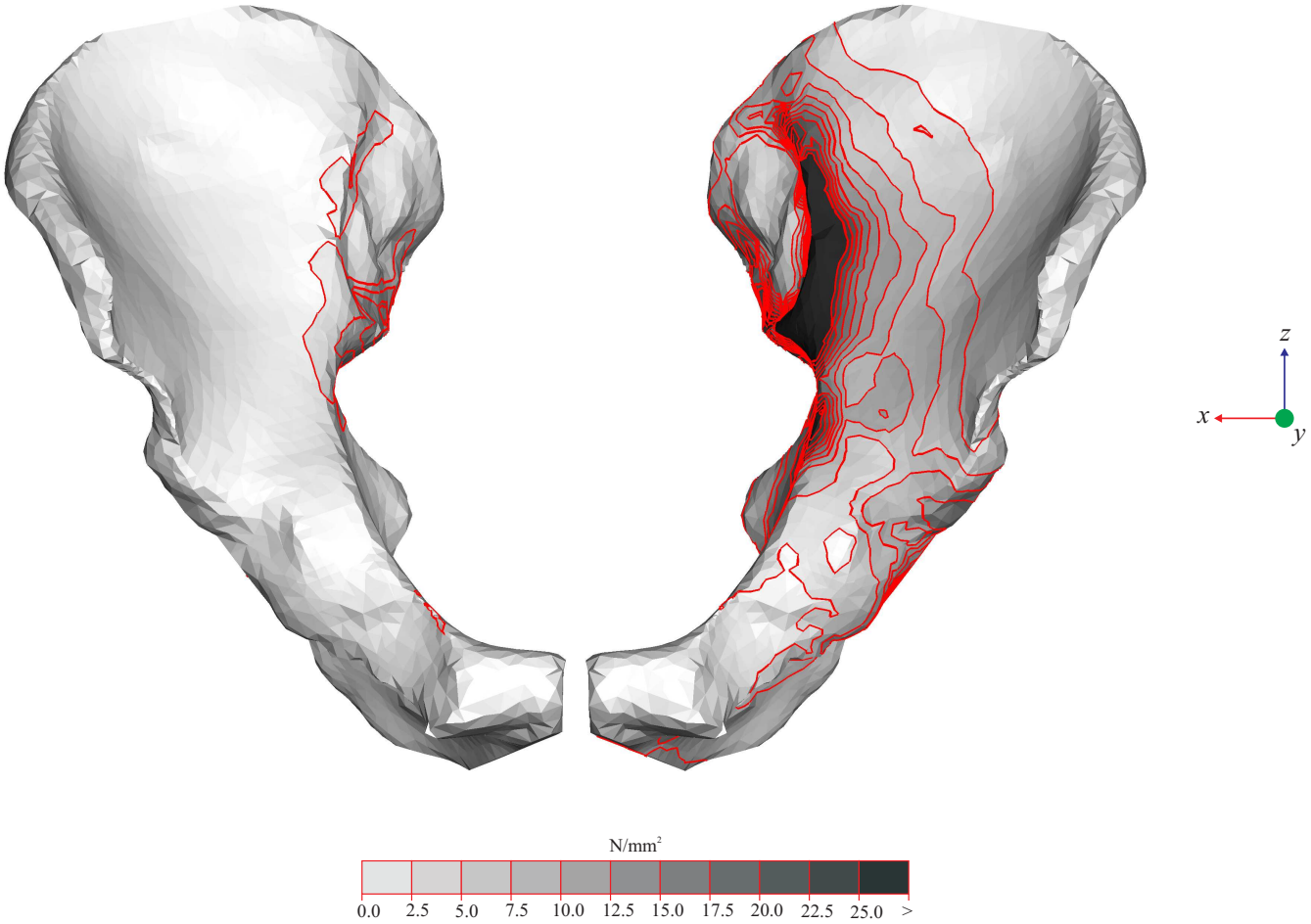

Figure 8.6: von Mises stresses in the cortical bone of the pelvis, following primary and revision arthroplasty, on the right and left hand sides, due to a single leg stance load case, excluding muscular and ligamentous contributions

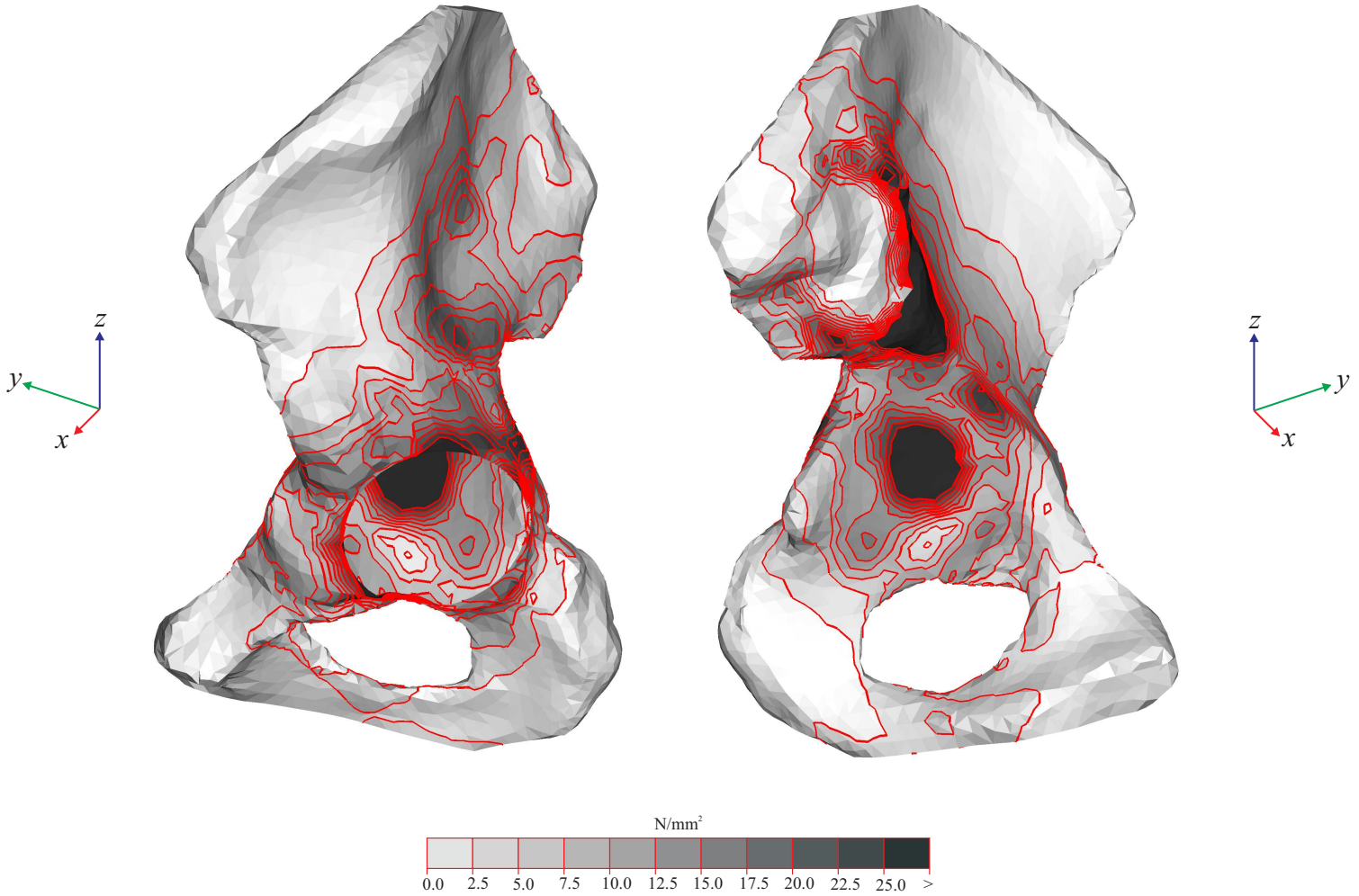

Figure 8.7: von Mises stresses in the cortical bone of left hemi pelvis, following primary and revision arthroplasty, on the right and left hand sides, due to a single leg stance load case, excluding muscular and ligamentous contributions

Figure 8.8 shows a frontal view, of the von Mises stresses found in the trabecular bone, for the RAEXML model of the pelvis. As for the model of the pelvis, following primary arthroplasty on both sides, it is observed that on both sides of the pelvis three are stress concentrations at the sacro-iliac joint, and the acetabulum. In comparison to the stresses found for the model of the pelvis, following primary arthroplasty on both sides (Figure 8.4), there is a significant increase in the extents of stress concentrations superior to, and at the rear of the acetabulum. The increase is larger than that found between the hemi pelvis models, following primary and revision arthroplasty (Chapter 6, Figures 6.7 and 6.15). It is thought that this is in some part due to the use of shell elements, as opposed to solid elements to represent the cortical bone, as stress transfer between the bone graft and cortical bone, in the plane of the shell elements was not possible.

It is found that as for the hemi pelvis models of primary, and revision hip arthroplasty the stresses in the cortical bone are similar between the model of the pelvis, following primary arthroplasty on both sides, and the model of the pelvis, following primary and revision arthroplasty, on the right and left sides. Changes in the distribution of stresses in the trabecular bone are observed, as was the case for the hemi pelvis models. In addition to the results shown here, the stresses in the bone graft were also investigated. These were found to be near identical to those found using the model of the hemi pelvis, following revision arthroplasty, and hence are not repeated here.

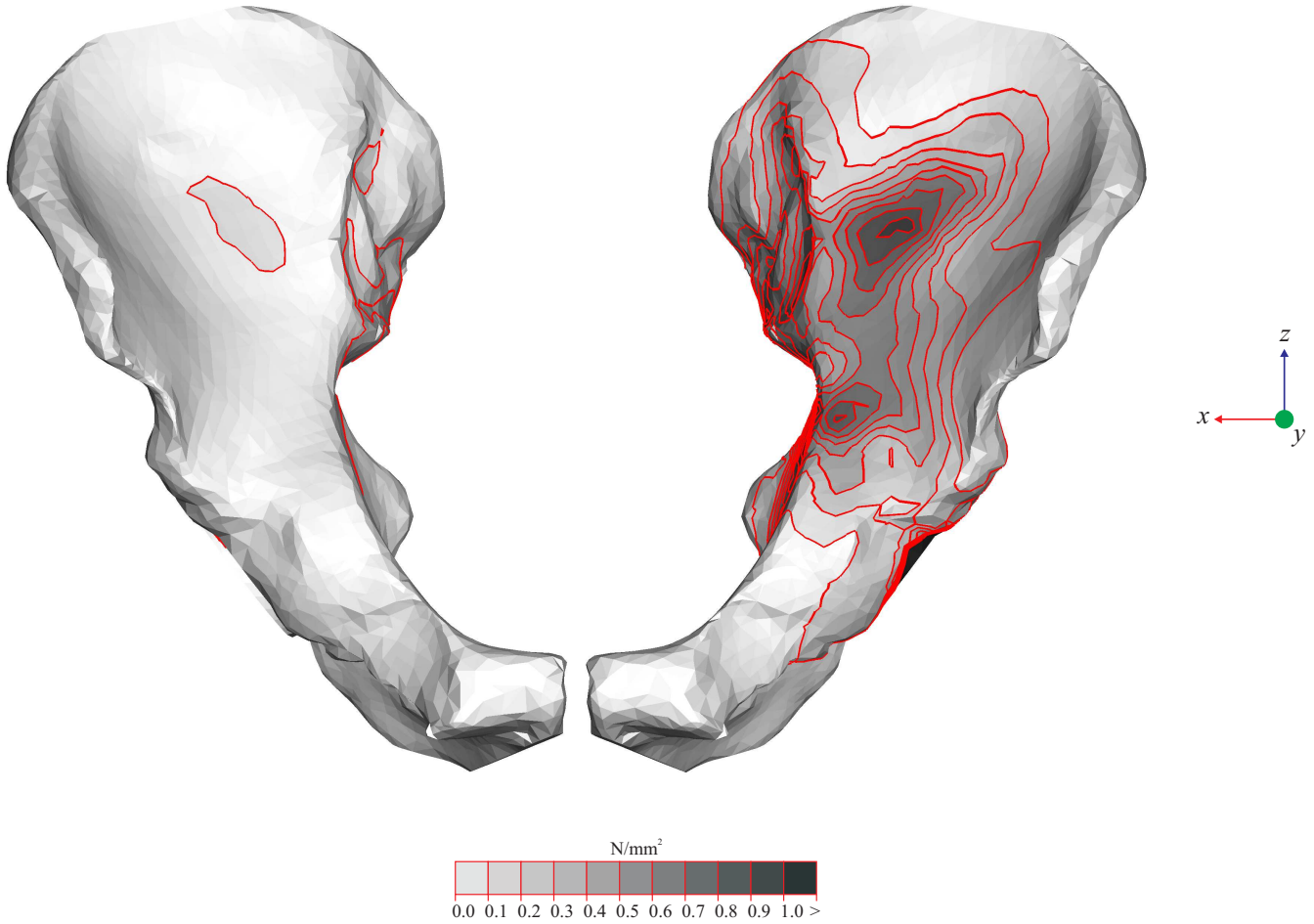

Figure 8.8: von Mises stresses in the trabecular bone of the pelvis, following primary and revision arthroplasty, on the right and left hand sides, due to a single leg stance load case, excluding muscular and ligamentous contributions

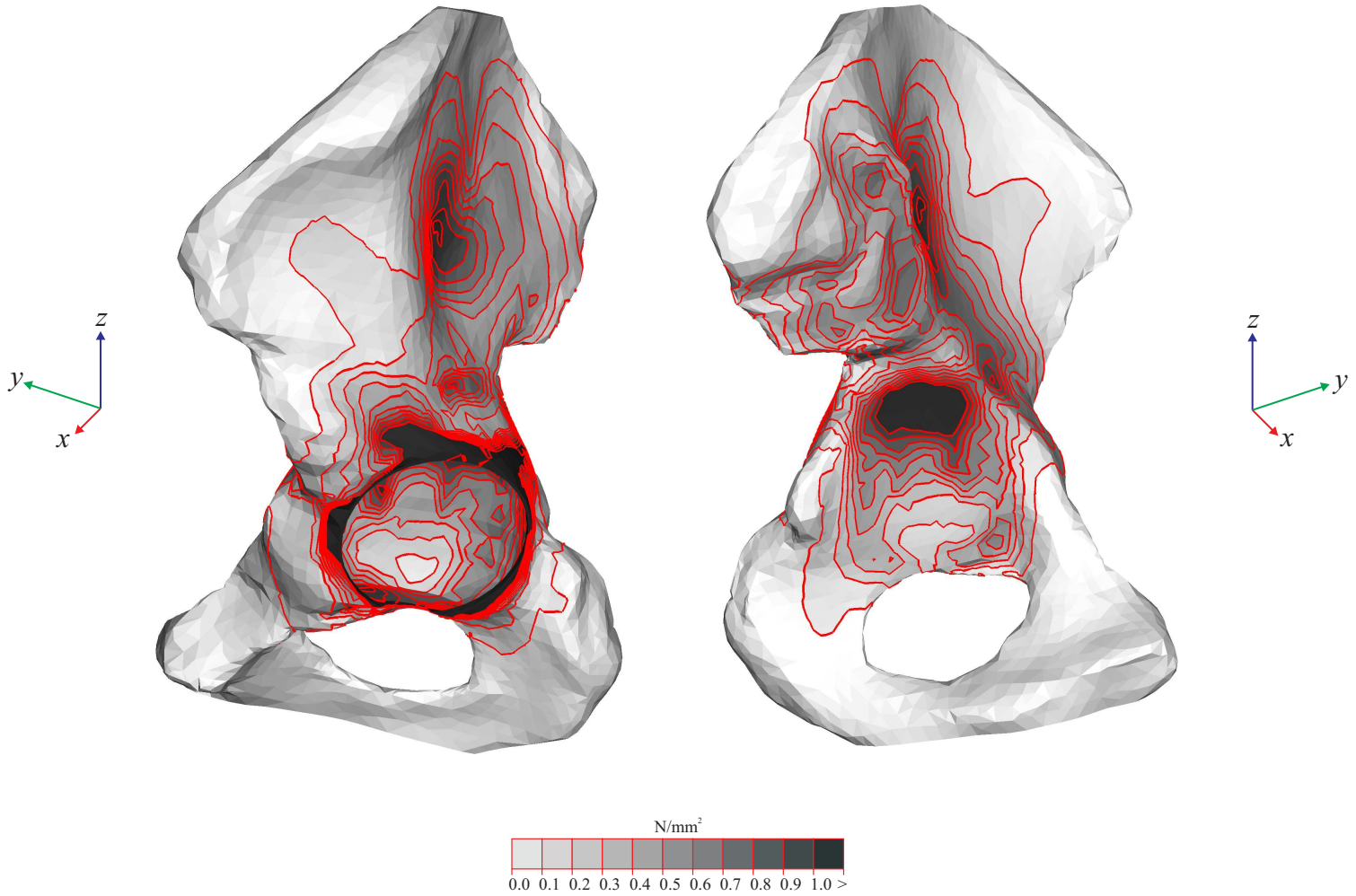

Figure 8.9: von Mises stresses in the trabecular bone of left hemi pelvis, following primary and revision arthroplasty, on the right and left hand sides, due to a single leg stance load case, excluding muscular and ligamentous contributions

8.3 Analysis of the pelvis, following primary arthroplasty on both sides, including muscular and ligamentous contributions (PAINCML model)

8.3.1 Model definition

The geometry, and materials definition of the PAINCML pelvis model, was the same as for the PAEXML pelvis model, with notable alterations made as detailed below.

A total of 42 muscles (21 on each hemi pelvis), and 7 ligaments were added to the complete pelvis model as non-linear spring (connector) elements using the process described in Chapter 7. Stiffness values of the muscles and ligaments in tension were taken as those given in the above chapter. The stiffness value of muscles and ligaments in compression was assumed to be close to zero. In addition near rigid connector elements were used to form a structure taken to be representative of the sacrum and the lumbar spine. The angle from horizontal, of the L5S1 disc in this structure was set to 45°.

Particular aspects that should be noted with regard to the modelling of the muscles are as follows: The insertion points (termination points for muscles originating on the pelvis) of the muscles on the femoral side, were defined based on Dostal and Andrews [109], for the anatomic position. Fixed constraints were applied at the insertion points. 20 muscles were defined, using multiple lines of action originating on the cortical bone of each hemi pelvis.

The psoas muscle was defined using a single connector element, running from a point on the sacro-lumbar structure, mentioned earlier, to a point in 3D space, representing the turning point of the iliopsoas muscle, at the edge of the iliac fossa. The multiple lines of action of the iliacus muscle, were also connected to this point. The iliopsoas muscle was defined using a single connector element, running from this point, to the insertion point on the femoral side. In addition, connector elements with significant stiffness in compression, and a value close to zero in tension were used to allow the transfer of force from the iliopsoas muscle back to the cortical bone of the pelvis. These ran from the turning point of the iliopsoas muscle, to an area around the anterior inferior iliac spine. With regard to the gluteus maximus muscle 50% of its stiffness was attributed to the connector elements originating on the cortical bone of each hemi pelvis. The remaining 50% of the stiffness was attributed to a single connector element running from a point on the rigid sacro-lumbar structure, to the gluteus maximus insertion point. With regard to the piriformis muscle 20% of its stiffness was attributed to the connector elements originating on the cortical bone of each hemi pelvis. The remaining 80% of its stiffness was attributed to a single connector element running from a point on the sacro-lumbar structure, to the piriformis insertion point.

Particular aspects that should be noted with regard to modelling of the ligaments are as follows: The superior pubic, and arcuate pubic ligaments were modelled as extending across the pubic-symphysis between the two halves of the pelvis. The inguinal ligament on each hemi pelvis was represented by two areas of multiple lines of action, extending to a reference point in 3D space equidistant to the central points of these two areas. The sacroiliac ligament ring, as discussed in the previous chapter, the sacrospinous ligament, the sacrotuberous ligaments, and the iliolumbar ligaments were rep-

resented by multiple lines of action, extending from the cortical bone of each hemi pelvis, to points on the sacro-lumbar structure. The stiffness of the sacrotuberous ligament was split 20:80% between the superior, and inferior parts. The stiffness of the iliolumbar ligament was split 50:50% between the superior, and inferior parts.

In addition to the connector elements used to model the muscles, and ligaments, connector elements, with significant stiffness in compression, and a value close to zero in tension were used. These were used in two areas. The first area was in modelling the interaction of the auricular surfaces of the sacro-iliac joints, with the sacro-lumbar structure. The second area was in modelling the pubic disc at the pubic-symphysis. Constraints applied at the sacro-iliac joints in the complete model of the pelvis, excluding muscular and ligamentous contributions were removed. A downward load of 850 N was applied at the centre of the L5S1 disc, in the sacro-lumbar structure to represent the weight of the upper body acting through the spine.

Figure 8.10 shows the cortical bone mesh, including the connector elements used to represent the ligaments, and the sacro-lumbar structure. These are seen to form the pelvic ring. Figure 8.11 shows posterior, and anterior views of the cortical bone mesh, including the connector elements used to represent the muscles around a patient's right hip joint. Figure 8.12 shows a frontal view of the 3D model of the pelvis, including muscles, ligaments, and the sacro-lumbar structure.

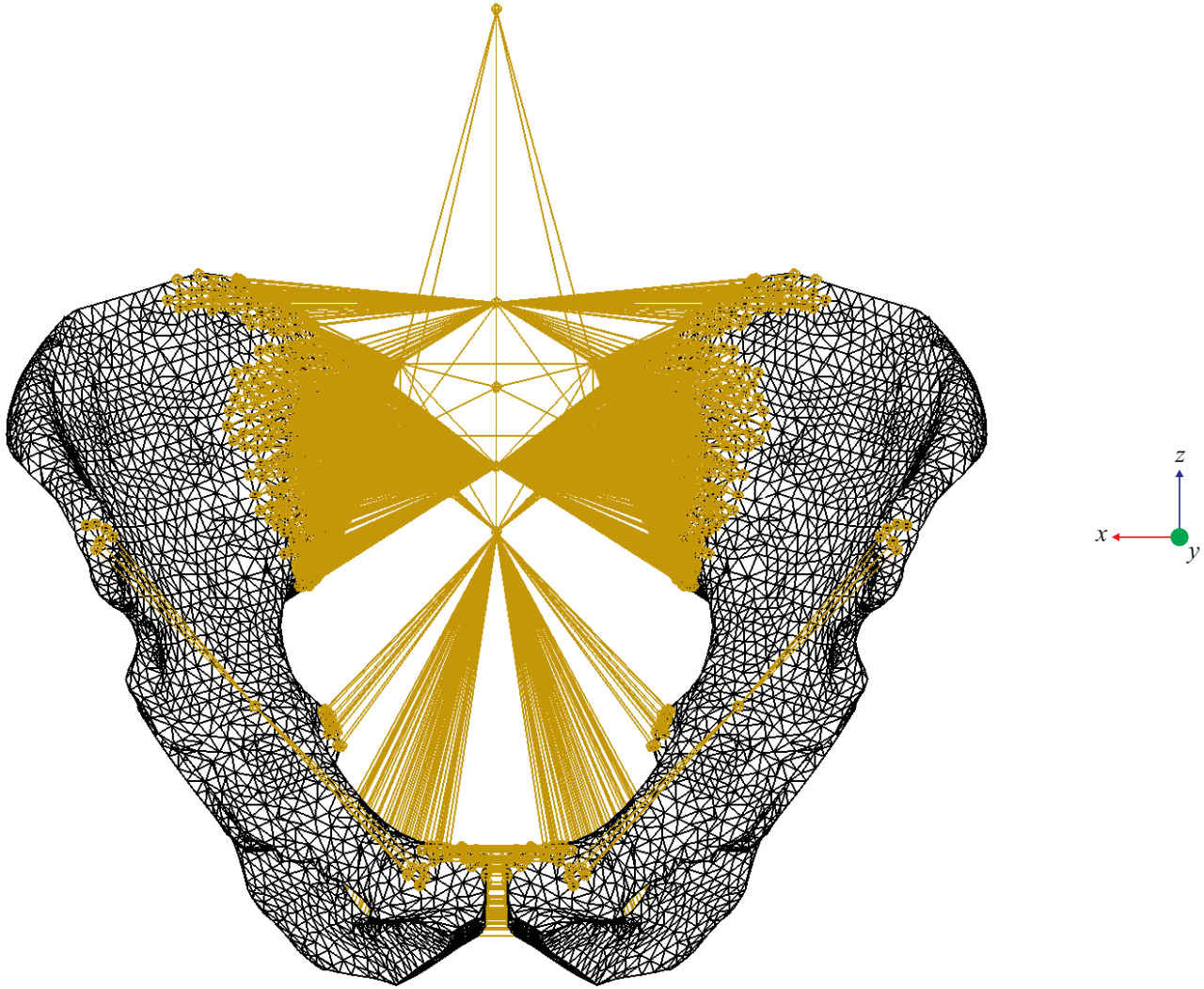

Figure 8.10: 3D mesh of the cortical bone, including connector elements representing the ligaments, sacro-lumbar structure, and inter-pubic disc

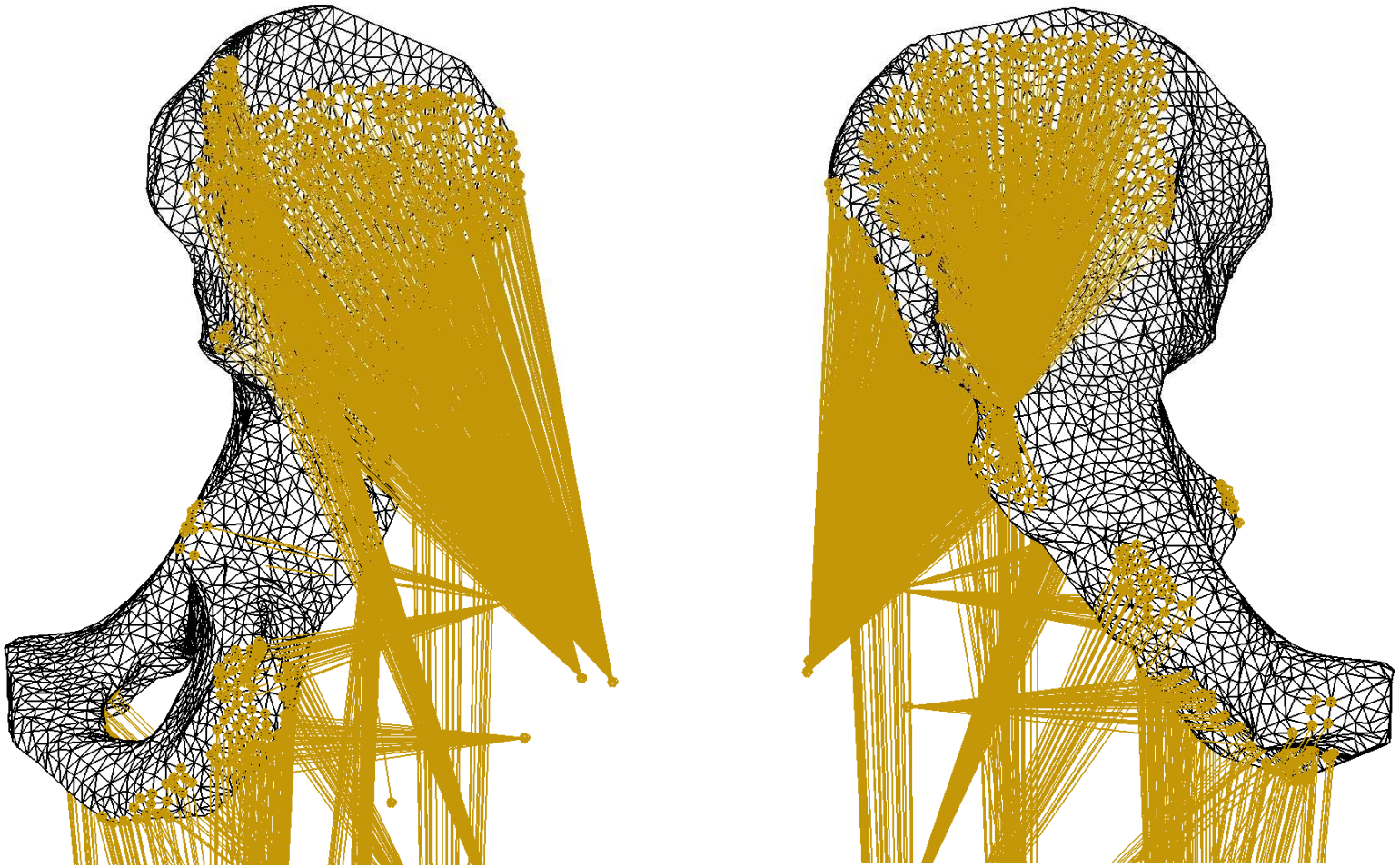

Posterior view

Anterior view

Figure 8.11: 3D mesh of the cortical bone, including connector elements representing the muscles

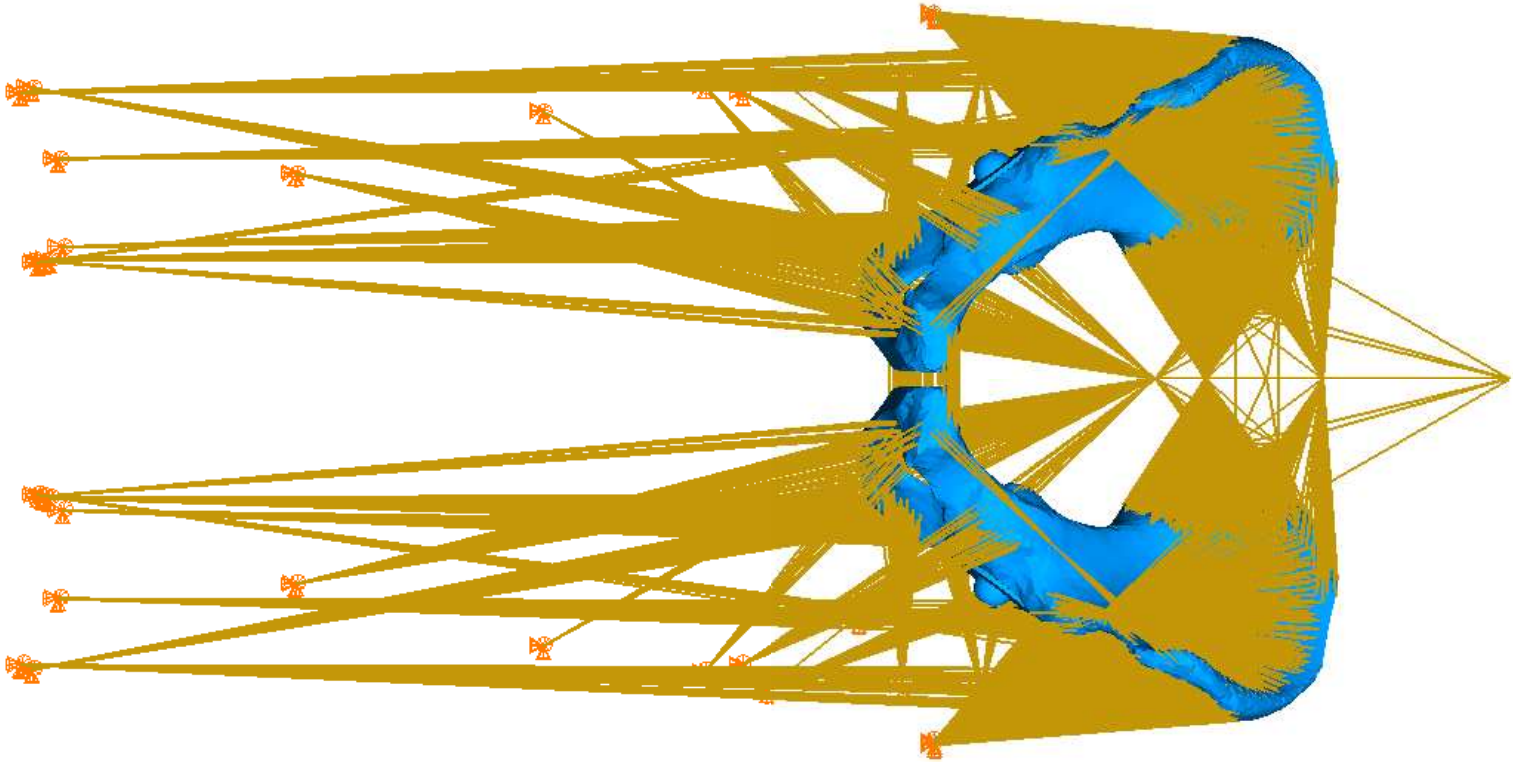

Figure 8.12: Frontal view of the 3D model of the pelvis, including muscles, ligaments, and the sacro-lumbar structure

8.3.2 Results and discussion

Figure 8.13 shows a frontal view, of the von Mises stresses found in the cortical bone, for the PAINCML model of the pelvis. In comparison to the distributions of stresses found in the pelvis model, excluding muscular and ligamentous contributions (Figure 8.2) it is observed that there is a significant reduction in stresses inferior to the sacro-iliac joint, due to the removal of constrained boundary conditions from this area. Higher stresses are seen in the right hemi pelvis, with stress transfer occurring through the sacro-lumbar structure. In general stresses were found to be more evenly distributed, with fewer regions of high stress concentrations. Figure 8.14 shows the von Mises stresses in the cortical bone of the patient's left hemi pelvis. Stresses in the cortical bone, in particular under the gluteus, and iliacus muscles are seen to be more evenly distributed than those found for the pelvis model, excluding muscular and ligamentous contributions. This shows that stresses in the cortical bone are influenced by the adopted boundary conditions.

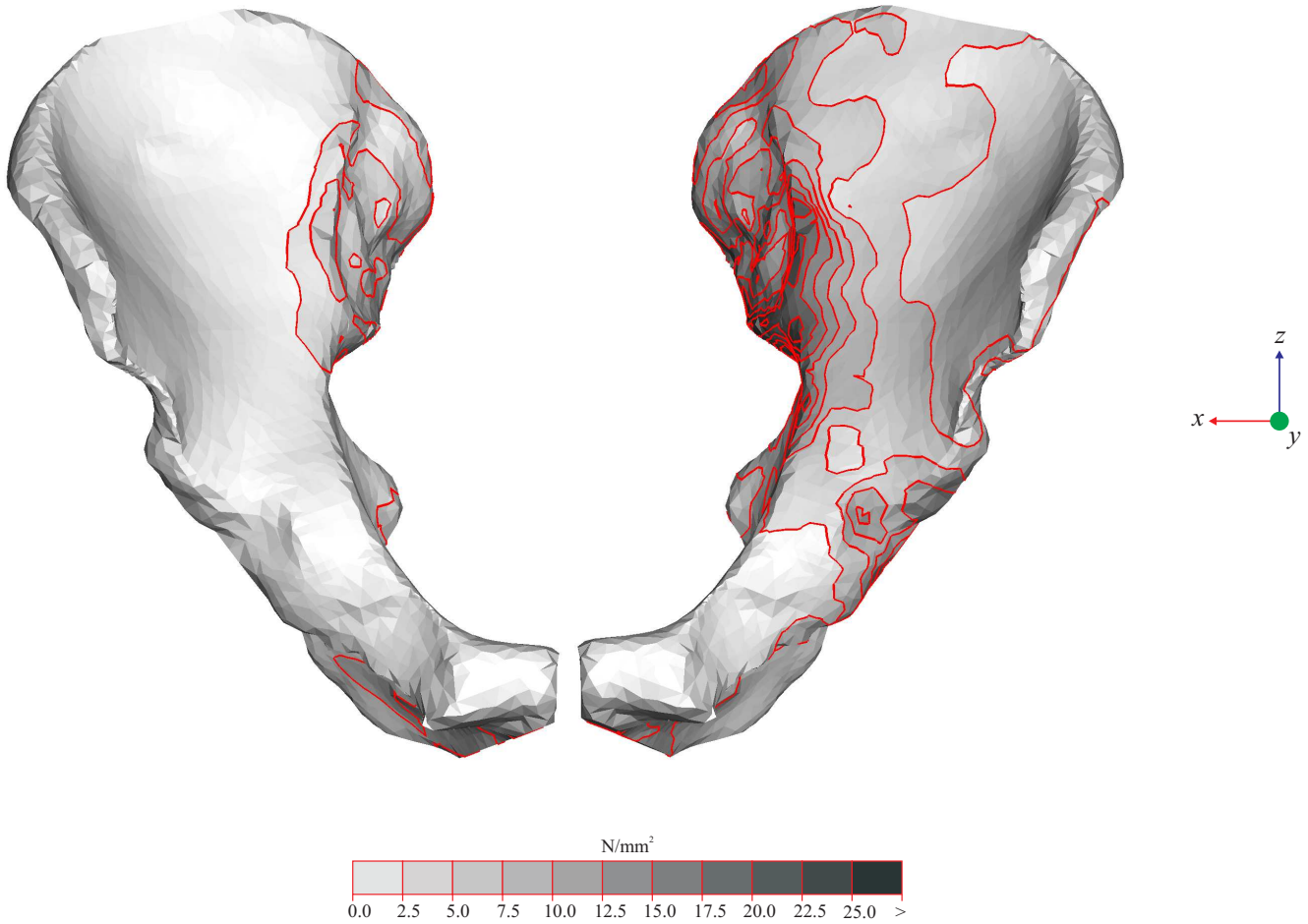

Figure 8.13: von Mises stresses in the cortical bone of the pelvis, following primary arthroplasty on both sides, due to a single leg stance load case, including muscular and ligamentous contributions

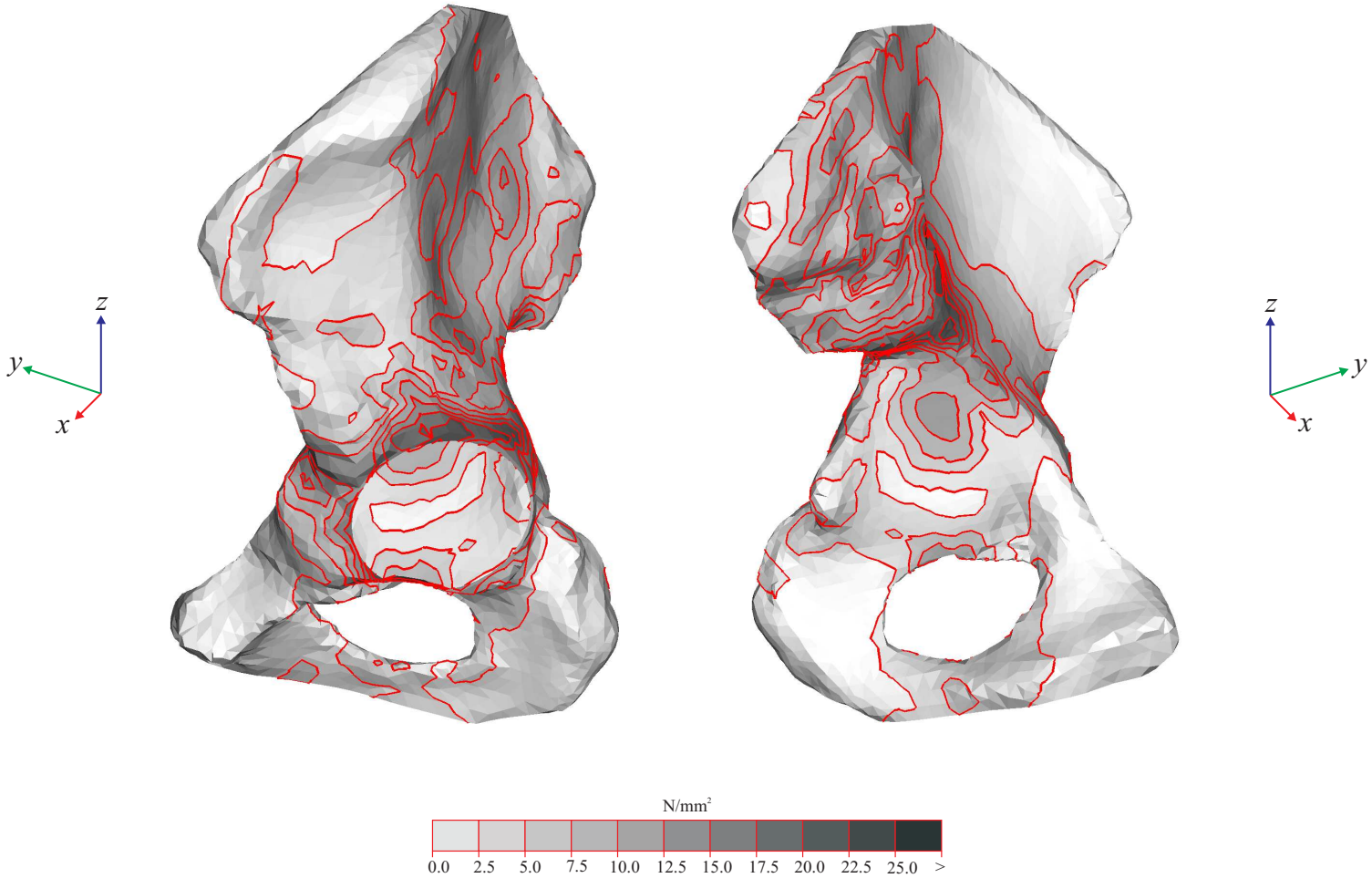

Figure 8.14: von Mises stresses in the cortical bone of left hemi pelvis, following primary arthroplasty on both sides, due to a single leg stance load case, including muscular and ligamentous contributions

Figure 8.15 shows a frontal view, of the von Mises stresses found in the trabecular bone, for the PAINCML model of the pelvis. It is observed that the distribution of stresses is similar to that found for the pelvis model, excluding muscular and ligamentous contributions, although as for the stresses in the cortical bone, reduced stress concentrations are seen close to the sacro-iliac joint. Figure 8.16 shows the von Mises stresses in the trabecular bone of the patient's left hemi pelvis. As for the model of the pelvis, excluding muscular and ligamentous contributions, there is an increase in stress contributions towards the superior edge of the acetabulum in comparison to the hemi pelvis model, following primary arthroplasty (Chapter 6, Figure 6.15).

It can be seen that the explicit inclusion of muscles and ligaments as non-linear connector elements alters the distribution of stresses in the cortical bone to a significant extent. It was found that the model of the pelvis, including muscular and ligamentous contributions, resulted in more even distribution of von Mises stresses, in comparison to the model of the pelvis, excluding muscular and ligamentous contributions. Significant changes to the distributions of stresses in the trabecular bone were not observed to the same extent.

The global behaviour of the pelvis model, including muscular and ligamentous contributions was verified by examining reaction forces present at the muscle insertion points, due to the single leg stance load case. The greatest forces were found in the gluteus medius, and gluteus minimus muscles, as expected, given the role of these muscles in supporting the body during single leg stance [88]. In addition, as expected, when loaded the sacro-lumbar structure tended to rotate in a forwards direction, resisted by the ligaments.

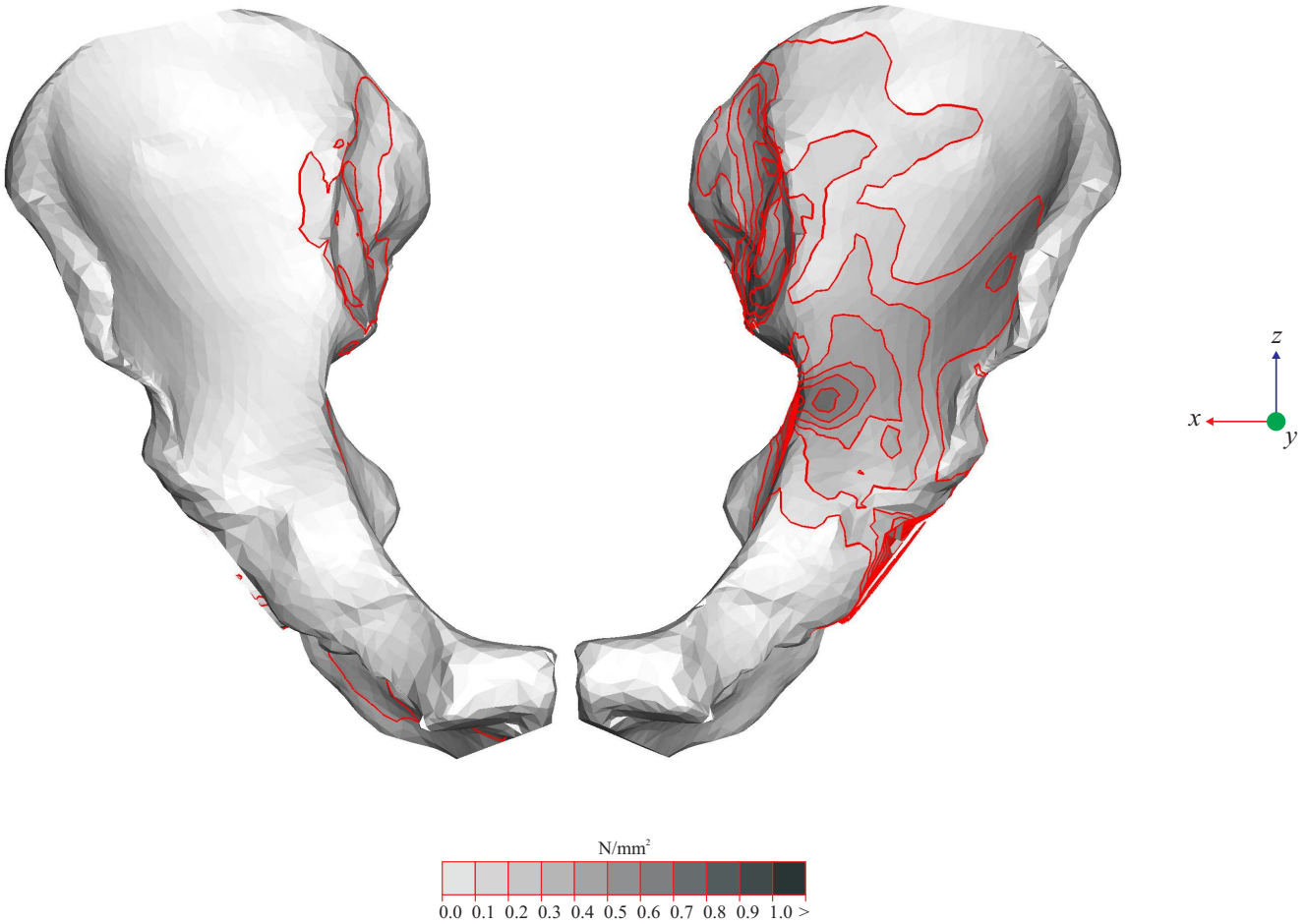

Figure 8.15: von Mises stresses in the trabecular bone of the pelvis, following primary arthroplasty on both sides, due to a single leg stance load case, including muscular and ligamentous contributions

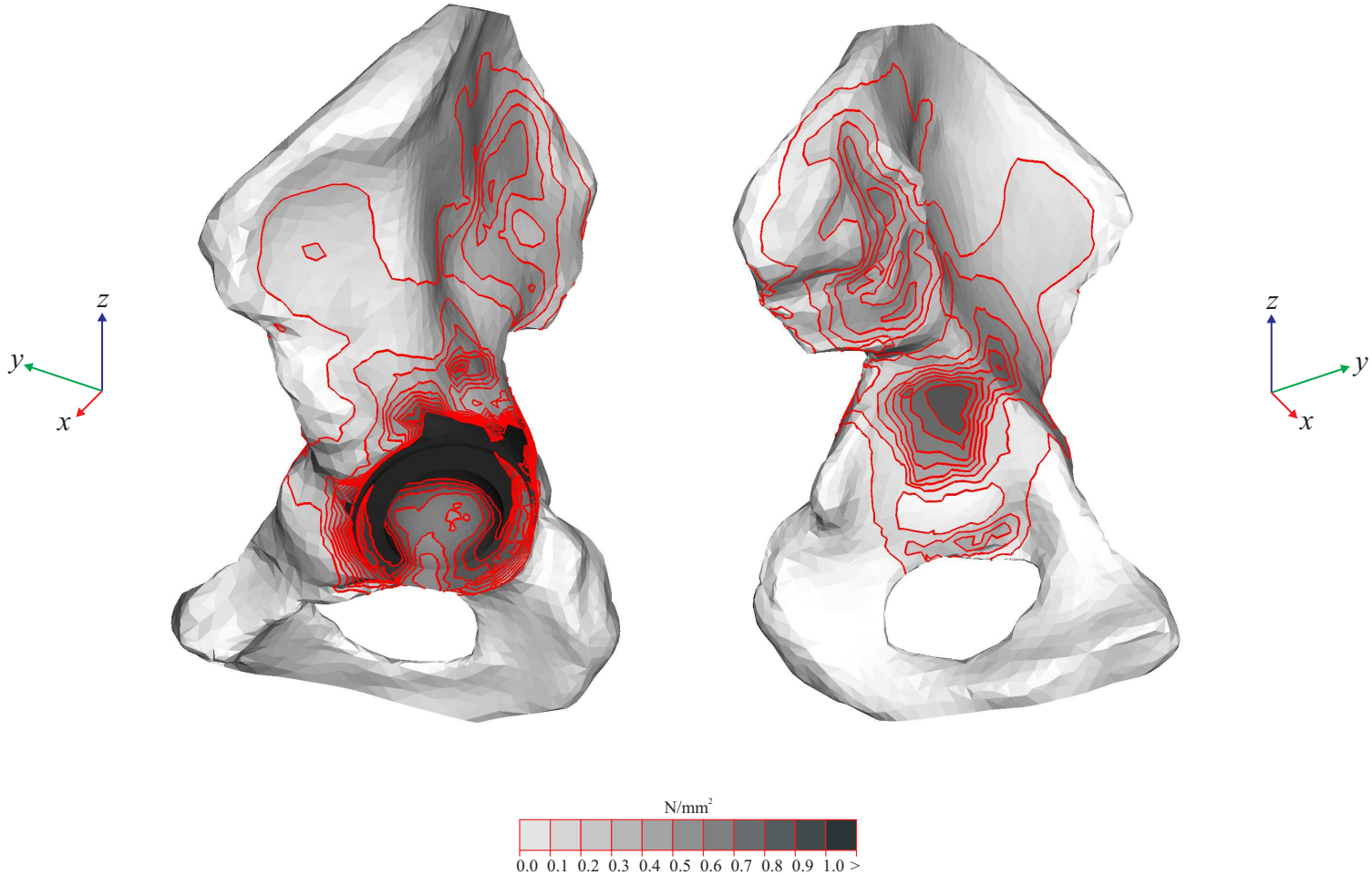

Figure 8.16: von Mises stresses in the trabecular bone of left hemi pelvis, following primary arthroplasty on both sides, due to a single leg stance load case, including muscular and ligamentous contributions

8.4 Analysis of the pelvis, following primary, and revision arthroplasty on the right and left sides, including muscular and ligamentous contributions (RAINCML model)

8.4.1 Model definition

The geometry, and materials definition of the RAINCML pelvis model, was the same as for the the RAEXML pelvis model, with notable alterations made to include muscles and ligaments as non-linear connector elements, as described in the previous section.

8.4.2 Results and discussion

Figure 8.17 shows a frontal view, of the von Mises stresses found in the cortical bone, for the RAINCML model of the pelvis. The distribution of stresses is seen to be similar to that found for the model of the pelvis, following primary arthroplasty on both sides, including muscular and ligamentous contributions (Figure 8.13). Figure 8.18 shows the von Mises stresses in the cortical bone of the the patient's left hemi pelvis (revision arthroplasty). In comparison to the distribution of stresses found for the model of the pelvis, following primary arthroplasty on both sides (Figure 8.14), there is an increase in the stress concentrations superior to the acetabulum. This

is consistent with the results found for the models of the pelvis, excluding muscular and ligamentous contributions, and the results found for the hemi pelvis models, following primary and revision arthroplasty.

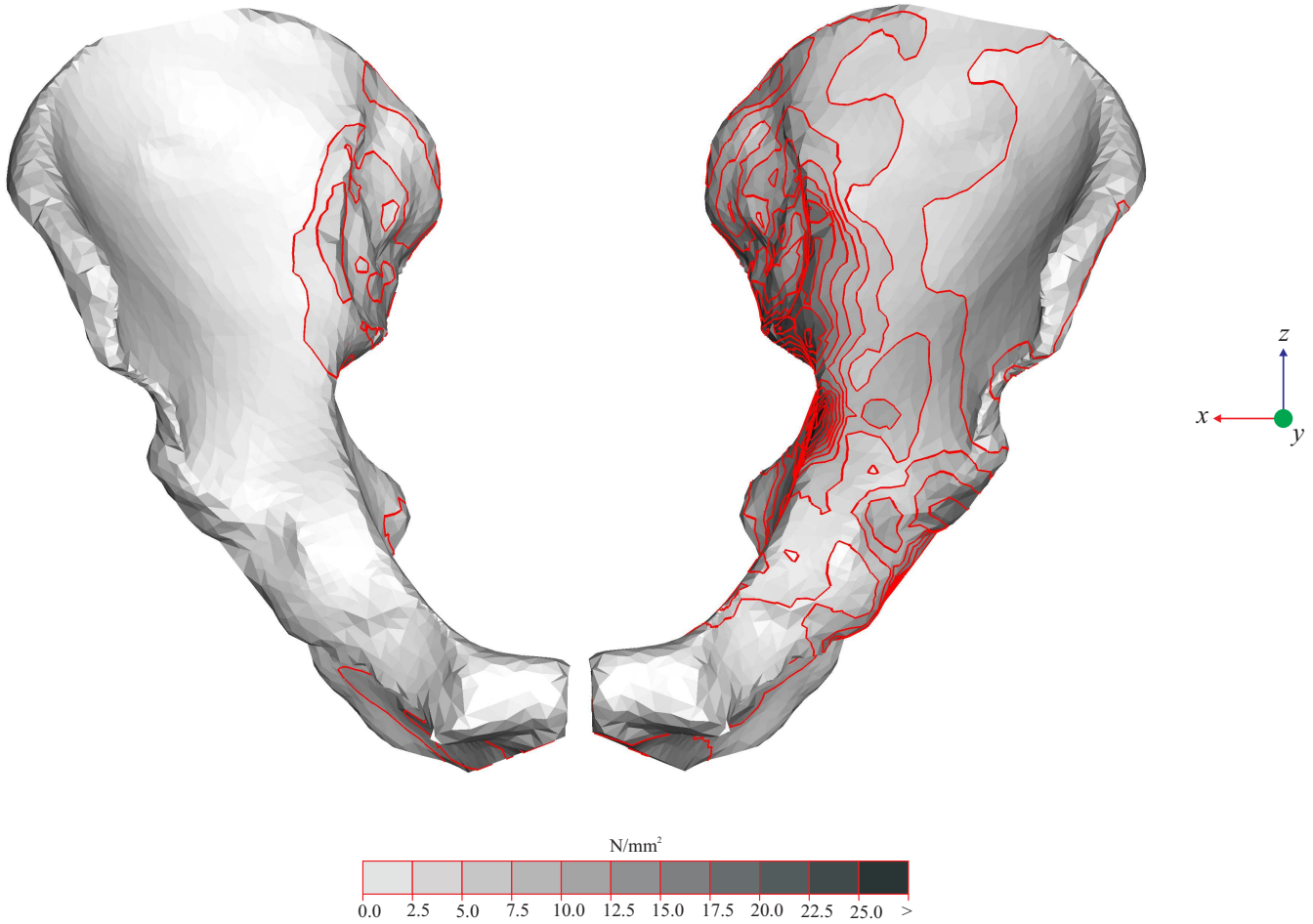

Figure 8.17: von Mises stresses in the cortical bone of the pelvis, following primary and revision arthroplasty, on the right and left hand sides, due to a single leg stance load case, including muscular and ligamentous contributions

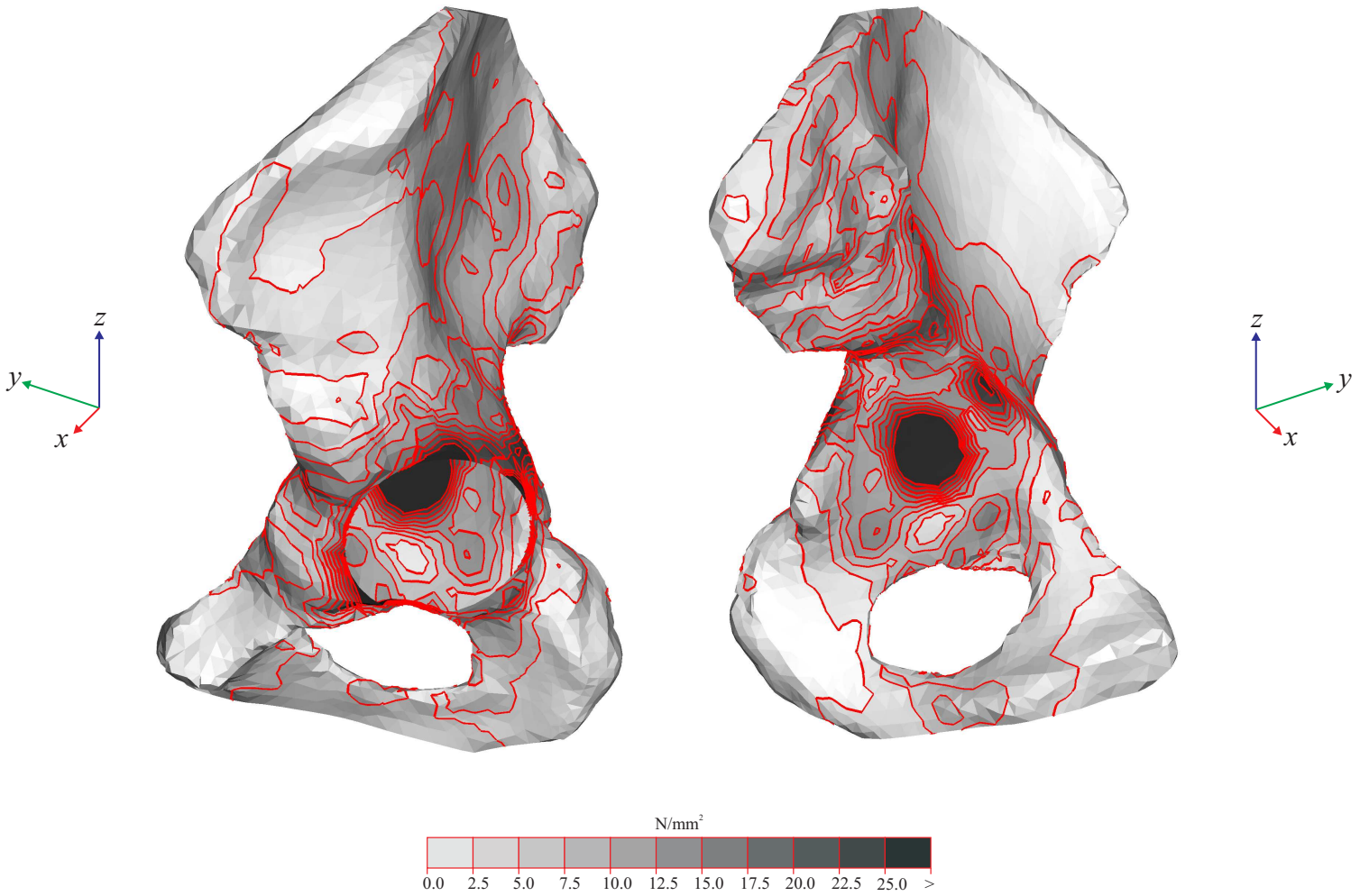

Figure 8.18: von Mises stresses in the cortical bone of left hemi pelvis, following primary and revision arthroplasty, on the right and left hand sides, due to a single leg stance load case, including muscular and ligamentous contributions

Figure 8.19 shows a frontal view, of the von Mises stresses found in the trabecular bone, for the RAINCML model of the pelvis. The distribution of stresses is seen to be similar to that found for the model of the pelvis, following primary and revision arthroplasty, on the right and left sides, excluding muscular and ligamentous contributions (Figure 8.8). Figure 8.20 shows the von Mises stress in the trabecular bone of the patient's left hemi pelvis. Stress concentrations are observed to occur at the superior edge, and at the rear of the acetabulum. However, stress concentrations do not extend towards the sacro-iliac joint, as for the RAEXML model of the pelvis.

As for the model of the pelvis, following primary and revision arthroplasty, on the right and left sides, excluding muscular and ligamentous contributions, in addition to the results shown here, the stresses in the bone graft were also investigated. Once again these were found to be near identical to those found using the model of the hemi pelvis, following revision arthroplasty, and hence are not repeated here.

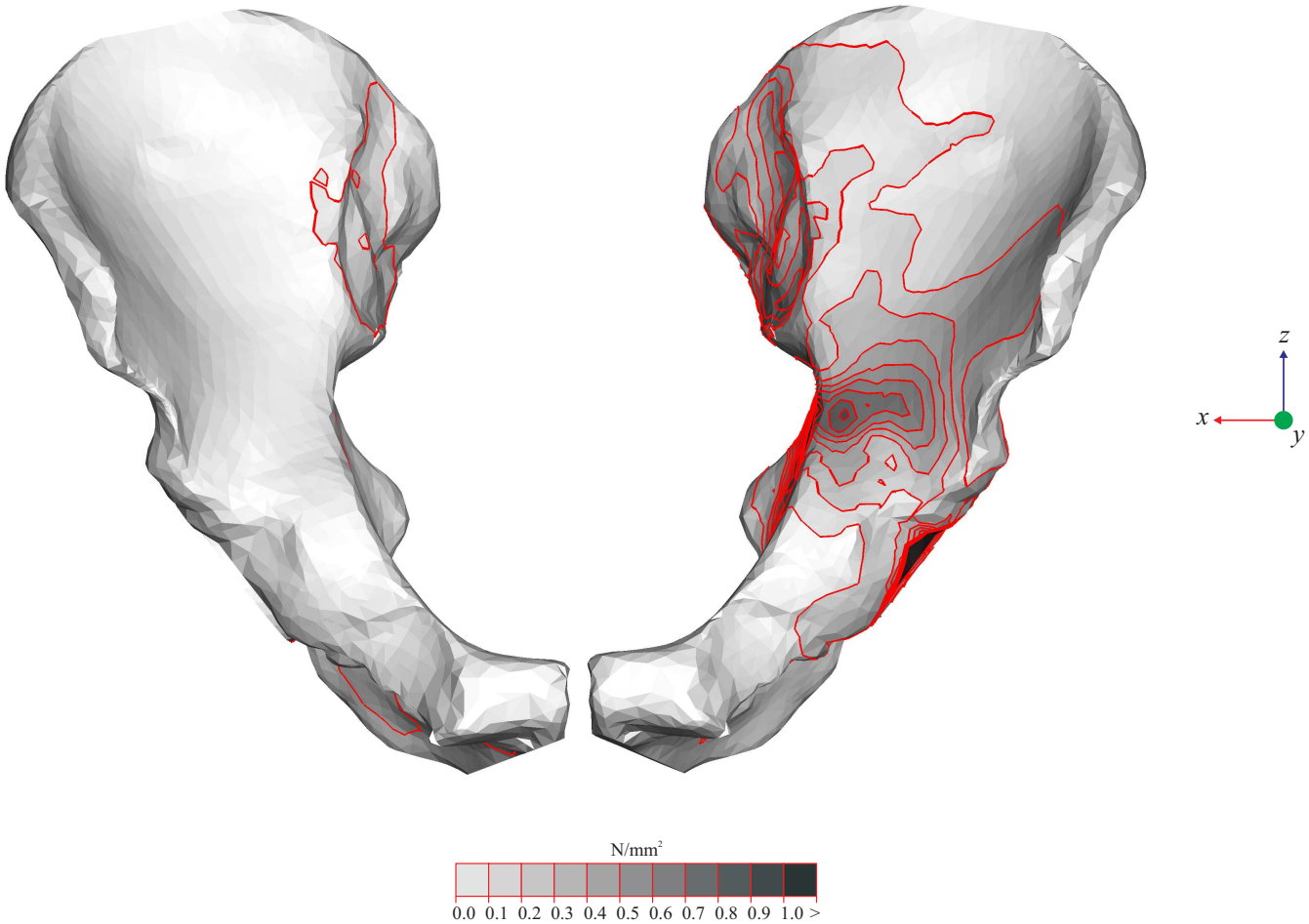

Figure 8.19: von Mises stresses in the trabecular bone of the pelvis, following primary arthroplasty on both sides, due to a single leg stance load case, including muscular and ligamentous contributions

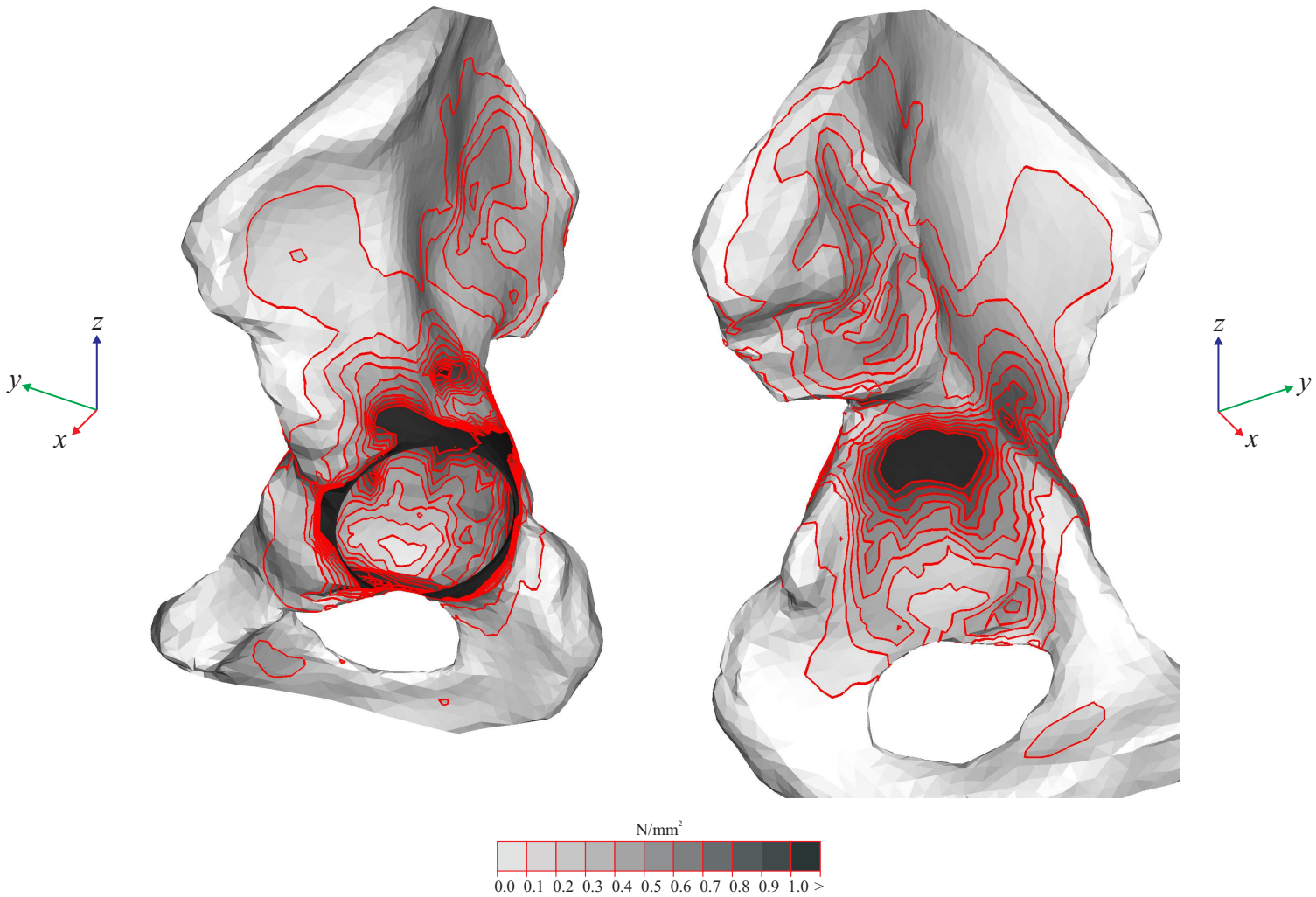

Figure 8.20: von Mises stresses in the trabecular bone of left hemi pelvis, following primary arthroplasty on both sides, due to a single leg stance load case, including muscular and ligamentous contributions

8.5 Conclusions

Comparing the results of the four complete pelvis models presented in this chapter, as well as the results of the hemi-pelvis models presented in Chapter 6 it can be seen that altering the boundary conditions of the models has a significant effect on the distribution of stresses in the cortical bone. The explicit inclusion of muscles and ligaments resulted in a more even distribution of stresses within the cortical bone, with stress concentrations due to constrained boundary conditions being removed. Thus it is clear that for analyses used to predict stresses within the cortical bone of the pelvis, care should be taken in assigning appropriate boundary conditions.

Dalstra et al. [25] included muscles in an implicit manner, for a model of the natural pelvis, as forces applied to the surface of the cortical bone. However, their investigation did not include the ligaments. In addition constrained boundary conditions were applied at the sacro-iliac joint of each hemi pelvis, while the pubic symphysis, appears to have been modelled as a continuum of cortical bone between the two halves of the pelvis. Thus their investigation found stress concentrations towards the sacro-iliac joints, and pubic symphysis, and cannot be compared in a direct manner to the results presented here. However the range of von Mises stresses found in the cortical, and trabecular bone, from their investigation, and from the results presented here were found to be similar.

The boundary conditions of the models were found to have a less significant effect on the stresses found in the trabecular bone, and in the case of models, following revision arthroplasty, the bone graft. The near identical

nature of the stresses found in the bone graft for the hemi pelvis model, following revision arthroplasty, and the complete pelvis models, following revision arthroplasty on the left side, excluding and including muscular and ligamentous contributions suggests that localised models of the acetabular construct may be suitable when investigating the behaviour of the bone graft, and acetabular cup within the bone graft bed. Although the results presented here are for one load case, representative of single leg stance, it is expected that other load cases would produce similar stresses in the bone graft, to those observed for the hemi pelvis model.

In conclusion this chapter has presented complete models of the pelvis, examining the effect of including muscles and ligaments, as well as the sacro-lumbar structure in an explicit manner. The effect on the distribution of stresses within the cortical bone was found to be significant from a clinical view, predicting a more even distribution, with fewer regions of stress concentration.

9

Conclusions and recommendations

This study considered a range of finite element models of the acetabular construct and the pelvis, following primary and revision hip arthroplasty. A significant proportion of the study focused on the mechanical behaviour of morsellised cortico-cancellous bone (MCB), and a constitutive model was

developed to include it in finite element analyses. In order to assign pseudo-realistic boundary conditions to the finite element model of the pelvis, the study used non-linear connector elements to represent muscles and ligaments. Inclusion of these in the model led to the development of a series of algorithms permitting automated distribution of the connector elements on the surface of the cortical bone.

The key conclusions resulting from this study are as follows:

9.1 Conclusions

9.1.1 Conclusions relating to MCB

- Previous literature indicates that the mechanical properties of MCB can be improved by impaction, washing, and the use of an appropriate particle size distribution. However a comprehensive constitutive model to be used in finite element analyses has so far not been proposed.

- Impaction of MCB does not have a significant effect on the development of the elastic modulus with cyclic loading. However impaction does have a significant effect in reducing the development of consolidation plastic strains with cyclic loading

- The elastic modulus of MCB is strongly dependent on the applied compressive stress. The change in elastic modulus with increasing load cycles is minor in comparison.

- The consolidation plastic strain experienced by MCB is strongly de-

pendent on the maximum applied compressive stress.

- MCB has visco-elastic properties, which can be described using a third order Prony series.

- The long term elastic modulus of MCB was found to be around 60% of the instantaneous elastic modulus, regardless of the initial applied compressive stress.

- A Drucker Prager Cap constitutive model can be used to describe the shear, and consolidation plastic behaviour of MCB.

9.1.2 Conclusions relating to the plane-strain model of the acetabular construct

Plane-strain finite element analyses of the acetabular construct, following revision hip arthroplasty were conducted using idealised load cases, and the Drucker Prager constitutive model for MCB. This showed that with increased bone graft bed depth, there was an increase in permanent rotation of the acetabular cup. However these rotations tended to stabilise with increasing load cycles. This indicates that there is an advantage in using the largest practical size of acetabular cup.

Plane-strain analyses were also conducted using the Drucker Prager Cap constitutive model for MCB. Comparison of the Drucker Prager and Drucker Prager Cap (DPC) analyses, showed a significant increase in the rotation of the acetabular cup, when consolidation (due to the cap) was included. Stabilisation of the rotations was also seen using the DPC constitutive model.

9.1.3 Conclusions relating to the hemi pelvis, and the pelvis models

3D hemi pelvis models were used to investigate the behaviour of the natural hip joint, and the hip joint following primary, and revision arthroplasty. Models of the natural hip joint, and the hip joint following primary arthroplasty were found to compare well with published studies, in terms of load transfer paths, and the distribution of stresses in the cortical, and trabecular bone.

The model of the hemi pelvis, following revision hip arthroplasty, was used to investigate the migration and rotation of the acetabular cup within the bone graft bed due to a series of physiological activities. Each activity was found to produce a unique pattern of migration, and irrecoverable rotation. In addition each activity gave rise to different stresses within the bone graft bed. The results were compared in a pseudo-quantitative manner with published literature, and clinical observations. The directions, and magnitudes of cup migration and rotation were found to be similar.

Provision for the inclusion of muscles and ligaments as non-linear spring elements within finite element analyses was discussed. Assumptions were made to allow muscles to be included as reactive, as opposed to active elements. A series of algorithms were developed, allowing the automated description of geometrically realistic muscle and ligament origination areas, on the pelvis. Models of the pelvis, following primary arthroplasty on both sides, and following primary, and revision arthroplasty on alternate sides were compared.

It was found that the inclusion of muscular and ligamentous contributions, as opposed to the use of fixed boundary conditions on the cortical bone did not have a significant effect on the stress distribution in the bone graft, or trabecular bone in the acetabular area. However the inclusion of muscular and ligamentous contributions had a significant effect on the stress distribution in the cortical bone, resulting in a more even distribution of stresses, with fewer areas of stress concentration. This indicates that care should be taken when drawing conclusions, regarding stresses in the cortical bone, away from the acetabular region, when fixed boundary conditions are applied. However fixed boundary conditions may be acceptable when investigating stress distributions in the acetabular region. These conclusions are based on the single leg stance load case considered.

9.2 Recommendations

The developed models of the pelvis, and the acetabular construct can be used in assessing and informing the design of cup fixation devices, to prevent migration and rotation of the cup, within the bone graft bed. The models can also be used to assess different designs of cup, for example large diameter vs. extended flange cups. The constitutive model developed for MCB can be used in the modelling of other joint arthroplasties, such as the knee, in which impaction grafting is used. In addition the constitutive model could be adapted, following further laboratory testing to assess the use of synthetic particles, and fibres in combination with MCB.

Future researchers may wish to investigate the inclusion of an active component, when modelling muscles within finite element models. It is clear that

the developed series of algorithms could be adopted by other researchers, modelling different joints in the body. In addition the algorithms could be extended to allow the inclusion of a femur in the pelvis model, with geometrically realistic insertion points.

Future researchers may also wish to examine the use of finite element models, including muscular and ligamentous contributions as verification, or in combination with optimisation models, attempting to find muscle forces during physiological activities. In addition the model of the pelvis, including muscles and ligaments could be used to investigate the effects of muscle and ligament damage, through accident or at the time of surgery.

References

[1] A.E. Gross. *The revision problem. In Revision Hip Arthroplasty: A practical approach to bone stock loss*, chapter 1, pages 1–3. Reed educational and professional publishing limited, Bath, 1997.

[2] D.W. Howie. *The revision problem. In Revision Hip Arthroplasty: A practical approach to bone stock loss*, chapter 2, pages 4–11. Reed educational and professional publishing limited, Bath, 1997.

[3] I. D. Learmonth, G. P. Grobler, D. M. Dall, and V. Jandera. Loss of bone stock with cementless hip arthroplasty. *Journal of Arthroplasty*, 10:257–263, 1995.

[4] Andrew D. Toms, Ross L. Barker, Richard Spencer Jones, and Jan Herman Kuiper. Impaction bone-grafting in revision joint replacement surgery. *Journal of Bone and Joint Surgery (Am)*, 86-A:2050–2060, 2004.

[5] G.A. Gie, L. Linder, R.S. Ling, J.P. Simon, T.J.J.H. Slooff, and A.J. Timperley. Impacted cancellous allografts and cement for revision total hip arthroplasty. *Journal of Bone and Joint Surgery (Br)*, 75-B:14–21, 1993.

[6] T.J.J.H. Slooff, R. Huiskes, J. van Horn, and A.J. Lemmens. Bone grafting in total hip replacement for acetabular protrusion. *Acta Orthopaedica Scandinavica*, 55:593–596, 1984.

[7] H. Iida, Y. Matsusue, K. Kawanade, H. Okumura, T. Yamamuro, and T. Nakamura. Cemented total hip arthroplasty with acetabular bone graft for developmental dysplasia. *Journal of Bone and Joint Surgery (Br)*, 82-B:176–184, 2000.

[8] S. Inao and T. Matsuno. Cemented total hip arthroplasty with autogenous acetabular bone grafting for hips with developmental dysplasia in adults. *Journal of Bone and Joint Surgery (Br)*, 82-B:375–377, 2000.

[9] Andrew T. M. Phillips. Finite element analysis of the acetabulum after impaction grafting. MEng honours thesis, The University of Edinburgh, 2001.

[10] A. T. M. Phillips, Pankaj, A. S. Usmani, and C. R. Howie. The effect of acetabular cup size on the short-term stability of revision hip arthroplasty: a finite element investigation. *Proceedings of the IMechE, Part H: Journal of Engineering in Medicine*, 218:239–249, 2004.

[11] A. T. M. Phillips, Pankaj, A. S. Usmani, and C. R. Howie. Numerical modelling of the acetabular construct following impaction grafting. In J. Middleton, N. G. Shrive, and M. L. Jones, editors, *Proceedings of Computer Methods in Biomechanics and Biomedical Engineering, Madrid*. FIRST Numerics, 2004. ISBN: 0-9549670-0-3.

[12] Ashit Bavadekar, Oliver Cornu, Bernard Godts, Christian Delloye, John Van Tomme, and Xavier Banse. Stiffness and compactness of morselized grafts during impaction — an in vitro study with human femoral heads. *Acta Orthopaedica Scandinavica*, 72:470–476, 2001.

[13] Stefan B. T. Bolder, B. Willem Schreurs, Nico Verdonschot, Jacco M. J. van Unen, Jean W. M. Gardeniers, and Tom. J. J. H. Slooff. Particle size of bone graft and method of impaction affect initial stability of cemented cups. *Acta Orthopaedica Scandinavica*, 74:652–657, 2003.

[14] N. T. Brewster, W. J. Gillespie, C.R. Howie, S. P. G. Madabhushi, A. S. Usmani, and D. R. Faibairn. Mechanical considerations in impaction bone grafting. *The Journal of Bone and Joint Surgery*, 81-B:118–124, 1999.

[15] Douglas G. Dunlop, Nigel T. Brewster, S. P. Gopal Madabhushi, Asif S. Usmani, P. Pankaj, and Colin R. Howie. Techniques to improve the strength of impacted bone graft. *The Journal of Bone and Joint Surgery (Am)*, 85-A:639–646, 2003.

[16] L. Fosse, H. Rønningen, J. Lund-Larsen, P. Benum, and L. Grande. Impacted bone stiffness measured during construction of morsellised bone samples. *Journal of Biomechanics*, 37:1757–1766, 2004.

[17] A. T. M. Phillips, Pankaj, D. T. Brown, T. Z. Oram, C. R. Howie, and A. S. Usmani. The elastic properties of morsellised cortico-cancellous bone graft are dependent on its prior loading. *Journal of Biomechanics*, 2005. In press, DOI: 10.1016/j.jbiomech.2005.03.032.

[18] N. Verdonschot, C. T. H. van Hal, B. W. Schreurs, P. Buma, R. Huiskes, and T. J. J. H. Slooff. Time-dependent mechanical properties of HA/TCP particles in relation to morsellized bone grafts for use in impaction grafting. *Journal of Biomedical Materials Research Part B — Applied Biomaterials*, 58:599–604, 2001.

[19] A. E. Anderson, C. L. Peters, B. D. Tuttle, and J. A. Weiss. A subject-specific finite element model of the pelvis accurately predicts cortical strains under acetabular loading. In *Proceedings of the 50th Annual Meeting of the Orthopaedic Research Society, Poster No: 1334*, 2004.

[20] A. E. Anderson, C. L. Peters, B. D. Tuttle, and J. A. Weiss. Development and validation of a subject-specific finite element model of the pelvis: assessment of model sensitivity. In J. Middleton, N. G. Shrive, and M. L. Jones, editors, *Proceedings of Computer Methods in Biomechanics and Biomedical Engineering, Madrid*. FIRST Numerics, 2004. ISBN: 0-9549670-0-3.

[21] D. R. Carter, R. Vasu, and W. H. Harris. Stress distributions in the acetabular region - ii. effects of cement thickness and metal backing of the total hip acetabular component. *Journal of Biomechanics*, 15:165–170, 1982.

[22] Michel Dalstra. *Biomechanical aspects of the pelvic bone and design criteria for acetabular protheses*. PhD thesis, University of Nijmegen, Netherlands, 1993.

[23] M. Dalstra, R. Huiskes, A. Odgaard, and L. van Erning. Mechanical and textural properties of pelvic trabecular bone. *Journal of Biomechanics*, 26:523–535, 1993.

[24] M. Dalstra, R. Huiskes, and L. van Erning. Development and validation of a three-dimensional finite element model of the pelvic bone. *Transactions of the ASME: Journal of Biomechanical Engineering*, 117:272–278, 1995.

[25] M. Dalstra and R. Huiskes. Load transfer across the pelvic bone. *Journal of Biomechanics*, 28:715–724, 1995.

[26] J. M. Garcia, M. Doblaré, B. Seral, F. Seral, D. Palanca, and L. Garcia. Three-dimensional finite element analysis of several internal and external pelvis fixations. *Transactions of the ASME: Journal of Biomechanical Engineering*, 122:516–522, 2000.

[27] V. K. Goel, S. Valliappan, and N. L. Svensson. Stresses in the normal pelvis. *Computers in Biology and Medicine*, 8:91–104, 1978.

[28] Rik Huiskes. Finite element analysis of acetabular reconstruction. *Acta Orthopaedica Scandinavica*, 58:620–625, 1987.

[29] S. Majumder, A. Roychowdhury, and S. Pal. Variations of stress in pelvic bone during normal walking, considering all active muscles. *Trends in Biomaterials and Artificial Organs*, 17:48–53, 2004.

[30] Hisashi Oki, Masao Ando, Hironori Omori, Yasuhiro Okumura, Kohei Negoro, Kenzo Uchida, and Hisatoshi Baba. Thoughts and progress - relation between vertical orientation and stability of acetabular component in dysplastic hip simulated by nonlinear three-dimensional finite element method. *Artificial Organs*, 28:1050–1054, 2004.

[31] Hironobu Oonishi, Hideo Isha, and Tatsuhiko Hasegawa. Mechanical analysis of the human pelvis and its application to the artificial hip joint — by means of the three dimensional finite element method. *Journal of Biomechanics*, 16:427–444, 1983.

[32] Douglas R. Pedersen, Roy D. Crowninshield, Richard A. Brand, and Richard C. Johnston. An axisymmetric model of acetabular components in total hip arthroplasty. *Journal of Biomechanics*, 15:305–315, 1982.

[33] E. Siggelkow, J. Seebeck, D. Hertig, K.-H. Widmer, and M. Fröhlich. Construction and validation of a finite element model of a human pelvis. In J. Middleton, N. G. Shrive, and M. L. Jones, editors, *Proceedings of Computer Methods in Biomechanics and Biomedical Engineering, Madrid*. FIRST Numerics, 2004. ISBN: 0-9549670-0-3.

[34] M. S. Thompson, M. D. Northmore-Ball, and K. E. Tanner. Effects of acetabular resurfacing component material and fixation on the strain distribution in the pelvis. *Proceedings of the IMechE, Part H: Journal of Engineering in Medicine*, 216:237–245, 2002.

[35] R. Vasu, D. R. Carter, and W. H. Harris. Stress distributions in the acetabular region - i. before and after total joint replacement. *Journal of Biomechanics*, 15:155–164, 1982.

[36] A.W. Blom, B. Grimm, A.W. Miles, J.L. Cunningham, and I.D. Learmonth. Subsidence in impaction grafting: the effect of adding a ceramic bone graft extended to bone. *Proceedings of the IMechE, Part H: Journal of Engineering in Medicine*, 216(6):265–270, 2002.

[37] S. B. T. Bolder. *Defect reconstruction with impacted morsellized bone grafts in total hip arthroplasty.* PhD thesis, Nijmegen University, Netherlands, 2004.

[38] Michael D. Brodt. Quantifying the mechanical properties of morselized human cancellous bone. Master's thesis, The University of Iowa, 1996.

[39] M. D. Brodt, C. C. Swann, and T. D. Brown. Tri-axial measurement of the mechanical properties of morselized human cancellous bone. In *Proceedings of the 43rd meeting of the Orthopaedic Research Society*, 1997.

[40] Michael D. Brodt, Colby C. Swan, and Thomas D. Brown. Mechanical behaviour of human morselized cancellous bone in triaxial compression testing. *Journal of Orthopaedic Research*, 16:43–49, 1998.

[41] David Brown. Investigation of the mechanical properties of impacted morsellised cancellous bone grafts used in revision hip arthroplasty. BEng honours thesis, The University of Edinburgh, 2003.

[42] Douglas Dunlop. *Mechanical and biological aspects of impaction bone grafting in revision hip surgery and the use of a new synthetic bone graft.* Doctor of medicine thesis, The University of Edinburgh, 2001.

[43] Hanspeter Frei, Philip Mitchell, Bassam A. Masri, Clive P. Duncan, and Thomas R. Oxland. Mechanical characteristics of the bone-graft-cement interface after compaction grafting. *Journal of Orthopaedic Research*, 23:9–17, 2005.

[44] E. B. W. Giesen, N. M. P. Lamerigts, N. Verdonschot, P. Buma, B. W. Schreurs, and R. Huiskes. Mechanical characteristics of impacted morsellised bone graft used in revision total hip arthroplasty. *The Journal of Bone & Joint Surgery (Br)*, 81-B:1052–1057, 1999.

[45] B. Grimm. *Mechanical properties of morsellised bone graft and synthetic bone graft extenders for impaction grafting.* PhD thesis, The University of Bath, 2003.

[46] Anneliese D. Heiner and Thomas D. Brown. A physical model for simulating fusion of impaction-grafted morselized cancellous bone. *Journal of Biomechanics*, 34:811–814, 2001.

[47] Anneliese D. Heiner, John J. Callaghan, and Thomas D. Brown. A laboratory simulation for morselized bone graft fusion: apparent modulus under operatively based femoral impaction kinetics. *Journal of Biomechanics*, 38:811–818, 2005.

[48] H. Ohashi, A. Koybayashi, Y. Kadoya, Y. Yamano, T. Wakui, and Y. Tanabe. Comparison of mechanical properties of impacted human morsellised cancellous allografts prepared by different bone mills. In *Proceedings of the 45th annual meeting of the Orthopaedic Research Society*, 1999.

[49] Tanya Oram. Investigation of the mechanical properties of impacted morsellised cancellous bone grafts used in revision hip arthroplasty. BEng honours thesis, The University of Edinburgh, 2003.

[50] Gösta Ullmark and Olle Nilsson. Impacted corticocancellous allografts — recoil and strength. *The Journal of Arthroplasty*, 14:1019–1023, 1999.

[51] Gösta Ullmark. Bigger size and defatting of bone chips will increase cup stability. *Archives of Orthopaedic and Trauma Surgery*, 120:445–447, 2000.

[52] Gösta Ullmark. *Morcelised Impacted Cortico-Cancellous Bone Allografts in Revision Surgery for Endoprosthetic Loosening with Osteolysis.* PhD thesis, Uppsala University, Sweden, 2001. Thesis summary.

[53] M. J. Voor, A. Nawab, A. L. Malkani, and C. R. Ullrich. Mechanical properties of compacted morselized cancellous bone graft using one-dimensional consolidation testing. *Journal of Biomechanics*, 33:1683–1688, 2000.

[54] M. J. Voor, J. E. White, J. E. Grieshaber, A. L. Malkani, and C.R. Ullrich. Impacted morselized cancellous bone: mechanical effects of defatting and augmentation with fine hydroxyapatite particles. *Journal of Biomechanics*, 37:1233–1239, 2004.

[55] V. Giddings, S. Kurtz, C. Jewett, J. Foulds, and A. Edidin. A small puch test technique for characterizing pmma used in total joint replacement. In *Proceedings of the 46th Annal Meeting, Orthopaedic Research Society, Florida*, page 0509, 2000.

[56] A. H. Gomoll and T. S. Thornhill. Time and storage dependent changes in mechanical properties of bone cement. In *Proceedings of the 46th Annual Meeting, Orthopaedic Research Society, Florida*, page 0220, 2000.

[57] Seok Bong Kim, Young Jick Kim, Taek Lin Yoon, Su A. Park, In Hee Cho, Eun Jung Kim, and In Ae Kim ang Jung-Woog Shin. The characteristincs of a hydroxyapatite-chitosan pmma bone cement. *Biomaterials*, 25:5715–5723, 2004.

[58] S. Kurtz, V. Giddings, O. Muratoglu, D. O'Connor, W. Harris, and J. Krevolin. Stresses in a highly crosslinked acetabular component for total hip replacement. In *In proceeding of the 46th Annal Meeting, Orthopaedic Research Society, Florida*, page 0222, 2000.

[59] A. Mori, I. Sakuramoto, N. Tomita, S. Kawano, K. Nagata, M. Utsumi, H. Moriya, and K. Kuramoto. Mechanical behaviour of uhmwpe when mixed with vitamin e. In *In proceedings of the 47th Annal Meeting, Orthopaedic Research Society, California*, page 1017, 2001.

[60] J. F. Orr, N. J. Dunne, and J. C. Quinn. Shrinkage stresses in bone cement. *Biomaterials*, 24:2933–2940, 2003.

[61] Lisa A. Pruitt. Deformation, yielding, fracture and fatigue behaviour of conventional and highly cross-linked ultra high molecular weight polyethylene. *Biomaterials*, 26:905–915, 2005.

[62] S. Saha and S. Pal. Mechanical properties of bone cement: a review. *Journal of Biomedical Materials Research*, 18:435–462, 1984.

[63] Carolyn Anglin, Patricia Tolhurst, Urs P. Wyss, and David R. Pichora. Glenoid cancellous bone strength and modulus. *Journal of Biomechanics*, 32:1091–1097, 1999.

[64] Harun H. Bayraktar, Elise F. Morgan, Glen L. Niebur, Grayson E. Morris, Eric K. Wong, and Tony M. Keaveny. Comparison of the elastic and yield properties of human femoral trabecular and cortical bone tissue. *Journal of biomechanics*, 37:27–35, 2004.

[65] M. Cuppone, B. B. Seedhom, E. Berry, and A. E. Ostell. The longitudinal young's modulus of cortical bone in the midshaft of humal femur and uts correlation with CT scanning data. *Calcified Tissue International*, 74:302–309, 2004.

[66] X. Neil Dong and X. Edward Guo. The dependence of transversely isotropic elasticity of human femoral cortical bone on porosity. *Journal of Biomechanics*, 37:1281–1287, 2004.

[67] M. S. Thompson, G. Flivik, R. Juliusson, A. Odgaard, and L. Ryd. A comparision of structural and mechanical properties in cancellous bone from the femoral head and acetabulum. *Proceedings of the IMechE, Part H: Journal of Engineering in Medicine*, 218:425–429, 2004.

[68] Charles H. Turner, Jae Rho, Yuichi Takano, Ting Y. Tsui, and George M. Pharr. The elastic properties of trabecular and cortical bone tissues are similar: results from two microscopic measurement techniques. *Journal of Biomechanics*, 32:437–441, 1999.

[69] Dieter Christian Wirtz, Norbet Schieffers, Thomas Pandorf, Klaus Radermacher, Dieter Weichert, and Raimund Forst. Critical evaluation of known bone material properties to realize anisotropic FE-simulation of the proximal femur. *Journal of Biomechanics*, 33:1325–1330, 2000.

[70] Fraser May. Investigation into the mechanical properties of bone graft used in revision hip arthroplasty. MEng honours thesis, The University of Edinburgh, 2005.

[71] Kenneth Taylor. Investigation into the mechanical properties of bone graft used in revision hip arthroplasty. MEng honours thesis, The University of Edinburgh, 2005.

[72] Abaqus version 6.4 documentation (www.abaqus.com).

[73] W. F. Chen. *Limit Analysis and Soil Plasticity*. Elsevier, 1975.

[74] G. Bergmann, F. Graiche, and A. Rohlmann. Hip joint loading during walking and running measured in two patients. *Journal of Biomechanics*, 26:969–990, 1993.

[75] G. Bergmann, G. Deuretzabacher, M. Heller, F. Graichen, A. Rohlmann, J. Strauss, and G.N. Duda. Hip forces and gait patterns from rountine activities. *Journal of Biomechanics*, 34:859–871, 2001. Including the HIP98 CD, ISBN: 3-9807848-0-0.

[76] D. J. Naylor, G. N. Pande, B. Simpson, and R. Tabb. *Finite Elements in Geotechnical Engineering*. Pineridge Press, Swansea, 1981.

[77] G. Bergmann, F. Graichen, and A. Rohlmann. Is staircase walking a risk for the fixation of hip implants? *Journal of Biomechanics*, 28:535–553, 1995.

[78] G. Bergmann, F. Graichen, J. Siraky, H. Jendrzynski, and A. Rohlmann. Mulitichannel strain gauge telemetry for orthopaedic implants. *Journal of Biomechanics*, 21:169–176, 1988.

[79] G. Bergmann, H. Kniggendorf, F. Graichen, and A. Rohlmann. Influence of shoes and heel strike on the loading of the hip joint. *Journal of Biomechanics*, 28:817–827, 1995.

[80] G. Bergmann, F. Graichen, A. Rohlmann, and L. Holger. Hip joint forces during load carrying. *Clincal Orthopaedics and Related Research*, 335:190–201, 1997.

[81] F. Graichen, G. Bergmann, and A. Rohlmann. Hip endoprosthesis for in vivo measurement of hip joint force and temperature. *Journal of Biomechanics*, 32:1113–1117, 1999.

[82] M. Ipavec, R.A. Brand, D.R. Pedersen, B. Mavcic, V. Kralj-Iglic, and A. Iglic. Mathematical modelling of stress in the hip during gait. *Journal of Biomechanics*, 32:1229–1235, 1999.

[83] W. A. Hodge, R. S. Fijan, K. L. Carlson, R. G. Burgess, W. H. Harris, and R. W. Mann. Contact pressures in the human hip joint measured in vivo. In *Proceeding of the National Academy of Sciences of the United States of America*, volume 83, pages 2879–2883, 1986.

[84] W.A. Hodge, K.L. Carlson, R.S. Fijan, R.G. Burgess, P.O. Riley, W.H. Harris, and R.W. Mann. Contact pressures from an instrumented hip prosthesis. *Journal of Bone and Joint Surgery (Am)*, 71-A:1378–1386, 1989.

[85] E. Ornstein, H. Franzen, R. Johnsson, P. Sandquist, A. Stefansdottir, and M. Sundberg. Migration of the acetabular component after revision with impacted morselized allografts: a radiostereometric 2-year follow-up analysis of 21 cases. *Acta Orthopaedica Scandinavica*, 70:338–342, 1999.

[86] Ewald Ornstein. *Hip revisions with impacted morselized allograft bone and cement*. PhD thesis, Lund University, Sweden, 2002.

[87] J. W. Schimmel. *Acetabular reconstruction with impacted morsellized cancellous bone grafts in cemented revision hip arthroplasty*. PhD thesis, Nijmegen University, Netherlands, 1995.

[88] Bernard Kingston. *Understanding muscles: a practical guide to muscle function*. Chapman & Hall Medical, 1996. ISBN: 0-412-60170-2.

[89] Roy Bechtel. Physical characteristics of the axial interosseous ligament of the human sacroiliac joint. *The Spine Journal*, 1:255–259, 2001.

[90] Greg J. Dakin, Raul A. Arbelaez, Fred J. Molz IV, Jorge E. Alonso, Kenneth A. Mann, and Alan W. Eberhardt. Elastic and viscoelastic properties of the human pubic symphysis joint: effects of lateral impact loading. *Journal of Biomechanical Engineering*, 123:218–226, 2001.

[91] Patrick Hanson and Henrik Sørensen. The lumbosacral ligament: an autopsy study of young black and white people. *Cells Tissues Organs*, 166:373–377, 2000.

[92] M. Vrahas, T. C. Hern, D. Diangelo, J. Kellam, and M. Tile. Ligamentous contributions to pelvic stability. *Basic Science*, 18:271–274, 1995.

[93] N. Zheng, L. G. Watson, and K. Yong-Hing. Biomechanical modelling of the human sacroiliac joint. *Medical & Biological Engineering & Computing*, 35:77–82, 1997.

[94] Roy D. Crowninshield and Richard A. Brand. A physiologically based criterion of muscle force prediction in locomotion. *Journal of biomechanics*, 14:793–801, 1981.

[95] Douglas R. pedersen, Richard A. Brand, and Dwight T. Davy. Pelvis muscle and acetabular contact forces during gait. *Journal of Biomechanics*, 30:959–965, 1997.

[96] Felix E. Zajac. Muscle and tendon: properties, models, scaling, and application to biomechanics and motor control. *Critical Reviews in Biomedical Engineering*, 17:359–411, 1989.

[97] Richard A. Brand, Douglas R. Pedersen, and James A. Friederich. The sensitivity of muscle force predictions to changes in physiological cross-sectional area. *Journal of Biomechanics*, 19:589–596, 1986.

[98] R. D. Crowninshield. Use of optimization techniques to predict muscle forces. *Journal of biomechanical engineering*, 100:88–92, 1978.

[99] R. D. Crowninshield, R. C. Johnston, J. G. Andrews, and R. A. Brand. A biomechanical investigation of the human hip. *Journal of biomechanics*, 11:75–85, 1978.

[100] Anna Fitzsimmons. *Hip joint forces in hip replacement patients and normal subjects during activities of daily living.* PhD thesis, The University of Strathclyde, 1995.

[101] Benedict William Stansfield. *Hip joint forces of 40 to 60 year old normal and total hip replacement subjects during walking and stair, ramp and camber negotiation.* PhD thesis, The Univeristy of Strathclyde, 2000.

[102] M. O. Heller, G. Bergmann, g. Deuretzbacher, L. Dürselen, M. Pohl, L. Claes, N. P. Haas, and G. N. Duda. Musculo-skeletal loading conditions at the hip during walking and stair climbing. *Journal of biomechanics*, 34:883–893, 2001.

[103] B. W. Stansfield and A. C. Nicol. Hip joint contact forces in normal subjects and subjects with total hip prostheses: walking and stair and ramp negotiation. *Clinical biomechanics*, 17:130–139, 2002.

[104] B. W. Stansfield, A. C. Nicol, J. P. Paul, I. G. Kelly, F. Graichen, and G. Bergmann. Direct comparison of calculated hip joint forces with those measured using instrumented implants. an evaluation of a three-dimensional mathematical model of the lower limb. *Journal of biomechanics*, 36:929–936, 2003.

[105] Scott Delp. *Surgery simulation: A computer graphics system to analyze and design musculoskeletal reconstructions of the lower limb.* PhD thesis, Stanford University, 1990.

[106] T. L. Wickiewicz, R. R. Roy, P. L. Powell, and V. R. Edgerton. Muscle architecture of the human lower limb. *Clinical Orthopaedics and Related Research*, 179:275–283, 1983.

[107] James A. Friederich and Richard A. Brand. Muscle fiber architecture in the human lower limb. *Journal of Biomechanics*, 23:91–95, 1990.

[108] Kathryne J. Stabile, Jamie Pfaeffle, Jeffrey A. Weiss, Kenneth Fischer, and Matthew M. Tomaino. Bi-directional mechanical properties of the

human forearm interosseus ligament. *Journal of Orthopaedic Research*, 22:607–612, 2004.

[109] William F. Dostal and James G. Andrews. A three-dimensional biomechanical model of hip musculature. *Journal of biomechanics*, 14:803–812, 1981.

[110] Interactive hip cd (www.primalpictures.com).

Appendix

- Non-linear elastic displacement driven *Abaqus* input file
- Non-linear elastic displacement driven *Fortran* subroutine
- Non-linear elastic force driven *Abaqus* input file
- Non-linear elastic force driven *Fortran* subroutine
- Non-linear visco-elastic *Abaqus* input file
- Non-linear elasto-plastic *Abaqus* input file

Non-linear elastic displacement driven *Abaqus* input file

```
* HEADING
NON-LINEAR ELASTIC DISPLACEMENT DRIVEN TEST
by ANDREW PHILLIPS
*NODE
1,0,0
2,25,0
3,25,100
4,0,100
*ELEMENT,TYPE=CAX4
1,1,2,3,4
*ELSET,ELSET=ES01
1
*MATERIAL,NAME=MCB
*USER DEFINED FIELD
*ELASTIC,DEPENDENCIES=1
 3.00,0.2,,0.0
29.64,0.2,,1.0
56.28,0.2,,2.0
82.92,0.2,,3.0
*SOLID SECTION,MATERIAL=MCB,ELSET=ES01
1
*BOUNDARY
1,2
2,1,2
3,1
*STEP
*STATIC
1,1
*END STEP
*STEP,INC=100
*STATIC,DIRECT
1,100
***DLOAD
**ES01,P3,3
*BOUNDARY
3,2,,-6.2849
4,2,,-6.2849
*END STEP
```

```
*STEP
*STATIC
*END STEP
*STEP,INC=100
*STATIC,DIRECT
1,100
***DLOAD,OP=MOD
**ES01,P3,0.1
*BOUNDARY
3,2,,-2.0776
4,2,,-2.0776
*END STEP
*STEP
*STATIC
*END STEP
```

Non-linear elastic displacement driven *Fortran* subroutine

```
      SUBROUTINE USDFLD(FIELD,STATEV,PNEWDT,DIRECT,T,CELENT,
     +  TIME,DTIME,CMNAME,ORNAME,NFIELD,NSTATV,NOEL,NPT,LAYER,
     +  KSPT,KSTEP,KINC,NDI,NSHR,COORD,JMAC,JMATYP,MATLAYO,LACCFLA)
      INCLUDE 'ABA_PARAM.INC'
      CHARACTER*80 CMNAME,ORNAME
      CHARACTER*3  FLGRAY(15)
      DIMENSION FIELD(NFIELD),STATEV(NSTATV),DIRECT(3,3),
     +  T(3,3),TIME(2)
      DIMENSION ARRAY(15),JARRAY(15),JMAC(*),JMATYP(*),COORD(*)
      !! THIS PART OF THE PROGRAM CALLS THE ELASTIC STRAIN !!
      !! EE has a different meaning in visco-elastic analyses !!
      !! So use E (equal to EE for elastic models) !!
      !! Cannot be combined with plastic models !!
      CALL GETVRM('E',ARRAY,JARRAY,FLGRAY,JRCD,JMAC,JMATYP,MATLAYO,
     +  LACCFLA)
      V1 = -(ARRAY(1)+ARRAY(2)+ARRAY(3))
      V2 = (V1*1.111111111111*3.00)/(2-V1*1.111111111111*26.64)
      FIELD(1) = V2
      RETURN
      END
```

Non-linear elastic force driven *Abaqus* input file

```
* HEADING
NON-LINEAR ELASTIC FORCE DRIVEN TEST
by ANDREW PHILLIPS
*NODE
1,0,0
2,25,0
3,25,100
4,0,100
*ELEMENT,TYPE=CAX4
1,1,2,3,4
*ELSET,ELSET=ES01
1
*MATERIAL,NAME=MCB
*USER DEFINED FIELD
*ELASTIC,DEPENDENCIES=1
 3.00,0.2,,0.0
29.64,0.2,,1.0
56.28,0.2,,2.0
82.92,0.2,,3.0
*SOLID SECTION,MATERIAL=MCB,ELSET=ES01
1
*BOUNDARY
1,2
2,1,2
3,1
*STEP
*STATIC
1,1
*END STEP
*STEP,INC=100
*STATIC,DIRECT
1,100
*DLOAD
ES01,P3,3
***BOUNDARY
**3,2,,-6.2849
**4,2,,-6.2849
*END STEP
```

```
*STEP
*STATIC
*END STEP
*STEP,INC=100
*STATIC,DIRECT
1,100
*DLOAD,OP=MOD
ES01,P3,0.1
***BOUNDARY
**3,2,,-2.0776
**4,2,,-2.0776
*END STEP
*STEP
*STATIC
*END STEP
```

Non-linear elastic force driven *Fortran* subroutine

```
      SUBROUTINE USDFLD(FIELD,STATEV,PNEWDT,DIRECT,T,CELENT,
     +  TIME,DTIME,CMNAME,ORNAME,NFIELD,NSTATV,NOEL,NPT,LAYER,
     +  KSPT,KSTEP,KINC,NDI,NSHR,COORD,JMAC,JMATYP,MATLAYO,LACCFLA)
      INCLUDE 'ABA_PARAM.INC'
      CHARACTER*80 CMNAME,ORNAME
      CHARACTER*3  FLGRAY(15)
      DIMENSION FIELD(NFIELD),STATEV(NSTATV),DIRECT(3,3),
     +  T(3,3),TIME(2)
      DIMENSION ARRAY(15),JARRAY(15),JMAC(*),JMATYP(*),COORD(*)
      !! THIS PART CALLS THE STRESS !!
      CALL GETVRM('S',ARRAY,JARRAY,FLGRAY,JRCD,JMAC,JMATYP,MATLAYO,
     +  LACCFLA)
      V1 = -(ARRAY(1)+ARRAY(2)+ARRAY(3))/3
      FIELD(1) = V1
      RETURN
      END
```

Non-linear visco-elastic *Abaqus* input file, to be used with the displacement driven *Fortran* subroutine

```
* HEADING
NON-LINEAR ELASTIC AND VISCO-ELASTIC TEST
by ANDREW PHILLIPS
*NODE
1,0,0
2,25,0
3,25,100
4,0,100
*ELEMENT,TYPE=CAX4
1,1,2,3,4
*ELSET,ELSET=ES01
1
*MATERIAL,NAME=MCB
*USER DEFINED FIELD
*DENSITY
0.000000001
*ELASTIC,DEPENDENCIES=1,MODULI=LONG TERM
 3.00,0.2,,0.0
29.64,0.2,,1.0
56.28,0.2,,2.0
82.92,0.2,,3.0
*VISCOELASTIC,TIME=PRONY
0.0916,0.0916,100
0.0916,0.0916,1000
0.0916,0.0916,10000
*SOLID SECTION,MATERIAL=MCB,ELSET=ES01
*BOUNDARY
1,2
2,1,2
3,1
*STEP
*STATIC
1,1
*END STEP
*STEP,INC=1000,AMPLITUDE=RAMP
*DYNAMIC,INITIAL=NO
0.03,30,0.001,1
```

```
*BOUNDARY
3,2,,-6.2849
4,2,,-6.2849
*END STEP
*STEP,INC=1000
*DYNAMIC,INITIAL=NO
21.6,21600,0.001,1000
*END STEP
*STEP,INC=1000,AMPLITUDE=RAMP
*DYNAMIC,INITIAL=NO
0.03,30,0.001,1
*BOUNDARY
3,2,,-2.0776
4,2,,-2.0776
*END STEP
*STEP,INC=1000
*DYNAMIC,INITIAL=NO
7.2,7200,0.001,1000
*END STEP
```

Non-linear elasto-plastic *Abaqus* input file, to be used with the force driven *Fortran* subroutine

```
*HEADING
PLASTIC DRUCKER PRAGER CAP TEST
by ANDREW PHILLIPS
USING C7 = 0.5 AND C8 = 5.0
*NODE
1,0,0
2,25,0
3,25,100
4,0,100
*ELEMENT,TYPE=CAX4
1,1,2,3,4
*ELSET,ELSET=ES01
1
*MATERIAL,NAME=MCB
*USER DEFINED FIELD
*ELASTIC,DEPENDENCIES=1
  4.14,0.2,,0.0
 40.90,0.2,,1.0
 77.66,0.2,,2.0
114.42,0.2,,3.0
*CAP PLASTICITY
0.05,40,0.5,0.00,0.005,1
*CAP HARDENING
0.05,0.000000
0.10,0.036464
0.20,0.067294
0.30,0.094001
0.40,0.117557
0.50,0.138629
0.60,0.157691
0.70,0.175094
0.80,0.191102
0.90,0.205924
1.00,0.219722
1.10,0.232630
1.20,0.244755
1.30,0.256187
```

```
1.40,0.267000
1.50,0.277259
1.60,0.287017
1.70,0.296321
1.80,0.305211
1.90,0.313723
2.00,0.321888
2.10,0.329732
2.20,0.337280
2.30,0.344553
2.40,0.351572
2.50,0.358352
2.60,0.364910
2.70,0.371260
2.80,0.377414
2.90,0.383385
3.00,0.389182
3.10,0.394816
3.20,0.400296
3.30,0.405630
3.40,0.410825
3.50,0.415888
3.60,0.420827
3.70,0.425646
3.80,0.430352
3.90,0.434950
4.00,0.439445
4.10,0.443841
4.20,0.448142
4.30,0.452353
4.40,0.456476
4.50,0.460517
4.60,0.464478
4.70,0.468361
4.80,0.472171
4.90,0.475909
5.00,0.479579
*SOLID SECTION,MATERIAL=MCB,ELSET=ES01
*BOUNDARY
1,2
2,1,2
```

```
3,1
*STEP
*STATIC
1,1
*END STEP
*STEP,INC=120
*STATIC,DIRECT
1,120
*DLOAD
ES01,P3,3
*END STEP
```

Publications

The following publications have been produced as a result of this research.

Journal papers

A.T.M. Phillips, Pankaj, A.S. Usmani, and C.R. Howie. The effect of acetabular cup size on the short term stability of revision hip arthroplasty: a finite element investigation. *Proceedings of the IMechE, Part H: Journal of Engineering in Medicine*, 218(4):239–249, 2004.

A.T.M. Phillips, Pankaj, D.T. Brown, T.Z. Oram, C.R. Howie, and A.S. Usmani. The elastic properties of morsellised cortico-cancellous bone graft are dependent on its prior loading. *Journal of Biomechanics*, 39(8), 1517-1526, 2006

Conference papers and oral presentations

A.T.M. Phillips, Pankaj, A.S. Usmani, and C.R. Howie. The effect of bone graft bed depth on the short term stability of revision hip arthroplasty: a finite element investigation. *European Cells and Materials*, 6(Supp. 2)23, 2003. Presented at the annual meeting of the Tissue and Cell Engineering Society, Cardiff, 2003.

A.T.M. Phillips, Pankaj, A.S. Usmani, and C.R. Howie. Numerical modelling of the acetabular construct following impaction grafting. In *Proceedings of Computer Methods in Biomechanics and Biomedical Engineering 6 - Madrid*. FIRST Numerics, 2004. ISBN: 0-9549670-0-3.

A.T.M. Phillips, K.W. Taylor, F.P. May, C.R. Howie, Pankaj, A.J. McLean, and A.S. Usmani. The elastic behaviour of morsellised cortico-cancellous bone: the importance of impaction technique. To be published in the *Journal of Bone and Joint Surgery (British)*. Presented at the annual meeting of the British Hip Society, Wrightington, 2005.

Conference poster presentations

A.T.M. Phillips, Pankaj, A.S. Usmani, C.R. Howie, H. Simpson, and B. Noble. Finite element investigation of the short term stability of the acetabular construct following revision hip arthroplasty. IStructE Young Researchers' Conference, London, 2004. Winner of the 2nd place poster prize.

A.T.M. Phillips, Pankaj, A.S. Usmani, and C.R. Howie. Development of a realistic 3D finite element model of the pelvis including muscle and ligament contributions. Scottish NHS Research Day, Edinburgh, 2005.